The University Of Sheffield.

The Development of Zirconolite Glass-Ceramics for the Disposition of Actinide Wastes

Stephanie May Thornber

A thesis submitted in partial fulfilment for the degree of Doctor of Philosophy

NucleUS Immobilisation Science Laboratory

Department of Materials Science and Engineering

The University of Sheffield

Date: 29th March 2018

Abstract

The UK has been reprocessing spent nuclear fuel since the 1950's [1] and has a resultant 140 tonne stockpile of civil separated PuO_2. Whilst the current UK Plutonium Policy is to fabricate the PuO_2 into Mixed Oxide (MOx) fuel, a significant portion of the stockpile material will be unsuitable for fuel fabrication rendering it as future higher activity waste. As such, there is a need for research and development of wasteforms and treatment methods for immobilising these high activity wastes. The UK has a catalogue of Pu-based wastes known as Pu-residues. These wastes are highly heterogeneous and both chemically and physically variable, thus require a flexible wasteform and waste treatment option that can accommodate the wide variations. It is envisaged that a waste immobilisation route suitable for Pu-residues may conform to future requirements for processing other stockpile material identified as waste.

The Nuclear Decommissioning Authority (NDA) has identified hot isostatic pressing (HIPing) as a potential thermal treatment option for consolidating Pu-residues into suitable wasteforms. HIPing provides a wide operating window and can process multiple wasteform materials into dense, hermetically sealed waste packages ready for long-term storage and eventual geological disposal. The flexibility of HIP means low volume, complex waste-streams, such as Pu-residues, can be treated on a case by case basis and ultimately processed on the same plant line into ceramic, glass-ceramic or metal encapsulated wasteforms. Advantages of HIP for processing PuO_2 wastes, such as the civil stockpile material, also include; significant waste volume reductions, excellent Pu accountancy throughout the plant-line and minimal secondary waste production.

This PhD project aimed to develop high fraction zirconolite glass-ceramics for the disposition of Pu-based higher activity wastes within the UK and utilised hot isostatic pressing as the thermal treatment method throughout. Following on from previous work in this area, conducted by the UK's National Nuclear Laboratory (NNL) and the Australian Nuclear Science and Technology Organisation (ANSTO), this thesis studied zirconolite glass-ceramics for Pu disposition, with primary focus on; formulation optimisation, the effect of CaF_2 as a waste digesting agent, the effect of Cl contamination and waste incorporation behaviour through surrogate studies and PuO_2 validation tests. The main results from this thesis are given below.

Formulation studies revealed a strong correlation between glass composition and the resultant crystalline phase assemblage in the glass-ceramics. An Al_2O_3 rich glass was found to promote a higher yield of zirconolite and subsequently reduced the abundance of accessory phases in the final wasteform. It was hypothesised that changes to the glass structure, with increased levels of Al_2O_3, resulted in a lower solubility of the ceramic forming oxides in the glass phase, thus promoted the formation of zirconolite. Through the formulation studies the stages of phase formation were also investigated and revealed information on intermediate phases and those precipitated from the melt during cooling.

CaF_2 was shown to be an effective waste digestion agent, but was eliminated from the glass-ceramic formulation to reduce the neutron source term of the wasteform. Through formulation investigations and waste incorporation trials, a glass-ceramic formulation and processing route that achieved full waste incorporation and suitable phase assemblages and microstructures, without the need for CaF_2, were achieved. This result meant the neutron source term of the wasteform was reduced by removal of the 100 % abundant ^{19}F ions, which partake in damaging (α,n)-reactions.

Some Pu-residue wastes are contaminated with Cl due to the degradation of PVC (polyvinyl chloride) packaging during storage. The Cl solubility limit of the optimised glass-ceramic formulation was found to be $3-4$ times higher than the conservative upper limit of contamination expected in the wastes. Contamination levels of this magnitude had no detrimental effects on the microstructure or phase assemblage of the glass-ceramics and did not inhibit CeO_2 incorporation.

Incorporation studies confirmed the preferential incorporation of actinide surrogates into the ceramic phase(s). The reduction of Ce was shown to promote the formation of a Ce-rich perovskite phase. The U study achieved near complete digestion of the UO_2 surrogate, with preferential incorporation into the zirconolite phase. The development of the glass-ceramic system and successful results of the surrogate studies, led to the fabrication and characterisation of PuO_2 bearing HIP samples. These samples were part of a validation study towards investigating the effect of controlled oxygen fugacity on the partitioning behaviour of Pu within the glass-ceramic wasteform. The results in this thesis, confirmed complete incorporation of the PuO_2 and achieved microstructures and phase assemblages that were indicative of those obtained through the surrogate studies.

This work has given a new insight into the mechanisms controlling phase formation and waste incorporation, essential for understanding these glass-ceramic wasteforms. This thesis demonstrates a clear progression from process and formulation optimisation, to surrogate studies and the consolidation of PuO_2 containing HIP samples, with promising and exciting results with regards to the development of the wasteform. A major part of this work focused on surrogate studies but the author was able to validate these results with PuO_2 at the Australian Nuclear Science and Technology Organisation (ANSTO). This was a huge advancement of this research that was unattainable within the UK's current capabilities. As well as wasteform development, this work has contributed to the advancements of the HIP technology for processing radioactive waste, through the installation of the Active Furnace Isolation Chamber (AFIC) at The University of Sheffield. The results from this project have a direct impact and current relevance to the UK's Pu management strategy and provides a framework of information that is applicable to the current industrial developments in this area of nuclear waste management.

Acknowledgements

Firstly, I would like to thank my supervisors Prof Neil Hyatt, Dr Martin Stennett and Dr Ewan Maddrell for their guidance and support throughout this project. I would also like to express my gratitude to all co-authors for their contributions to the results and outcomes of this research. Special thanks go to the entire Immobilisation Science Laboratory research group, especially Prof Russell Hand, Dr Claire Corkhill, Dr Laura Gardner, Colleen Mann, Luke Boast and Seb Lawson, for all their help, in the form of knowledge, time, support, alcohol, food, weekend jaunts and continued friendship. I am lucky to have worked with such wonderful people and to call them all dear friends!

Some of the most important people who impacted this project were the technicians throughout the Materials Science Department; Dr Martin Stennett, Mike Bell, Kyle Arnold, Ian Watty Watts, Ben Palmer, John Lowndes, Neil Hind, Frank Fletcher, Dax and Mouldy. They were there in my times of need when equipment was broken or missing, if I was ever short of consumables and when I needed an emotional lift. The technicians as a whole were one of the biggest influences throughout my PhD and I thank you all dearly for your continued help, support and bad jokes.

A special thanks to Dr Daniel Gregg, Dr Lou Vance and the entire ANSTO team for their support and friendship during my placement. It was an opportunity that would not have been possible without their supervision, expert knowledge and years of experience. Similarly, a special thanks to Sam Moricca and AIP for their expert knowledge, services and innovative technologies. I look forward to continuing collaborations and working together again in the future.

My biggest thanks goes to Dr Paul Heath for training me on equipment, providing unofficial supervision, proof reading chapters, listening to my rants, wiping my tears, making me laugh and pouring the wine. I cannot thank you enough or express my gratitude for your constant encouragement, patience, love and support throughout the last 4 years. I would also like to take this opportunity to express my utmost love and respect for all my friends and family who have given their love, encouragement and undoubted support throughout my PhD.

Finally, I would like to thank all funding bodies that funded this studentship and allowed me the opportunity to further my education and embark on a research career within the nuclear industry.

Publications

The author has contributed to the following publications during the production of this thesis:

1. **S. M. Thornber**, P. G. Heath, G. Da Costa, M. C. Stennett, N. C. Hyatt, The effect of pre-treatment parameters on the quality of glass-ceramic wasteforms for plutonium immobilisation, consolidated by hot isostatic pressing, *Journal of Nuclear Materials,* (2017), **485**, pp.253-261
2. E. Maddrell, **S. Thornber**, N. C. Hyatt, The influence of glass phase composition on crystalline phase stability in glass-ceramic wasteforms, *Journal of Nuclear Materials,* (2014), **456**, pp.461-466
3. **S. M. Thornber**, M. C. Stennett, D. Gregg, E. R. Vance, N. C. Hyatt, A preliminary validation study of PuO_2 incorporation in zirconolite glass-ceramics, *MRS advances*, (2018), pp.1-7
4. **S. M. Thornber**, M. C. Stennett, N. C. Hyatt, Investigation of Ce incorporation in zirconolite glass-ceramics for UK plutonium disposition, *MRS advances*, (2017), pp.1-6
5. **S. M. Thornber**, P. G. Heath, E. Maddrell, M. C. Stennett, N. C. Hyatt, Investigation of processing parameters for the consolidation of actinide glass-ceramic wasteforms by hot isostatic pressing, *MRS advances*, (2017), pp.1-6
6. **S. M. Thornber**, E. Maddrell, M. C. Stennett, N. C. Hyatt, The consolidation of glass-ceramic wasteforms by hot isostatic pressing: Sample optimisation, *WM2016 conference proceedings*, (2016), pp.1-6
7. N. C. Hyatt, **S. M. Thornber**, N. Kaltsoyannis, S. Sutherland-Harper, S. M. Pimblott, T. B. Scott, R. Springell, S. Rennie, M. Fairweather, L. Tovey, C. Boxall, J. A. Hriljac, W. E. Lee, C. Gasparrini, R. J. Lunn, D. Read, D. Gregg, E. R. Vance, S. Moricca, R. Persaud, J. Moller, P. G. Heath, The DISTINCTIVE University Consortium: Transforming high activity materials research in the UK, *WM2018 conference proceedings*, (2018), *in-press*
8. N. C. Hyatt, L. J. Gardner, **S. M. Thornber**, C. L. Corkhill, P. G. Heath, M. C. Stennett, R. Hand, Hot isostatically pressed ceramic wasteforms for high dose spent absorbents, *WM2018 conference proceedings*, (2018), *in-press*

The author has presented the work in this thesis at the following UK and international conferences:

Oral Presentations

- **S. M. Thornber**, M. C. Stennett, N. C. Hyatt, D. Gregg, E. R. Vance, The incorporation of U and Pu in glass-ceramic wasteforms, *41st MRS Scientific Basis for Nuclear Waste Management conference*, Sydney, Australia, 1st Nov, 2017. Proceeding paper
- **S. M. Thornber**, M. C. Stennett, N. C. Hyatt, Investigation of Ce incorporation in zirconolite glass-ceramics for UK plutonium disposition, *40th MRS Scientific Basis for Nuclear Waste Management conference*, Boston, USA, 28th Nov, 2016. Proceeding paper
- **S. M. Thornber**, M. C. Stennett, N. C. Hyatt, Consolidation of glass-ceramic wasteforms by hot isostatic pressing: Sample optimisation, *Waste Management Symposium,* Arizona, USA, 9th Mar, 2016. Proceeding paper

- **S. M. Thornber**, M. C. Stennett, N. C. Hyatt, Optimisation of processing parameters for the consolidation of actinide glass-ceramic wasteforms by hot isostatic pressing, *39th MRS Scientific Basis for Nuclear Waste Management conference,* Montpellier, France, 5th Nov, 2015. Proceeding paper
- **S. M. Thornber**, M. C. Stennett, E. Maddrell, N. C. Hyatt, The development of glass-ceramic wasteforms by hot isostatic pressing for actinide immobilisation, *IAEA meeting and workshop*, Manchester, UK, 3rd Jun, 2015
- **S. M. Thornber**, M. C. Stennett, E. Maddrell, N. C. Hyatt, The development of glass-ceramic wasteforms by hot isostatic pressing for actinide immobilisation, *1st DISTINCTIVE annual conference*, Sheffield, UK, Apr 15th, 2014
- **S. M. Thornber**, M. C. Stennett, E. Maddrell, N. C. Hyatt, Glass-ceramics and full ceramics for the immobilisation of plutonium residues, *NDA waste packaging and storage group meeting,* Sellafield, UK, 19th Nov, 2014

Poster Presentations

- **S. M. Thornber**, M. C. Stennett, N. C. Hyatt, The development of glass-ceramic wasteforms for Pu-bearing waste-streams, *DISTINCTIVE annual symposium*, Bristol, UK, April 2016
- **S. M. Thornber**, E. Maddrell, P. G. Heath, M. C. Stennett, N. C. Hyatt, Optimisation of zirconolite actinide glass-ceramics consolidated by hot isostatic pressing, *DISTINCTIVE annual symposium*, Sheffield, UK, April 2015
- **S. M. Thornber**, E. Maddrell, M. C. Stennett, N. C. Hyatt, Zirconium based glass-ceramics and full ceramics as future wasteforms for plutonium immobilisation, *Thermal Treatment of Radioactive Wastes*, Birchwood, UK, January 2015
- **S. M. Thornber**, E. Maddrell, P. G. Heath, M. C. Stennett, N. C. Hyatt, Hot isostatic pressing of glass-ceramics for the long-term disposal of plutonium, *Radioactive Frontiers in Decommissioning and Nuclear waste management*, Lancaster, UK, November 2014

The author has received the following awards for the work presented in this thesis:

Awards

- The Roy G. Post Graduate Scholarship – Waste Management Symposium, 2016
- Longenecker and Associates Inc. Scholarship award – Waste Management Symposium, 2016
- Industrially sponsored research student poster prize – The University of Sheffield, sponsored by TATA steel, 2015
- NDA best oral presentation prize – DISTINCTIVE annual conference, 2015

Contents

1 Introduction

As of April 1st 2016, the UK holds over 130,000 m^3 of nuclear waste requiring treatment and consolidation for long-term storage and disposal [2]. A further 4,360,000 m^3 is expected to arise in the future, with the vast majority arising from the decommissioning of all current reactor sites. These values include medical waste, research and development waste and waste generated from nuclear power, all of which require suitable treatments for safe disposal.

The UK classifies nuclear waste into four main categories; very low level waste (VLLW), low level waste (LLW), intermediate level waste (ILW) and high level waste (HLW), based on their radioactivity and heat levels. The bounds of each category are defined as follows [3]:

- **VLLW** – radioactivity must be below 4 MBq per tonne of beta / gamma activity and is disposed of in specified landfill sites.
- **LLW** – radioactivity levels above the threshold for VLLW and up to 4 GBq per tonne of alpha or 12 GBq per tonne for beta and gamma activity. These wastes are currently disposed of in a low level waste repository (LLWR) at a near surface facility site in Cumbria UK, which has been in operation since 1995. LLW constitutes 95 % of the total volume of all nuclear waste but only a minor percentage of the overall activity.
- **ILW** – wastes with activity levels that exceed the upper alpha limits of LLW but do not generate heat above 2 kW/m^3 [4]. Due to the high activity and long-lived isotopes in ILW, an engineered wasteform is required to encapsulate or immobilise the waste ready for geological disposal. Cementation is currently the primary route for treating ILW [5].
- **HLW** – wastes with activity levels equal to and above ILW that generate heat due to energy output from radionuclide decay. Immobilisation is essential, with vitrification being the primary treatment option of spent fuel raffinates in the UK. The immobilised waste is kept in highly engineered storage facilities whilst awaiting construction of a geological disposal facility (GDF) for long-term storage. HLW makes up the smallest volume of nuclear waste but constitutes 95 % of all activity.

For final disposal of radioactive waste, the UK plans to construct a multi-barrier geological disposal facility [6,7]. The highly engineered facility will provide a safe and secure place for the final disposal of both the ILW and HLW inventory in the UK. The multi-barrier approach utilises multiple layers of containment to protect against radionuclide release to the geosphere during the long-term storage of the waste. Figure 1.1 is a schematic of the GDF concept detailing the individual barriers. The primary barrier is the wasteform in which the radionuclides are immobilised. The wasteform canister provides the second barrier and aids handling and transportation of the wasteform. As part of the safety case, the GDF design will handle ILW and the heat generating HLW differently [6]. To avoid an increase in temperature in the HLW repository, the waste packages are expected to be deposited through shafts and tunnels and kept separate from the larger ILW vaults. Individual ILW waste packages will likely be packed into 3 m^3 boxes and stacked on-top and along-side each other in the repository. A backfill (either cement or bentonite clay) will fill all available space within the repository before final closure. The final barrier is the host rock surrounding the repository set approximately 500 – 1000 m below the Earth's surface. At this depth the movement of ground water is very slow, further minimising the risk of water ingress, leaching of the primary wasteform barrier and transport of radionuclides to the biosphere.

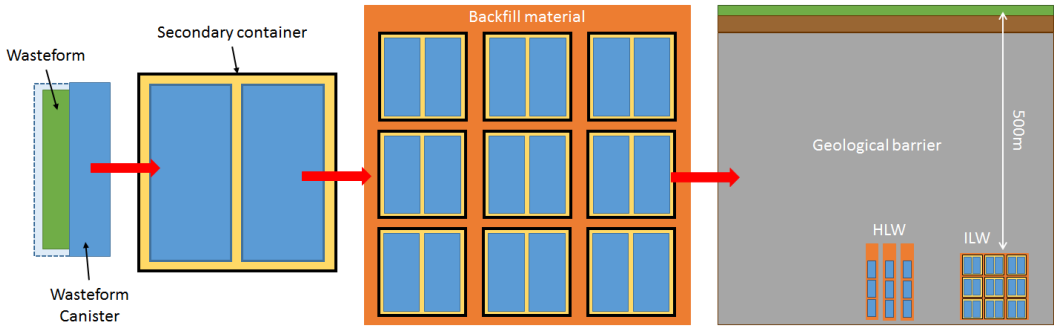

Figure 1.1: Schematic of the multi-barrier concept proposed for the geological disposal facility.

1.1 Plutonium material in the UK

The UK currently stores over 120 tonnes of separated civil PuO_2 obtained by fuel reprocessing (Table 1.1). At the end of the Thermal Oxide Reprocessing Plant's (THORP) operative life in 2018, the total stockpile is estimated to reach 140 tonnes [8]. In 2009 the NDA began a

"credible options analysis" that detailed three possible options for the long-term management of the Pu inventory [9];

1) Immobilisation and disposal as waste.
2) Reuse as MOx (mixed oxide) fuel before eventual disposal as spent nuclear fuel.
3) Continued storage and management.

The Department of Energy and Climate Change (DECC)[1] later collated the data to determine a credible option to move forward with [10,11]. In 2013 the UK government decided to fabricate the PuO_2 into MOx fuel [8,12].

Table 1.1: Summary of the National total and breakdown of Pu stock in the UK as of 31st December 2014. (Taken from the Office of Nuclear Regulations (ONR) website [13])

National totals 31st December 2014	**Rounded to 100 kg Pu, with quantities less than 50 kg reported as such (Tonnes)**
Unirradiated separated Pu in product stores at reprocessing plants.	122.1
Unirradiated separated Pu in the course of manufacture or fabrication and Pu contained in unirradiated semi-fabricated or unfinished products at fuel or other fabricating plants or elsewhere.	0.8
Pu contained in unirradiated MOx fuel or other fabricated products at reactor sites or elsewhere.	1.9
Unirradiated separated Pu held elsewhere.	1.5
Total	**126.3**

Whilst the current UK government policy is to reuse the PuO_2 as an energy source by fabricating MOx fuel, a significant portion of the material will not be fit for purpose and will require immobilisation. The current policy identifies the need for immobilisation options for these materials and has not closed the discussion on the alternative options for Pu management [11]. As such, it is possible that immobilisation technologies designed for

[1] Currently known as the Department of Business, Energy and Industrial Strategy (BEIS).

Pu-based waste-streams may be applied to the bulk separated PuO_2 stockpile material in the future.

As well as the bulk PuO_2 stockpile, there is a category of Pu based wastes known as Pu-residues. These materials have higher Pu concentrations than PCM (plutonium contaminated material) intermediate level wastes, but are not economically viable for fuel fabrication thus have been classified as higher activity waste-streams [14]. These wastes originate predominantly from early research and development work, but also include secondary wastes from reprocessing and MOx fuel production, and contaminated material from the PuO_2 stockpile that has been deemed unsuitable for fuel fabrication [15,16]. Originally 0.5 tonnes of Pu-residues were identified, however this value has since grown and has the potential to significantly increase as the civil PuO_2 stockpile is considered for immobilisation [15,17]. Pu-residues are chemically impure and physically diverse and have been categorised into > 50 classes by the NDA [18]. Due to the complexity and high variability of these wastes each one will need to be considered on a case by case basis when selecting suitable disposition routes.

1.2 Wasteform requirements

For a wasteform to be accepted for disposal it must satisfy the minimum wasteform requirements set out by both international and national regulatory bodies; the International Atomic and Environment Agency (IAEA), Nuclear Decommissioning Authority (NDA) and Radioactive Waste Management (RWM) [19–22]. Specifications cover both the wasteform and the wasteform container to satisfy; health and safety requirements during consolidation, handling, storage and transportation, as well as social and economic factors, practicality and safety requirements for eventual geological disposal. The main safety requirement stated by IAEA is to "*confine and retain radioactivity in the* waste" [20]. The IAEA outlines some essential requirements for waste packages [19–21] including;

- **Labelling** – all waste packages must be identifiable. Each package must be labelled / marked sufficiently with correct documentation available detailing the contents, radionuclide inventory, dose rate, heat output and waste origin, so future identification can be made.

- **Compliance**: each waste package must comply with transport, storage and disposal requirements, such as the external dose rate, surface contamination levels and authorised radionuclide limits. The physical dimensions, mass, manoeuvrability and ability to stack the waste packages in storage, must also be assured.
- **Characterisation**: analysis of the waste, wasteform properties, materials and method compatibility and all processing steps, must be conducted and reported to ensure suitable wasteform performance and an ease of processing before commercial acceptance. It is important to assess the mechanical, chemical and physical properties of the wasteform, as well as "*degradation-induced changes*" [20].

Consideration should be given to the many properties and potential hazards applicable to all stages of the waste life cycle, during the development of waste treatment options and wasteform formulations. Some properties and hazardous factors to be considered are listed below [20]:

- **Mechanical:** mechanical and compressive strength, thermal expansion, impact resistance, fire resistance, corrosion resistance.
- **Physical:** thermal stability and heat generation, free liquid content, tolerance to radiation damage, leach resistance, physical stability and long-term integrity.
- **Chemical:** chemical flexibility, compositional limits, loading capacity, chemical toxicity, organics and / or combustible materials, chemical durability, leach resistance and thermal stability, resistance to gas generation and devitrification.
- **Processing:** details of each processing step, parameters and limitations, container filling techniques, contamination control, batch / continuous feed, secondary wastes produced and arrangements for temporary storage, decontamination and maintenance.

Other factors to consider include; cost, remote processing and handling, total volumes and process flexibility (processing range and flexibility to treat different wastes and materials).

Vitrification is the primary immobilisation route for HLW raffinates, but Pu-rich wastes are problematic for vitreous wasteforms. Pu has a limited solubility / loading capacity in vitreous materials and can separate from the glass melt [23]. The high density of PuO_2 and associated compounds can result in segregation in the melt causing a heterogeneous distribution

through the final wasteform, which can be detrimental to its proliferation resistance and final wasteform performance properties [24]. Processing limitations are also problematic for vitrifying Pu-based wastes, because of the need to maintain melt properties for handling and pouring, without affecting the wasteform properties, but also, because of the need for accurate materials accountancy. This can be difficult due to residues remaining in the melter after discharging the melt. As a result, alternative wasteform materials and consolidation techniques are under review for processing the complex and variable Pu-residue waste-streams. The NDA has identified hot isostatic pressing (HIPing) as a potential consolidation technique for treating these wastes, with potential wasteform materials including glass-ceramics, full ceramics and metallic encapsulation [18,25,26]. This thesis will investigate the use of HIP to consolidate glass-ceramic wasteforms for the disposition of Pu-residue wastes.

1.3 Project aims

This project intended to develop a high fraction zirconolite glass-ceramic wasteform, consolidated by hot isostatic pressing, for the disposition of Pu-based higher activity wastes within the UK. To achieve this the following aims were established:

1) **To determine a processing route and glass-ceramic formulation that optimises the wasteform quality and crystalline phase assemblage.**

The sample preparation process was studied with the intention to establish a set of parameters for attaining high quality, reproducible HIP samples. Once a processing route was determined, formulation investigations were performed that examined the effect of glass composition on the crystalline phase assemblage output. Previous work by the National Nuclear Laboratory (NNL) highlighted the dependence of the crystalline phase assemblage on glass composition due to an error made when batching, but it was not investigated further. This thesis aimed to underpin the relationship between glass composition and the glass-ceramic phase assemblage, to determine an optimised formulation that maximised the yield of zirconolite. To do so, a matrix of samples with different glass compositions and glass fractions was fabricated to produce a qualitative phase map of the crystalline phases attained in each sample.

2) **To investigate the effectiveness of CaF_2 as a waste digesting agent and to minimise its requirement within the glass-ceramic wasteform to reduce its overall neutron source term.**

The formulations studied in this thesis did not include CaF_2 like previous glass-ceramic formulations. CaF_2 is believed to aid waste digestion but increases the neutron source term of the wasteform due to the 100 % abundance of ^{19}F that partakes in (α,n)-reactions. This thesis aimed to establish a glass-ceramic system that obtains a high fraction of zirconolite and achieves successful waste incorporation without the addition of CaF_2. Waste incorporation experiments were performed with CeO_2, with and without CaF_2 additions, to determine whether or not CaF_2 does improve waste digestion. The effects of milling parameters and reducing conditions were also studied as alternatives to CaF_2 to achieve better waste incorporation.

3) **To determine the Cl solubility limit of the optimised glass-ceramic formulation.**

It is known that some Pu-residues are contaminated with Cl impurities from the degradation of PVC packaging. It was important to investigate if the new glass-ceramic formulation could accommodate Cl into its structure to levels in excess of those expected in the wastes. The glass-ceramics were fabricated with increasing levels of Cl impurities, from 0.3 – 2.5 wt. %, to determine the Cl solubility limit of the glass-ceramic system. CeO_2 incorporation was also studied to ensure the Cl impurities did not affect waste digestion.

4) **To investigate the waste incorporation behaviour of the glass-ceramic wasteform using CeO_2 and UO_2 surrogates, before progressing to PuO_2 incorporation experiments.**

Confirmation of preferential CeO_2 incorporation into the target zirconolite phase led to the fabrication and characterisation of U and Pu bearing samples. Glass-ceramic wasteforms are designed to partition actinides into the ceramic phase and incorporate the miscellaneous waste material in the glass, yet the effect of different reducing conditions on the behaviour of the actinide partitioning has not been previously studied. Due to the limitations of Ce and U as Pu surrogates, it was necessary to perform these experiments with PuO_2. The Ce and U samples provided a suite of data that proved the performance of the glass-ceramic system was adequate before progressing to the Pu. A suite of Pu-doped samples were fabricated and characterised at the Australian Nuclear Science and Technology Organisation (ANSTO)

with different redox agents and canister materials, to promote varying degrees of Pu reduction. The aim was to gain an understanding of how different reducing conditions affect the behaviour of the Pu and the performance of the glass-ceramic as an actinide bearing wasteform.

2 Literature Review

This chapter provides a summary of information and previous work considered to be relevant to this thesis. The aim is to provide the reader with an understanding of the relevance this thesis has within the area of research and its contribution to existing knowledge.

2.1 The waste

2.1.1 Plutonium

Plutonium (Pu) is a radioactive element produced in nuclear reactors. Pu is not a naturally occurring element and is made through neutron capture by ^{238}U. Many isotopes of Pu have been characterised, with the most common being; ^{238}Pu, ^{239}Pu, ^{240}Pu, ^{241}Pu and in smaller quantities, ^{242}Pu and ^{244}Pu. These isotopes are all radioactive and undergo alpha decay, except ^{241}Pu which undergoes beta decay to ^{241}Am. The half-life and specific activity of each isotope are summarised in Table 2.1 [27].

Pu was produced in the 1940s for use in nuclear weapons during World War II. ^{239}Pu is the most common Pu isotope generated in nuclear reactors and is utilised in nuclear weapons due to its fissile nature [28]. ^{241}Pu is also fissile but less abundant. The quality of Pu and potential use for nuclear weapons is determined by its ^{240}Pu concentration. ^{240}Pu is prone to spontaneous fission thus must be limited in weapons grade material. Isotopes ^{238}Pu, ^{242}Pu and ^{244}Pu are not fissile but can be fissionable if bombarded by neutrons with high enough energy [28].

Table 2.1: Summary of radioactive properties of Pu isotopes. (Adapted from [27])

Isotope	Half-life (y)	Specific Activity (MBq/g)	Decay Mode	Fissile?
^{238}Pu	88	629,000	α	N
^{239}Pu	24,000	2,331	α	Y
^{240}Pu	6,500	8,510	α	spontaneous
^{241}Pu	14	3,700,000	β	Y
^{242}Pu	380,000	148	α	N

The concentrations of each individual isotope within a waste-stream depend on many factors including the type of reactor, type of fuel, burn-up of the fuel and age of the material [29]. All these factors, as well as; the composition of the waste, whether or not it produces heat and the concentrations of daughter products such as ^{241}Am and ^{235}U, must be taken into account when considering potential treatment options and immobilisation routes for each waste-stream. For Pu material to be suitable for mixed oxide (MOx) fuel fabrication, it should consist of two-thirds fissile isotopes, ^{239}Pu and ^{241}Pu. At this level, approximately 7 – 11 % Pu is mixed with depleted U [30]. If weapons grade Pu is used, only 5 % is needed for effective MOx fuel due to the purer nature of the material and higher concentration of fissile isotopes.

Fission is the splitting of a nucleus when hit with a high energy neutron. The nucleus splits into two smaller nuclei and emits 2 – 3 high energy neutrons that can cause further fission events. Criticality in a nuclear reactor is when the chain of fission events is self-sustaining, such that one or more of the emitted neutrons from one fission event, go on to cause fission of another atom [31]. This, however, must be avoided in actinide wasteforms. One concern when disposing of Pu-based wastes is criticality safety due to the wastes typically having higher fissile material concentrations than spent nuclear fuel (SNF) [32]. There is a risk that the rate of fission events / neutron production leads to a supercritical system with an uncontrollable fission chain reaction [33]. Figure 2.1 shows the decay chain of ^{239}Pu. ^{239}Pu decays to ^{235}U meaning the amount of fissile material remains the same despite the decay and can lead to potential criticality concerns [34]. Criticality control is essential in actinide bearing wasteforms to ensure long-term integrity of the waste package and long-term safe immobilisation of the radionuclides.

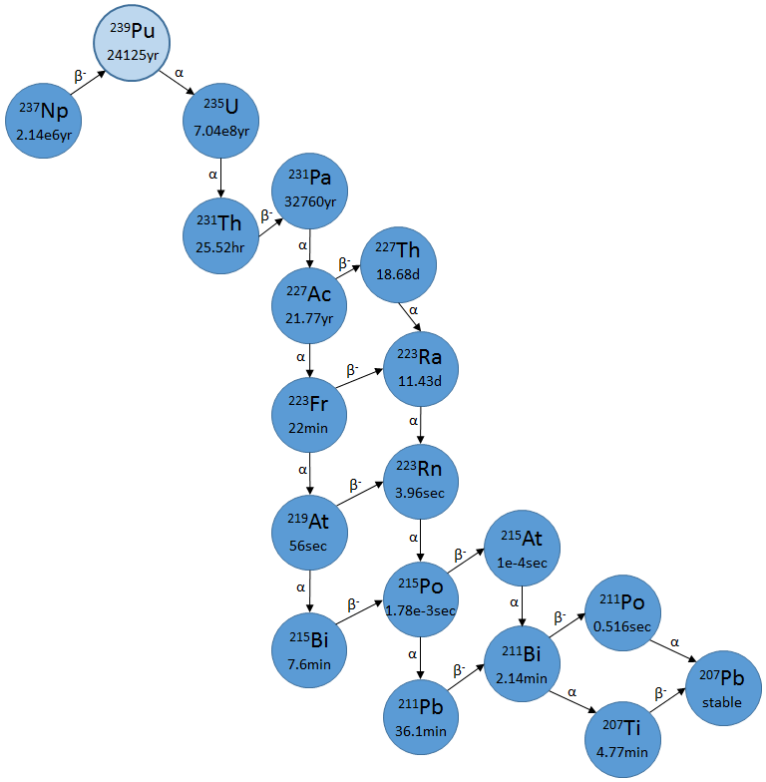

Figure 2.1: Decay chain for ^{239}Pu. (Adapted from [35])

One way to avoid criticality is to dilute the fissile material with non-fissile material or by having lower waste loadings. This means a higher number of waste packages need to be processed, stored and disposed of, which may have significant cost implications. Another way is to incorporate neutron absorbing elements such as B, Hf or Gd [34]. Neutron absorbers can capture neutrons in the wasteform to maintain a sub-critical system. However, there is a risk that neutron absorbers may be leached out of the wasteform faster than the actinides. This could lead to a criticality event during storage or long-term disposal, especially if there is a significant concentration of long-lived radioisotopes remaining. Each radionuclide has a different half-life and it is important that long-lived actinides and daughter products are retained in the wasteform to ensure the longevity of the wasteform.

2.1.2 Reprocessing

At the end of its reactor life, spent nuclear fuel (SNF) still contains up to 97 % of the original U and 1 % Pu. The PUREX (plutonium uranium redox extraction) process utilises solvent extraction to separate U and Pu from SNF. The THORP plant at Sellafield has operated the PUREX process since 1994 [36,37].

The SNF is first stripped of its zircaloy cladding and the fuel pellets are dissolved in nitric acid [38]. Any solids and undissolved particles in the aqueous solution are removed by a semi-continuous centrifuge mechanism and the fluid is conditioned to ensure the correct acidity, U concentration and Pu oxidation are achieved [38,39].

The PUREX process separates compounds by first mixing two immiscible liquids together [39]. The nitric acid solution (aqueous phase) is mixed with an organic phase TBP (tri-butyl phosphate). Control of the Pu oxidation state is important to achieve separation, first from the fission products and minor actinides and then to separate it from the U. The U and Pu first transfer to the organic phase, separating them from the fission products and minor actinides in the aqueous phase that are then dealt with as waste. The oxidation conditions are then controlled to ensure Pu returns to the aqueous phase to separate it from the U [39]. The Pu^{4+} is reduced to the insoluble Pu^{3+} state, which separates into the aqueous phase. The two products are then extracted as solids and treated and stored separately. THORP achieves the soluble Pu^{4+} oxidation state by cooling the fluid to 60 °C and blasting NO_2 through as a temporary reducing atmosphere [38].

2.1.3 Pu-residues

Pu-residues are a category of Pu-based waste-streams that originate from multiple sources and are highly heterogeneous, both chemically and physically. While at present, the civil separated PuO_2 stockpile is not classified as waste, it is estimated that about 5 % of the total PuO_2 stockpile will be classified as waste for immobilisation in the future [37,40]. The Pu concentration in residues varies from high to low but is always in excess of plutonium contaminated materials (PCM) classification. The physical forms of the wastes include powders, caked sludges, fuel pellets and fuel pins [15,16,41]. These wastes are currently stored at the UK's Sellafield site in aluminium or stainless steel canisters and many are contained in PVC packaging inside.

The NDA has categorised Pu-residues into > 50 classes, each of which has its own challenges associated with treatment and disposal [18]. By sub-dividing the residues into smaller categories, different wasteforms can be developed for specific groups of wastes. Multiple wasteform matrices have been studied for Pu disposition including glass, ceramics and glass-ceramics [18]. Glass-ceramics are a leading option for low purity residues containing

glass formers, where the glass phase is intended to accommodate the impurities and the ceramic phase immobilises the actinides. Full ceramics are considered more favourable for high purity streams as higher actinide loadings can be achieved, and metallic encapsulation for solid wastes, such as fuel rods and cladding [15].

Some Pu-residues contain significant proportions of refractory compounds (e.g. ZrO_2 and Al_2O_3) that have limited solubility in vitrified materials and have very high melting temperatures, which make efficient incorporation into glass wasteforms difficult [23]. Some material has been classified as waste due to Cl contamination from the degradation of the PVC storage liners [42]. The Cl poses additional difficulties for processing due to its volatility. Whilst in most residues actinides are present in oxide forms, some streams contain both PuO_2 and Pu metal particles thus require flexible processing and atmospheric control [17]. These compositional challenges are to be considered in order to produce high performance wasteforms suitable for long-term disposal and processing methods that are time and cost efficient.

The treatment and handling of Pu has its hazards and challenges including; safety and criticality concerns, long-term properties, cost and the socio-political impact. Wasteforms for Pu disposition need to meet specific requirements and be designed around the waste [34]. The key requirements considered by both the US's Department of Energy (DOE) [24,43,44] and the UK's Department of Energy and Climate Change (DECC) [22] in any decision towards the disposition of Pu include [34];

- **High waste loading:** high waste loadings are desirable to minimise the number of waste packages to be processed and maintained. At the same time, there are limitations to the loading of Pu to ensure criticality control.

- **High durability:** successful retention of radionuclides during storage and geological disposal is desirable for a wasteform containing short and long lived radionuclides. Both short-term and long-term leaching resistance should be proven through scientific demonstrations (e.g. dissolution tests, natural analogues).

- **Flexibility:** the heterogeneous nature of Pu waste-streams means any wasteform must be flexible to accommodate a vast array of elements and impurities without

detrimental effects to the overall performance and retention of Pu and other actinides. This typically requires a multiphase system.

- **Ease of processing:** as well as being flexible to process all variations of Pu-residues, the treatment process needs to be cost effective, feasible, safe for both workers and the environment (e.g. worker exposure dose and off-gases to atmosphere), allow for accurate actinide accountancy and be compatible with the waste and precursor materials.

- **Proliferation resistance:** as a minimal requirement for proliferation resistance the spent fuel standard must be satisfied to ensure the "*plutonium is roughly as inaccessible for weapons use as the much larger and growing stock of plutonium in civilian spent fuel*" [45].

In addition to the wasteform requirements, both DOE [24] and DECC [12] consider five main aspects when considering any decision towards immobilising Pu wastes. These include environmental impact, personnel health and safety, proliferation resistance, cost, wasteform performance within a repository environment and the technological readiness and application of the proposed processing route.

2.2 Glass

For a material to be categorised as a glass it must have a liquid-like structure when solid and continuously return to a liquid when heated [46]. Shelby describes a glass as "*an amorphous solid completely lacking in long range order, periodic atomic structure and exhibiting a region of glass transformation behaviour*" [47]. According to Shelby's definition, for a material to be a glass it must lack long range order and have a glass transformation range [47]. The lack of long range order confers to a glass its amorphous nature although the glass still has short range structure comprising well defined M – O bond lengths and M – O – M angles. To describe a glass transformation range, an enthalpy versus temperature plot (or V-T diagram), such as Figure 2.2 is used [47]. If a liquid is cooled to below its melting point and experiences a sudden drop in enthalpy, the liquid undergoes atomic rearrangement to form a crystalline structure. If the liquid is cooled fast enough that crystallisation does not take place, a supercooled liquid is formed.

As the temperature is dropped, gradual atomic rearrangement takes place. However, as the temperature cools the viscosity increases, making atomic rearrangements increasingly difficult, thus the equilibrium structure can no longer be reached during the given experimental time. Eventually the viscosity is so great that no more atomic rearrangements can take place, resulting in the non-equilibrium structure becoming fixed. When in this "frozen state" the material is referred to as being vitreous. The temperature region between the frozen and equilibrium states is often defined by a single temperature; the glass transition temperature (T_g), as an indication of the transformation range. T_g can be affected by many factors including experimental technique, heat rate and glass composition, thus is only used as a guide not as a true material property [47]. It is defined as the temperature at which viscosity is 10^{13} P, which is central to the approximated viscosity range for the glass transformation range (10^8 – 10^{15} P) [46,48].

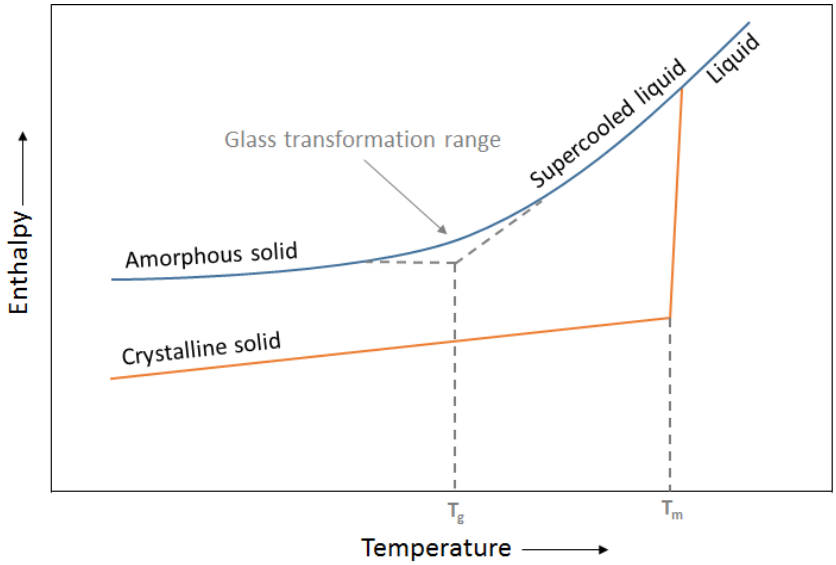

Figure 2.2: Enthalpy versus temperature diagram showing the stages of glass formation compared to the solidification of a crystalline solid. T_g is the glass transition temperature and T_m is the melting temperature. (Adapted from [47])

The primary type of glass used in nuclear waste disposal is borosilicate glass. In sections *2.2.1* and *2.2.2*, the basic glass structure and the specific roles of Na, Al and B within (sodium) - aluminoborosilicate glasses relevant to this thesis, are presented.

2.2.1 Glass structure

Most descriptions of glass structures are based on the principles set out by Zachariasen for glass formation [49]. Zachariasen stated that a glass must form a 3-D network but contain no periodicity or symmetry. For this to be true the bonding between atoms must allow more bond angles and bond lengths than in a crystalline equivalent, where specific angles and distances are required to keep the long range order. Due to the random and variable nature of the atomic bonds in a glass matrix, the energy associated with each bond will be different. This concurs with the "continuous rearrangement" discussed by Shelby and Varshneya with regards to the glass transformation range, such that, the migration of atoms and number of broken bonds increases gradually with temperature until the liquid state is reached [46,47]. In comparison, because all bonds in a crystalline structure are equal they will dissociate at the same temperature resulting in a sudden and abrupt increase in enthalpy as shown in the V-T diagram in Figure 2.2.

Zachariasen's model depicts four considerations that must be obeyed for oxides to form a glass structure [49]:

1) Oxygen atoms may be linked to a maximum of 2 cations.
2) The number of oxygens surrounding a cation must be small (triangles / tetrahedra).
3) The polyhedra may only link by sharing corners, not faces or edges.
4) To create a 3-D network at least 3 corners of a polyhedra must be shared.

Zachariasen's rules are known to be insufficient when considering some glass networks and bulk glass structures, however, later models are derived from these four original points, with scientific work supporting Zachariasen's model [50–52]. Greaves used EXAFS spectroscopy to investigate the environment of modifier atoms within a glass network [51]. Greaves built upon the "Continuous Random Network" (CRN) principle set out by Zachariasen's rules, to generate the "Modified Random Network" (MRN). Extended X-ray absorption fine structure (EXAFS) was used to study the environments of modifier ions, which are highly sensitive to the morphology of the network, to gain information on the structure of the glass. Modifier ions are known to break up the glass network but Greaves identified that increased concentrations of modifiers generate channels through the glass structure (Figure 2.3). These channels of ionic bonding within the covalently bonded network lower the viscosity of the

glass and allow for better migration through the structure. This modified random network combines the CRN with the local structure and non-bridging oxygens of the modifying cations [51].

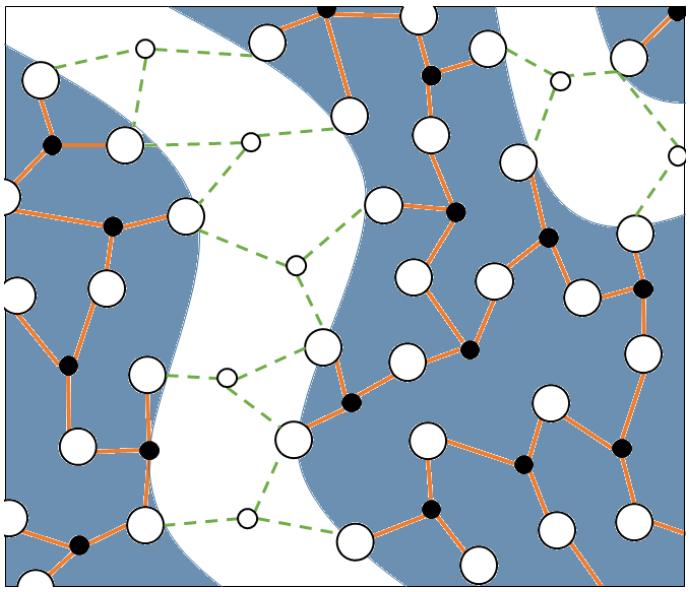

Figure 2.3: Schematic representation of the modified random network (MRN) associated with glass structure. (Adapted from [51])

Silicate glass is the most common type of glass where the primary component is SiO_2. At high processing temperatures, around 1800 °C, SiO_2 can form a usable glass without the need for other additives. Other elemental additions are utilised to control the processing parameters, manageability of the glass and the final properties with respect to the desired application. Most glasses consist of network formers, network modifiers, and intermediates [46,47]. These are defined as:

- **Network formers:** are the primary components of a glass structure, consisting of cation – anion bonded polyhedra, connected in short and medium range orders. The nomenclature of the glass identifies the main network formers, for example; significant levels of B_2O_3 and SiO_2 make borosilicate glasses. Some examples of network formers include SiO_2, B_2O_3 and P_2O_3.
- **Network modifiers:** will not favourably form a glass network on their own but instead break up the network and alter the structure and properties of the glass as desired. Some examples of network modifiers are flux agents and property modifiers. Flux agents such as alkali oxides (e.g. Na_2O) are added to reduce the

temperature required to form the glass melt. Fluxing agents can also undesirably affect the properties of the glass such as its durability behaviour.

- **Intermediates:** are oxides that can act as either glass formers or glass modifiers depending on the conditions and environment but are not as amenable to forming a glass individually (e.g. Al_2O_3).

The structural bonding of cations and anions in the glass network leads to regions of short and medium range order. Short range order refers to individual polyhedra of oxygens bonded to individual cations. Si is usually found tetrahedrally co-ordinated to oxygen, B can either be 3-fold or 4-fold co-ordinated and Al is known to exist in 4-, 5- and 6-fold co-ordination [53].

The random nature of glass structures results from small variations in bond angle and rotation between network polyhedra. The connectivity of a glass network also refers to the concentration of bridging and non-bridging oxygens (BO and NBO, respectively) [53,54]. In an idealistic glass structure all oxygen anions bridge two polyhedra together. NBOs refer to oxygens that do not connect two polyhedra and occur due to impurities and defects in the glass.

2.2.2 Role of elemental additions

B_2O_3

B_2O_3 was originally added to silicate glasses to improve their process-ability and final performance properties. B_2O_3 additions can help to lower the viscosity of the melt and inhibit unwanted crystallisation, as well as improve thermal expansion resistance and mechanical strength [55]. The role of B_2O_3 in the glass network is as a network former but the structural units formed depend largely on the overall composition of the glass. B can be integrated in 3- or 4-fold co-ordination but also forms larger intermediate structures within the glass network. Boroxyl species combine multiple BO_3 and BO_4 units into larger structures, such as those in Figure 2.4 The abundance of these structures is known to vary with composition and concentration of alkali oxides [54,55].

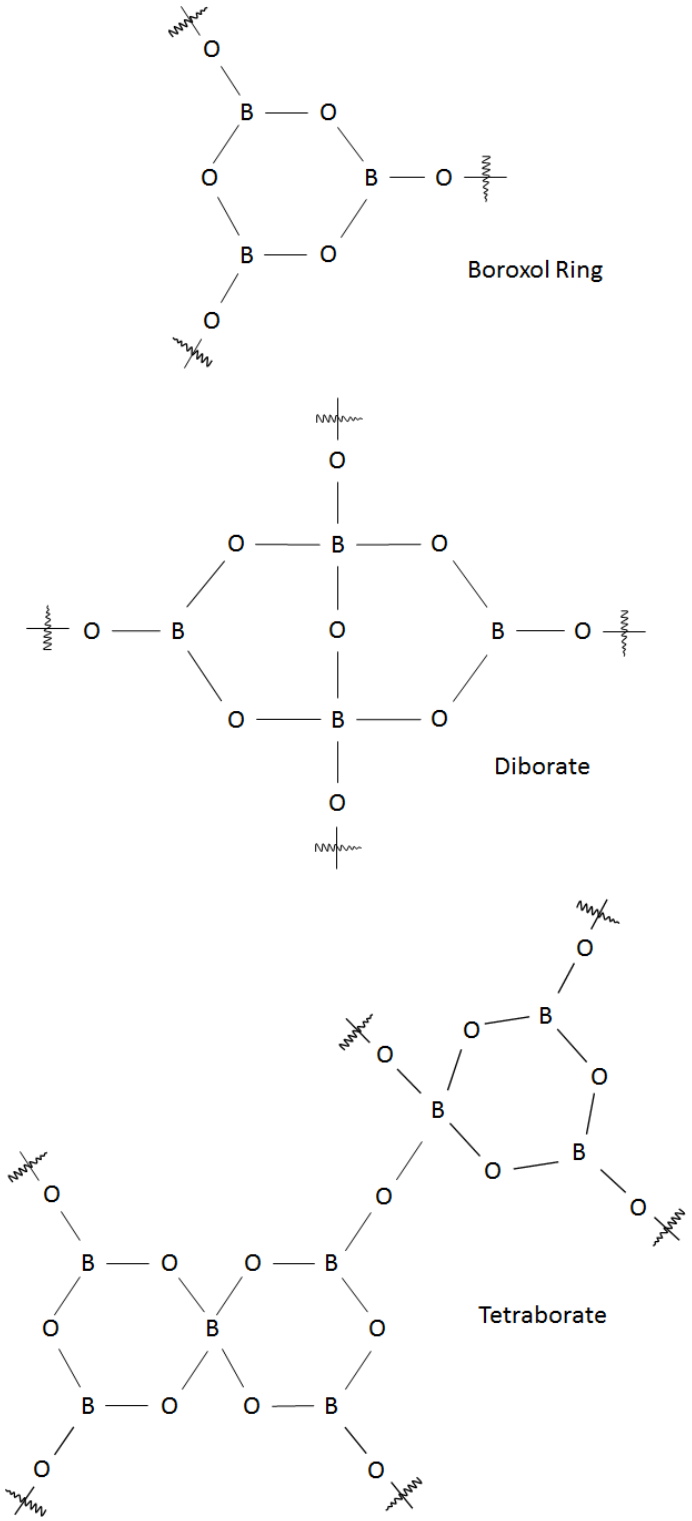

Figure 2.4: Examples of boron complexes observed in borate compounds. Bridging oxygens are indicated with the crossed bond lines. (Adapted from [55])

The ratio of BO_3 to BO_4 units is known to vary with alkali concentration. Initially, alkali additions cause trigonal units to convert to tetragonal units causing a net increase in the N_4 species. The alkali cations associate with the N_4 units as charge compensators, thus no NBOs are formed and the glass network becomes increasingly connected [54]. However, increasing the alkali concentration above 16 mol. % does not continue to have this effect. Originally it was thought that at 16 mol. % alkali addition, the system reached a concentration limit of N_4 units, after which, NBOs form resulting in the reverse effect on properties due to the depolymerisation of the glass network. Experimental data has since shown that different properties peak at different alkali concentrations showing it is not as simple as first presumed (Figure 2.5). This phenomenon is termed the Boron Anomaly.

Biscoe and Warren detailed the boron anomaly to be the conversion of trigonal BO_3 units to tetragonal BO_4 units linearly with increasing alkali additions without the formation of NBOs [56]. With the increasing glass connectivity, the viscosity and thermal expansion properties were found to increase. However, after 16 mol. % alkali additions the viscosity and thermal expansion properties decrease due to the production of NBOs rather than further unit conversions. It was later experimentally demonstrated by Bray and O'Keefe that the increase in BO_4 units becomes hindered around N_4 = 45% due to superstructural units [57]. BO_3 units are present both as individual species and as components in boroxyl rings. The initial increase in tetragonal units corresponds to the conversion of non-ring BO_3 units but those in boroxyl rings remain [46]. Figure 2.5 demonstrates the effect of alkali concentration on the intermediate range complexes and shows how experimental data has changed the original "simple" model [54].

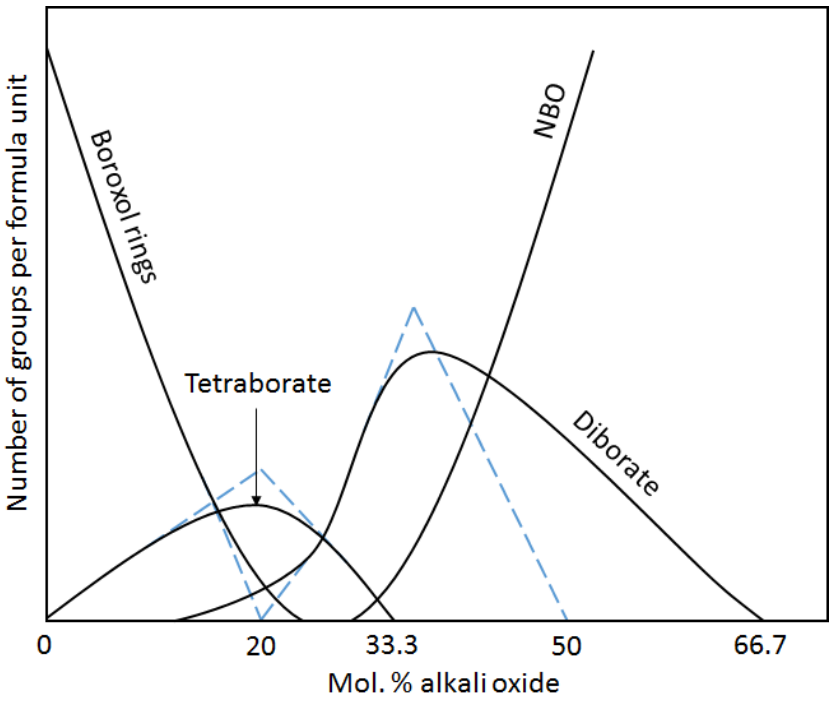

Figure 2.5: Effect of alkali concentration on the relative concentration of intermediate range units in alkali borate glasses. The dashed lines indicate the simple theory, the solid lines represent experimental results. (Adapted from [54])

Al_2O_3

Al_2O_3 is known to act as an intermediate within a glass, such that it can either be present as a network former or as a network modifier. When sufficient alkali cations are present to charge compensate AlO_4 tetrahedra, the Al acts as a network former. The AlO_4 tetrahedra replace SiO_4 tetrahedra in the glass network and increase the connectivity of the glass by removing NBOs [54]. This results in increased viscosity and T_g but also improves the glass durability. When there is insufficient alkali cations present for charge compensation, nuclear magnetic resonance (NMR) has shown Al can stabilise in 5- and 6-fold co-ordination [54,58]. These species act as modifiers and break up the connectivity of the glass network by producing NBOs [59], thus having an opposite effect on the glass properties.

Na_2O

Na_2O is a network modifier that stabilises network forming tetrahedra by charge compensation, or breaks up the glass network by forming NBOs [54]. In a sodium aluminosilicate glass network, if the Na_2O concentration is equal to the Al_2O_3 concentration, the glass is fully polymerised with no NBOs, as the Na^+ ions fully charge compensate the AlO_4

tetrahedra ($[AlO_{4/2}]^-$) resulting in a fully connected network [60,61]. However, in more complicated systems the Na^+ can associate with other ions including B and Si, leading to the production of NBOs. The reduction in connectivity leads to lower glass viscosities and lower T_g. Na^+ preferentially charge compensates AlO_4 tetrahedra ($[AlO_{4/2}]^-$), which, in the presence of B_2O_3, causes BO_4 tetrahedra ($[BO_{4/2}]^-$) to convert to 3-fold species due to the lack of available cations for stabilisation [59]. This results in NBOs on the B – O site.

Zheng *et al.* looked at the effect of Al_2O_3 : SiO_2 ratio on; the Na^+ stabilisation of AlO_4 tetrahedra, the conversion of BO_4 tetrahedra to trigonal species and the formation of NBOs with Si and B [59]. NMR was used to study the role of Na_2O in the structure and the effect on the stabilisation of Al, B and Si units. The NMR data revealed an increase in the stabilisation of 5- and 6-fold co-ordinated Al species with increased Al_2O_3 content due to the reduced availability of cations for stabilisation of the tetragonal species. Similarly, as the concentration of Al_2O_3 was increased the signal for tetragonal BO_4 units gradually decreased as a result of Na^+ preferentially compensating the AlO_4 tetrahedra. Thus there was a concurrent increase in the signal for trigonal BO_3 species.

Connelly *et al.* developed a model to predict the preferential charge compensation of different cation species within alkali aluminoborosilicate glasses [58]. The model used Pauling bond strength values as a measure of different units' stabilities within the glass. For glass forming ions the bond strength values were estimated from their Q^n species and effective unit charge in order to account for NBOs in the structure. By calculating the "co-ordination stabilisation index" (CSI) the model determined an order of preferential charge compensation for different cation species, such that $[AlO_{4/2}]^- > [ZrO_{6/2}]^{2-} > [TiO_{5/2}]^- > [BO_{4/2}]^- > [SiO_{3/2}O^-]$. The CSI was calculated as the stability of the cation species that does not need charge compensation, minus the stability of the cation species that does need charge compensation. For example, the stability of 4-fold Al units minus the stability of 6-fold Al units [58]. The model results show tetragonal $[AlO_{4/2}]^-$ units are preferentially charge compensated first, which agrees with other literature that details the effective and complete stabilisation of tetragonal $[AlO_{4/2}]^-$ with cation charge compensation [46,47,59,61].

2.2.3 Glass wasteforms for Pu disposition

Vitrification is the current accepted method for treating and immobilising HLW [23,62–64]. The random nature of the glass structure and its ability to incorporate so many elements enables these materials to immobilise waste into durable and passively safe wasteforms [64]. Borosilicate glasses are commonly utilised as HLW wasteforms and are able to incorporate 30 – 40 elements in its structure [65]. Vitrified wasteforms have been shown to have excellent wasteform properties such as durability, radiation tolerance, thermal stability, and mechanical integrity [64,66], but are known to have limitations with regards to actinide solubility and the incorporation of refractory elements [24]. Problematic elements for glass wasteforms include; Pu and other actinides, CaF_2, Cl, Tc and high concentrations of Al_2O_3, ZrO_2, Cs and Sr, some of which are present in Pu-residues [67].

Vitreous wasteforms undergo devitrification at elevated temperatures (300 – 400 °C) and pressures (300 – 1000 bar), the lesser of which are expected to be experienced in the geological repository. Such conditions may be detrimental to the retention of radionuclides and / or associated neutron absorbers [24,68–70]. If neutron absorbers are preferentially leached out at a faster rate than the actinides, the risk of criticality increases. The mobility of B within LaBS (Lanthanide borosilicate) glass can be higher than that of Pu thus posing the risk of faster leaching [24,68,69].

LaBS glass was originally developed for storage and transportation of actinide materials and was considered as an alternative to borosilicate glass for Pu disposition [24,34]. LaBS glass has a higher Pu solubility than standard borosilicate glass compositions, achieving more than 10 wt. % Pu incorporation in stirred melts [24,71], but simultaneously has a limited capacity for U incorporation, which could lead to criticality concerns in the geological repository. LaBS was developed for the temporary containment of nuclear waste, which means actinides are easily retrieved from the glass using available techniques such as the PUREX process [24]. LaBS glass also requires high processing temperatures around 1450 °C, compared to borosilicate glasses, which are typically processed between 1100 – 1200 °C [72]. LaBS glass was used as a control during the Plutonium Immobilisation Project (PIP), where its performance was compared against ceramic wasteform options [34,73]. The ceramic

wasteform incorporated higher actinide loadings and had better radionuclide retention rates than the LaBS glass. The PIP is discussed in more detail in section *2.3.3*.

When considering the treatment of Pu-residues by vitrification there are multiple limitations / challenges that need addressing. Due to the high refractory content of Pu-residues the temperatures required to achieve a glass melt are very high making the process highly energy intensive and costly [74]. Vitrification also requires the discharge of the glass from the melter system, which requires control of the melt properties and manageability. The discharging process adds uncertainty to accountability and criticality concerns regarding Pu, due to the residue left in the melter after pouring the glass melt [75]. Due to the high mass of Pu, and its potential to crystallise in vitreous materials, it can settle to the bottom of the melter and be present in high proportions in the residue material [24,67]. Over time this concentration could build to criticality levels and will require maintenance / disposal of the melter itself. The viscosity must be controlled for pouring, which again requires very high temperatures and puts limitations on the composition of the melt. As well as the manageability of the glass for processing, the wasteform properties must also be retained. The restraints on glass composition for processing efficiency, subsequently limits the compositional options for the wasteform and could severely impede the final wasteform properties.

2.3 Ceramics

Ceramic wasteforms have been developed as alternative wasteforms for HLW immobilisation for many years [76–80]. Compared to the accepted borosilicate glass matrix, ceramic wasteforms have been proven to have equivalent or superior wasteform properties for Pu immobilisation.

Ceramic wasteforms have better chemical durabilities and waste loading capabilities than borosilicate glass materials, which have subsequent advantages of fewer waste packages and cost savings. A qualitative comparison of the various wasteform options and how they each affect and contribute to wasteform properties is shown in Figure 2.6 [81]. The process windows of different thermal treatment options are also demonstrated, highlighting the wide operating window provided by hot isostatic pressing (HIP).

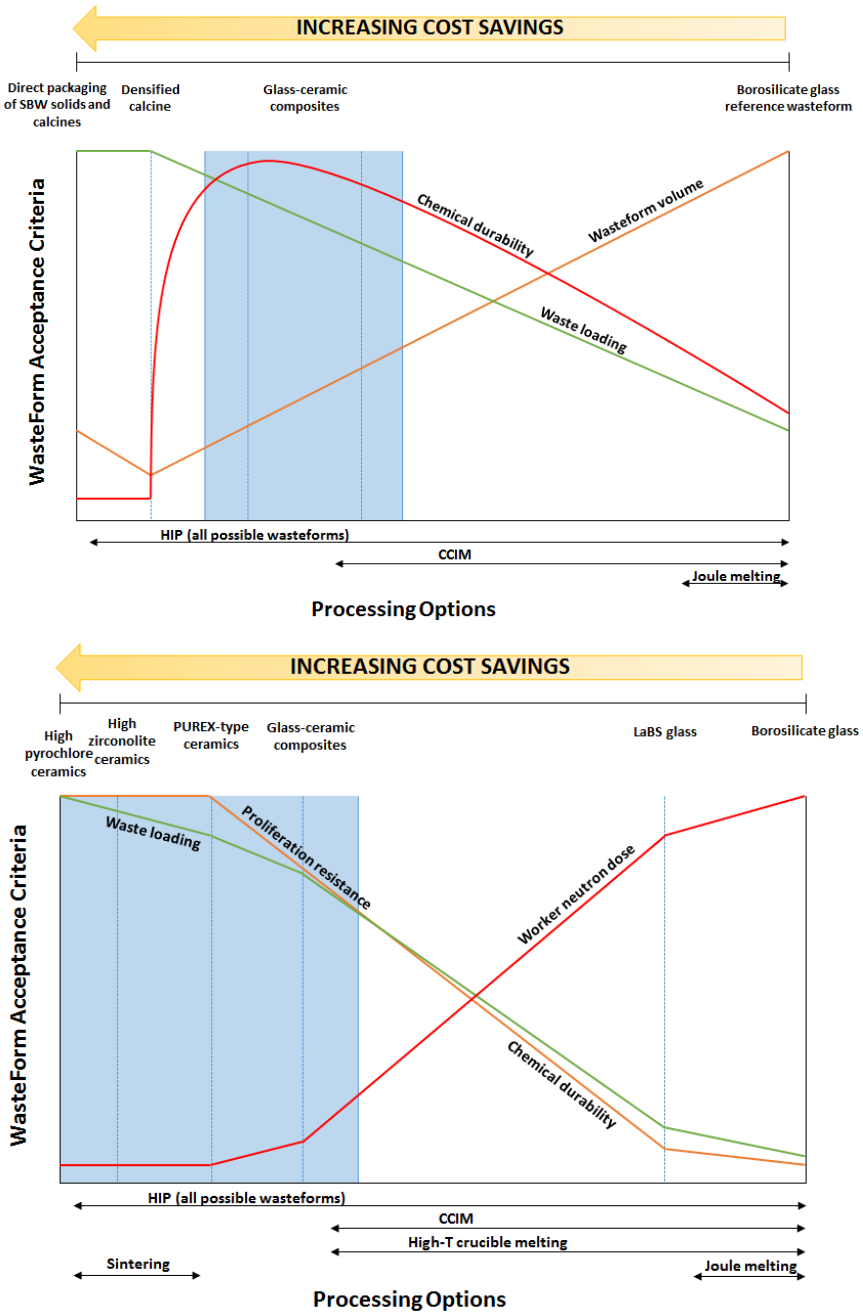

Figure 2.6: Qualitative comparisons of wasteform material options and thermal treatment options for the disposition of Idaho calcines (top) and Pu-based waste-streams (bottom). (Adapted from [81])

2.3.1 Zirconolite

Zirconolite is a proven host phase for actinide disposition, with favourable properties including its chemical flexibility, compatibility with silicate glasses and its long-term durability [82]. Through research on both natural and synthetic zirconolite samples, this naturally occurring mineral has established itself as a primary host phase for actinides in ceramic based HLW wasteforms [79,83–88].

Nominal structure

The nominal structure of zirconolite ($CaZrTi_2O_7$) is a monoclinic structure notated as zirconolite-2M (space group C2/c) [23]. Zirconolite-2M can also be described as a compressed pyrochlore structure [89] or an anion-deficient fluorite structure [90]. It is a derivative of the pyrochlore structure, $A_2B_2O_7$, where Ca^{2+} and Zr^{4+} ions sit on the A-site and Ti^{4+} ions on the B-site. Figure 2.7 is a schematic of the zirconolite-2M structure showing the parallel, alternated, two layer structure of Ti^{4+} octahedra and Ca^{2+} – Zr^{4+} polyhedra layers. The A-site cations, Ca^{2+} and Zr^{4+}, are 8- and 7-fold co-ordinated, respectively and each only occupy one lattice site. The Ti^{4+} ions can occupy three sites; two in 6-fold co-ordination and one partially occupied in 5-fold co-ordination [23]. The 6-fold Ti^{4+} ions arrange themselves in hexagonal tungsten bronze (HTB) motifs while the 5-fold co-ordinated Ti^{4+} ions sit off-centre inside the six-membered rings [90,91]. The Ca^{2+} and Zr^{4+} cations arrange themselves in alternate rows parallel to [110] and are layered between the Ti^{4+} HTB in the (001) plane [83,91,92]. The effective ionic radii of Ca^{2+} is 1.12 Å, Zr^{4+} is 0.78 Å and Ti^{4+} is 0.51 Å in 5-fold and 0.605 Å in 6-fold [93]. The large lattice sites of the Ca^{2+} and Zr^{4+} ions in the zirconolite structure allow for large actinide and rare earth elements to substitute into the lattice (see Figure 2.9 in section *2.3.2*). The partially filled Ti^{4+} sites make the mineral phase even more flexible by allowing charge compensation substitutions. Zirconolite can accommodate many elements, including; Na, K, Ca, Sr, Ba, Pb, Y, REE, Bi, Zr, U, Th, Pu, Am and Cm on its 7- and 8-fold co-ordinated lattice sites and Al, Ta, Nb, Ti, Fe and Mn on its 6-fold co-ordinated lattice sites [70]. As well as significant actinide incorporation, its ability to accommodate neutron absorbers helps maintain criticality safety during long-term storage and disposal.

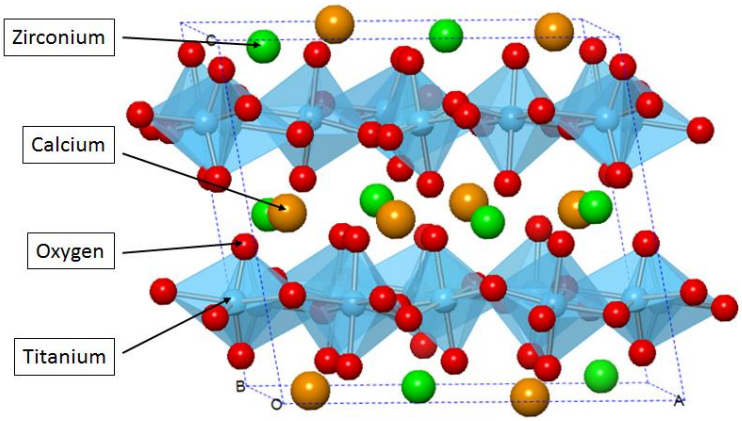

Figure 2.7: Representation of the zirconolite-2M monoclinic structure. (Adapted from [89])

Elemental incorporation

Extensive research on zirconolite as a single phase ceramic wasteform and as an actinide host phase in multiphase systems (Synroc) and glass-ceramics, has demonstrated the excellent properties and performance of the mineral for actinide waste immobilisation [63,76,79,91,92,94–96]. The role of zirconolite in Synroc and in glass-ceramic systems shows its flexibility and effectiveness in more complex environments. These wasteforms are discussed in more detail in sections *2.3.2* and *2.4*.

Elemental incorporation in zirconolite for actinide immobilisation has been proven through inactive actinide surrogate studies, such as Ce and Nd [97–99], low-activity U surrogates [91,100] and Pu incorporation experiments [101–103]. The large size of the Ca^{2+} and Zr^{4+} lattice sites allow for substitution of trivalent and tetravalent ions, respectively. Trivalent ions including Ce^{3+}, Nd^{3+} and Pu^{3+} have been shown to preferentially substitute on the Ca^{2+} site [94]. This is due to coulombic effects when displacing ions of higher charge from a lattice site and also due to the larger ionic radii of trivalent ions and the Ca site [104,105]. Due to their equivalent charge, it is preferential for tetravalent substitutions to occur on the Zr^{4+} site rather than substitute on the Ca^{2+} site, which requires addition charge compensation mechanisms. Gilbert *et al.* studied the energetics of Ce and Pu substitutions into zirconolite and show that Pu^{4+} for Zr^{4+} substitutions are most favourable, more so than Ce^{4+} due to the larger ionic radii of the Ce ion than the Zr ion [104]. Gilbert *et al.* also shows that the incorporation of Pu^{3+} is energetically unfavourable, which is in agreement with observations that Pu^{3+} is found in the glass phase of glass-ceramic wasteforms [104]. Hence, it is important

to maintain Pu^{4+} in the wasteforms to maximise its incorporation into the target ceramic phase and minimise its presence in the glass phase as a trivalent species.

Structural transitions

With increased doping of the zirconolite structure, structural transitions occur. A series of experiments conducted by a team at ANSTO showed phase transitions with increasing substitutions of Ce, U and Pu dopants [91,97,106]. The zirconolite-2M monoclinic structure was found to transition to zirconolite-4M, zirconolite-3T and even a pyrochlore structure with increasing dopant levels. Substitution of 0.15 f.u. (formula units) U^{4+} on the Zr site stabilised the monoclinic zirconolite-2M structure [91]. Further substitution saw the full stabilisation of zirconolite-4M by 0.4 f.u., with a mix of zirconolite-2M and zirconolite-4M observed between 0.15 – 0.4 f.u.. A similar trend was observed between 0.4 – 0.7 f.u. substitutions, where the zirconolite-4M structure transitioned into the pyrochlore structure. These gradual transitions show there are miscibility gaps between the end members [91,107].

The U-doped samples were heat treated under argon atmosphere for reducing conditions to obtain U^{4+} ions [91]. When targeting U^{4+} on the Ca site, additional charge compensators, Al and Mg, were added to substitute on the Ti sites. Single phase zirconolite-2M was obtained up to 0.2 f.u. substitution with minor phases; brannerite, zirconia and uraninite observed at 0.3 f.u.. From the measured compositional data of the zirconolite phase, the majority of the U was stabilised on the Ca site as U^{4+} [91]. The measured charge compensators were slightly low thus indicated a small amount of U^{4+} substituted on the Zr sites.

In separate work, Meng *et al.* reported similar structural transitions with increased Ce substitutions [108]. Ce was targeted for both the Ca and Zr sites as Ce^{3+} and Ce^{4+}, respectively. Increased substitution favoured zirconolite-4M and later a pyrochlore structure. A perovskite phase was also present most likely due to the presence of Ce^{3+}. Perovskite readily accommodates Ce^{3+} due to its equivalent ionic radii to the 12-fold Ca site (1.34 Å) [93,107]. The samples discussed by Meng *et al.* were synthesised under atmospheric conditions thus are not directly comparative to the samples in this thesis that were processed under reducing conditions. However, other substitution studies, under oxidising and reducing conditions, have shown similar results [97,109].

Polytypes

There are many similarities between the structures of the zirconolite polytypes, with the main differences coming from the stacking sequences and number of layers in each sequence (or module) [110]. The zirconolite-2M structure has just been described and is derived from the fluorite structure. The nominal structure has a two layer stacking sequence of HTB layers and $Ca^{2+} – Zr^{4+}$ polyhedra. The zirconolite-4M structure is a mix of zirconolite-2M and pyrochlore, such that, it has a four layer HTB stacking sequence that alternate with layers of $Ca^{2+} – Zr^{4+}$ polyhedra (zirconolite-2M) and layers of $Ca^{2+} – Ti^{4+}$ polyhedra (pyrochlore) [106]. The pyrochlore structure is similar to the zirconolite-2M structure but has different anion displacements and cation ordering, with cations located centrally in the HTB octahedra as opposed to the partially occupied Ti sites [110,111]. Zirconolite-4M is only stable over a small dopant range, which Begg *et al.* correlated to the effective ionic radii of the Zr lattice sites [106]. Begg *et al.* proposed the 4M structure is only stabilised when the occupancy of the Zr site has effective ionic radii in the range 0.083 – 0.084 nm, which corresponds to 0.4 f.u. Pu^{4+} substitution. This was also in agreement with the Ce^{4+} and U^{4+} work that achieved similar substitutions due to the closely matching radii of the substituting ions [91,97]. Due to the similarities between the zirconolite-2M and pyrochlore end members, it is unsurprising that increased doping leads to structural transitions between the different polytypes as a result of the unit cell increase. The presence of zirconolite-4M could be interpreted as an intermediate phase due to the miscibility gap between the zirconolite-2M and pyrochlore structures [94,109,110].

Begg *et al.* doped zirconolite ceramics with increasing levels of PuO_2 for target stoichiometry $CaZr_{1-x}Pu_xTi_2O_7$ and consolidated the ceramics in air and under 3.5 % H_2/N_2 atmosphere [106]. The air samples showed similar results to those discussed above for Ce / U, such that increased Pu substitution resulted in zirconolite-2M to zirconolite-4M transition and finally to the pyrochlore structure. The energy dispersive X-ray (EDX) spectra showed that the Pu substitution levels in each of the three phases were independent of the amount of PuO_2 added. The zirconolite-2M structure contained around 0.15 f.u. Pu, zirconolite-4M contained about 0.4 f.u. and pyrochlore 0.6 f.u.. The consistency in these values confirmed the solid solution limits for each polytype [106].

When processed under reducing conditions, the zirconolite-4M structure does not form. In the lower waste loaded samples zirconolite-2M was the primary phase and it was proposed that zirconolite-3T was stabilised with higher loadings [106]. Zirconolite-3T is a trigonal structure with six individual layers in the stacking sequence; three $Ca^{2+} – Zr^{4+}$ polyhedra layers plus three HTB layers. Similar to zirconolite-2M, it has alternating layers of Ti HTB octahedra and $Ca^{2+} – Zr^{4+}$ polyhedra layers. The $Ca^{2+} – Zr^{4+}$ layers rotate at 120 ° and occupy all three possible orientations [112]. In contrast, zirconolite-2M $Ca^{2+} – Zr^{4+}$ layers only occupy two orientations [112]. In the trigonal structure, the HTB layers have a stacking angle of 60° resulting in a perfect hexagonal symmetry [110]. This is demonstrated schematically in Figure 2.8. Whilst there is very limited refined information on the zirconolite-3T structure, it is believed to have two Ca sites resulting from its symmetry [106,110]. The reducing conditions applied by Begg *et al.* promoted Pu^{3+}, which has a larger ionic radii than Pu^{4+}, thus would preferentially substitute on the Ca site and be unfavourable for zirconolite-4M stabilisation on the grounds of the Zr site effective ionic radii [106]. Due to the reduction of Pu^{4+} a Pu-doped perovskite phase also formed. This phase increased in abundance with increasing levels of PuO_2, such that the previously single phase pyrochlore sample (x=0.6) converted to single phase perovskite under the reducing conditions [106].

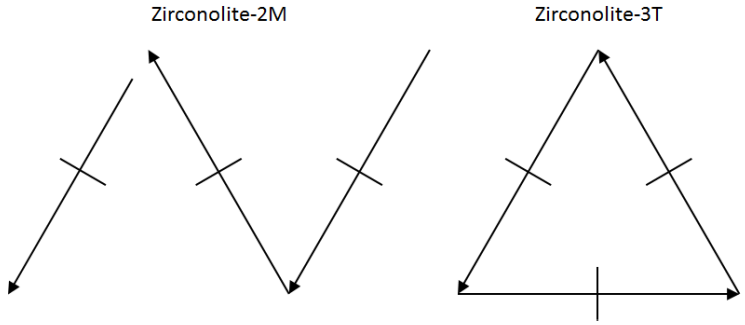

Figure 2.8: Schematic representation of the stacking vectors of the HTB layers in zirconolite-2M and zirconolite-3T. In 3T the stacking angle is exactly 60 °, in 2M it is approximately 60 °. The lines in the centre of each vector represents the orientation of the $Ca^{2+} – Zr^{4+}$ layers. (Adapted from [110])

Radiation damage

Actinide bearing wasteforms are exposed to radiation damage from α-decay events. α-decay produces two particles; a recoil nucleus and the emitted α-particle. The recoil nucleus retains

the majority of the kinetic energy from the decay event and causes more structural damage to the wasteform. The recoil nucleus dissipates its energy through elastic collisions generating thousands of atomic displacements through the material [83]. Two major consequences of α-decay events are volume expansion and amorphisation. Volume expansion can lead to cracking of the wasteform and a subsequent surface area increase, allowing water ingress and faster leaching of radionuclides. Wald *et al.* measured the unit cell of ^{244}Cm doped zirconolite after increasing dose exposure up to 10^{23} α/m^3 and measured a maximum volume expansion of 2.1 %, with an isotropic nature preferentially almost perpendicular to the (001) plane [83,113].

Radiation induced amorphisation is a result of the accumulation of atomic displacements, from α-recoil damage, which destroy the long-range crystalline structure. When this effect occurs as a result of α-damage it is often referred to as metamictisation and produces a metamict material when the free energy of the damaged region is equal to that of the amorphous state [114–116]. With increased temperatures, recrystallization of the starting material can occur. This phenomenon is strongly affected by temperature and can occur partially at lower temperatures or can achieve full recrystallization of the starting material at higher temperatures. Partial recrystallization can occur simultaneously with amorphisation during irradiation and can occur at temperatures expected in HLW wasteforms [117–120].

Mineral zirconolites have been found containing U and Th [88,121,122]. These materials are hundreds of thousands of years old and are partially or completely metamict from the α-decay of the radionuclides. The amorphised structures still retain measurable amounts of the U and Th confirming the long-term radionuclide retention of the ceramic. Radiation damage studies have been conducted on natural mineral samples and doped synthetic zirconolite samples exposed to accelerated irradiations [77,102,118,123–126]. Ewing *et al.* demonstrated the effect of increased radiation exposure on the gradual amorphisation of the zirconolite structure using Transmission Electron Microscopy (TEM) on various natural samples [83,85]. After $> 10^{26}$ α/m^3 the natural samples were determined to be fully amorphous, however some samples revealed nanoscale crystalline regions that were thought to be a result of recrystallization effects. Further exposure to electron beam heating proved recrystallization does occur. Micro-porosity was also observed and identified as He bubbles generated from α-decay in the material. In comparison, the synthetic zirconolite

showed continued reduction of the long-range crystalline order, reaching an X-ray amorphous structure after $1.6 \times 10^{25} \alpha/m^3$. Other factors affecting the amorphisation and recrystallization of these structures include impurities, time and thermal history, which for natural analogues may be largely unknown and account for the discrepancies with synthetic samples. That said, the results were in excellent agreement and showed both the capability of zirconolite to withstand high levels of α-radiation and the successful demonstration of long-term behaviours and performance through accelerated laboratory experiments.

2.3.2 Synroc

Synroc is a synthetic rock material composed of multiple crystalline phases designed for the immobilisation of nuclear waste. Originally proposed by Ringwood *et al.* [70,95] in the 1970s, Synroc formulations have been developed to combine different mineral phases that could each accommodate different elemental species into their structure with the aim of producing a superior wasteform to borosilicate glass [70,127–130]. The utilisation of titanate based minerals was based upon their proven ability to incorporate and retain many elements, including U and Th, over long timescales. Multiple versions of synroc, some of which are listed in Table 2.2, have been trialled since the 1970s, with various phase assemblages and phase fractions [70,131]. The multiple variations have proven its flexibility and wide operating window in terms of phase assemblage, waste feed incorporation and process-ability, for optimum performance of the wasteform.

Table 2.2: Summary of Synroc and ceramic variants. (Adapted from [131])

Name	Mineralogy (wt. %)	Waste loading	Fabrication Process
Synroc – A	40% Ba-feldspar 30% hollandite 20% perovskite 10% zirconia kalsilite and / or leucite	10% HLW	Melting and crystallising 1330 °C
Synroc – B	40% hollandite 35% zirconolite 25% perovskite	None	Hot pressing 1200 – 1400 °C
Synroc – C	33% hollandite 28% zirconolite 19% perovskite 15% rutile 5% noble metal alloy	20% HLW	Hot pressing 1150 °C
Synroc – D	46% spinel solid solution 19% zirconolite 17% nepheline 15% perovskite 3% hollandite	63% HLW sludge	Hot pressing 1050 – 1100 °C
Synroc – E	79% rutile 7% zirconolite 7% perovskite 5% hollandite 2% pyrochlore	7% HLW	Hot pressing 1300 °C
Synroc – F	90% pyrochlore 5% hollandite 5% rutile	50% U-rich HLW	Cold pressing and sintering 1250 – 1400 °C
Synroc – FA	89% pyrochlore 8% perovskite 3% uraninite	50% U-rich HLW	Cold pressing and sintering 1250 – 1400 °C
Mixed waste ceramic	36% nepheline 31% spinel solid solution 12% zirconolite 12% perovskite 5% rutile, 4% whitlockite	40% residue	Cold pressing and sintering 1150 – 1200 °C
Pu ceramic zirconolite-rich	80% zirconolite (with some pyrochlore) 10% hollandite 10% rutile <1% PuO2	12% Pu	Cold pressing and sintering 1325 – 1400 °C
Pu ceramic pyrochlore-rich	85% pyrochlore 10% brannerite 5% rutile <1% uraninite solid solution	10% Pu and 21% U	Cold pressing and sintering 1275 – 1400 °C

Synroc-C, composed of zirconolite ($CaZrTi_2O_7$), hollandite ($BaAl_2Ti_6O_{16}$), perovskite ($CaTiO_3$) and rutile (TiO_2), was initially developed for the immobilisation of liquid wastes from light water reactors and has proven to be highly effective at immobilising actinides [132]. While zirconolite is the primary host for actinide and rare earth element immobilisation, the perovskite phase also accepts actinides but to a lesser extent. The hollandite and perovskite are present to account for Cs and Sr, respectively, and rutile may be present to accommodate Tc [129,132]. Figure 2.9 demonstrates the different lattice sites available for radionuclide immobilisation within Synroc-C and the sites suitable for actinide disposition [42]. Again, the fractions of each phase are flexible to accommodate for changes in the waste feed composition.

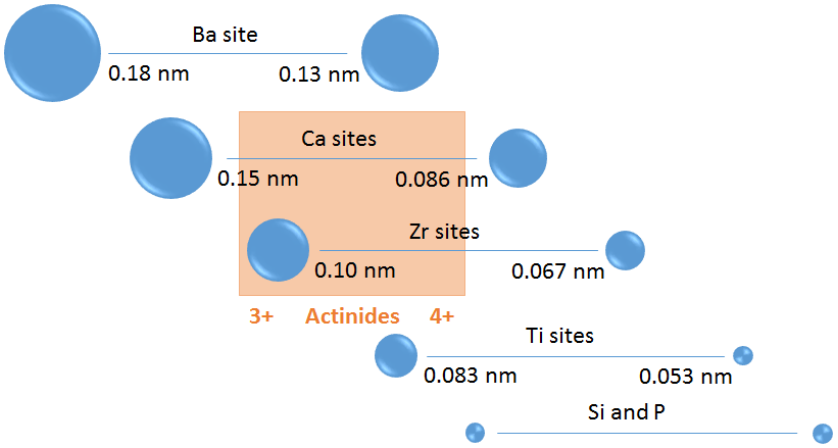

Figure 2.9: Schematic of different lattice sites and corresponding ionic radii for elemental substitutions. Ca and Zr sites are suitable for actinide ions hence the utilisation of zirconolite and / or pyrochlore in the Synroc formulations. (Adapted from [42])

2.3.3 Plutonium Immobilisation Project (PIP)

During the 1990s, the Plutonium Immobilisation Project (PIP) was set up to study ceramic materials for the immobilisation of surplus weapons-grade Pu [131,133,134]. This project was conducted between multiple national laboratories[2] in America and Australia and was set up to develop a suitable ceramic wasteform formulation and processing route for the

[2] Argonne National Laboratory (ANL), Lawrence Livermore National Laboratory (LLNL), Pacific Northwest National Laboratory (PNNL), Savannah River Technology Centre (SRTC), and the Australian Nuclear Science and Technology Organisation (ANSTO).

disposition of excess weapons-grade Pu material [131]. Many formulations were tested during the PIP with respect to the waste feed in question and durability of natural analogues, which led to the selection of a pyrochlore based ceramic wasteform [131,135]. Borosilicate and LaBS glass were used as control samples and highlighted the superior performance of ceramic wasteforms for actinide disposition.

Through the PIP, Synroc-C was shown to incorporate up to 11.8 wt. % ^{238}Pu in experiments studying the effect of α-decay on the structure and properties of Synroc-C [132]. The durability properties through this work were reported to exceed those of equivalent borosilicate glass samples, with leach rates between 15 – 450 times lower for various elements [136,137]. In order to increase actinide loading capacities, further developments targeted zirconolite-rich and pyrochlore-rich ceramics. By maximising the yield of the actinide host phase the capacity for Pu and U was increased. Phase diagrams were generated by Ebbinghaus *et al.* [138,139] showing the effect and success of actinide incorporation and the phase development between zirconolite and pyrochlore structures. Through the composition investigations the formation of zirconolite-4M was observed over a range of compositions when processed in oxidising conditions but was not stabilised under reducing conditions [138]. This was in agreement with the waste incorporation studies discussed previously.

2.4 Glass-ceramics

Glass-ceramics are proposed for immobilising impure streams of Pu-residues that may contain glass forming compounds. Glass-ceramics consist of small ceramic crystals homogeneously distributed throughout a glass matrix [140]. Conventionally, glass-ceramics are prepared via a route of controlled heat treatments. The process can be a single heat treatment where the temperature is controlled to promote nucleation and crystal growth over time, or by varying the temperature with regards to the glass transition (T_g) and the glass liquidus temperatures (T_L). The route taken is governed by the nucleation and growth rate curves of the material [23]. Rate curves determine the temperature range that best promotes nucleation and growth. If the rate curves overlap, nucleation and growth can occur in a single heat treatment by holding just above the T_g or by slowly cooling the melt. If the rate curves do not overlap, the nucleation and growth occur separately; the melt must first

be cooled to the T_g for nucleation, then heated again to just below the T_L, before the final cooling. These heat treatments are schematically shown in Figure 2.10 with the associated rate curves.

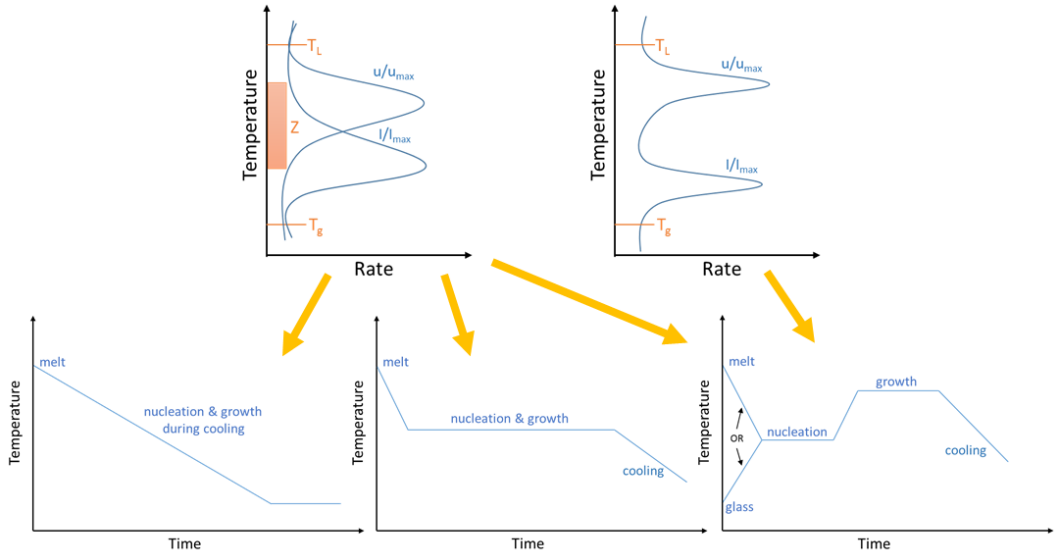

Figure 2.10: Nucleation and growth rate curves with the relevant heat treatment routes for preparing glass-ceramics. (Adapted from [23])

One benefit of glass-ceramics for the immobilisation of Pu-residues is the dual barrier system [17]. It has been identified that each stream of Pu-residues must be considered on a case by case basis and that full ceramics may be more suitable for immobilising purer PuO_2 waste-streams. However, for less pure wastes with more impurities and potential glass formers, glass-ceramics provide a dual-barrier system for immobilising the Pu and encapsulating the impurities. Research has shown actinides preferentially partition into the more durable ceramic phase, whilst the miscellaneous material of the waste feed is incorporated into the glass. Studies have shown actinide partitioning ratios up to 100 : 1 between the ceramic and glass phases [15,100,141]. Day *et al.* [142] compared Fe and Ni buffered samples on the behaviour of actinide partitioning and showed the reducing conditions had a strong effect on the partitioning ratio. Samples with Fe additions only achieved a partitioning ratio of 20 : 1 compared to 100 : 1 for Ni buffered samples [100,142]. Pu recovery tests reported by Day *et al.* [17] showed Fe-buffered samples were more susceptible to Pu recovery than Ni-buffered samples, with a worst case value similar to a best case value for borosilicate glass. These results show that Fe is more reducing than Ni, thus

more Pu^{3+} enters the glass phase. A more recent study by Zhang *et al.* [143] however, did not observe significant differences between Fe and Ni buffered samples. Pu^{3+} was targeted in the Fe buffered samples but was not confirmed due to the overly dominant Fe signal by diffuse reflectance spectroscopy (DRS). The Pu was preferentially incorporated in the zirconolite phase for all samples and the Fe samples had lower initial release rates in the durability tests compared to the Ni samples. Whilst this would suggest more Pu^{3+} was present in the Ni buffered samples, the DRS data confirmed the Pu was overwhelmingly tetrahedral. The reason for the variations in the leach rates was said to be unknown.

The ability of glass to incorporate a large range of elements adds flexibility to the wasteform to accommodate impurities and changes in the waste feed. Durability studies show preferential dissolution of the glass phase, coupled with the excellent resistance of a full ceramic, thus excellent actinide retention [144]. Stewart *et al.* developed zirconolite glass-ceramics for Pu-residues immobilisation in conjunction with British Nuclear Fuels Ltd.[3] (BNFL) [82]. Through multiple studies of both zirconolite and pyrochlore glass-ceramics and full ceramics, zirconolite was selected for residues containing glass formers, due to its ability to accommodate both actinides and neutron absorbers in its structure. Samples were prepared in 30 ml HIP canisters packed with pressed pellets [82]. The canisters were baked-out at 600 – 650 °C prior to sealing and HIPed at 1320 °C for 2 h under 100 MPa of pressure. U and Th were utilised as Pu surrogates and added in conjunction to other elements representative of a typical waste-stream. A matrix was compiled with different concentrations of the waste constituents, including; double actinides, double cations, double glass formers and double anions, all of which were compared against the standard baseline composition. Characterisation of the samples showed only minor changes to the final zirconolite composition across the samples, with a composition in the region of $Ca_{0.32\text{-}0.45}Na_{0.13\text{-}0.14}Gd_{0.37\text{-}0.41}U_{0.12\text{-}0.18}Th_{0.035\text{-}0.07}Zr_{0.94\text{-}1.03}Ti_{1.20\text{-}1.46}Al_{0.25\text{-}0.30}Fe_{0.04\text{-}0.15}Cr_{0.08\text{-}0.34}Mg_{0.05\text{-}0.13}O_7$. EDX analysis confirmed preferential partitioning of the actinide surrogates into the zirconolite phase, which when coupled with MCC-1 leaching data, proved excellent radionuclide retention rates. The leachate data were consistent across all samples and showed preferential dissolution of the glass phase [15,82]. This illustrates that the

[3] Currently known as the National Nuclear Laboratory (NNL)

glass-ceramic wasteforms can achieve actinide retention rates equivalent to Synroc and full ceramics, far superior to borosilicate glass [17,100].

This dual barrier system also provides excellent proliferation resistance by having the actinide host phase encapsulated in the secondary amorphous phase, making Pu recovery far more difficult. Aggressive retrievability tests on PuO_2 doped HIPed glass-ceramics were conducted to estimate the number of 10 kg HIP canisters that would be required to recover 1 kg of Pu [144]. Powdered samples were subjected to 5 M of sulphuric or nitric acid for one week at 22 °C. The results varied depending on the acid solution, reducing agents and waste loading, but even with the worst case results, the glass-ceramics were far superior to borosilicate glass exposed to the same conditions [17,100]. Results showed a high of 173 ppm of Pu in solution (7% of total Pu inventory) after 7 days in the nitric acid for the glass-ceramics, whereas the equivalent borosilicate glass sample measured at 1060 ppm (44% of total Pu inventory) [17]. It was concluded, between 7,000 – 28,000 kg (700 – 2800 canisters) of the glass-ceramic wasteform would be required to retrieve 1 kg of Pu when subjected to the same aggressive conditions [144]. These results confirm the excellent durability and proliferation resistance of the glass-ceramic wasteform.

Some Pu-residues are contaminated with Cl due to the degradation of PVC packaging during storage. The levels of Cl contamination are not expected to exceed 0.2 wt. % but the exact form and chemical environment of the Cl is currently unknown [42,145,146]. Studies on the incorporation of Cl impurities into glass-ceramic and full ceramic wasteforms consolidated by HIP showed successful incorporation into the glass phase, or in an amorphous phase at triple points between ceramic grains [146]. No changes to the microstructure or phase assemblage were detected except for the formation of $BaCl_2$ in samples formulated with hollandite for Cs immobilisation. $BaCl_2$ was detrimental to the durability and Cl retention rates [145]. Pu-residues however, do not contain Cs thus it was decided to remove the hollandite from the ceramic / glass-ceramic formulations. Successful incorporation of 1.4 – 1.5 wt. % of Cl was achieved in the glass-ceramics without detrimental effects to the structure or behaviour of the wasteform [146].

Previous glass-ceramic formulations studied were based around CaF_2 rich waste-streams thus were formulated to be Al_2O_3 rich in order to digest the waste [15,17,147]. Since then, CaF_2 rich Pu-residue waste-streams were reclassified, but the CaF_2 was believed to aid waste

digestion thus was incorporated into later formulations as a digesting agent [82,143,147]. However, the (α,n)-reaction of ^{19}F, to yield ^{22}Na and one neutron, is problematic as far as worker dose uptake, wasteform integrity and criticality are concerned [148–150]. Equations 1 – 4 demonstrate these (α,n)-reactions and the resultant daughter products. In addition, the daughter nuclei produced are often in metastable states and stabilise by releasing high energy gamma rays (γ) (see equations 1 and 2) [150]. Despite being a neutron absorber, B, present in the glass phase of all previous glass-ceramic formulations, also contributes to (α,n)-reactions and the emission of high energy neutrons (equation 3 and 4) [24,132,148,150,151]. The exposure dose to workers handling the waste packages has been calculated to increase 8-fold due to the (α,n)-reactions generated by the presence of B alone [24,132]. Subsequently, for these wasteforms to be produced and handled safely, extra shielding would be required, increasing the overall lifetime cost of handling the waste.

$^{19}F + \alpha \rightarrow {}^{22}Na^{*} + {}^{1}_{0}n$; $^{22}Na + \gamma$ (1528 keV) **Eq. 1**

$^{19}F + \alpha \rightarrow {}^{22}Ne^{*} + {}^{0}_{1}p$; $^{22}Ne + \gamma$ (1275 keV) **Eq. 2**

$^{10}B + \alpha \rightarrow {}^{13}N + {}^{1}_{0}n$ **Eq. 3**

$^{11}B + \alpha \rightarrow {}^{14}N + {}^{1}_{0}n$ **Eq. 4**

Previous glass-ceramic formulations had glass fractions around 50 – 60 wt. % [82,144,147,152,153]. The fraction of glass to ceramic is a compromise between achieving high actinide loading capacities and having enough glass to incorporate the waste impurities and to dilute the actinide concentration for criticality safety. Scales *et al.* [15] states that "*different zirconolite glass-ceramic formulations were tested in order to accommodate a span of possible waste loadings*", but the specific details and variations of such studies are not detailed comparatively in the literature. The effect of the glass composition on the crystalline phase assemblage of the glass-ceramic was demonstrated at NNL, when precursor masses were interchanged accidentally during batching, resulting in an unexpected final phase assemblage [147,154]. Nothing was found in the literature that investigated the effect of glass composition on the crystalline phase assemblage outcome of zirconolite glass-ceramics. As such, it was imperative to investigate the crystalline phase assemblage

with respect to the glass composition during this project, to determine an optimum formulation that maximised the yield of zirconolite. This work is discussed in Chapter 5.

2.5 Hot isostatic pressing

Hot Isostatic pressing was originally developed by Battelle Memorial Institute in America in the 1950s for the diffusion bonding of zircaloy nuclear fuel pins [155,156] and is now used in many industries including aerospace and automotive [157]. The most common application of HIP is the densification of cast parts to remove porosity and casting defects, to improve material properties and performance. HIPing simultaneously applies high temperatures and pressures to consolidate and / or densify samples. The combination of temperature and pressure means samples can be consolidated at lower temperatures than conventional sintering (maintaining a fine grain size) and at lower pressures than is required for cold isostatic pressing (CIPing) [158]. The temperatures and pressures applied by HIP result in bodies of near theoretical density, which improves the working life of high performance parts and can improve the durability of materials for radioactive waste disposal. HIPing provides advantages over conventional processing techniques, including; an ability to process complicated shapes, consolidate powder samples and produce products of high, uniform densities at lower temperatures [159].

HIP was first developed for encapsulating nuclear waste in Sweden in the late 1970s [160–163] and has since been developed by US laboratories[4], NNL, ANSTO, and private enterprises including, GeoRoc Ltd., AIP Inc., WINCO (Westinghouse Idaho Nuclear Company) and Battelle Energy Alliance, as well as University institutions [164–172]. The flexibility and adaptability of HIP to process different wastes and materials was soon recognised as a major advantage for consolidating difficult waste-streams. Although HIP has not been commercialised for full scale waste treatment yet, it is the selected method for processing America's Idaho HLW calcines [173] and Australia's ^{99}Mo production waste [174–176] and is a leading proposed method for treating the UK's Pu-residue wastes [8,18,177].

[4] Laboratories including Pacific Northwest National Laboratory (PNNL), Argonne National Laboratory (ANL), Lawrence Livermore National Laboratory (LLNL) and Idaho National Laboratory (INL)

2.5.1 Structure of a HIP

A generic HIP structure consists of an electric resistive heating furnace located inside a pressure vessel. Figure 2.11 is a simplified schematic cross-section of a HIP pressure vessel. The furnace design determines its maximum operating temperature. Each furnace consists of heating elements, insulating fire-brick, thermocouples and a thermal barrier. The thermal barrier locks over the furnace to protect the pressure vessel walls from direct heat.

Within the walls of the pressure vessel is a coolant filled water jacket that acts as the primary cooling system to the pressure vessel. A secondary cooling system is used to remove heat from the circuit. An inert gas, typically argon, is pumped into the pressure vessel and the pressure is increased by a compressor. Other components include the vacuum pump, valves, gas inlet, external compressor and the PLC (programmable logic controller). A typical HIP cycle starts by first purging the pressure vessel with gas and evacuating the chamber to vacuum pressure. This removes air and water from inside the vessel to avoid corrosion and oxidation during the cycle. Gas is then pumped in to equilibrate with the gas cylinders before the furnace and compressor initialise to increase the temperature and pressure conditions.

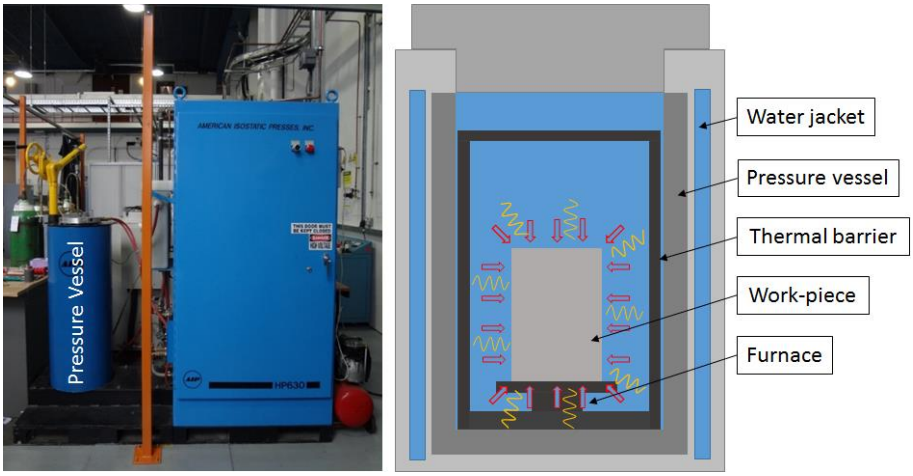

Figure 2.11: A simplified schematic of a cross-section of a HIP pressure vessel.

2.5.2 Densification by HIP

The main application of HIPing is densification and pore removal. Pores may generate from the initial packing of powder samples, gas evolution through the cycle or during solid state diffusion [158]. Applying pressure during sintering speeds up the densification process by

increasing the contact stress between particles [159]. This means samples can be processed quicker and at lower temperatures resulting in finer grain structure and better strength properties. During sintering, the driving force for pore closure is to reduce its surface area. Equation 5 defines this in terms of pressure [158,178]. As the radius of the pore decreases (surface area decreases) the pressure inside the pore increases. The internal pore pressure acts against pore removal, however, as the pore gets smaller and the pressure increases, the internal gas acts to find a state of lower energy by either dissolving into the material, moving to a larger pore of lower energy, or rising to the materials surface [158]. As such, smaller pores are removed first. With HIP, the external pressure far exceeds the internal pore pressure thus accelerates this process.

$$P = \frac{2\gamma}{r} \qquad \textbf{Eq. 5}$$

Where P is pressure, r is the radius of curvature of the pore surface and γ is the specific energy of the internal surface of the pore (J/m^2) [158].

Grain boundary migration also aids the sintering process by reducing the number of grain boundaries present and therefore the overall energy of the system [158]. This results in grain growth where small grains are engulfed by larger grains. Closed pores can also be engulfed by grain boundary migration leaving behind isolated pores within grains. During the latter stages of the HIP cycle these isolated pores are removed by diffusion into the material. At high temperatures densification also takes place by viscous flow, where individual particles have more energy to move and achieve better packing by filling voids.

2.5.3 Advantages of HIP for nuclear waste treatment

Hot isostatic pressing is a batch process able to consolidate nuclear waste into solid, monolithic wasteforms, hermetically sealed inside stainless steel canisters. The HIP canister provides the primary containment for the wasteform after consolidation and aids the transportation, handling and storage of the waste packages. The canister will also act as a containment layer as part of the multi-barrier geological disposal system, which could lead to potential cost savings during disposal.

The batch process allows for plant flexibility when processing low volume complex wastes but also helps towards Pu criticality, accountancy and safeguards when treating Pu-based waste-streams. The hermetically sealed nature of the waste during processing means there are no secondary wastes produced and there is no requirement for discharging the melt. No off-gases are produced during processing so there is no need for a large off-gas treatment system as with vitrification plants. However, the front end process, to get the waste in a suitable form for HIP, can be very complex and may involve; drying, calcining, mixing, granulation and / or size reduction. As such, the front end stages will produce minor waste and off-gases that need to be considered and drawn into the plant design for appropriate treatment [146,179].

Ensuring a wasteform is near theoretical density will help retard ground water ingress in the geological repository and improve durability properties against radionuclide release. The HIP process ensures complete removal of interconnected porosity to produce the high density wasteforms. The presence of the HIP canister acts as a surface barrier, sealing any open porosity on the wasteform surface. Each HIP canister must be evacuated under vacuum prior to sealing to remove air from inside the canister that would inhibit densification [168]. Prior to canister packing, the waste and precursors are dried and calcined to minimise the amount of water and volatiles going inside the canister and a “bake-out” step is utilised to remove any remaining volatiles from inside the packed canisters before crimping and sealing the evacuation tube. The bake-out applies heat to the canister, whilst still connected to the evacuation line, to liberate water and volatiles and to draw them out of the canister [168]. This stage of the front end process is important for consolidating dense, durable wasteforms.

Other thermal treatment options such as vitrification, cold crucible induction melting and Joule heater melting are often limited by their maximum processing capabilities and the melt properties required for manageability and wasteform performance [67]. In comparison, HIP has a large operating window and is not limited by the wasteform properties. This allows flexibility to process a range of different wastes and materials, at optimum parameters, on a single plant line.

One of the major advantages of HIP is the significant volume reductions achieved. Compared to alternative treatment options HIPing achieves superior volume reductions, which lead to significant cost savings for the storage and geological disposal of the waste packages [180].

For ILW, cementation results in a large volume increase from the starting waste volume, as demonstrated in Figure 2.12 [175]. It was estimated that 2000 litres of radiopharmaceutical wastes will be produced per year from the production of ^{99}Mo. Cementation would result in an estimated volume of 52,000 litres of encapsulated waste packages per annum, compared to 500 litres per annum when processed by HIP [134,175]. The ability to tailor each wasteform matrix to each specific waste-stream means waste loadings can be optimised and the total number of wasteforms needing processing can be reduced, subsequently reducing the final waste volume even further.

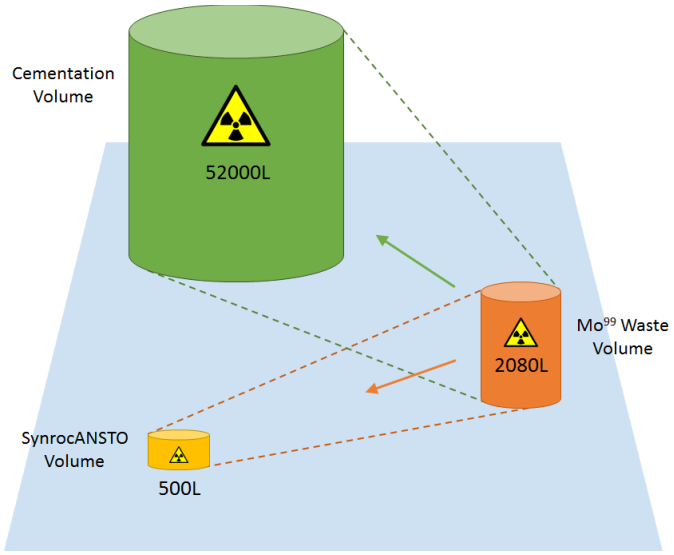

Figure 2.12: Schematic representation of the volume reduction generated by HIP compared to the volume increase of cementation. The schematic example is given for ILW ^{99}Mo production waste processed into a Synroc wasteform via HIP. (Adapted from [134])

In order to commercialise HIP as a waste treatment technology, scalability must be assessed. Small scale PuO_2 samples have proven wasteform capabilities and inactive scale-up trials have shown the scalability of the HIP process [15,166,181]. A scale-up project conducted by GeoRoc Ltd. processed intermediate level Magnox fuel pond sludges by HIP into ceramic / glass-ceramic wasteforms from a 50 ml scale to > 100 L scale and produced the first demonstration 102 L HIP canister for nuclear waste treatment (Figure 2.14) [181]. This project successfully demonstrated the scalability of HIP from straight walled research canisters to full scale bellows canisters, whilst achieving equivalent wasteform products and a cylindrical waste package suitable for storage and geological disposal [181]. This project also demonstrated the large waste volume reduction achieved by HIP; 160 L of Magnox

sludge waste simulant was treated and processed with suitable precursors in the 103 L canister and obtained a consolidated 40 L volume final waste package; a total waste volume reduction of 75% (Figure 2.14) [180]. It was calculated that HIP technology could reduce the raw waste volume by 80 %, with a 55 % volume saving compared to vitrification [180].

Figure 2.13: Proven scalability of the HIP process for treating nuclear waste. ILW Magnox pond sludge simulant was treated and processed by HIP from the 50 ml laboratory scale to > 100 L. (Images courtesy of GeoRoc Ltd.)

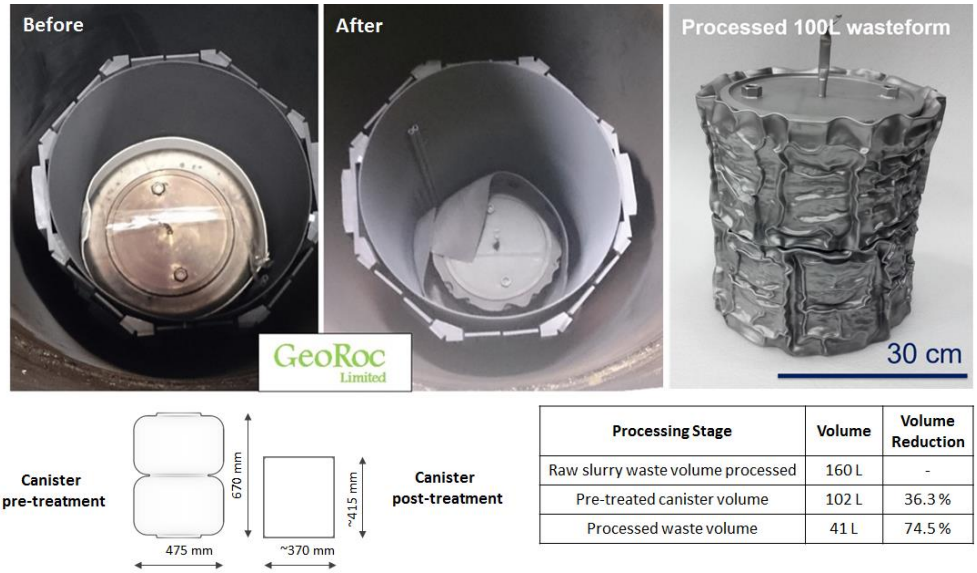

Processing Stage	Volume	Volume Reduction
Raw slurry waste volume processed	160 L	-
Pre-treated canister volume	102 L	36.3 %
Processed waste volume	41 L	74.5 %

Figure 2.14: A 102 L HIP canister before and after processing. The overall waste volume reductions achieved from the raw waste material to the final waste package are summarised. (Images courtesy of GeoRoc Ltd.)

2.5.4 Selected wastes for HIP

Idaho calcines (USA)

The Idaho calcine wastes originate from spent nuclear fuel reprocessing from 1953 – 1994 [182]. The liquid raffinates produced were later dried into granular calcines and stored in stainless steel containers approximately 3.5 m across and 16.7 m high. There are approximately 4,400 m^3 of the calcine waste stored in vessels inside six reinforced concrete silo storage tanks (approximately 24 m high by 18 m across) at the Idaho Nuclear Technology and Engineering Centre (INTEC) [166]. The dried calcine form was intended to be suitable for long-term interim storage of the waste, but analysis of the calcines revealed high toxicity, hazardous solvents and hydrogen fluoride present, thus the wastes require further treatment to be accepted for geological disposal [166]. In 2010, the Department of Energy (DOE) officially selected HIP for the treatment of the Idaho Calcines [173] due to its benefits over vitrification, significant volume reduction and the subsequent life cycle cost savings [81,166]

Mo-99 (Australia)

ANSTO are expanding their demonstration plant and have plans to construct a full scale waste processing plant for the treatment of ^{99}Mo production wastes [174,183]. ^{99}Mo is used in radiopharmaceuticals and nuclear medicine for diagnostic purposes. Produced in the on-site OPAL reactor at ANSTO, ^{99}Mo is transported across Australia and shipped around the world in Gentech® Generators that allow medical technicians to activate and extract ^{99m}Tc for patients [184]. ANSTO are expanding their production capabilities and plan to construct the SyMo waste treatment plant that will utilise the HIP technology to process the ILW raffinates from ^{99}Mo production into stable wasteforms.

Pu-residues (UK)

In 2002 the UK's BNFL[5], in collaboration with ANSTO, developed wasteform options and processing routes for the disposition of Pu-residues stored at the Sellafield site [17]. The

[5] Currently known as National Nuclear Laboratory (NNL)

project was suspended due to high rises in cost of the R&D but was reinstated under a Nuclear Decommissioning Authority (NDA) funded programme to demonstrate its technology readiness level (TRL) for treating the civil separated Pu stockpile through laboratory scale Pu active trials [185]. NNL are currently working to install an active glovebox line at the NNL Central Laboratory at Sellafield to commence active Pu trials by 2020 [185].

3 Materials and Methods

This chapter details the experimental procedures and analytical methods used throughout this project, with specific parameters and variations between chapters given. The experimental procedure for the uranium and plutonium samples is detailed separately in Chapter 8, as this work took place in different laboratory facilities at the Australian Nuclear Science and Technology Organisation (ANSTO).

3.1 Reagents

The choice of starting reagents was important in order to simplify the front-end procedure of the HIP cycle and ensure high quality reproducible samples. It was important to avoid carbonate materials and hygroscopic compounds, which would decompose at increased temperatures. Due to the hermetically sealed nature of HIP canisters, the decomposition and volatilisation of compounds would be trapped inside the HIP canister and inhibit the densification of the sample, thus produce a poor quality wasteform. The starting reagents for the basic glass-ceramic formulations included ceramic formers; calcium titanate ($CaTiO_3$), anatase (TiO_2), zirconium oxide (ZrO_2), and glass formers; quartz sand (SiO_2), anhydrous sodium silicate (Na_2SiO_3), anhydrous borax ($Na_2B_4O_7$) and aluminium oxide (Al_2O_3). By utilising $CaTiO_3$ and anhydrous forms of the Na_2SiO_3 and $Na_2B_4O_7$ compounds, both calcium carbonate ($CaCO_3$) and sodium carbonate (Na_2CO_3) were avoided. Thus, the release of CO_2 from the decomposition of carbonate materials and the volatilisation of absorbed water from hygroscopic reagents, were minimised. Particle size distribution (PSD) of the starting materials was conducted using a Malvern Mastersizer 3000 (Figure 3.1).

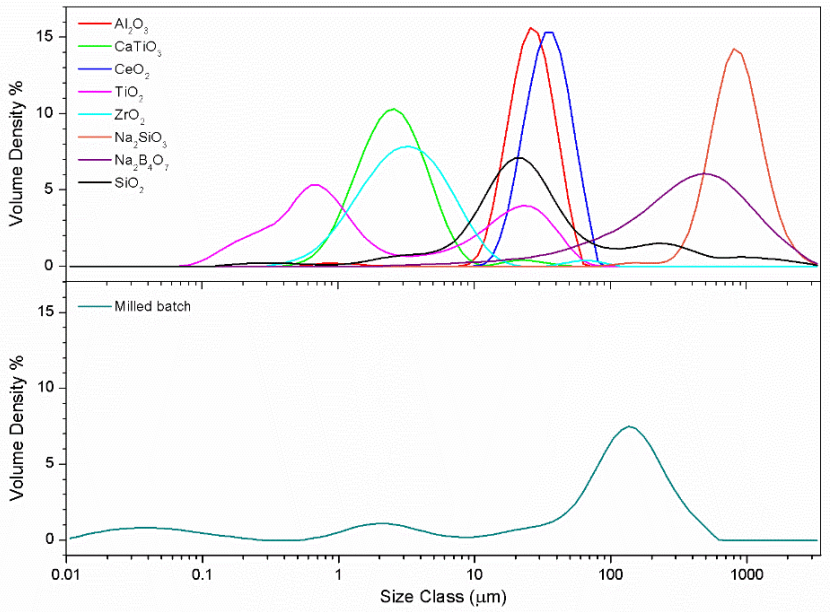

Figure 3.1: Comparative plot of PSD data for starting materials (top) and for a batch after 30 min milling at 500 rpm in a planetary mill. CeO_2 is included as the waste analogue precursor for Chapters 6 and 7.

3.2 Batching and milling

3.2.1 Batch calculations

The target glass-ceramic formulations varied as the project progressed and specific formulations are given in each Chapter. In general, for the batch calculations, the glass formers were dealt with separately to the ceramic formers. The general chemical formula for the glass-ceramic systems throughout this thesis is given in equation 6, where x and y are varying additions of CeO_2 as detailed in individual Chapters, and z signifies Al_2O_3 additions. The fraction of glass to ceramic was also investigated in Chapter 5 where samples were batched for 30 wt. %, 50 wt. % and 70 wt. % glass fractions. The conclusions gained from Chapter 5 allowed for an optimised formulation (equation 7) that maximised the yield of zirconolite to be selected, and subsequently used for all further experiments investigating waste incorporation (Ce Chapter 6, UO_2 / PuO_2 Chapter 8) and Cl contamination (Chapter 7).

$$Ca_{1-x}Zr_{1-y}Ce_{x+y}Ti_{2-2x}Al_{2x}O_7 + Na_2Al_{1+z}B_{1-z}Si_6O_{16}$$ **Eq. 6**

$$70\ \text{wt. \%}\ Ca_{1-x}Zr_{1-y}Ce_{x+y}Ti_2O_7 + 30\ \text{wt. \%}\ Na_2Al_2Si_6O_{16}$$ **Eq. 7**

3.2.2 Milling

Prior to batching the oxides were dried at 180 °C. All precursors were weighed out on a 4 decimal place balance within ± 0.005 g error. The powders were milled in a Fritsch planetary mill at 500 rpm with isopropanol as a milling agent. The batches were dried at 85 °C and were passed through a 500 µm sieve to break up large lumps.

Experimental Parameters

Chapters 4, 5: 25 g batches were milled in SiAlON 50 ml volume milling pots with 10 – 12 ml of isopropanol for 5 min.

Chapters 6, 7: 25 g batches were milled in SiAlON 50 ml volume milling pots with 10 – 12 ml of isopropanol for 30 min.

Chapters 6: Powders were milled in a stabilised zirconia 250 ml volume milling pot in 50 g batches with 22 – 25 ml of isopropanol for 30 min.

3.3 HIP canister preparation and packing

Straight walled HIP canisters were fabricated from 316 stainless steel. The canisters were fabricated from 38.1 mm ($1\frac{1}{2}$ inch) tubing with 1.8 mm thick walls cut to approximately 35 mm lengths. The base and lid of the canister were prepared from 2 mm thick disks cut from a solid 316 stainless steel rod with a 35 mm diameter (Figure 3.2). The tubing for the canister walls was lathed on both ends to remove 0.25 mm from the inside of the wall to a depth of 1 mm. This allowed the end disks to fit inside the tubing with a snug fit to a maximum depth of 1 mm, and sit proud by 1 mm above the canister wall for welding. A 6.35 mm hole was drilled into the centre of the lid for the evacuation tube. The evacuation tube (6.35 mm diameter tubing, 1.65 mm wall thickness) was welded into the lid (sealing on

both sides) and was used to evacuate the canister of air and volatiles before final sealing ready for processing. Each canister had an approximate internal volume of 30 ml.

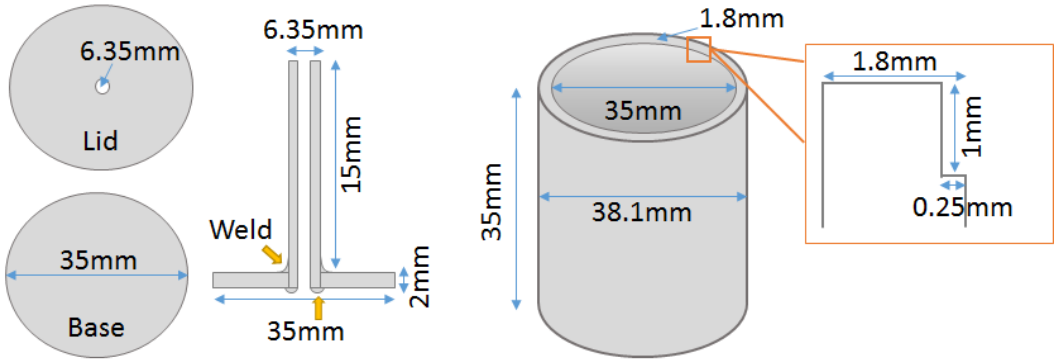

Figure 3.2: Schematic diagram of canister components.

The lid connection was designed to make welding easier for the operator but also provide a "safety-wall" between the weld-torch and the powder during welding. All welding was performed using a Miller Dynasty 200 TIG welder with a current of 45 Amps.

Calcined powders were manually packed into the HIP canisters. Powders were manually tapped down and compacted with a mallet as much as possible to achieve a suitable packing density. Insufficient packing would result in more deformation of the canister, more strain on the welds and could lead to canister failure. For the U samples powders were pressed into pellets. This ensured better packing density thus controlled compaction of the canister for easier opening, and reduced dust production when preparing each sample. On an industrial scale plant the method of canister filling would be different and would likely utilise granulation and vibratory packing to avoid blockages, minimise dust production and maximise canister packing [41,186].

The lids were welded to the packed canisters with a steel wool filter added to the inside of the lid at the base of the evacuation tube. This filter stops powder entering the vacuum pump line during evacuation of the canister. The evacuation tube was then connected to a vacuum pump to remove all air from inside the canister. This is an essential step for the production of a dense material to provide a differential pressure between the inside and outside of the canister during processing [159]. If the air is not removed the pressure inside the canister would increase during the HIP cycle and resist compaction from the external forces resulting in a porous sample. The canisters were evacuated to $3-5$ Pa vacuum pressure at room

temperature. The temperature was then increased for the bake-out step to remove any water and volatiles from the canister. Once the initial vacuum pressure had been reached it was assumed all volatiles had been removed. Final sealing of the canister involved crimping the evacuation tube, using a hydraulic hand press up to 400 bar. A second crimp was applied above the first crimp, before breaking the second crimp, ensuring not to damage the first and sealing with a weld. At this stage the sample was ready for processing.

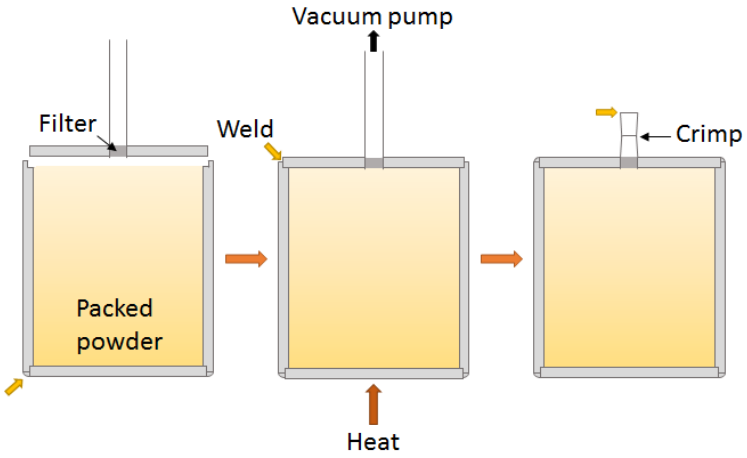

Figure 3.3: Schematic diagram of the sealing process for each HIP canister.

3.4 Processing – HIP cycle

All HIP samples in this thesis were processed with a basic HIP cycle recipe that used the same temperature and pressure conditions as previous work conducted by NNL [154]. Samples were consolidated at 1250 °C for 4 h under 103 MPa (15,000 psi) of argon gas pressure, using a molybdenum furnace. The temperature and pressure were applied simultaneously to reach the target set-points at the same time. The temperature ramp rate was 10 °C/min to 1250 °C. Unfortunately, the time scale and scope of this project did not allow the author to investigate different cycle conditions.

The cycle recipe shown in Figure 3.4 shows the individual steps of the HIP cycle. Prior to the pressure increase, the pressure vessel was purged by inputting 1.4 MPa (200 psi) of gas, venting and applying a 250 torr vacuum, before a second purge ensures the pressure vessel is clear of any remaining oxygen that would cause oxidation of the furnace during the cycle. A gas input of 10 MPa (1500 psi) is needed to avoid damage to the compressor when it initialises, at which point the temperature begins to ramp at 10 °C/min. During the 4 h dwell

the “pressure makeup” is ON so the dwell conditions are maintained during the whole dwell period. The HIP returns to room conditions with a controlled cool of 10 °C/min and simultaneously vents the gas pressure.

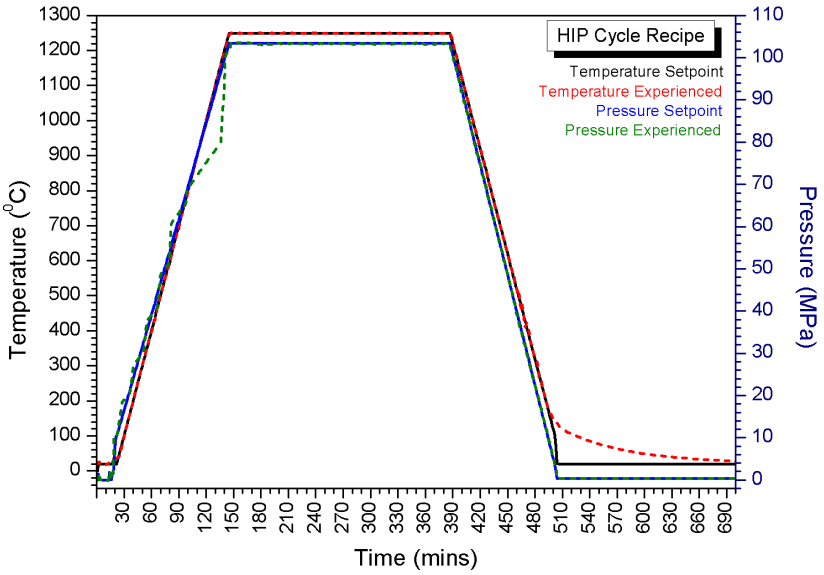

Figure 3.4: The temperature – pressure profiles for a standard HIP cycle recipe of 1250 °C, 103 MPa (15,000 psi). The set-point data (solid lines) is plotted alongside the experienced data (dotted lines).

3.5 Densification measurements

Before and after processing, the mass, dimensions and volume of the HIP canisters were measured in order to calculate the volume reduction during processing and densification achieved. Each measurement was taken in triplicate to obtain average values. Dimensions (including; height, top diameter and middle diameter) were taken using a micrometer and the volume was measured using Archimedes’ water displacement method. Material densification was calculated for the consolidated glass-ceramic materials by helium gas pycnometry on powder samples for the true density and water displacement measurements on monoliths for the bulk density.

3.6 Sample retrieval

Retrieving the HIPed material from the stainless steel canisters proved difficult due to the combination of metal, glass and ceramic, for which no blade is suitable for cutting through

all materials. After trying multiple methods to open the HIP canisters and retrieve the samples, the most efficient way was to use a 3 step process:

1) The canister lid and base were removed using a HHH ferrous blade on a Buehler Abrasimet™ 250 saw. The blade cut just deep enough to reach the composite material inside. The canister is then rotated in the clamp to repeat the cut until the lid was separated.
2) Either, the sides of the canister were removed by cutting into quarters on the Abrasimet™ 250, or a 10mm central core was taken using a diamond drill bit.
3) The removed material was sectioned into monoliths using a diamond blade on a Buehler IsoMet™ low speed saw, or crushed using a percussion mortar for powder samples.

Due to the compaction of individual canisters, the removal of the canister walls was not always possible. In such cases, as much of the canister was removed as possible using the Abrasimet™ 250 saw and the sample was crushed in a vice to remove pieces suitable for SEM and XRD analysis.

3.7 Scanning Electron Microscopy (SEM)

Scanning electron microscopy (SEM) gives information on the surface / near surface structure of monolithic bulk samples. A beam of high energy electrons is passed through a series of lenses that focus the beam through an aperture and onto the surface of a sample. The incident beam of electrons results multiple types of emissions that can be used to give different information on the sample structure. The primary emissions are secondary electrons, backscattered electrons and X-rays [187].

3.7.1 Structure of the microscope

An atom consists of a positive nucleus surrounded by negative electrons in electron shells. Each electron shell has a different binding energy depending on its distance from the nucleus, orbital configuration and atomic charge. Electrons closest to the nucleus in the K-shell require the most energy to overcome the binding energy and emit an electron. Each individual electron excitation or emission from an atom has a unique energy associated with it, which can be used to gain information about the sample.

The electron source in an SEM is typically a tungsten filament, which when heated, emits both visible photons and electrons. The emitted electrons are accelerated to a known energy, between 10 – 30 keV, by a potential difference across two anodes [187]. The high energy electrons are focused into a small, concentrated beam by passing through a series of lenses and magnetic fields. The magnetic fields deflect the electrons causing them to move across the lenses in a helical motion and converge in the centre. The magnetic field is generated by a current flowing through a wire coil. These lenses and coils are shown in Figure 3.5, a simplified schematic representation of the structure of a scanning electron microscope [187].

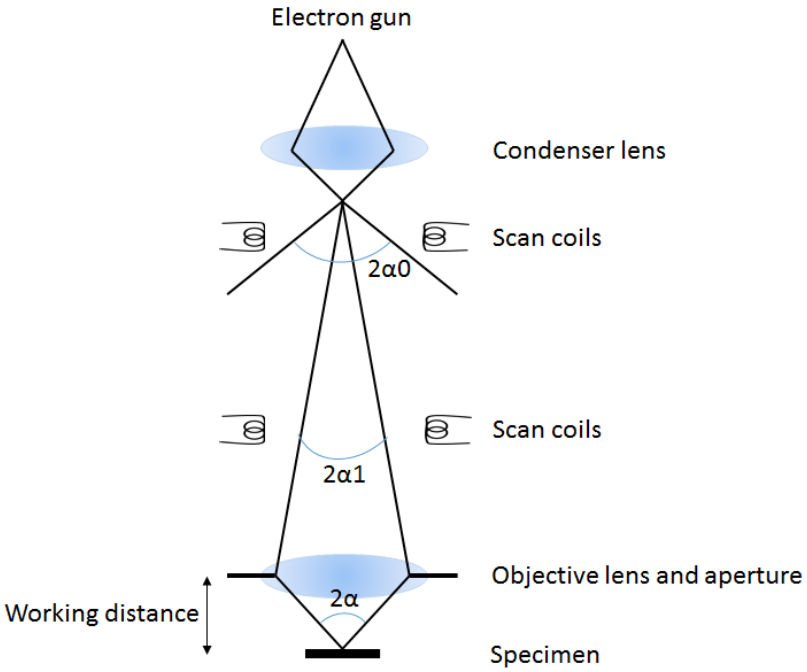

Figure 3.5: Schematic diagram of a two lens scanning electron microscope. (Adapted from [187])

3.7.2 Secondary emissions

When electrons interact with atoms in a sample, either elastic or inelastic interactions take place. Elastic scattering occurs when an electron interacts with an atom causing a change of direction with negligible energy loss. This is due to the Coulombic interaction known as Rutherford scattering, whereby the electrostatic interaction between the negative electron and positive nucleus results in the deflection of the electron in a new direction without a

physical collision [187]. Inelastic scattering results in an electron losing energy through collisions and interactions within the sample. The electron may gradually lose kinetic energy through multiple interactions and become trapped within the sample (absorption), or cause the emission of atomic electrons (known as secondary electrons) and / or electrostatic energies (X-ray photons) that can escape the sample surface [187]. These detectable energies (Figure 3.6) can be used to gain information about the sample.

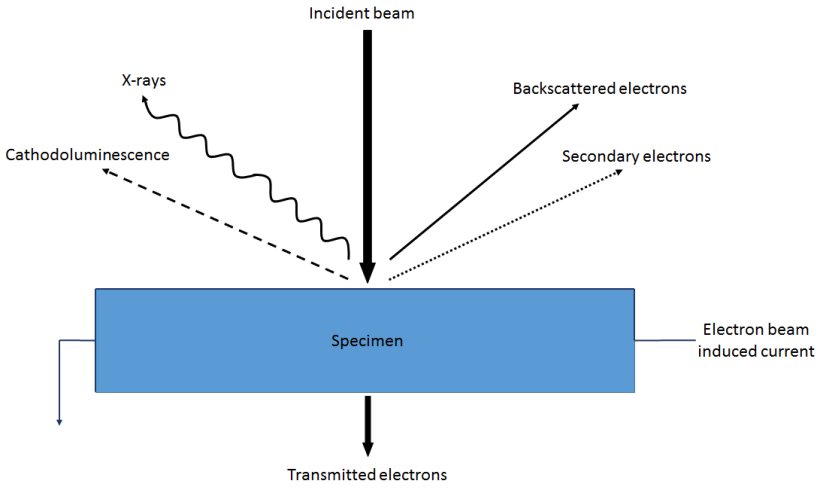

Figure 3.6: Schematic diagram of resultant signals produced by an SEM incident electron beam. (Adapted from [187])

Secondary electrons (SE)

Secondary electrons (SE) are electrons emitted from the surface of the sample with less than 50 keV of energy [187,188]. Such electrons may be incident electrons that have lost the bulk of their energy through collisions at the near surface of the sample, or outer-shell atomic electrons emitted by the transfer of energy during a collision with an incident electron. Due to the low energy of SE, many are trapped within the interaction volume due to inelastic scattering. Only those near the sample surface with the correct deflection angle are detected [188]. As such, SE only give details of the near surface region of the sample. Figure 3.6 indicates the penetration depth for SE comparative to backscattered electrons (BSE) and X-rays. SE, however, are emitted with a smaller scattering angle than BSE and therefore obtain better resolution of the sample surface [187,188].

Backscattered electrons (BSE)

Backscattered electrons (BSE) are incident electrons deflected more than 90° from the sample and retain most of their incident energy (more than 50 keV). The number of BSE released (backscattering coefficient) is known to increase proportionally with atomic number, giving information on the chemical composition of the sample [188]. BSE have a larger penetration depth than SE and are less abundant thus do not achieve as good a resolution.

Energy dispersive X-rays (EDX)

Energy dispersive X-rays (EDX) are produced due to atomic relaxations in the sample structure. When a high energy electron excites an inner-shell electron to produce an electron-hole pair, an outer-shell electron quickly fills the electron hole emitting a photon of energy equal to the relaxation [187,188]. This energy is characteristic to the relaxation and atomic number of the atom involved. Photons with energy in the visible range can be used for cathodoluminescence and X-ray photons can be used for elemental mapping. EDX maps show the distribution of each element throughout the sample and can be displayed as a map, line scan or point scan.

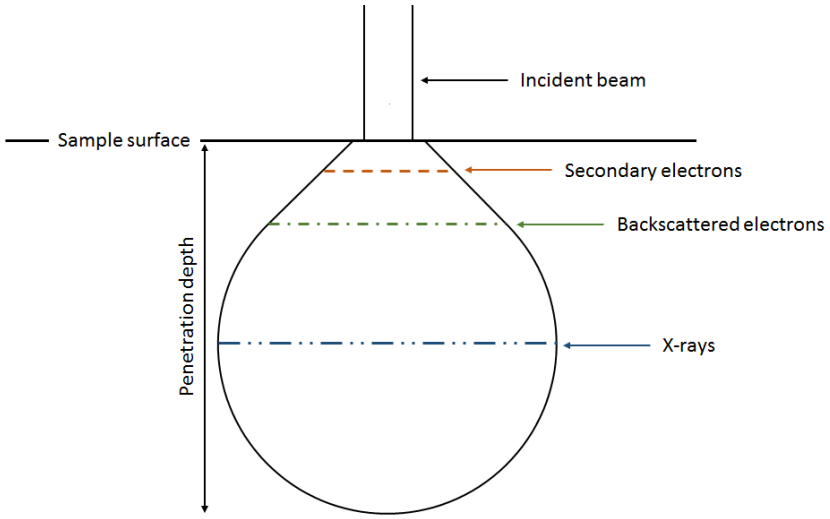

Figure 3.7: Schematic diagram of the relative penetrative depths of secondary electrons (SE), backscattered electrons (BSE) and energy dispersive X-rays (EDX). (Adapted from [187])

Experimental Parameters

Sectioned samples were cold mounted in epoxy resin before grinding and polishing. Samples were ground on a Buehler Automet™ 250 using SiC grit papers of increasingly finer grits, from P600 to P1200 grades. Samples were then polished to a 1 µm finish using diamond paste and diamond suspension solutions. The samples were carbon coated and electrodag silver paste was applied to provide a conductive pathway for electrons to travel from the sample surface.

Images were collected at various magnifications on a Hitachi TM3030 analytical microscope with an integrated Bruker Quantax EDX spectrometer. A 15 kV accelerating voltage was used at a working distance of 8 mm. EDX maps were collected for a minimum of 10 min.

3.7.3 Electron Probe Micro – Analysis (EPMA)

Electron probe micro-analysis (EPMA) is a non-destructive quantitative chemical analysis technique that utilises a small spot size, multiple spectrometers (wavelength dispersive spectroscopy) and analytical crystals, to obtain a more precise chemical analysis with a higher sensitivity and accuracy than SEM-EDX [189]. Like SEM-EDX, EPMA utilises the X-ray emissions from a sample exposed to a beam of high energy electrons. Wavelength dispersive spectroscopy (WDS) is often used in EMPA to detect specific elements within a sample. A series of spectrometers are aligned in sequence, vertically around the sample chamber and the analytical crystal is oriented at a specific angle [190]. The X-rays are incident on the crystal and only those with wavelengths that satisfy Bragg's Law at the given angle are detected (see section *3.8*). This allows for individual elements to be detected and quantified in the sample. In order to detect a series of elements the orientation of the crystal and detector must change along the Rowland circle. The sample, crystal and detector sit on the Rowland circle to enable focusing of the X-rays. Figure 3.8 demonstrates the Rowland circle and experimental setup within WDS – EPMA [190]. The data detected is compared against a standard of a known composition and corrected for sample effects and experimental errors, to produce the data as wt. % of oxides and / or element.

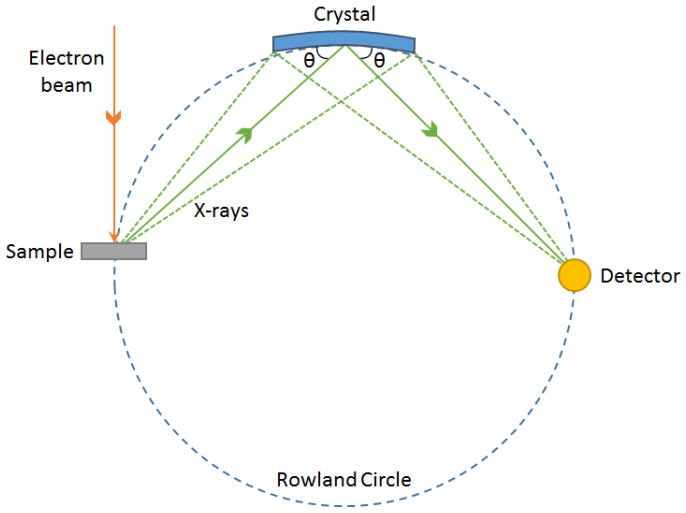

Figure 3.8: Schematic representation of the experimental setup between the sample, analytical crystal and detector on the Rowland circle within a wavelength dispersive spectrometer (Adapted from [190]).

Experimental Parameters

The EPMA data was collected by Dr Chris Hayward at the EPMA Facility, School of Geosciences at the University of Edinburgh.

Chapter 5: EPMA compositional analysis was performed on five samples for compositional analysis of the glass phase. Data was collected using a Cameca SX100 instrument with beam conditions of 10 kV and 5 µm beam diameter. A current of 0.5 nA was used for major elements and a current of 20 nA was used for minor elements. The 0.5 nA current was used to minimise the error associated with Na mobility, whilst an air jet and the low voltage was required for analysis of the B. Data was standardised against multiple standards; Na – Jadeite (Na : 11.34 %, Al : 13.23 %, Si : 27.78 %, Fe : 0.17 %, O : 47.65 %), Si – Wollastonite (Mg : 0.17 %, Al : 0.03 %, Si : 24.00 %, Ca : 34.32 %, Mn : 0.05 %, Fe : 0.28 %, O : 41.37 %), Ti – rutile (Ti : 59.34 %, O : 39.89 %, Mg : 0.01 %, Fe : 0.59 %, Nb : 0.17 %), Zr – zircon (Si : 15.24 %, Mn : 0.03 %, Zr : 49.14 %, Hf : 0.82 %, O : 34.77 %), Al – spinel (Mg : 17.08 %, Al : 37.93 %, O : 44.99 %), and for B a sample of international simple glass (ISG) was used; 60.2 SiO_2, 16.0 B_2O_3, 12.6 Na_2O, 3.8 Al_2O_3, 5.7 CaO, 1.7 ZrO_2 (mol. %) [191].

3.8 X-Ray Diffraction (XRD)

Powder X-ray diffraction (XRD) is an analytical technique used to gain structural information on phases present in a sample. Data collected can be used for phase analysis, phase quantification and crystal structure determination [192]. A divergent beam of X-rays are generated from a high energy beam of electrons hitting a metal target (generally Cu or Mo) resulting in the ionisation of electrons from the metal atoms [193]. For Cu, 1s electrons are ionised and 2p electrons fill the electron holes in the 1s shell. X-rays are emitted with specific wavelengths equal to the energy associated with the transition of the 2p electrons. Due to the spin states of the 2p electrons two wavelengths are generated from Cu; $K\alpha_1$ = 1.54051 Å and $K\alpha_2$ = 1.54433 Å, which are averaged to an X-ray wavelength of 1.5418 Å (referred to as Cu Kα radiation). The $K\alpha_2$ signal can be removed if a monochromator is present.

For diffracted X-rays to be detected, they must obey Bragg's Law [193,194]. Bragg's Law assumes crystallites consist of parallel planes, which X-rays either scatter off at all angles or transmit through and scatter off an adjacent plane. The diffracted beam of X-rays must be scattered at an angle equal to the angle of incidence, θ. For detection, the diffracted X-rays must be in phase with each other, such that the phase difference between diffracted beams is an integer number of wavelengths (n). At all angles other than θ the diffracted beams will be out of phase and result in destructive interference. The phase difference depends on both the angle of diffraction and the distance travelled so the inter-planar spacing must also be considered (d). Figure 3.9 is a schematic representation of Bragg's Law and the interaction of two X-ray beams with adjacent crystal planes [193]. Beams **1** and **2** have equal angles of incidence, and diffracted beams **1'** and **2'** are diffracted at the same angle (θ). For the diffracted beams to be in phase with each other, the extra distance travelled by beam **2-2'** ($2d\sin\theta$) must be equal to a whole number of wavelengths (nλ), thus obeying Bragg's Law (equation 8).

$$n\lambda = 2d\sin\theta \qquad \textbf{Eq. 8}$$

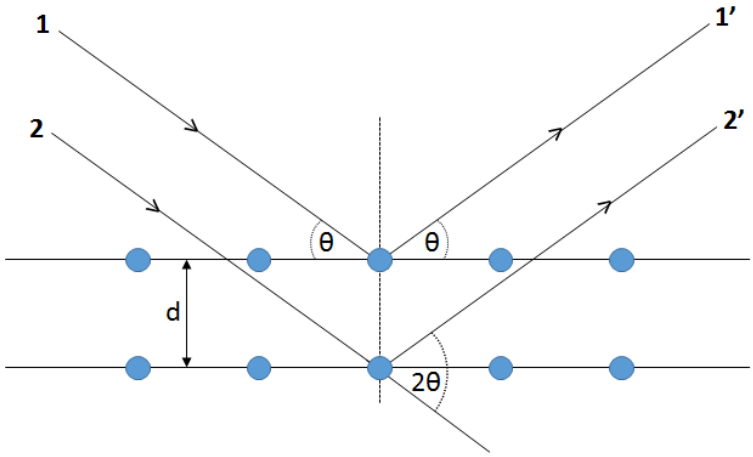

Figure 3.9: Schematic derivation of Bragg's Law. (Adapted from [193])

XRD utilises fine powder samples where crystallites are orientated randomly throughout. Due to the random nature of powder samples, all lattice planes can be present at all orientations. Many crystallites are orientated such that Bragg's angle is achieved thus diffraction can occur for the lattice planes exposed [193,194]. As a result, XRD patterns consist of multiple reflections for each type of crystallite corresponding to different planes. These can be used to identify phases present and determine information on the crystal structure. XRD data are plotted as the intensity of the diffracted X-rays against the angle between diffracted and undiffracted X-rays, 2θ.

Experimental parameters

Power samples were crushed using a percussion mortar and sieved to <150 µm. The powders were refined in a micromill for 3 min at 30 oscillation/sec. Samples were analysed using a Bruker D2 PHASER diffractometer with Cu Kα radiation (1.5418 Å). Data were acquired between 10° ≤ 2θ ≤ 70°, with a 0.02° step size for a count time of 3.25 sec per step under normal fluorescent conditions (Lynxeye discriminator settings; lower = 0.110, upper = 0.250). A Ni filter was present on the source and a slit size of 1 mm was used. Data analysis was conducted on PDF - 4+ software for phase identification.

3.8.1 Phase quantification

Rietveld refinements were performed on four samples with various glass compositions and glass fractions. Rietveld refinement fits a crystallographic model to an experimental profile

via a least squares refinement [195]. By fitting the width, height and peak position of individual reflections in the experimental data, information can be extracted about the crystal structure and phase abundance.

Chapter 5: The refinements were performed to determine quantitative phase analysis of the glass-ceramic samples and how the phase assemblage changed with changes to the glass formulation. XRD samples were prepared with 10 wt. % MgO (calcined at 900 °C) mixed in as an internal standard to allow quantification of the glass phase. The refinements were performed using the GSAS software package [196].

3.9 Thermo – Gravimetric Analysis (TGA)

Thermo-gravimetric analysis (TGA) measures the mass of a sample as a function of time or temperature under a controlled atmosphere (N_2) [197]. The mass of the sample is measured when heated at a constant rate to identify temperatures at which the sample begins to decompose. This could be a loss of water from hygroscopic compounds or the breakdown of a compound such as $CaCO_3$.

3.9.1 TGA – Mass Spectroscopy (TGA-MS)

Thermal analysis is often coupled with mass spectroscopy (MS). Ionised particles are accelerated through a vacuum and deflected by magnetic fields according to their mass and charge [198]. Lighter ions and / or higher charged ions are deflected more than heavy ions or ions with a lower charge, separating them for detection. The relative abundance of detected ions is plotted against their mass : charge ratio allowing individual ions to be identified. This information coupled with the TGA data means the compounds lost from the sample at specific temperatures can be identified.

Experimental parameters

Chapter 4: TGA data were collected on a PerkinElmer STA 8000 TGA / DTA heated at 10 °C/min to 1250 °C in alumina crucibles under an Ar atmosphere. MS data were collected using a Hiden mass spectrometer, heated to 1000 °C at 10 °C/min under N_2 atmosphere.

3.10 Solid State Nuclear Magnetic Resonance (NMR)

Solid state nuclear magnetic resonance (NMR) is an analytical technique used to gain structural information at the atomic level within crystalline and disordered materials [199]. By utilising the magnetic moment of different nuclei that have nuclear spin energies > 0, NMR measures variations in relaxation energies to identify different structural environments for specific nuclei.

In an externally applied magnetic field, nuclei with nuclear spin energies > 0 undergo Zeeman Interactions and separate from the ground energy state into individual energy levels [199,200]. Each energy level corresponds to nuclei with different shielding and structural environments, which experience different magnetic fields as a result. When exposed to plane-polarised pulsed radiofrequency radiation, low energy levels absorb the radiofrequency photons and are excited to higher energy levels [199,201]. When the radiofrequency radiation is removed, the excited states undergo relaxation to their initial state and emit a photon of radiofrequency radiation. These relaxations are measured by producing a voltage in a coil and are recorded as a function of time (Free Induction Decay (FID)). From this data the NMR spectra is extracted by Fourier Transformation [199,201]. The variations in relaxation energies are very small and are a direct result of changes in the structural environments between individual nuclei. This makes NMR highly sensitive to structural changes and consequently gives information on specific atomic structures and local environments present in crystalline and disordered materials.

3.10.1 Magic Angle Spinning (MAS)

In solid state NMR often the resolution of the data needs enhancing. As a result of the bulk material and all elemental nuclei being present, other effects interfere with the data resolution, such as dipole-dipole interactions, magnetic shielding, chemical shift anisotropy, field-independent quadrupolar interactions and spin-spin coupling [202]. These can result in a broadening of the NMR data. Magic angle spinning (MAS) is often used in solid state NMR to help eliminate these additional effects. MAS utilises a “magic angle” of 54.74°, at which the sample is oriented to the magnetic field. The sample is then rotated at high frequencies (5 – 35 kHz) about the axis of symmetry to remove the effects of chemical shift anisotropy

from the measured data [202]. The magic angle results in the first-order polynomial ($1\text{-}3cos^2\theta$) becoming equal to zero, thus removes the effects of dipole-dipole interactions and anisotropic chemical shift, which now equal zero, and allows for analysis of the isotropic chemical shifts [203].

Experimental parameters

Chapter 5: ^{27}Al (spin, I = 5/2), ^{23}Na (I = 3/2) and ^{11}B (I = 3/2) MAS-NMR experiments were performed at 208.6, 211.7 and 256.8 MHz, respectively, on a 18.8 T Bruker AVANCE III 850 spectrometer using 3.2 mm probe heads operating at spinning frequencies of 20 – 22 kHz. The ^{27}Al NMR spectra were recorded with a 0.6 µs pulse length, 4096 scans and a 0.5 s recycle delay. The ^{23}Na NMR analyses were conducted with a 1 µs pulse length, 2048 scans and a 0.5 s recycle delay. The ^{11}B MAS-NMR experiments were performed with a 1 µs pulse length, 4096 scans and a 0.5 s recycle delay. The ^{27}Al, ^{23}Na and ^{11}B chemical shifts were referred to liquid $Al(NO_3)_3$ (1M), NaCl (1M) and solid $NaBH_4$ as 0, 0 and –42.06 ppm, respectively.

3.11 Helium Gas Pycnometry

Gas pycnometry uses gas displacement to measure the volume and true density of a sample. A known mass of a powder sample is added to the sample chamber. When empty the chamber holds a specific known volume of gas equal to that of a reference chamber. The gas in the sample chamber is transferred to the reference chamber and the pressure difference is measured as the gas expands into the empty chamber. The change in pressure allows for computational measurement of the volume of the sample [204]. With the mass and volume data, the software calculates the density of the sample. Powder samples largely eliminate closed porosity that would contribute to the volume measurement thus the true volume and true density of the material is measured. The gas pycnometry measurements were coupled with water displacement density measurements on monolithic samples to determine the percentage of densification of the HIPed samples. The monolith samples were weighed in air and submerged in water to measure the mass when buoyant. Using Archimedes' principle (equation 9) the density of the final HIPed product was calculated. To determine the wasteform densification percentage, the monolith density was calculated as a percentage of the pycnometry true density value.

$$\rho_s = \frac{m_a \times \rho_f}{m_a - m_f}$$ **Eq. 9**

Where ρ_s is the density of the sample, ρ_f is the density of the fluid (density of water 1 g/cm^3), m_a is the mass of the sample in air and m_f is the apparent mass of the sample in the fluid.

Experimental parameters

All pycnometry measurements were performed using an AccuPyc-1340-II gas pycnometer using helium as the gas medium. Powder samples were run in a 1 cm^3 chamber to a fill pressure of 12.5 psig for 20 purges and 20 cycles each.

3.12 X-ray Absorption Near – Edge Spectroscopy (XANES)

Synchrotron radiation (SR) utilises high energy electrons travelling near the speed of light to generate X-rays. The high energy electrons are accelerated by a linear accelerator, known as the Linac, before entering the storage ring [205]. The electrons travel around the storage ring guided by bending magnets, undulators and wigglers that change the direction of travel. Every change of direction results in the emission of X-rays with a range of wavelengths. The X-rays enter the beamline where a monochromator is used to select the desired energy, by step scanning across an energy range.

There are two main types of measurements performed using SR; transmission and fluorescence measurements.

Transmission

Transmission data measures the absorption of X-rays by the sample. The intensity of the beam is measured before and after the sample and the loss of intensity corresponds with the level of absorption [205]. These experiments use powder samples homogeneously distributed and pressed with PEG (poly-ethylene-glycol) into pellets. The sample is ground into a fine powder and is gently mixed with 100 mg of PEG at a ratio determined by the atomic mass of the sample using Hephaestus software [206]. Once uniformly combined the powder is pressed into thin pellets of 10 – 13 mm diameter. The thickness and concentration

of the pellets is important to ensure the X-rays can transmit through, but that enough are absorbed for a readable signal.

Fluorescence

Fluorescence experiments use bulk monolith samples and a detector positioned perpendicular to the X-ray beam to detect emitted photons. X-rays absorbed by the sample result in the excitation of an electron from an inner orbital. The relaxation of an outer-shell electron to occupy the vacancy results in the emission of a photon with an energy characteristic to the energy difference between the two electron shells [205]. For any given element, one specific relaxation is measured for XANES and EXAFS, for example, the Ce L_3 signal corresponds to the $2p^6 4f^0 5d^0 \rightarrow 2p^5 4f^0 5d^1$ electron transition [207–209]. The emitted photons travel in random directions and only those traveling in the direction of the detector are picked up. The detector, such as the pin-diode shown in Figure 3.10, detects X-rays emitted perpendicular to the beam but picks up other emissions as well, including elastically scattered incident X-rays and photons from elements not of interest in the sample [205]. Consequently, fluorescence data has a lower resolution and more noise associated with it than transmission data.

Experimental parameters

Chapter 6: Ce L_3 XANES data were collected at the DELTA beamline facility in Germany on beamline 10. The experimental setup enabled us to get Ce L_3 XANES data on transmission and fluorescent samples. Figure 3.10 shows the set-up of the beamline that consisted of a meter long tube filled with helium, ionisation chambers before the helium tunnel and after the sample, and a pin-diode detector used for fluorescence experiments. A couple of things to note about the experimental setup include the helium tunnel, the pin-diode detector and the monochromator. Whilst clear data were obtained, these components contributed to the background noise and experimental error.

- **Helium tunnel**: interaction with the He particles can cause deflection and absorption of the X-rays. The further the beam has to travel before contacting the sample provides more opportunities for such beam fluctuations and X-ray loss.

- **Pin-diode detector:** the detector was not tuneable to only select fluorescence emissions, thus the detection of all photons contributed to the background.
- **Monochromator:** all data collected had glitches present at specific energies. These could be correlated to monochromator and motor imperfections. The glitches were present at the same energy in all data so were removed during analysis as an experimental glitch.

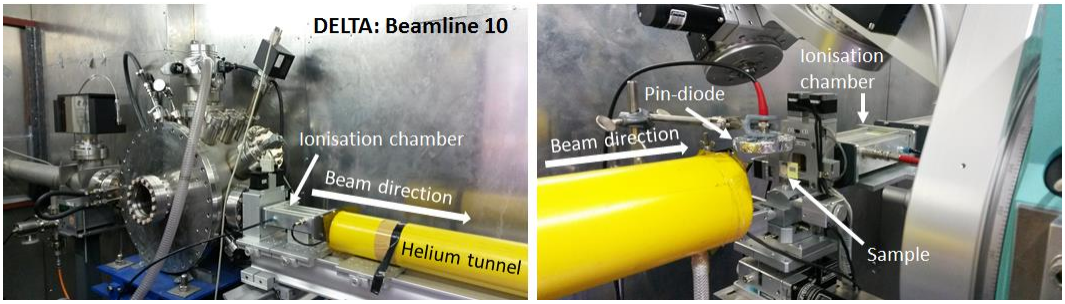

Figure 3.10: Pictures of the DELTA beamline 10 showing the setup of the beamline.

Transmission data were collected to gain information about the oxidation state of Ce with the samples. Fluorescence data were also collected on monolith samples to observe how the oxidation state of Ce changed from the edge to the centre of the canister. Monolith samples were sectioned from the HIPed samples on a Buehler IsoMet™ low speed saw to achieve parallel sides. For XANES analysis, flat, parallel sided samples are required. As such these monolithic samples were not cold mounted and were ground and polished manually to avoid fracturing the cross-sections.

Chapter 7: Cl K-edge XANES data were acquired on the XMAS bending magnet beamline (BM28) at the European Research Synchrotron Radiation Facility, Grenoble, France. The XMAS beamline was configured with a fixed exit, double crystal, Si (111) monochromator; a rhodium coated toroidal mirror of silicon crystal that focused the beam to a spot size of 1 mm. Harmonic rejection was provided by rhodium coated pyrex mirrors [210]. Cl K-edge XANES data were acquired at room temperature in fluorescence mode, using a Vortex Si drift detector, with the samples orientated at an incidence angle of 45° between the beam and detector, under a helium atmosphere.

The absolute energy scale was calibrated to the L_3 absorption edge of a Rh reference foil set at E_0 = 3004.0 eV [211]. Since the XMAS beamline utilised an optically encoded

monochromator, the energy drift between scans was expected to be negligible and this was verified by periodic acquisition of data from the Rh reference foil. A comprehensive full account of the specifications for soft XAFS measurements has been previously published [210].

Samples were prepared as 6 mm pellets of a homogenous dispersion of analyte powder in ca. 100 mg of PEG as a binder. Data reduction and analysis were performed using the Athena, Artemis and Hephaestus software [206]. Data acquisition and analysis were restricted to the near-edge region due to the presence of trace Ar within the He gas environment and consequent absorption edge at 3207.0 eV [211], which prevented reliable background subtraction for analysis of the extended X-ray absorption fine structure (EXAFS).

4 Process optimisation

The effect of pre-treatment parameters on the quality of glass-ceramic wasteforms for plutonium immobilisation, consolidated by hot isostatic pressing.

Stephanie M. Thornber[a], Paul G. Heath[a], Gabriel P. Da Costa[a, b], Martin C. Stennett[a], Neil C. Hyatt[a, *]

[a]*Immobilisation Science Laboratory, Department of Materials Science & Engineering, The University of Sheffield, Sir Robert Hadfield Building, Mappin Street, Sheffield S1 3JD, UK*

[b]*Department of Chemical Engineering & Pretroleum Engineering, Universidade Federal Fluminense, Rua Passo da Patria 156, CEP 24210-240, Niteroi, RJ, Brazil*

Journal of Nuclear Materials **485** (2017) pp. 253-261.

Author contributions: Stephanie M. Thornber designed and developed the experimental matrix, fabricated, characterised and analysed all samples and wrote the scientific report. Paul G. Heath helped plan the experimental matrix and provided useful communications. Gabriel P. Da Costa fabricated and characterised the glass frit HIP sample. Martin C. Stennett provided useful communications and Neil C. Hyatt provided project oversight and supervision.

4.1 Introduction

Hot Isostatic Pressing (HIPing) is a process which simultaneously applies heat and pressure to consolidate and sinter materials. The use of isostatic pressures during consolidation, applied using an inert gas, promotes densification, eliminating internal porosity. The potential benefits of HIPing are increasingly being recognised for the processing of radioactive wastes to produce passively safe wasteforms. The UK's Nuclear Decommissioning Authority (NDA) has identified HIP as a potential method for treating Pu-residues at the Sellafield site [18,177]. The UK's policy for dealing with the large PuO_2 stockpile at Sellafield is to fabricate MOx fuel, however, a recent analysis has highlighted the need to adopt a dual track approach to plutonium management with parallel development of a stockpile disposition pathway [11]. Aside from the potentially reusable plutonium stockpile, approximately 0.5 tonnes of material is not economically viable for reuse and has

been identified as waste [26]. These Pu-residues are classified as higher activity waste due to the Pu content exceeding that of plutonium contaminated material wastes.

Zirconolite glass-ceramics are an attractive matrix for the immobilisation of low purity plutonium residues, which may also contain glass forming contaminants. In these materials, plutonium and other actinides are targeted for incorporation within the ceramic phase zirconolite, prototypically $CaZrTi_2O_7$, by substitution of the Ca and / or Zr sites. This phase has been demonstrated to exhibit the exceptional stability toward aqueous dissolution and radiation damage required for geological disposal [17]. The glass phase provides the wasteform with the flexibility to accommodate the impurities associated with the plutonium feedstock [17]. In addition, the presence of a liquid glass phase during high temperature processing assists in the densification of the wasteform product.

Hot isostatic pressing is a highly flexible process with a large operating window, allowing effective processing of different waste-streams and different immobilisation matrices without the challenges associated with vitrification. The utilisation of a batch process enables robust plutonium accountancy, an important aspect for criticality and safeguards concerns. Actinide loadings in zirconolite based glass-ceramics exceed those observed in vitrified wasteforms, enabling higher actinide loadings and a reduced number of wasteforms for processing [65,212,213]. Coupling this with the significant volume reductions per waste package during the HIP process (up to 60 % volume reduction), there are potentially significant cost savings associated with the lifetime waste management costs.

Successful processing of radioactive wastes by HIPing typically requires the waste and glass / ceramic forming precursors to be dried and mixed before being packed into a stainless steel canister. The canister is evacuated at room temperature via an evacuation tube in the lid. Elevated temperatures may also be applied during this evacuation, in a process commonly referred to as a “bake-out” step [168]. A bake-out step is utilised to remove water and other volatiles from inside the canister, which could inhibit densification and create porosity in the final wasteform. The selection of glass / ceramic forming precursors is important to minimise the addition of potential volatiles in the HIP canister, hence metal carbonates and hygroscopic reagents are typically avoided (as in this study). When an acceptable vacuum is achieved, typically < 25 Pa, the evacuation tube is crimped and sealed by welding. This paper highlights the importance of optimising the in-canister evacuation and bake-out process to

achieve high quality, dense glass-ceramic products. The time taken to evacuate each canister could severely limit the operational throughput of a waste treatment plant operating HIP technology, hence it is important to optimise the process at a laboratory scale before scaling up to full size HIP canisters.

With the aim to improve sample throughput whilst maintaining sample quality and reproducibility, we investigated the use of a waste / precursor *ex-situ* calcination step as an alternative or supplement to the in-canister bake-out on laboratory scale 30 ml canisters. The final wasteform microstructures and phase assemblages are discussed with respect to the pre-treatment parameters, as well as the final densities and time taken for each canister evacuation.

4.2 Experimental

Our target glass-ceramic phase assemblages for UK plutonium disposition are zirconolite ($CaZrTi_2O_7$) distributed within a sodium aluminoborosilicate glass matrix. The materials fabricated in this study were formulated prior to optimisation of the glass-ceramic formulation and comprise zircon ($ZrSiO_4$) as the dominant crystalline phase, accompanied with other minor crystalline phases as described below. Although these materials do not comprise the optimised phase assemblage, they are considered to be a valid and useful test bed to understand the impact of pre-treatment parameters on the behaviour of the glass / ceramic precursors. The effectiveness of the *ex-situ* calcination and / or in-canister bake-out step on the quality of the wasteform product was judged on the basis of the wasteform phase assemblage, microstructure and entrained porosity. Table 4.1 lists the oxide precursors used to fabricate the glass-ceramic wasteforms in this study. The high glass fraction and high B_2O_3 content result in the stabilisation of zircon as the major crystalline phase as noted above and described in the previous study [214].

Powder samples were batched to a 70 : 30 wt. % ratio of glass to ceramic with the target glass phase, $Na_2Al_{0.5}B_{1.5}Si_6O_{16}$. The batches were mixed in a planetary mill at 500 rpm for 5 min with isopropanol as a milling agent. The dried batches were packed and sealed into stainless steel HIP canisters (approximately 36 x 38 mm (h x d)).

All samples were heat treated to remove volatiles. Samples underwent an *ex-situ* calcination prior to canister packing, an in-canister bake-out, or a combination of the two. The pre-treatments for each sample are given in Table 4.2. For the calcinations, the batched and milled powders were heated for 16 h in an alumina crucible in a muffle furnace, the in-canister bake-outs were performed on the filled HIP canisters whilst under vacuum. The duration of the in-canister bake-out was sample dependant and was determined by the time taken for the vacuum pressure to return to the maximum pressure achieved when evacuated at ambient temperature. When the temperature is increased, the vacuum pressure drops off due to the release of volatiles from inside the canister, thus, when the pressure returns to the maximum that was achieved at ambient temperature, it is assumed all volatiles have been removed.

Table 4.1: Raw reagents used and their corresponding weight percentages for a 70 : 30 wt. % glass : ceramic mix.

	Reagent	Wt. %
Glass formers	SiO_2	45.2
	Na_2SiO_3 – anhydrous	10.6
	Al_2O_3	3.60
	$Na_2B_4O_7$ – anhydrous	10.6
Ceramic formers	$CaTiO_3$	12.0
	TiO_2	11.0
	ZrO_2	7.00

Table 4.2: Sample matrix and individual sample pre-treatments.

Sample	Pre-treatment	
	***Ex-situ* Calcination (°C)**	**In-canister Bake-out (°C)**
A	-	300
B	-	600
C	600	300
D	600	-
E*	600	-

*Sample was fabricated from a glass frit precursor.

Sample E was fabricated using a glass frit precursor to compare against the use of oxide precursors. Sample E was batched with the same glass : ceramic fraction (70 : 30 wt. %) and used a frit of the same target glass composition, $Na_2Al_{0.5}B_{1.5}Si_6O_{16}$, instead of the glass

forming oxide reagents. The glass frit was produced by melting stoichiometric quantities of $Na_2B_4O_7$, Al_2O_3 and SiO_2 at 1500 °C for 5 h before pouring through a stainless steel mesh into cold water to produce a granular frit material. The glass frit was crushed and sieved to < 150 µm before milling with the ceramic forming oxides. This batch was calcined overnight at 600 °C to dry the ceramic forming oxides but did not have an in-canister bake-out prior to the HIP cycle.

All samples were HIPed at 1250 °C for 4 h under 103 MPa (15,000 psi) of pressure using argon gas as the pressure medium. The HIPed canisters were opened using a Buehler Abrasimet™ 250 saw or Buehler IsoMet™ 1000 saw. Samples were polished and carbon coated for analysis using a Hitachi TM3030 analytical scanning electron microscope (SEM) with a 15 kV accelerating voltage and a working distance of 8 mm. Compositional analysis was conducted with a Bruker Quantax Energy Dispersive X-ray spectrometer system (EDX). Samples were ground and sieved for X-ray diffraction (XRD) using a Bruker D2 PHASER diffractometer with Cu Kα radiation (1.5418 Å); data were acquired between $10° \leq 2\theta \leq 70°$, with a step size of 0.02°, using a Lynxeye position sensitive detector. Thermogravimetric analysis (TGA) and mass spectroscopy (MS) were performed on the raw powders using a PerkinElmer STA 8000 TGA / DTA and a Hiden Mass Spectrometer. Samples were heated to 1250 °C at a heating rate of 10 °C/min. The PerkinElmer TGA /DTA was operated under an argon atmosphere whilst the Hiden Mass Spectrometer TGA was operated under a nitrogen atmosphere. Archimedes' water displacement method was used to calculate the bulk density of the glass-ceramic wasteforms and HIP canister densifications. Helium gas pycnometry was used to approximate the theoretical density of the materials produced, each sample was run for 20 cycles under 12.5 psig of helium gas pressure.

4.3 Results

4.3.1 Raw materials

Powder X-ray diffraction (XRD) of the raw batch material before and after the overnight calcination was performed to characterise any significant changes to the raw reagents during either of the *ex-situ* calcination or in-canister bake-out high temperature pre-treatments. The XRD data in Figure 4.1 revealed no major changes in the phases present and hence no

evidence for gross decomposition of, or reaction between, the reagents up to 600 °C. However, minor changes were apparent with the appearance of a reflection attributed to cristobalite (SiO_2) at $2\theta = 23.73$ ° (PDF card 04-008-7818) and the reduction of a minor sodium silicate (Na_2SiO_3) reflection at $2\theta = 29.36$ ° (PDF card 00-016-0818).

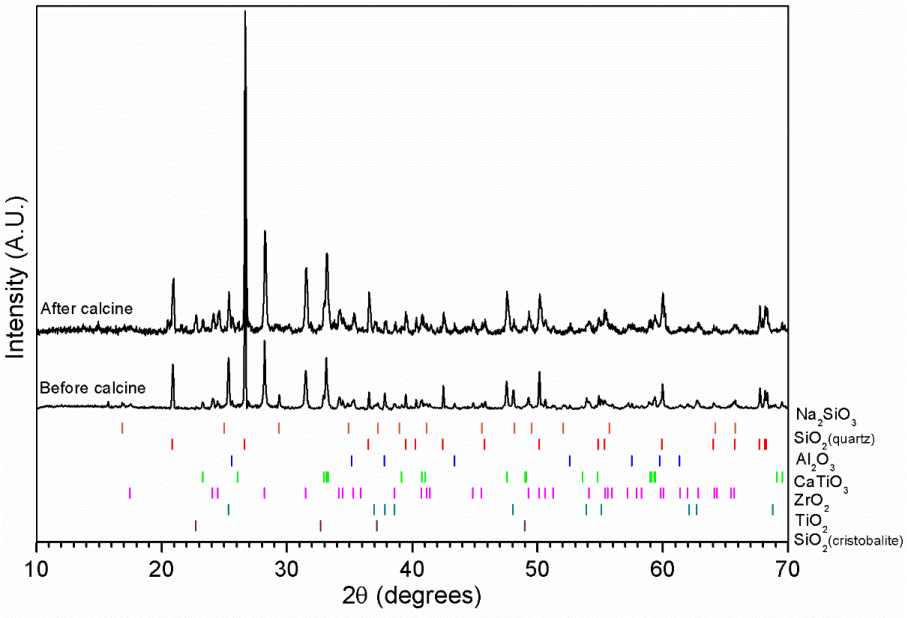

Figure 4.1: XRD data for the raw batch constituents before and after *et-situ* calcination at 600 °C for 16 h in air. The relative intensity of reflections associated with Na_2SiO_3 are reduced post-calcination and a new reflection at $2\theta = 23.73$ ° relative to cristobalite was seen after calcination.

Thermogravimetric analysis (TGA) (Figure 4.2a) revealed a mass loss of 0.8 wt. % from the milled precursor material between 250 °C and 700 °C (i.e. not subject to either *ex-situ* calcination or in-canister bake-out). This mass loss was not evident after *ex-situ* calcination of the precursor material at 600 °C for 16 h. Given the consistency of the XRD data in Figure 4.1, the observed mass loss was not the result of a reaction or decomposition of reagents, and was inferred to be associated with adsorbed volatiles. Borax ($Na_2B_4O_7$) is commonly found as a decahydrate compound. Although it was batched in an anhydrous form in this study, it has the capacity to rehydrate. The borax decahydrate compound is reported to lose eight moles of bound water up to 142 °C, with the remaining two moles retained up to 600 °C [215]. The dehydration behaviour of the milled batch material appeared consistent with that expected for the borax constituent. Further investigation of the borax reagent by TGA coupled with mass spectroscopy (MS) demonstrated the liberation of water (between

ca. 60 – 800 °C) and carbon dioxide (between ca. 200 – 700 °C) corresponding to the mass loss observed in TGA analysis of the milled batch material, as shown in Figure 4.2b. Consequently, we attribute the evolved gas from the milled batch material as being primarily associated with hydration and carbonation of the borax reagent, although we cannot rule out minor contributions from other reagents.

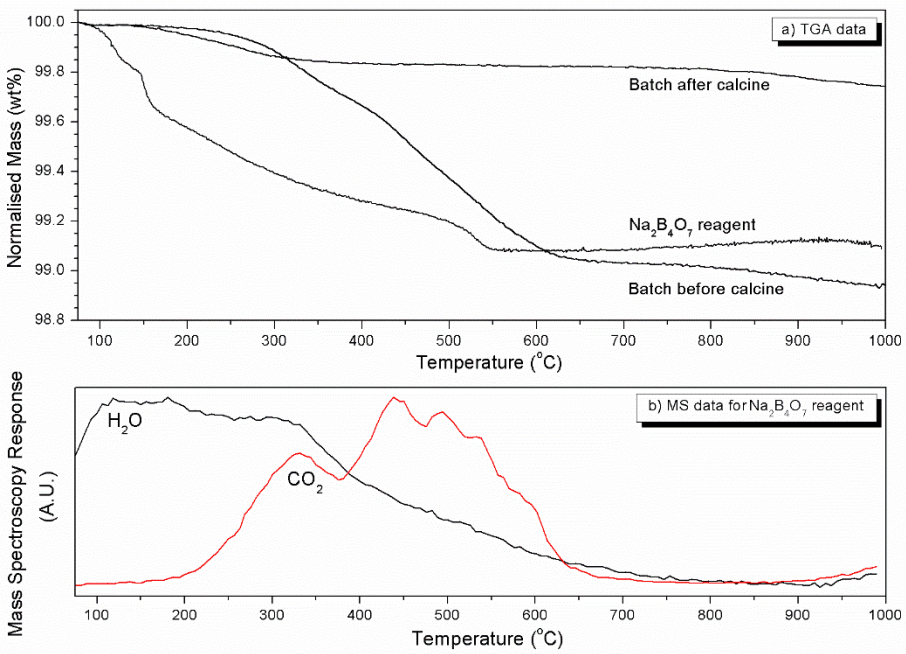

Figure 4.2: a) TGA analysis of the borax $Na_2B_4O_7$ reagent and the raw batch constituents before and after *ex-situ* calcination at 600 °C showing a mass loss of 0.8 wt. % between 250 °C and 700 °C, which is not apparent after *ex-situ* calcination. b) Mass Spectroscopy response for the borax reagent showing the evolution of H_2O and CO_2 over the mass range corresponding to the mass loss observed up to 700 °C in TGA data.

4.3.2 HIPed material

Backscattered electron (BSE) micrographs revealed similar microstructures for samples A – D. No porosity was evident in high magnification BSE images of samples B – D (Figure 4.3), whereas sample A had visible entrained porosity throughout. The entrained porosity within Sample A was a result of the low temperature 300 °C in-canister bake-out, which was insufficient to fully remove the adsorbed water and CO_2 inventory from the borax reagent, as shown by the TGA-MS data in Figure 4.2. The glass-ceramic microstructures are otherwise consistent across all samples independent of the specific pre-treatment, as described below.

Further characterisation of the HIPed materials by SEM-EDX, Figure 4.4, combined with XRD data, Figure 4.5, established the major crystalline phase as zircon ($ZrSiO_4$), with minor rutile (TiO_2), and trace accessory phases of sphene ($CaTiSiO_5$), jadeite ($NaAlSi_2O_6$), quartz (SiO_2) and brookite (TiO_2) (PDF cards: 01-071-0991, 01-078-4188, 01-085-0395, 04-015-8184, 01-086-1630 and 00-015-0875, respectively). These ceramic phases were observed to be homogeneously distributed in the sodium aluminoborosilicate glass matrix. The phase assemblage was consistent with the previously investigated phase diagram, defined by glass : ceramic and Al_2O_3 : B_2O_3 ratio, as described above and elsewhere [214]. Sodium has been reported to have a stabilising effect on brookite [216], which may explain the presence of this TiO_2 polymorph as a trace phase, crystallised from the glass matrix.

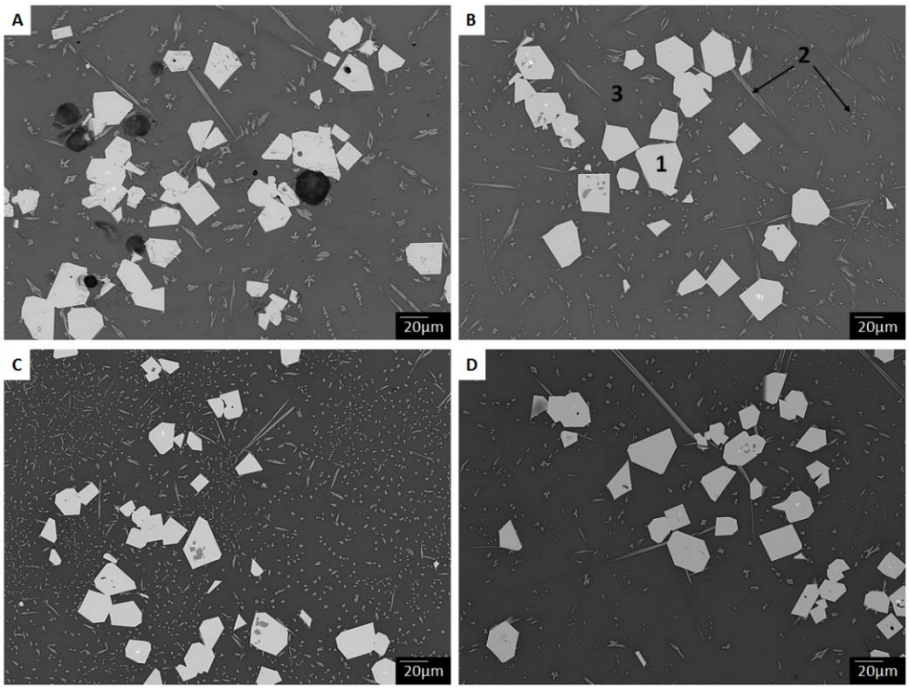

Figure 4.3: BSE micrographs of samples A – D showing similar microstructures and phase assemblage independent of the pre-treatment applied, except for the presence of significant porosity in sample A. Major phases identified; 1) Zircon – $ZrSiO_4$, 2) Rutile – TiO_2 and 3) Amorphous glass phase.

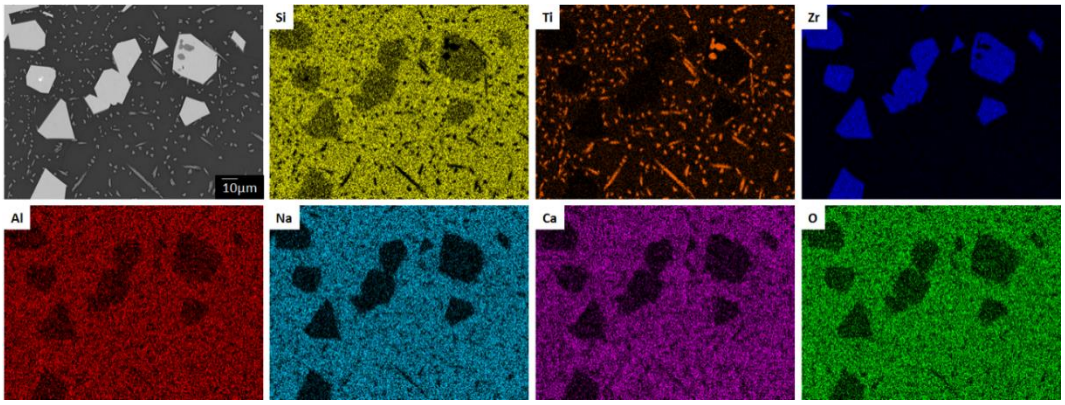

Figure 4.4: EDX map for sample C (600 °C *ex-situ* calcination plus 300 °C in-canister bake-out) showing the distribution of elements between the major crystalline phases and glass matrix.

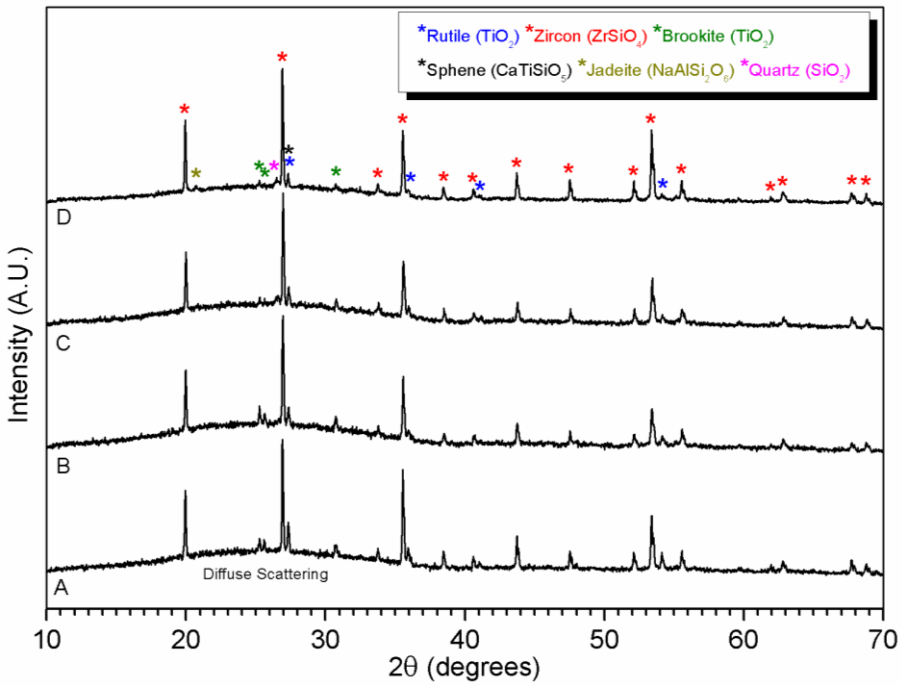

Figure 4.5: XRD data for samples A – D (A: in-canister bake-out at 300 °C, B: in-canister bake-out at 600 °C, C: *ex-situ* calcination at 600 °C plus in-canister bake-out at 300 °C, D: *ex-situ* calcination at 600 °C). The phase assemblage is the same across all samples with only a small change in relative intensity of reflections associated with minor and trace phases.

The density of the materials and compaction of canisters were determined using a combination of water displacement measurements and helium gas pycnometry. The low

density of sample A in Table 4.3 corresponds to the entrained porosity and incomplete densification. Samples B – D have high relative densities, > 98 % theoretical. Table 4.3 shows that the overnight calcination reduces the packing density of the batch in the HIP canister due to inconsistent agglomeration of the powder. This could be ameliorated by grinding the powder after the calcination; however, this would exacerbate the rehydration process by increasing the powder surface area. As a result, the powder was packed into the canisters immediately after the calcination to minimise the time from the furnace to canister evacuation, thus minimising the time available for the uptake of water (this period was kept to 60 ± 15 mins when preparing each sample).

Table 4.3: Summary table of material and canister densifications for samples A – D. The pycnometry data was collected on powder samples of the HIPed product whilst the monolithic density was measured by water displacement. The material densification was calculated as a percentage of the monolithic data over the pycnometry data. The overall canister densification was calculated from water displacement data before and after HIP.

Sample	**Total time for canister evacuation (mins)** (±2.5)	**Powder packing density (g/cm^3)** (±0.04)	**Pycnometry density after HIP (g/cm^3)**	**Monolith density after HIP (g/cm^3)**	**Material densification (%)** (±2%)	**Canister internal volume densification (%)** (±2%)	**Overall canister densification (%)** (±2%)
A (300°C in-canister bake-out)	960	1.66	2.791 (± 0.002)	2.718 (± 0.003)	97	31	22
B (600°C in-canister bake-out)	480	1.57	2.744 (± 0.004)	2.776 (± 0.006)	101	41	29
C (600°C *ex-situ* calcination + 300°C in-canister bake-out)	150	1.37	2.779 (± 0.003)	2.758 (± 0.002)	99	47	34
D (600°C *ex-situ* calcination)	45	1.38	2.829 (± 0.002)	2.780 (± 0.002)	98	44	32
E (600°C *ex-situ* calcination)	<190*	1.62	2.843 (± 0.001)	2.788 (± 0.002)	99	40	28

*The evacuation was interrupted, meaning the evacuation time could not be determined with precision.

4.3.3 Use of a glass frit precursor

Sample E was fabricated from a glass frit precursor of the same stoichiometric composition as the target glass phase in samples A – D ($Na_2Al_{0.5}B_{1.5}Si_6O_{16}$). The frit was batched with the ceramic forming reagents and milled under the same conditions as samples A – D. Due to the high content of refractory components SiO_2 and Al_2O_3 in the glass batch, the glass melt was highly viscous when poured at 1500 °C to form a frit. The glass was confirmed to be fully amorphous by XRD (data not shown). As for samples A – D, the HIPed wasteform fabricated from a glass frit comprised zircon ($ZrSiO_4$) as the major crystalline phase. The XRD plot in Figure 4.6 compares XRD data for sample E against sample D that had the same pre-treatment (*ex-situ* calcination). Figure 4.6 shows excellent agreement between the two samples, with only minor variations in the minor phases present. Zircon was accompanied with minor phases rutile (TiO_2) and sphene ($CaTiSiO_5$), and trace phases quartz (SiO_2), jadeite ($NaAlSi_2O_6$), baddeleyite (ZrO_2) and aluminium titanate (Al_2TiO_5) (PDF cards: 01-071-0991, 01-078-4188, 00-025-0177, 01-086-1630, 00-022-1338, 00-013-0307, 04-011-9497, respectively). As expected, zircon was present as large angular crystals and the minor phases were distributed in the glass matrix, shown in Figure 4.7. Bright spots present at the centre of the zircon crystals were Zr rich and correspond with baddeleyite (ZrO_2) reflections present in the XRD data. The overall crystallite size was significantly smaller than those in the oxide samples, implying a reduced rate of crystal growth.

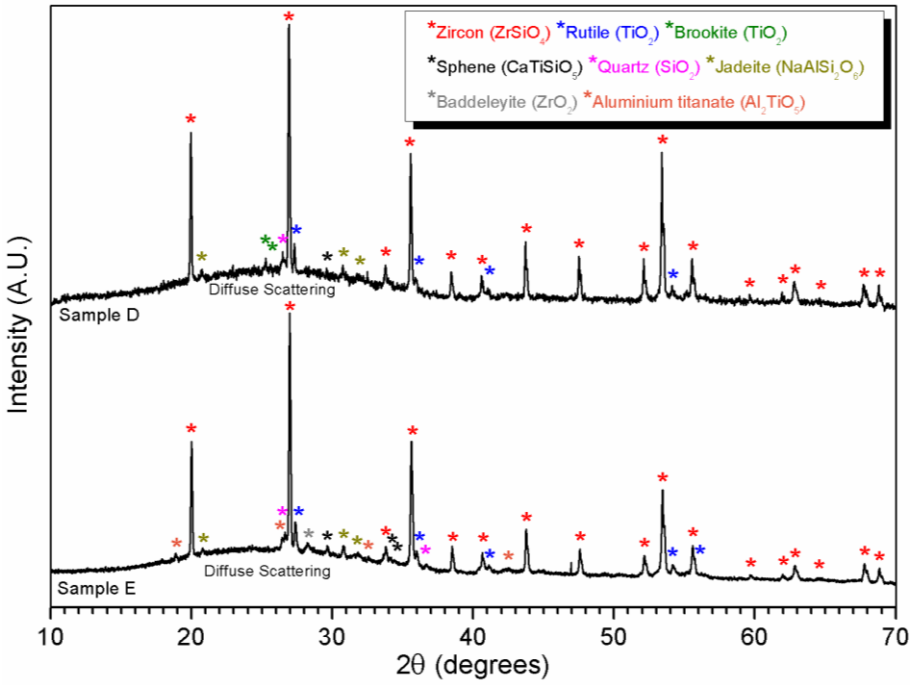

Figure 4.6: Sample E XRD data compared against Sample D, which had the same pre-treatment (600 °C *ex-situ* calcination) showing similar crystalline phase assemblages.

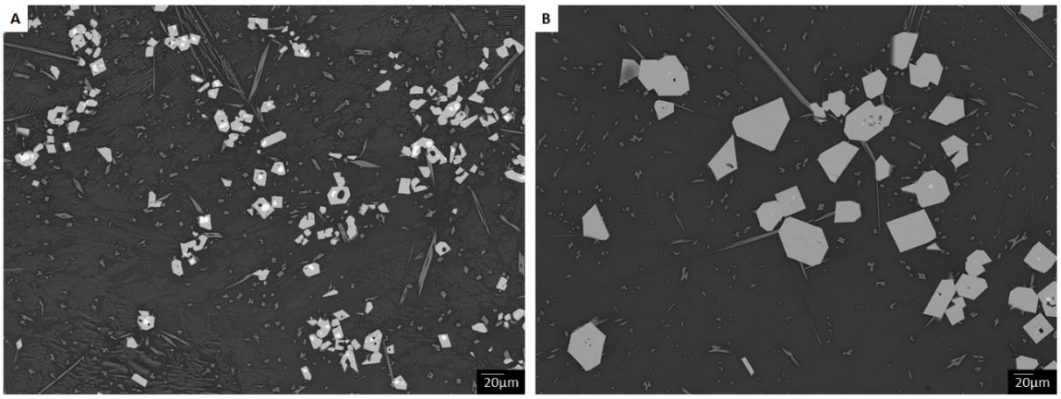

Figure 4.7: SEM images comparing microstructure and crystal size for A) sample E – glass frit precursor and B) sample D – oxide precursors (both with 600 °C *ex-situ* calcination).

4.4 Discussion

It has been shown, at laboratory scale, that high temperature pre-treatment of the reagent batch, prior to the HIP cycle, is necessary for achieving high quality wasteform materials when using oxide precursors. The in-canister 300 °C bake-out was insufficient to remove the adsorbed water and CO_2 associated with the borax reagent as identified by the TGA-MS data.

This resulted in the evolution of trapped volatiles during the HIP cycle, creating a porous wasteform product. The liberation of volatiles, as a gas, pressurises residual porosity and provides an opposing force to sintering, thus inhibiting densification. In extreme cases the internal gas pressure may increase beyond that of the external isostatic pressure and overcome the deformation resistance of the canning material, resulting in porosity and canister expansion [217]. The level of volatiles present in the non-heat treated powders was not enough to cause expansion of the canister, but did increase the amount of porosity present in the final wasteform. These consequences are undesirable; full densification of the wasteform was not achieved, the entrained porosity provides a pathway for water ingress and potentially increases the risk of radionuclide release during geological disposal, and irregular canister deformation puts additional stress on the welds, which could result in canister failure during processing. The *ex-situ* and in-canister high temperature (600 °C) pre-treatments both successfully removed the entrained volatile constituents, producing high quality, dense HIPed wasteforms. The final densities and densification factors for each canister are listed in Table 4.3, which highlights the lower density of sample A due to the entrained porosity.

The *ex-situ* and in-canister pre-treatments did not result in any significant reactions between precursors except for the loss of adsorbed water and CO_2. The final wasteform microstructure and phase assemblage were not significantly disrupted by the pre-treatment process, appearing consistent across all four samples. Zircon formed as the major phase in 10 – 30 µm crystallites distributed homogeneously throughout the glass matrix, with minor phase rutile (TiO_2) and additional trace phases; sphene ($CaTiSiO_5$), jadeite ($NaAlSi_2O_6$), quartz (SiO_2) and brookite (TiO_2). The Zr-rich spots present in sample E could imply the ZrO_2 particles act as nucleation sites for zircon formation. It is thought that the minor and trace phases present in the HIPed wasteforms recrystallized from the glass during the slow cooling step of the HIP cycle, but the zircon crystals formed at the processing temperature. This would explain the larger size of the zircon crystals, which had more time for crystal growth relative to the other crystalline phases. Further work is underway to identify the mechanisms controlling crystalline phase formation.

Small variations were observed in the fractions of trace phases, but this was within the normal variation expected between identical laboratory scale HIP samples, based on repeat

experiments. This is encouraging with respect to optimising sample quality and reproducibility, as well as sample throughput. The *ex-situ* calcination afforded an equivalent product to the in-canister bake-out without detrimental effects to the microstructure, phase assemblage or densification. The option of utilising this *ex-situ* process to improve sample throughput may now be considered.

The high temperature (600 °C) in-canister bake-out effectively evacuated the canister and removed volatiles to produce a dense wasteform. However, it required several hours to reach optimum vacuum pressure, even when using laboratory scale sample volumes (30 ml). Sample B (600 °C in-canister bake-out) took 8 h for complete evacuation before sealing. This could severely limit the throughput of waste packages on a full scale HIP plant or necessitate the use of multiple bake-out stations operating in parallel. The *ex-situ* calcination has been shown to produce a material of comparable quality and provided the most rapid canister evacuation - Sample D (600 °C *ex-situ* calcination only) was prepared after only 45 min evacuation.

There may also be an accompanying effect of increased gas permeability through the sample due to the lower packing density of the powders caused by agglomeration during the *ex-situ* calcination because of the high glass fraction. A lower packing density typically increases gas permeability [218], which, along with the prior removal of volatiles, also results in a faster canister evacuation rate. The packing density of the batched powders is considered an important factor in the densification of the materials. Close packed particles aid the sintering process by improving heat transfer through the material, accelerating grain boundary growth and removing interconnected porosity [219,220]. Evacuation of the canister reduces the effective internal pore pressure during sintering that acts against densification by pushing grain boundaries apart. This reduction in pore pressure maximises the effect of the external isostatic pressure on the densification. Consequently, a high packing density is desirable when fabricating powder wasteforms, but because of the reduced gas permeability associated with a high packing density, optimisation of the evacuation and bake-out stages is important to maximise sample throughput and efficiency of the HIP plant line. It is also relevant to note that the powders were packed manually with an applied uniaxial pressure in the laboratory, however, this process will be different on an industrial scale HIP plant where vibratory packing will likely be utilised.

From the final canister densifications and material densities it can be concluded that the reduced packing density did not inhibit the compaction of the canister or final wasteform quality. Although the single *ex-situ* calcination at 600 °C provided the shortest evacuation time, it cannot be assumed prompt HIPing of the calcined batch will always be possible. Consequently, it was considered to couple the 600 °C *ex-situ* calcination with the 300 °C in-canister bake-out (sample C), as a suitable compromise between assuring sample quality and reproducibility, and enhancing wasteform throughput (2.5 h evacuation). This two-step procedure afforded a wasteform with no entrained porosity, uniform densification and a predictable phase assemblage and microstructure.

The HIP sample fabricated from a glass frit afforded a comparable microstructure and phase assemblage to the samples fabricated from oxide precursors, with zircon as the major crystalline phase. It was observed that the zircon crystallites were significantly smaller in size within the sample fabricated from a glass frit, compared to the crystallites within the samples fabricated from oxide precursors. One possible explanation for this observation is that crystal growth is limited when a glass frit is utilised due to slower diffusion rates before reaching full melt conditions. Slower diffusion rates may have inhibited the growth of the crystals, and may also explain the presence of ZrO_2 at the centre of the zircon crystals as a result of incomplete diffusion. However, further investigation is required to resolve this hypothesis.

Using a glass frit precursor is a potentially preferable method for batching the glass-ceramic wasteforms, to mitigate hydration and carbonation issues with the oxide precursor materials. The frit was formed by quenching the melt from 1500 °C. The melt was viscous but fully amorphous. Changes to the glass-ceramic formulation to attain the desired zirconolite based phase assemblage, could make the glass difficult to produce. A highly refractory glass would require high temperatures and high energy consumption to produce a homogeneous melt, and may also result in a glass too viscous to pour from the melter system. This could present problems or introduce limitations that can be avoided by using oxide precursors, which have been shown to achieve high quality glass-ceramic wasteforms when utilising high temperature pre-treatments. Further development will continue to use oxide precursors and implement the two step pre-treatment during sample preparation, comprising an *ex-situ* calcination at 600 °C followed by an in-canister bake-out at 300 °C.

4.5 Conclusions

Hot isostatic pressing is a proposed method to consolidate glass-ceramic wasteforms for immobilisation of plutonium residues. The preparation of HIP canisters was investigated to increase sample throughput and the efficiency of the HIP process. The limiting step was the bake-out during evacuation of the canisters, which is essential for producing high quality wasteforms. A high temperature in-canister bake-out achieved excellent material densification by removing all volatiles, including adsorbed water and carbon dioxide from the problematic anhydrous borax reagent. The overnight high temperature *ex-situ* calcination also produced a high quality material and reduced the required bake-out time by two thirds. As a compromise between sample throughput, quality and reproducibility, it was resolved to use the two step pre-treatment comprising a high temperature *ex-situ* calcination followed by a low temperature in-canister bake-out for future laboratory scale research. Using a glass frit is potentially a more straight forward way of adding the glass formers and achieved similar products to using oxide precursors, however the utility of this approach depends on the composition and refractory nature of the glass.

5 Formulation optimisation

Crystalline phase assemblage as a function of glass composition in zirconolite glass-ceramics for plutonium disposition.

Stephanie M. Thornber[a], Paul G. Heath[a], Shikuan Sun[a], Prashant Rajbhandari[a], Grégory Tricot[b], Chris Hayward[c], Martin C. Stennett[a] , Russell J. Hand[a] & Neil C. Hyatt[a,*]

[a]*Immobilisation Science Laboratory, Department of Materials Science & Engineering, The University of Sheffield, Sir Robert Hadfield Building, Mappin Street, Sheffield S1 3JD, UK*

[b]*LASIR UMR-CNRS 8516, Université de Lille, Sciences et Technologies, Villeneuve d'Ascq F-59655, France*

[c]*EPMA Facility, School of Geosciences, University of Edinburgh, The King's Buildings, James Hutton Road, Edinburgh, EH9 3FE, UK*

Author contributions: Stephanie M. Thornber designed and developed the experimental matrix, fabricated, characterised and analysed all samples and wrote the scientific report. Paul G. Heath helped design the ambient pressure experimental matrix and provided useful communications. Shikuan Sun performed the Reitveld refinements and provided useful communications. Prashant Rajbhandari analysed and contributed the MAS-NMR data to the scientific report. Grégory Tricot conducted the MAS-NMR experiments. Chris Hayward conducted the EPMA analysis. Martin C. Stennett and Russell J. Hand provided useful communications. Neil C. Hyatt provided project oversight and supervision.

5.1 Introduction

The UK stores around 140 tonnes of separated PuO_2 at the Sellafield site. The current UK plan for dealing with the stockpile is to process usable material into MOx fuel while developing a suitable disposition route for the material that is not suitable for reprocessing [8,11]. This material has been classified as higher activity waste and requires a suitable disposal route for disposition. These waste-streams are highly variable and require flexible matrices for immobilisation. Glass-ceramics consolidated by hot isostatic pressing (HIPing) are being developed to immobilise impure streams of Pu-residues in the UK that are likely to contain glass forming impurities [16,18]. As a thermal treatment technique HIP is flexible to different processing conditions and can accommodate different wastes and materials on a single plant line [26]. This allows the wasteform to be tailored around the waste properties,

not the requirements of the processing method. Whilst the ceramic phase provides higher waste loading capacity and better durability properties, the glass component adds flexibility to the wasteform to accommodate the impurities and compositional variations of the waste-streams [23]. Actinides have been shown to partition into the more durable ceramic phase, whilst the glass acts as a secondary barrier hosting the residual waste material and provides enhanced proliferation resistance. Dissolution data shows glass-ceramics have a leach resistance equivalent to full ceramics, as a result of the partitioning of the actinides and the preferential dissolution of the glass phase [17].

The target formulation for the glass-ceramic system is zirconolite (nominally $CaZrTi_2O_7$) distributed in an alkali aluminoborosilicate glass. As one of the major phases in Synroc, zirconolite has been shown to have excellent wasteform properties [221]. Actinides and rare earth elements, including Pu, readily substitute on the Ca and Zr sites due to similar ionic radii. Research has also shown that zirconolite can undergo other elemental substitutions on the Ti sites for charge compensation, with little effect on the structure and overall behaviour of the glass-ceramic [212]. Zirconolite has excellent durability and radiation tolerance properties, reported in the literature for both synthetic and natural analogues [84,88,127]. Natural analogues have shown zirconolite to retain natural U and Th after complete amorphisation, providing promising results for long-term radionuclide retention properties in a geological disposal facility [88,127].

Whilst the target glass-ceramic phase assemblage is zirconolite distributed in a sodium aluminoborosilicate glass matrix, previous work has shown the crystalline phase assemblage changed as the glass composition varied [147]. It is important to understand the mechanisms controlling the phase assemblage and to find an optimum formulation that yields zirconolite as the only / dominant crystalline phase. In this study, we vary the Al_2O_3 : B_2O_3 ratio and glass : ceramic fraction to study the dependence of the crystalline phase assemblage with respect to the glass composition and glass fraction. Alongside the matrix of HIPed samples, a series of ambient pressure samples were fabricated in a muffle furnace to study the mechanisms controlling the formation of the crystalline phases.

5.2 Experimental

5.2.1 Effect of glass fraction / composition

An 18 sample matrix (Table 5.1) was formulated to investigate the effects of glass composition and glass fraction on the crystalline phase assemblage achieved in the glass-ceramics. The target glass composition, denoted as $Na_2Al_{1+x}B_{1-x}Si_6O_{16}$ (where x = 0, 0.2, 0.4, 0.6, 0.8, 1.0), varied the ratio of Al_2O_3 : B_2O_3, and each composition was fabricated for three different glass fractions; 30 wt. %, 50 wt. % and 70 wt. %. The complete matrix is summarised in Table 5.1, where all the starting formulations targeted $CaZrTi_2O_7$ as the ceramic phase, by batching $CaTiO_3$, TiO_2 and ZrO_2 in a 1 : 1 : 1 molar ratio as the remaining wt. % fraction.

Batched powders were milled at 500 rpm for 30 min in a planetary mill with isopropanol as the milling medium. The dried batches were calcined at 600 °C for 16 h in a muffle furnace before being packed into stainless steel HIP canisters. The packed canisters were baked-out at 300 °C before sealing. High density samples were achieved by HIPing at 1250 °C for 4 h with an applied gas pressure of 103 MPa (15000 psi), where argon was utilised as the pressure medium.

Table 5.1: Full sample matrix of different glass fractions and different glass compositions. $CaTiO_3$, TiO_2 and ZrO_2 were batched in a 1 : 1 : 1 molar ratio as the remaining wt. % fraction.

Glass Fraction (wt. %)	Glass Composition: $Na_2Al_{1+x}B_{1-x}Si_6O_{16}$					
	***x* = 0**	***x* = 0.2**	***x* = 0.4**	***x* = 0.6**	***x* = 0.8**	***x* = 1.0**
30	$Na_2AlBSi_6O_{16}$*	$Na_2Al_{1.2}B_{0.8}Si_6O_{16}$	$Na_2Al_{1.4}B_{0.6}Si_6O_{16}$	$Na_2Al_{1.6}B_{0.4}Si_6O_{16}$	$Na_2Al_{1.8}B_{0.2}Si_6O_{16}$	$Na_2Al_2Si_6O_{16}$*
50	$Na_2AlBSi_6O_{16}$	$Na_2Al_{1.2}B_{0.8}Si_6O_{16}$	$Na_2Al_{1.4}B_{0.6}Si_6O_{16}$	$Na_2Al_{1.6}B_{0.4}Si_6O_{16}$	$Na_2Al_{1.8}B_{0.2}Si_6O_{16}$	$Na_2Al_2Si_6O_{16}$*
70	$Na_2AlBSi_6O_{16}$	$Na_2Al_{1.2}B_{0.8}Si_6O_{16}$	$Na_2Al_{1.4}B_{0.6}Si_6O_{16}$	$Na_2Al_{1.6}B_{0.4}Si_6O_{16}$	$Na_2Al_{1.8}B_{0.2}Si_6O_{16}$	$Na_2Al_2Si_6O_{16}$*

The shaded samples were analysed by EPMA and NMR.

* Samples were quantified by Rietveld Refinement.

The processed canisters were opened to retrieve monolithic and powder samples for analysis by scanning electron microscopy (SEM) and X-ray diffraction (XRD). Monolithic samples were polished to 1 µm finish and carbon coated for analysis using a Hitachi TM3030 analytical scanning electron microscope (SEM) with a 15 kV accelerating voltage at a working distance of 8 mm; all images obtained in backscattered electron (BSE) mode. Compositional analysis was conducted with a Bruker Quantax energy dispersive X-ray spectrometer (EDX). Five samples, indicated in Table 5.1, were characterised by electron probe micro-analysis (EPMA) at the EPMA Facility, School of Geosciences, University of Edinburgh. Data were collected using a Cameca SX100 instrument with beam conditions of 10 kV and 5 µm beam diameter. A current of 0.5 nA was used for major elements and a current of 20 nA was used for minor elements. The 0.5 nA current was used to minimise the error associated with Na mobility, whilst an air jet and the low voltage were required for analysis of the B. Data was standardised against multiple standards; Na – Jadeite (Na : 11.34 %, Al : 13.23 %, Si : 27.78 %, Fe : 0.17 %, O : 47.65 %), Si – Wollastonite (Mg : 0.17 %, Al : 0.03 %, Si : 24.00 %, Ca : 34.32 %, Mn : 0.05 %, Fe : 0.28 %, O : 41.37 %), Ti – rutile (Ti : 59.34 %, O : 39.89 %, Mg : 0.01 %, Fe : 0.59 %, Nb : 0.17 %), Zr – zircon (Si : 15.24 %, Mn : 0.03 %, Zr : 49.14 %, Hf : 0.82 %, O : 34.77 %), Al – spinel (Mg : 17.08 %, Al : 37.93 %, O : 44.99%) and for B a sample of international simple glass (ISG) was used; 60.2 SiO_2, 16.0 B_2O_3, 12.6 Na_2O, 3.8 Al_2O_3, 5.7 CaO, 1.7 ZrO_2 (mol. %) [191].

Powder samples were ground for X-ray diffraction (XRD) using a Bruker D2 PHASER diffractometer with Cu Kα radiation (1.5418 Å). Data were acquired between $10° \leq 2\theta \leq 70°$, with a 0.02° step size, using a Lynxeye position sensitive detector. Reitveld refinements were performed using the GSAS software package [196] for quantitative phase analysis of four samples indicated in Table 5.1; 30 wt. % $Na_2AlBSi_6O_{16}$, 30 wt. % $Na_2Al_2Si_6O_{16}$, 50 wt. % $Na_2Al_2Si_6O_{16}$ and 70 wt. % $Na_2Al_2Si_6O_{16}$. Powder XRD samples were prepared with 10 wt. % MgO (calcined at 900 °C) as an internal standard, in order to determine the weight fraction of the glass phase in the glass-ceramics. The XRD data were collected under the same experimental conditions as described above (Bruker D2 PHASER diffractometer, Cu Kα radiation, $10° \leq 2\theta \leq 70°$, with a 0.02° step size).

Nuclear magnetic resonance (NMR) data were collected for five samples indicated in Table 5.1; 30 wt. % glass $Na_2AlBSi_6O_{16}$, 30 wt. % glass $Na_2Al_{1.4}B_{0.6}Si_6O_{16}$ and 30, 50 and 70 wt. %

glass $Na_2Al_2Si_6O_{16}$, to study the effect of the glass fraction and composition on the environment and speciation of ^{27}Al, ^{23}Na and ^{11}B in the glass. The ^{27}Al, ^{23}Na and ^{11}B magic angle spinning nuclear magnetic resonance (MAS-NMR) experiments were performed at 208.6, 211.7 and 256.8 MHz, respectively, on a 18.8 T Bruker AVANCE 850 III spectrometer using 3.2 mm probe heads operating at spinning frequencies of 20 – 22 kHz. The ^{27}Al NMR spectra were recorded with a 0.6 µs pulse length (corresponding to a π/2-pulse determined on a liquid), 4096 scans and a 0.5 s recycle delay. The ^{23}Na NMR analyses were conducted with a 1 µs pulse length (liquid π/10-pulse), 2048 scans and a 0.5 s recycle delay. The ^{11}B MAS-NMR experiments were performed with a 1 µs pulse length (liquid π/12-pulse), 4096 scans and a 0.5 s recycle delay. The ^{27}Al, ^{23}Na and ^{11}B chemical shifts were referred to liquid $Al(NO_3)_3$ (1M) and NaCl (1M) and solid $NaBH_4$ as 0, 0 and –42.06 ppm, respectively. The three recycle delay values used for the NMR experiments were chosen to provide quantitative measurements.

A single phase $CaZrTi_2O_7$ sample was achieved at 70 wt. % ceramic with glass phase; $Na_2Al_2Si_6O_{16}$. This formulation was reproduced using a glass frit precursor of the same target glass composition. From previous work, it was expected the use of a glass frit would attain a similar phase assemblage as the sample fabricated from oxide precursors, with additional minor phases present due to slower reaction kinetics [222,223]. To produce the $Na_2Al_2Si_6O_{16}$ glass, stoichiometric quantities of Na_2SiO_3, Al_2O_3 and SiO_2 were heated at 1750 °C for 5 h. The viscosity of the melt was too high to pour thus, the melt was removed from the alumina crucible after cooling to room temperature. XRD analysis confirmed the glass was fully amorphous. The glass was crushed and sieved to <150 µm before being batched and milled with the ceramic forming oxides. This sample underwent the same pre-treatments and processing conditions as described above to mirror the oxide based samples.

5.2.2 Study of crystalline phase formation mechanisms

To study the mechanisms controlling phase formation, a series of samples were heated in alumina crucibles in a muffle furnace in the laboratory. Three compositions (Table 5.2) were chosen according to the phase assemblage attained when HIPed and to evaluate variations of glass : ceramic and $Al_2O_3 : B_2O_3$ ratios on the phase assemblage. From previous work reported in [223], the high glass fraction formulation (70 wt. % $Na_2Al_{0.5}B_{1.5}Si_6O_{16}$) was

expected to yield zircon ($ZrSiO_4$) as the major crystalline phase. The low glass fraction formulation (30 wt. % $Na_2Al_2Si_6O_{16}$) was expected to yield $CaZrTi_2O_7$ as the major crystalline phase. The intermediate glass formulation (50wt. % $Na_2Al_{1.6}B_{0.4}Si_6O_{16}$) was expected to yield a mixed phase assemblage comprising $CaZrTi_2O_7$, $ZrSiO_4$, $CaTiSiO_5$ and TiO_2, according to the results from the HIPed samples discussed in section *5.3.1*. Powder batches were milled as described above and heated in alumina crucibles in a muffle furnace up to 1250 °C. To assess the development of the phase assemblage during the HIP cycle, three heat treatments were performed. All samples were heated to 1250 °C at 5 °C/min and subject to either a 0 h or 4 h dwell. For each dwell period, samples were removed from the furnace at temperature and quenched in cold water. For the third heat treatment the samples were cooled at 10 °C/min after a 4h dwell. Powder XRD was used to determine the resultant phase assemblage.

Although not a direct comparison to HIP conditions, it was expected these samples would provide useful information towards determining the crystallisation mechanisms in the glass-ceramic systems. The resultant phase assemblages of the slow cooled samples were in excellent agreement with their HIPed equivalents. By using the same non-carbonated / anhydrous reagents as the HIP samples, the loss of volatiles was kept to a minimum despite being open to the atmosphere when heated, but the lack of pressure was evident in the poor densification of the final material.

Table 5.2: Sample matrix for ambient pressure furnace experiments. All samples were heated to 1250 °C at 5 °C/min. Samples were removed from the furnace at temperature and quenched in cold water or cooled at 10 °C/min in the furnace.

Glass fraction	Glass Composition	Dwell period	Quench or Cool
30 wt. %	$Na_2Al_2Si_6O_{16}$	0 h 4 h 4 h	Quench Quench Cool
50 wt. %	$Na_2Al_{1.6}B_{0.4}Si_6O_{16}$	O h 4 h 4 h	Quench Quench Cool
70 wt. %	$Na_2Al_{0.5}B_{1.5}Si_6O_{16}$	O h 4 h 4 h	Quench Quench Cool

5.3 Results

Scanning electron microscopy (SEM) and powder X-ray diffraction (XRD) were used to characterise the microstructure and crystalline phase assemblage of the HIPed samples. From these data sets, a correlation between the crystalline phase assemblage and the glass fraction / composition was determined.

Across the 18 sample matrix, common major crystalline phases were identified as zirconolite ($CaZrTi_2O_7$), zircon ($ZrSiO_4$), rutile (TiO_2) and sphene ($CaTiSiO_5$) (PDF cards: 04-007-6895, 01-080-1807, 01-080-2533, 01-085-0395, respectively). Trace phases were identified in some samples with higher glass fractions including; α-quartz (SiO_2), α-cristobalite (SiO_2), zirconium titanate ($Zr_{0.9}Ti_{0.1}O_2$) and sillimanite (Al_2SiO_5) (PDF cards: 01-083-0539, 04-008-7743, 04-013-6877, 04-007-7378, respectively) in some of the 70 wt. % glass fraction samples; and a sodium-calcium-aluminosilicate compound (PDF card: 01-079-1148) in some of the 50 wt. % glass fraction samples.

5.3.1 Effect of glass fraction / composition

For all glass compositions, the smaller glass fractions resulted in a higher yield of $CaZrTi_2O_7$ (based on the batched quantity), compared to samples with the same glass composition but greater glass fractions. Figure 5.1 and Figure 5.2 compare BSE micrographs and XRD data for samples of glass composition $Na_2AlBSi_6O_{16}$ at each glass fraction. Changing the glass fraction resulted in the formation of the same crystalline phases but had a substantial impact on their relative proportions, such that at 50 wt. % and 70 wt. % glass, $ZrSiO_4$ was stabilised as the major phase and $CaZrTi_2O_7$ was an accessory phase.

As the Al_2O_3 content in the glass phase was increased (from $Na_2AlBSi_6O_{16}$ to $Na_2Al_2Si_6O_{16}$), the formation of $CaZrTi_2O_7$ was favoured and the abundance of accessory phases reduced. Figure 5.3 and Figure 5.4 show the BSE micrographs and XRD data for samples of glass composition $Na_2Al_2Si_6O_{16}$ at each glass fraction. $CaZrTi_2O_7$ was now the major crystalline phase for all glass fractions. Figure 5.5 shows the XRD data for 30 wt. % glass samples with gradually increased levels of Al_2O_3 in the glass phase ($Na_2Al_{1.2}B_{0.8}Si_6O_{16}$, $Na_2Al_{1.4}B_{0.6}Si_6O_{16}$, $Na_2Al_{1.8}B_{0.8}Si_6O_{16}$, $Na_2Al_2Si_6O_{16}$). The relative intensities of (h k l) reflections associated with the accessory phases were reduced systematically with the gradual increase of Al_2O_3. This

resulted in the single phase $CaZrTi_2O_7$ glass-ceramic at 30 wt. % (see Figures 5.3, 5.4 and 5.5). This effect of increased Al_2O_3 was observed across all glass fractions, however, single phase $CaZrTi_2O_7$ was only achieved at 30 wt. % glass.

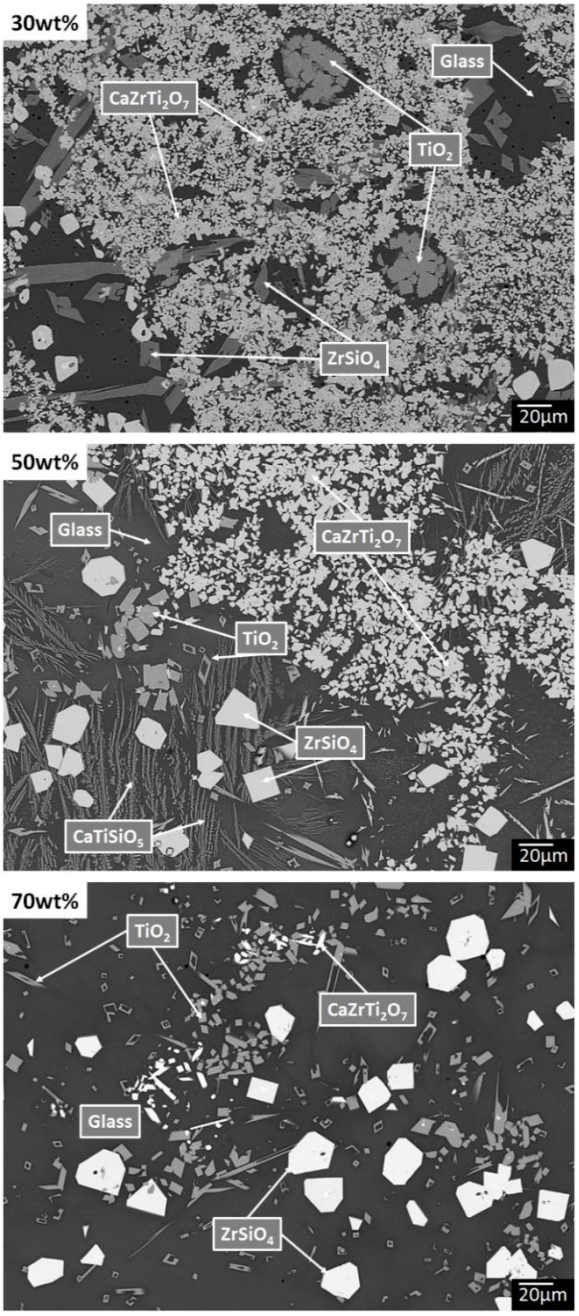

Figure 5.1: BSE micrographs comparing the results of increasing glass fraction on the microstructure for glass composition $Na_2AlBSi_6O_{16}$.

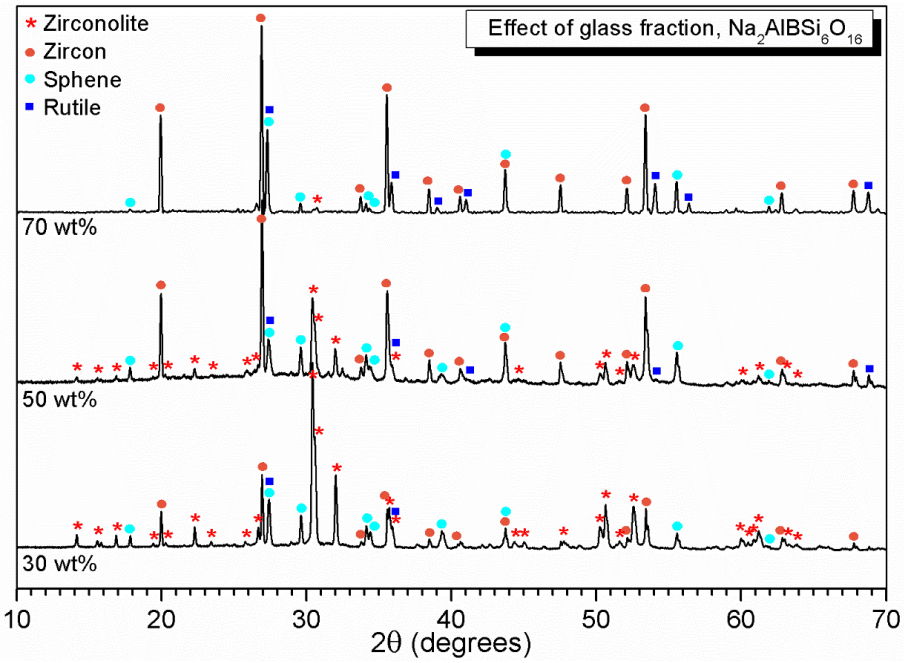

Figure 5.2: Effect of glass fraction: XRD patterns for each glass fraction with the same glass composition $Na_2AlBSi_6O_{16}$.

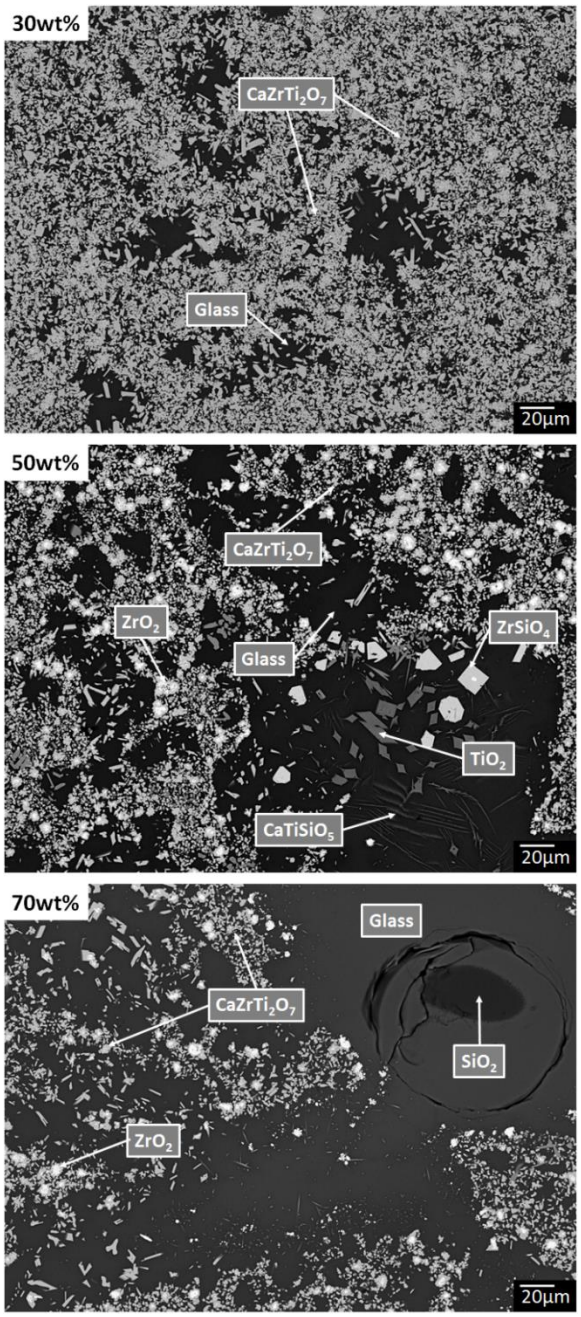

Figure 5.3: BSE micrographs comparing the results of increasing glass fraction on the microstructure for glass composition $Na_2Al_2Si_6O_{16}$.

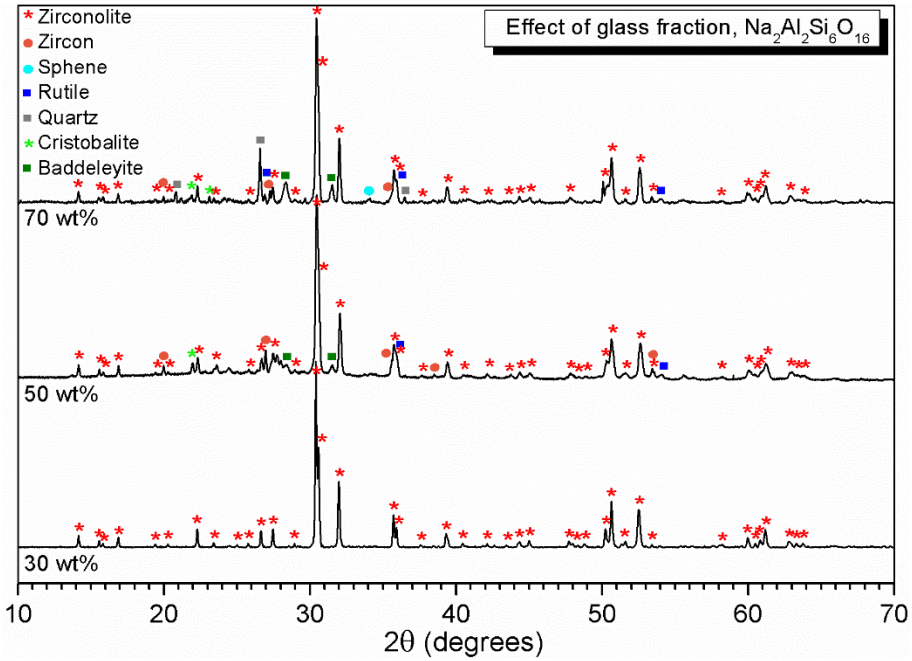

Figure 5.4: Effect of glass fraction: XRD patterns for each glass fraction with the same glass composition $Na_2Al_2Si_6O_{16}$.

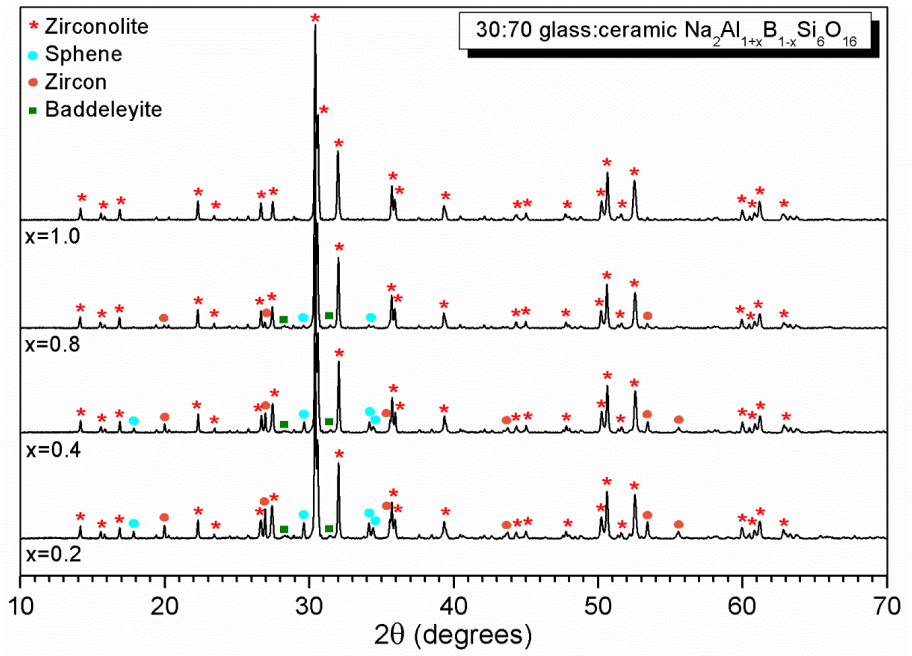

Figure 5.5: Effect of glass composition: XRD patterns for 30 wt. % glass fraction samples with increasing Al content in the glass composition (bottom to top: $Na_2Al_{1.2}B_{0.8}Si_6O_{16}$, $Na_2Al_{1.4}B_{0.6}Si_6O_{16}$, $Na_2Al_{1.8}B_{0.8}Si_6O_{16}$, $Na_2Al_2Si_6O_{16}$).

Rietveld refinements were performed on four samples; 30 wt. % $Na_2AlBSi_6O_{16}$ and $Na_2Al_2Si_6O_{16}$, 50 wt. % $Na_2Al_2Si_6O_{16}$ and 70 wt. % $Na_2Al_2Si_6O_{16}$. Table 5.3 summarises the outcomes of these refinements, which confirmed concomitantly less $CaZrTi_2O_7$ as the glass fraction increased and that all samples had higher proportions of glass than was targeted by formulation. This suggested that some of the $CaZrTi_2O_7$ forming oxides (CaO, TiO_2 and ZrO_2) were incorporated into the glass phase. Across the samples of the same glass formulation, $Na_2Al_2Si_6O_{16}$, the abundance of accessory phases reduced with increased glass fraction, which showed less crystalline material was formed in the high glass samples.

The refinements for the two 30 wt. % samples confirmed the $Na_2Al_2Si_6O_{16}$ formulation yielded a single phase $CaZrTi_2O_7$ glass-ceramic product and that the $Na_2AlBSi_6O_{16}$ sample was composed of 21 % accessory phases; $CaTiSiO_5$, $ZrSiO_4$ and ZrO_2. The ZrO_2 was most likely relic reagent, such that increasing the Al_2O_3 increased the yield of $CaZrTi_2O_7$ at the expense of accessory phases $CaTiSiO_5$, $ZrSiO_4$ and ZrO_2. It is expected that refinement data for 50 wt. % and 70 wt. % samples would yield the same trends as seen for the 30 wt. % samples across the $Na_2Al_{1+x}B_{1-x}Si_6O_{16}$ glass formulation.

Table 5.3: The crystalline phase abundance calculated by Rietveld Refinement of powder XRD data. An internal standard of 10 wt. % MgO was used to refine the glass component of the glass-ceramics.

Glass Fraction	Target glass composition	Phases present	Target wt. %	Refined wt. % (±0.2)	Rwp value (%)	Rp value (%)	Chi2
30 wt. %	$Na_2Al_2Si_6O_{16}$	Zirconolite	70	56.2	4.91	3.85	5.95
		Glass	30	43.8			
30 wt. %	$Na_2AlBSi_6O_{16}$	Zirconolite	70	39.4	5.01	3.83	6.50
		Glass	30	39.2			
		Sphene	0	14.2			
		Zircon	0	6.9			
		Baddeleyite	0	0.2			
50 wt. %	$Na_2Al_2Si_6O_{16}$	Zirconolite	50	29.5	7.93	5.99	16.66
		Glass	50	59.8			
		Zircon	0	1.4			
		Baddeleyite	0	0.7			
		Rutile	0	7.1			
		Cristobalite	0	1.5			
70 wt. %	$Na_2Al_2Si_6O_{16}$	Zirconolite	30	11.3	3.88	2.99	4.41
		Glass	70	83.2			
		Zircon	0	0.2			
		Baddeleyite	0	2.2			
		Quartz	0	2.1			
		Sphene	0	0.5			
		Rutile	0	0.4			

The single phase $CaZrTi_2O_7$ glass-ceramic was replicated using a glass frit precursor. The resultant phase assemblage was in good agreement with the oxide based HIP sample and previous work [223]; $CaZrTi_2O_7$ was yielded as the major crystalline phase with TiO_2 (rutile) and ZrO_2 (baddeleyite) present as accessory phases, shown in Figure 5.6. The presence of the accessory phases was thought to be a consequence of insufficient milling, implied by the large size of the TiO_2 regions, and due to slower reaction mechanisms associated with using the glass frit as opposed to well distributed oxide precursors. The ZrO_2 corresponded with Zr-rich regions at the centre of $CaZrTi_2O_7$ crystals in the SEM-EDX data (Figure 5.7), thought to be a result of slower diffusion rates relative to the use of oxide precursors.

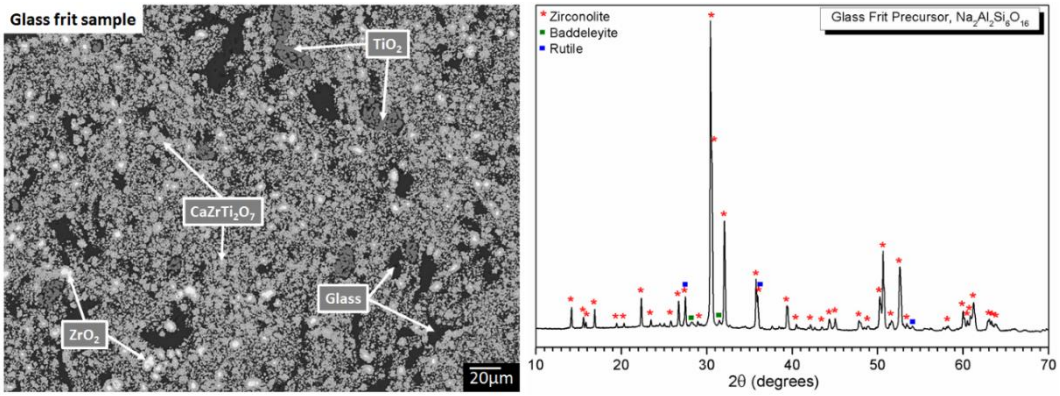

Figure 5.6: Glass frit fabricated HIP sample for 30 wt. % glass fraction and glass composition $Na_2Al_2Si_6O_{16}$. BSE micrograph showing the microstructure and XRD showing the crystalline phase assemblage.

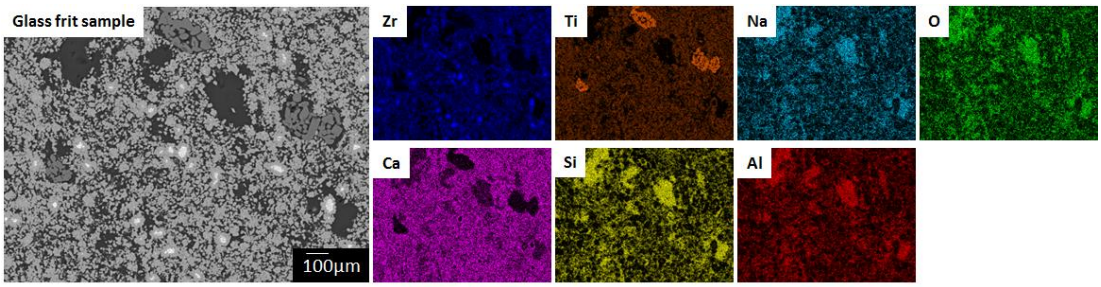

Figure 5.7: SEM-EDX micrographs of a HIP sample fabricated from a glass frit precursor. The microstructure and elemental distribution was in agreement with samples fabricated using oxide precursors.

One-dimensional ^{27}Al, ^{23}Na and ^{11}B MAS-NMR spectra for five HIPed samples are displayed in Figures 5.8, 5.9 and 5.10. The ^{27}Al NMR spectra presented a strong resonance peak centred

at 55 – 60 ppm, indicating that essentially all Al was present as tetrahedral units $^{[4]}$Al. A weak resonance, was just discernible above the background, centred at 10 ppm, which could be associated with a trace component of 5-fold co-ordinated Al species. With decreasing Al_2O_3, in the 30 wt. % samples, the resonance peak of $^{[4]}$Al units exhibited an up-field chemical shift. The chemical shift observed indicated a change in the local environment of the Al species as a result of decreased Al_2O_3, and increased B_2O_3, in the glass. It is known that not all B is charge compensated as $^{[4]}$B units, thus, the chemical shift may be a result of there being more free Na (not associated with Al or B units) to stabilise other species such as Si (e.g. $[SiO_{3/2}O^{-}]$). Alternatively, if the reduced Al_2O_3 (increased B_2O_3) increased Ca solubility in the glass, the chemical shift may be correlated to Ca charge compensated $^{[4]}$Al species. A similar shift was observed when the glass fraction was increased from 30 wt. % to 50 wt. % and 70 wt. %, despite the glass formulation remaining constant. This may be a result of an increased abundance / availability of Si causing a shielding effect in the second co-ordination sphere of some $^{[4]}$Al species, such as Al-O-Si.

The ^{11}B NMR spectra are presented in Figure 5.9. Two resonance peaks centred around 16 ppm and – 1 ppm, which can be assigned to $^{[3]}$B (3-fold co-ordinated) and $^{[4]}$B (4-fold co-ordinated) species, respectively. The relative intensity of the $^{[3]}$B resonance increased at the expense of $^{[4]}$B with increasing Al_2O_3 content. Similar results were observed in the literature such that, an increase in Al_2O_3 and / or decrease in B_2O_3, produced a systematic reduction of $^{[4]}$B units [224]. Although the change in calculated N_4 units was small (Figure 5.9), it confirmed that less $^{[4]}$B units were formed with increased Al_2O_3.

Further insight was obtained from the deconvolution of the ^{11}B NMR spectra. The signals were decomposed using MQMAS and Gaussian / Lorentzian models respectively in DMFit software [225]. The NMR parameters used for the fitting are presented in Table 5.4. Two distinct $^{[3]}$B sites centred around 17 ppm and 15 ppm, and two $^{[4]}$B sites centred around 0 ppm and – 1.5 ppm were identified. The former two sites are assigned to ring and non-ring $^{[3]}$B species, whilst the latter two correspond to $^{[4]}$B connected to 3 x Si and $^{[4]}$B connected to 4 x Si respectively, based on previously reported chemical shifts [226]. It is noteworthy that an increase in Al_2O_3 induced an increase in non-ring $^{[3]}$B particularly at the expense of $^{[4]}$B species.

The ^{23}Na MAS-NMR results are reported in Figures 5.10 and 5.11 and Table 5.5. The NMR

curves obtained for the studied samples exhibit similar evolution, which consisted of a broad isotropic peak centred around –13 to –15 ppm and a sharp peak near –3 ppm. The presence of these peaks suggested the presence of Na fractions in both amorphous (broad isotropic peak) and crystalline (sharp peak) phases within the assemblage. Deconvolution of the ^{23}Na NMR data revealed three Na environments; two broad peaks indicative of amorphous environments and a third peak suggestive of a crystalline environment. The deconvolutions were performed using a Gaussian fit and revealed a broadening of the sharp peak as the glass fraction increased. This may suggest the displacement of crystalline Na ions into an amorphous environment. It is noteworthy that the ^{23}Na NMR data had a negative chemical shift between the 30 wt. % $Na_2Al_2Si_6O_{16}$ sample and the samples with increased B_2O_3 and higher glass fractions, similar to the shift observed in the ^{27}Al NMR data.

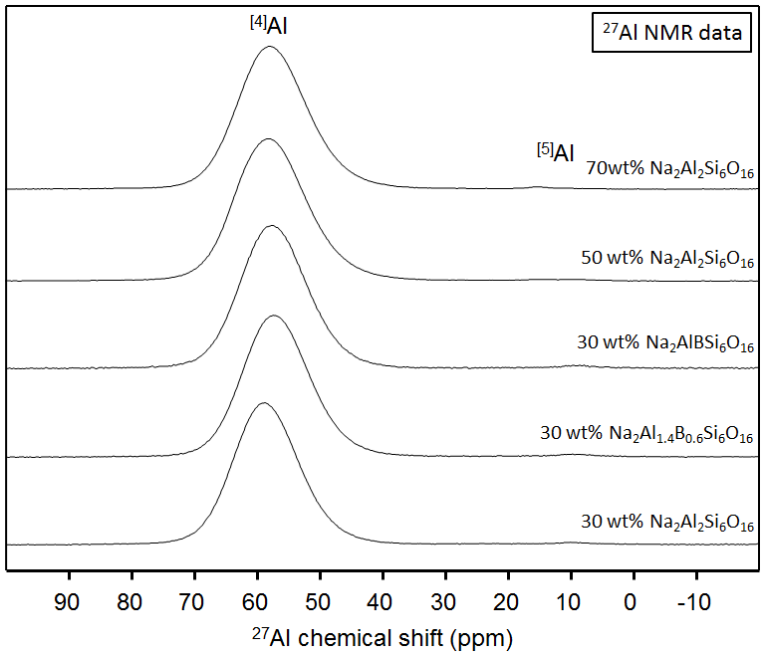

Figure 5.8: ^{27}Al NMR data confirming all Al was present as tetrahedral units. A chemical shift was observed between the 30 wt. % $Na_2Al_2Si_6O_{16}$ sample and those with increased B_2O_3 content and increased glass fraction.

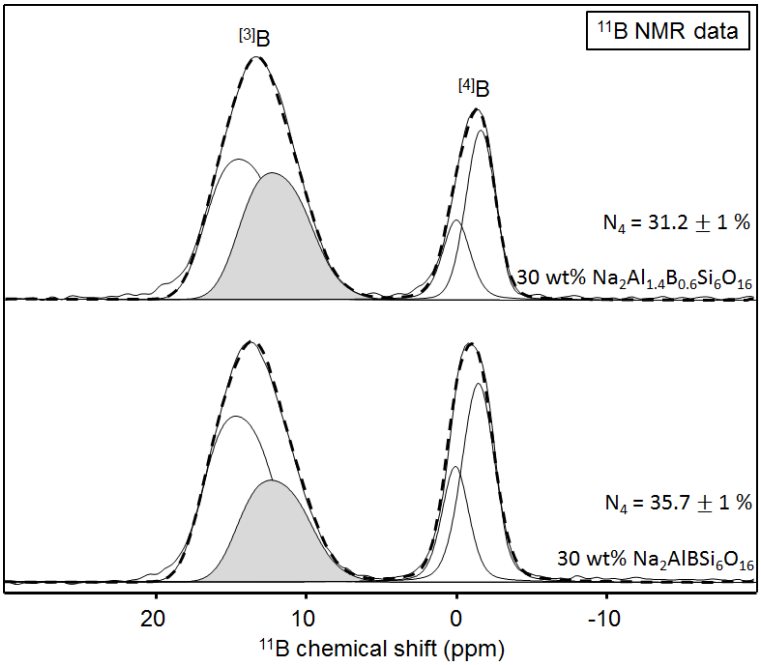

Figure 5.9: ^{11}B NMR data showing reduced $^{[4]}B$ units with increased Al_2O_3 concentration.

Table 5.4: NMR parameters used for spectrum simulation of the studied samples.

Sample		$^{[3]}B_a$	$^{[3]}B_b$		$^{[4]}B_a$	$^{[4]}B_b$
30 wt. % $Na_2AlBSi_6O_{16}$	δ_{CS} / ppm (±0.1)	17.7	15.3	δ_{CS} / ppm (±0.1)	0.1	-1.4
	C_Q / MHz (±0.1)	2.9	2.9	C_Q / MHz (±0.1)	2.1	2.6
	η_Q (±0.1)	0.4	0.3	η_Q (±0.1)	0.7	0.8
	% (±2)	38.2	23.7	% (±2)	12.7	25.4
30 wt. % $Na_2Al_{1.4}B_{0.6}Si_6O_{16}$	δ_{CS} / ppm (±0.1)	17.6	15.3	δ_{CS} / ppm (±0.1)	0.1	-1.5
	C_Q / MHz (±0.1)	2.9	2.9	C_Q / MHz (±0.1)	2.1	2.3
	η_Q (±0.1)	0.4	0.3	η_Q (±0.1)	0.7	0.9
	% (±2)	36.2	33.1	% (±2)	9.9	20.8

C_Q: quadruple coupling constant; δ_{cs}: chemical shift, η_Q: asymmetry constant, %: relative proportion.

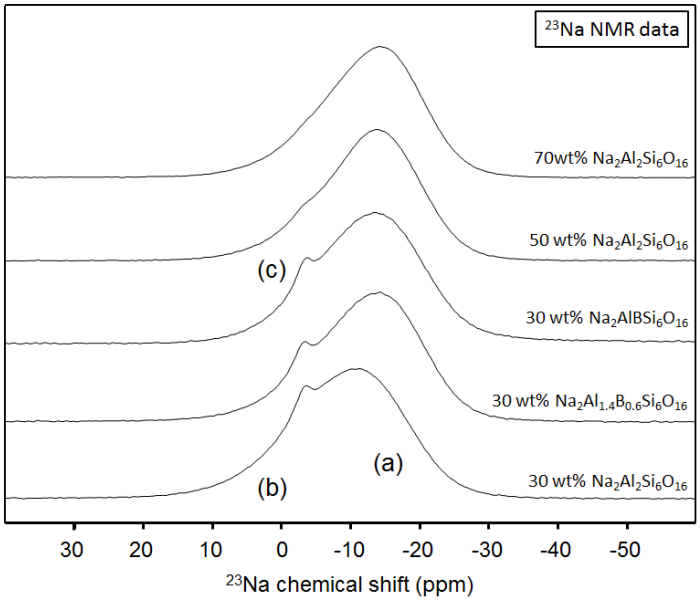

Figure 5.10: ^{23}Na NMR data showing three Na environments including a crystalline peak in the 30 wt. % samples.

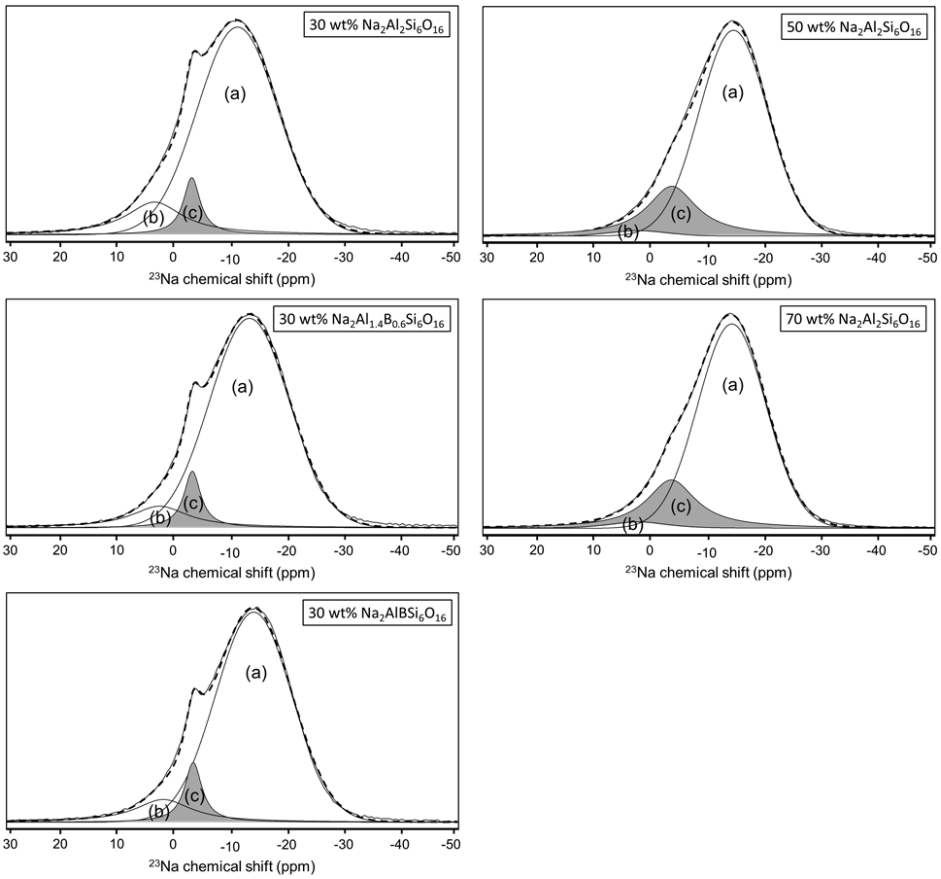

Figure 5.11: ^{23}Na MAS-NMR deconvolutions revealed three Na environments.

Table 5.5: ^{23}Na NMR deconvolutions were performed using a Gaussian fit.

Na environment	30 wt. % $Na_2AlBSi_6O_{16}$		30 wt. % $Na_2Al_{1.4}B_{0.6}Si_6O_{16}$		30 wt. % $Na_2Al_2Si_6O_{16}$		50 wt. % $Na_2Al_2Si_6O_{16}$		70 wt. % $Na_2Al_2Si_6O_{16}$	
	δ_{CS} / ppm (±0.1)	% (±2)	δ_{CS} / ppm (±0.1)	% (±2)	δ_{CS} / ppm (±0.1)	% (±2)	δ_{CS} / ppm (±0.1)	% (±2)	δ_{CS} / ppm (±0.1)	% (±2)
a	-11.0	81	-13.0	85	-13.8	83	-14.4	79	-14.3	79
b	3.7	12	2.8	8	2.2	9	2.5	2	2.5	2
c	-2.9	7	-3.0	7	-3.1	8	-3.5	19	-3.4	19

δ_{cs}: chemical shift, % error.

SEM-EDX was used to evaluate how the final glass composition varied with changes to the target stoichiometry. Figure 5.12 shows the measured EDX compositions for target glass composition $Na_2Al_2Si_6O_{16}$ at each glass fraction. The Ca, Zr and Ti signals measured in the glass remained relatively constant with increased glass fractions, which implied no major changes to the solubilities were experienced. In comparison, Figure 5.13 shows the measured glass compositions for three 30 wt. % glass samples with variable compositions from across the matrix; $Na_2AlBSi_6O_{16}$, $Na_2Al_{1.4}B_{0.6}Si_6O_{16}$ and $Na_2Al_2Si_6O_{16}$. An apparent increase of Zr in 30 wt. % sample $Na_2AlBSi_6O_{16}$, suggested an increase in the Zr solubility within the low Al_2O_3 glass. Interestingly, the same sample had a higher Si signal than the other samples despite containing Si-bearing crystalline phases. The 30 wt. % sample with glass formulation $Na_2Al_2Si_6O_{16}$, did not contain silicate phases thus was expected to have more Si in the glass. It must be noted that due to the error associated with this compositional analysis technique, no robust conclusions could be draw from these data; due to the fine grain size it was not possible to ensure phase overlap did not occur, thus the apparent increase of Zr in sample 30 wt. % $Na_2AlBSi_6O_{16}$ may have been a result of a crystalline phase and not increased solubility in the glass phase; from the EDX spectra the oxygen signal was clearly overestimated, which will have skewed the normalisation of elemental at. % and there does not appear to be a clear trend across the Na, Al and Si signals to confirm robust glass compositions were detected. For a more precise quantitative approach the same five samples, indicated in Table 5.1, were analysed by electron probe micro-analysis (EPMA).

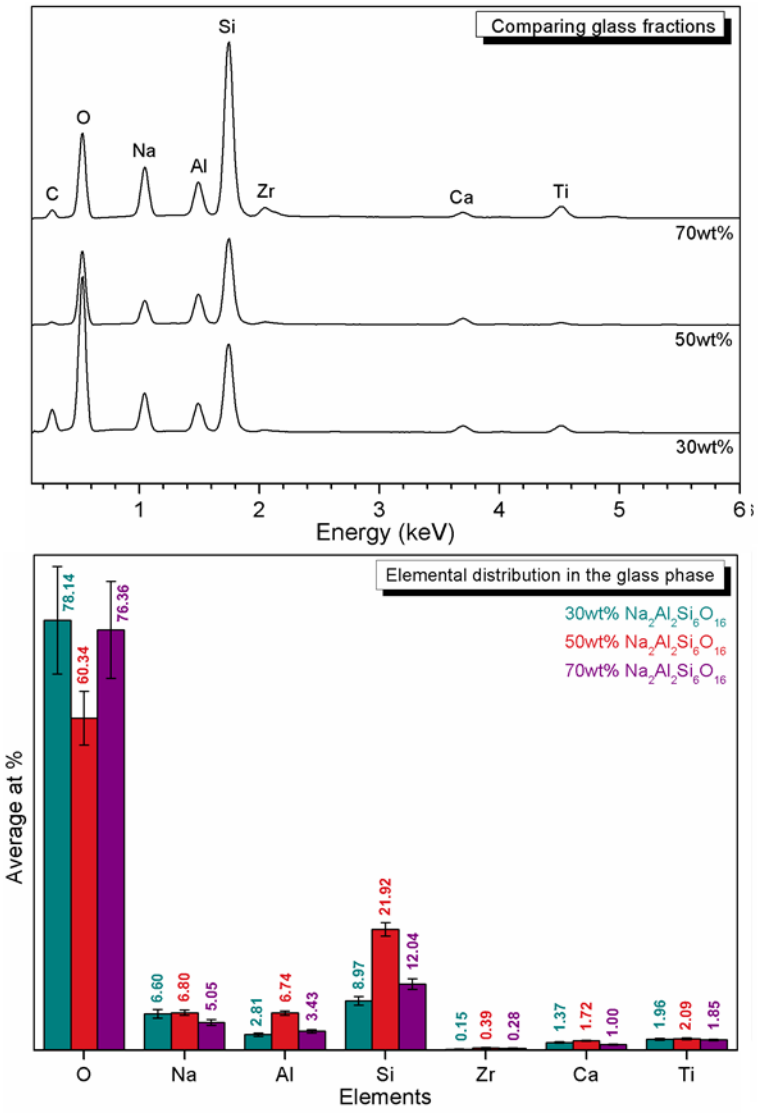

Figure 5.12: SEM-EDX spectra comparing the elemental contributions to the glass phase in samples with increasing glass fraction. Target glass stoichiometry; $Na_2Al_2Si_6O_{16}$.

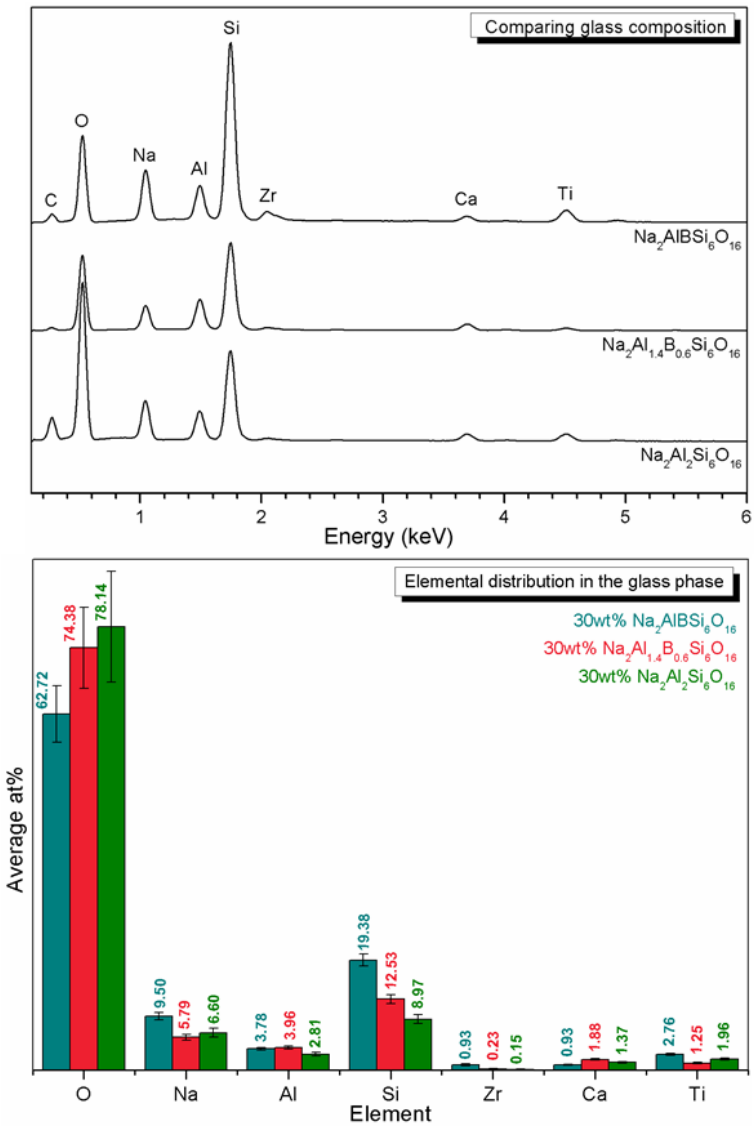

Figure 5.13: SEM-EDX spectra of the glass phase for 30 wt. % glass samples with target glass stoichiometries; $Na_2Al_2Si_6O_{16}$, $Na_2Al_{1.4}B_{0.6}Si_6O_{16}$ and $Na_2AlBSi_6O_{16}$.

The quantitative EPMA data for 30 wt. % samples; $Na_2AlBSi_6O_{16}$, $Na_2Al_{1.4}B_{0.6}Si_6O_{16}$ and $Na_2Al_2Si_6O_{16}$ are summarised in Figure 5.14,

Table 5.7 and Table 5.7. The averaged measured elemental mol. % from the EPMA data was compared against the expected elemental mol. % calculated from the target stoichiometries and batch calculations. From the expected data the Na levels could be expected to remain fairly constant across the formulations and the Al was expected to increase systematically as it was increased by formulation ($Na_2Al_{1+x}B_{1-x}Si_6O_{16}$). Irrespective of crystalline phases, the Si was expected to reduce slightly, on a molar basis, with increasing Al concentration and the

samples were targeted for all Ca, Zr and Ti to be consumed in the crystalline phase(s). The EPMA data revealed some consistencies with the expected data as well as some variations. The Al increased systematically within errors and the B reduced to zero, as was targeted by the formulations. The Zr signal systematically increased as the Al content in the glass-ceramic decreased ($Na_2Al_{1+x}B_{1-x}Si_6O_{16}$), which implied a reduced solubility of Zr in the Al-rich glass compositions and was in agreement with the SEM-EDX data. The Ca signal was highest in the $Na_2Al_2Si_6O_{16}$ composition. This was indicative of increased solubility in the glass and may have been responsible for the chemical shift observed in the ^{27}Al MAS-NMR data, due to Ca charge compensating some Al species.

The Na signal did not appear to follow a clear trend, which was a direct result of Na migration during analysis. During the characterisation, the Na mobility was mitigated against as much as possible but there was still reasonable error associated with its measurement. Within errors the Si signal decreased with increasing Al, however, this data does not consider the crystalline phases present. From the XRD and SEM data, it was thought that low Al, $Na_2AlBSi_6O_{16}$, would yield less Si in the glass due to the presence of Si-bearing crystalline phases, zircon ($ZrSiO_4$) and sphene ($CaTiSiO_5$).

The strong Ti signal in the 30 wt. % $Na_2Al_2Si_6O_{16}$ sample was thought to be the detection of a minor crystalline phase, however the SEM and XRD data confirmed the sample to be single phase zirconolite ($CaZrTi_2O_7$). It is possible that the Ti signal did correspond to Ti in the glass, although such a significant increase between the $Na_2Al_{1.4}B_{0.6}Si_6O_{16}$ and $Na_2Al_2Si_6O_{16}$ compositions was unexpected.

The molar percentage of Ca, Zr and Ti incorporated in the glass phase was estimated from the EPMA data. Assuming that no mass was lost from the starting 50 g batches and that the proportion of glass was as targeted by the formulation; 30 wt%, the number of moles of Ca, Zr and Ti measured in the glass were calculated. These results were then compared against the number of moles batched to determine the amount incorporated in the glass phase. The results summarised in Table 5.6, showed that the amount of Ca incorporated in the glass increased with increased Al, whilst the amount of Zr decreased. Due to the errors associated with the data and the assumptions made in the calculation, these results are only semi-quantitative.

Table 5.6: Molar percentages of Ca, Zr and Ti incorporated into the glass phase calculated from the measured EPMA data and compared with the starting number of moles batched. It was assumed that no mass was lost from the 50 g starting batches and that the fraction of glass was 30 wt%, as batched.

	30 wt% $Na_2Al_2Si_6O_{16}$	30 wt% $Na_2Al_{1.4}B_{0.6}Si_6O_{16}$	30 wt% $Na_2AlBSi_6O_{16}$
	mol % of element in glass	**mol % of element in glass**	**mol % of element in glass**
Ca	17 %	6.6%	2.9%
Zr	1.8%	2.0%	3.4%
Ti	12%	2.0%	5.4%

The bottom two plots in Figure 5.14 show the expected and measured elemental compositions for glass composition $Na_2Al_2Si_6O_{16}$ with increased glass fractions. On a molar basis the changes to glass fraction were not expected to affect the elemental compositions in the glass, thus the expected data remained constant for each sample. The measured data fluctuated between the three samples with no consistent trends identifiable. Analysis of additional samples in the matrix may help identify trend behaviours with respect to glass fraction.

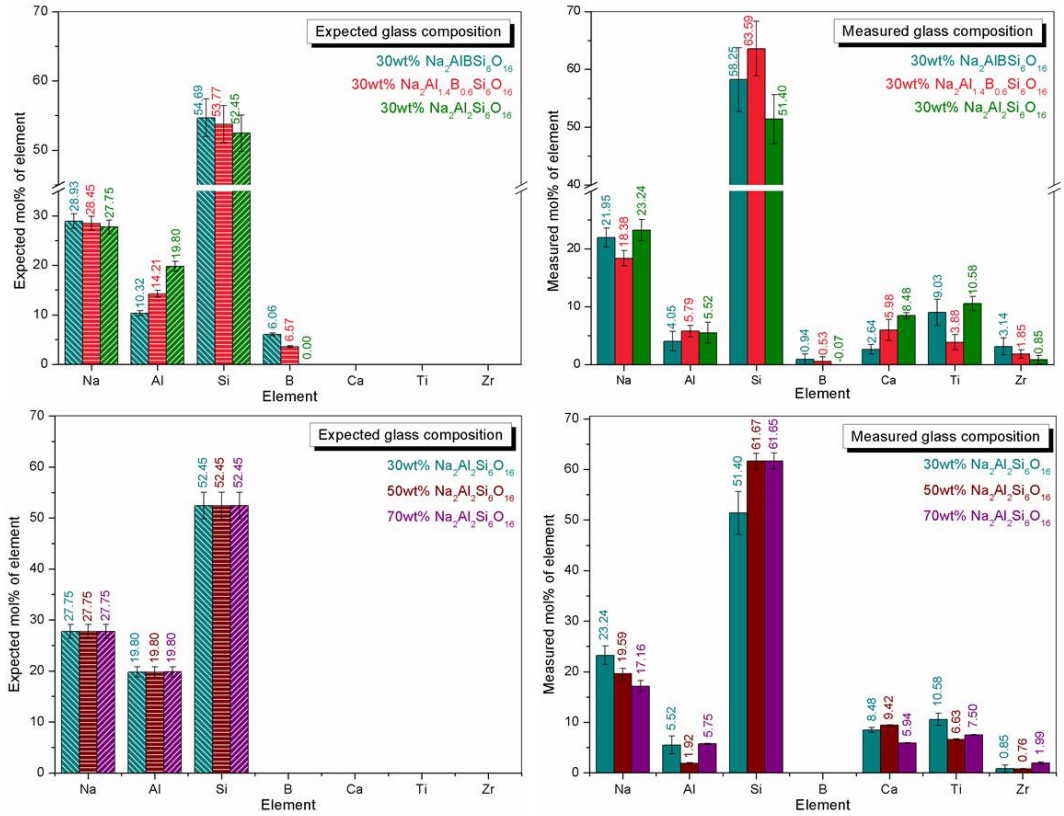

Figure 5.14: The expected mol. % of elements in the target glass phases compared against the measured data collected by EPMA. Top: 30 wt. % glass with increasing Al_2O_3. Bottom: $Na_2Al_2Si_6O_{16}$ glass composition with increasing glass fraction.

Table 5.7: Expected and measured mol. % ratios for the three 30 wt. % glass samples of varying compositions and the 50 wt. % and 70 wt. % samples with glass composition $Na_2Al_2Si_6O_{16}$. Expected data was calculated from the target stoichiometry and batch calculations, whilst the measured data was calculated from the raw EPMA data averaged over 10 measurements.

	30 wt. % $Na_2AlBSi_6O_{16}$		30 wt. % $Na_2Al_{1.4}B_{0.6}Si_6O_{16}$		30 wt. % $Na_2Al_2Si_6O_{16}$		50 wt. % $Na_2Al_2Si_6O_{16}$		70 wt. % $Na_2Al_2Si_6O_{16}$	
	Expected mol. % (±0.1)	Measured mol. %	Expected mol. % (±0.1)	Measured mol. %	Expected mol. % (±0.1)	Measured mol. %	Expected mol. % (±0.1)	Measured mol. %	Expected mol. % (±0.1)	Measured mol. %
Na	28.9	22 (±1.0)	28.5	18 (±1.0)	27.8	23 (±1.3)	27.7	20 (±1.1)	27.7	17 (±1.1)
Si	54.7	58 (±1.3)	53.8	64 (±1.5)	52.5	51 (±1.5)	52.4	62 (±1.5)	52.5	62 (±1.6)
Ca	0.0	2.6 (±0.1)	0.0	6.0 (±0.1)	0.0	8.5 (±0.1)	0.0	9 (±10.1)	0.0	5.9 (±0.1)
B	6.1	0.9 (±0.3)	3.6	0.5 (±0.3)	0.0	-0.1 (±0.2)	0.0	0.0	0.0	0.0
Al	10.3	4.1 (±0.1)	14.2	5.8 (±0.1)	19.8	5.5 (±0.1)	19.8	1.9 (±0.1)	19.8	5.8 (±0.1)
Ti	0.0	9.0 (±0.1)	0.0	3.9 (±0.1)	0.0	10.6 (±0.1)	0.0	6.6 (±0.1)	0.0	7.5 (±0.1)
Zr	0.0	3.1 (±0.2)	0.0	1.9 (±0.2)	0.0	0.9 (±0.2)	0.0	0.8 (±0.13)	0.0	2.0 (±0.2)

5.3.2 Ambient pressure results

These samples, described in Table 5.2, were designed to understand the development of the phase assemblage during high temperature processing. Figures 5.15, 5.16 and 5.17 compare the XRD data for the three heat treatments given to each composition; 70 wt. % glass fraction $Na_2Al_{0.5}B_{1.5}Si_6O_{16}$, 50 wt. % glass fraction $Na_2Al_{1.6}B_{0.4}Si_6O_{16}$, 30 wt. % glass fraction $Na_2Al_2Si_6O_{16}$, respectively. However, the absence of applied pressure during processing resulted in the formation of friable and porous products that could not be prepared for SEM / SEM-EDX analysis. The phase assemblage of each composition closely matched the corresponding HIPed samples with the relative intensity of $ZrSiO_4$ reflections increasing from the 30 wt. % glass sample to the 70 wt. % glass sample. The 30 wt. % $Na_2Al_2Si_6O_{16}$ samples produced a high yield of $CaZrTi_2O_7$ and the 70 wt. % $Na_2Al_{0.5}B_{1.5}Si_6O_{16}$ samples produced $ZrSiO_4$ with no detectable $CaZrTi_2O_7$, consistent with our previous study [223].

The 70wt. % glass fraction composition gave $ZrSiO_4$ as the major crystalline phase for all heat treatments (Figure 5.15). After 0 h dwell, $ZrSiO_4$ had already formed as a major phase, but the presence of intense reflections associated with α-quartz and α-cristobalite, showed complete digestion of SiO_2 and homogenisation of the melt had not yet been achieved. After the 4 h dwell, $ZrSiO_4$ was the only crystalline phase present showing the SiO_2 was incorporated into the melt during the dwell period. No other crystalline phases formed during the dwell at this composition, however accessory phases; rutile (TiO_2), brookite (TiO_2) and zirconium-titanate ($Zr_{0.86}Ti_{0.14}O_2$) (PDF-card numbers: 01-078-4188, 04-002-2753, 04-013-6878, respectively) were crystallised during the 10 °C/min cool.

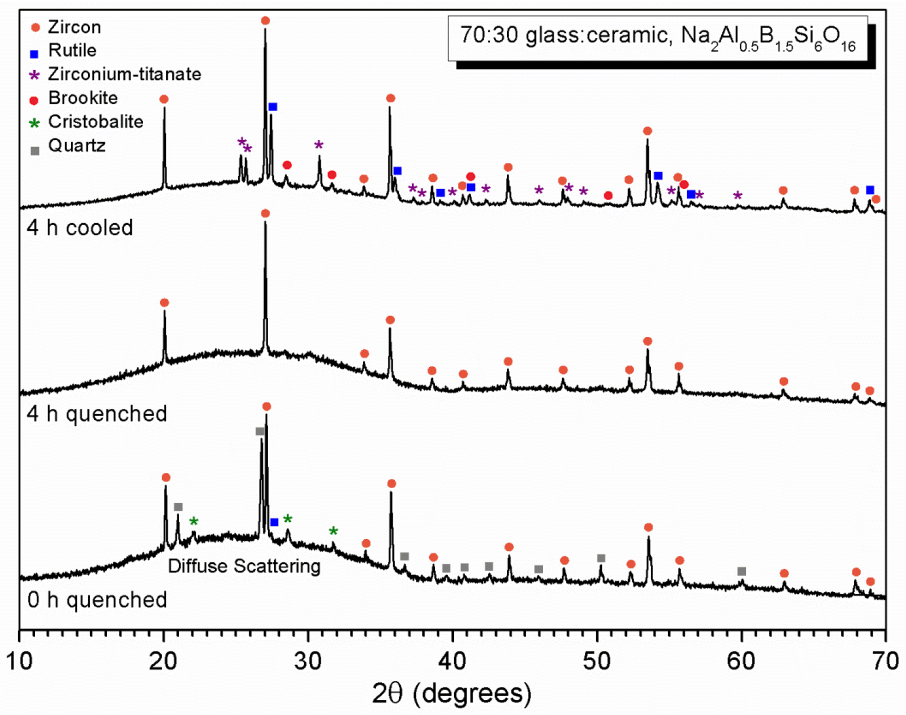

Figure 5.15: XRD data for 70 wt. % glass composition $Na_2Al_{0.5}B_{1.5}Si_6O_{16}$ after each heat treatment. Incomplete incorporation of batch components was evident after 0 h dwell and precipitation of other accessory phases during the cool down is highlighted by the single phase zircon ($ZrSiO_4$) identified after 4 h dwell and quench.

The 50 wt. % and 30 wt. % glass compositions (Figure 5.16 and Figure 5.17) processed at ambient pressure produced phase assemblages in good agreement with their HIPed counterparts, such that $CaZrTi_2O_7$ formation was favoured over $ZrSiO_4$ at higher Al_2O_3 concentrations and lower glass fractions. The 30 wt. % glass fraction sample (glass phase $Na_2Al_2Si_6O_{16}$) had a lower abundance of accessory phases than the 50 wt. % glass fraction composition (glass phase $Na_2Al_{1.6}B_{0.4}Si_6O_{16}$). After 0 h dwell, $CaZrTi_2O_7$ had already formed as the major crystalline phase, thus begins to form during the temperature ramp like $ZrSiO_4$. Interestingly, after the 4 h dwell, the relative intensity of reflections associated with the minor $ZrSiO_4$ phase, and trace TiO_2, ZrO_2 and $CaTiSiO_5$ phases, were significantly reduced. It is thought at these compositions, the $ZrSiO_4$ and $CaTiSiO_5$ act as intermediate phases in the formation of $CaZrTi_2O_7$, shown by the increase in $CaZrTi_2O_7$ at the expense of these phases with increased reaction time. Unfortunately, due to the lack of pressure during heating, the samples were not robust enough to prepare monolithic SEM samples for microstructural analysis. That said, the reduction of TiO_2 and ZrO_2 relative reflection intensities between the

0 h dwell and 4 h dwell data, suggested that these phases were relic reagents. Their final presence in the slow cooled samples, and that of zirconium-titanate ($Zr_{0.86}Ti_{0.14}O_2$) in the 70 wt. % sample, implied that these phases recrystallized from the melt as it equilibrated during cooling. It was not possible from the available data to determine whether relic reagents were present and recrystallised, or whether the $CaZrTi_2O_7$ formed by reaction between reagents or the intermediate phases. It is hoped increased time resolution will enable the observation of the systematic phase evolution during the ramp to temperature and dwell periods by conducting high temperature *in-situ* neutron diffraction experiments.

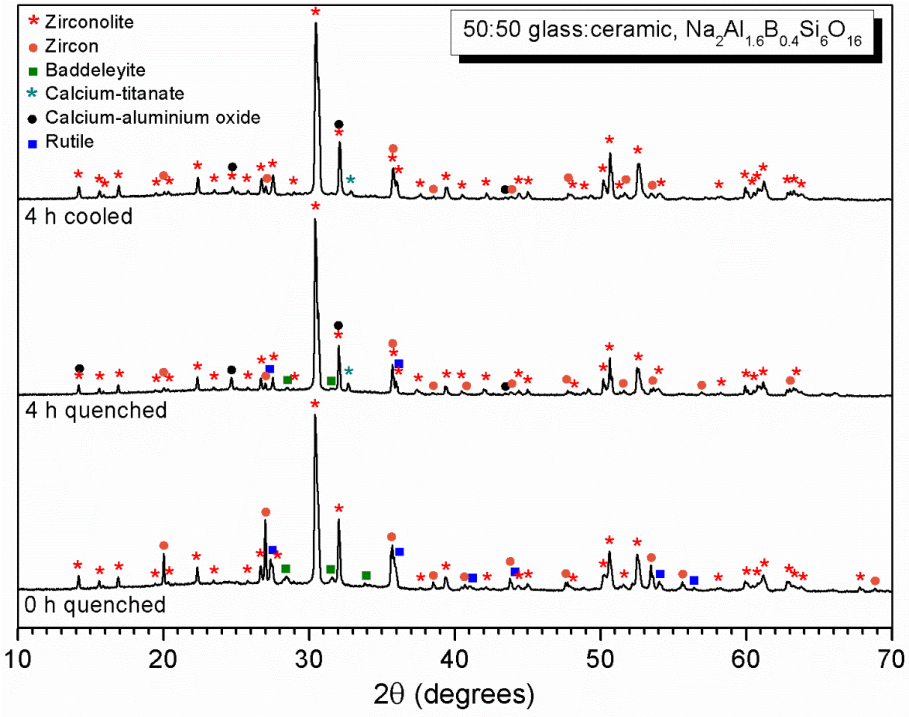

Figure 5.16: XRD data for 50 wt. % glass composition $Na_2Al_{1.6}B_{0.4}Si_6O_{16}$ after each heat treatment. Incomplete incorporation of batch components was evident after 0 h dwell and precipitation of secondary phases during the cool down highlighted by the single phase zircon ($ZrSiO_4$) identified after 4 h dwell and quench.

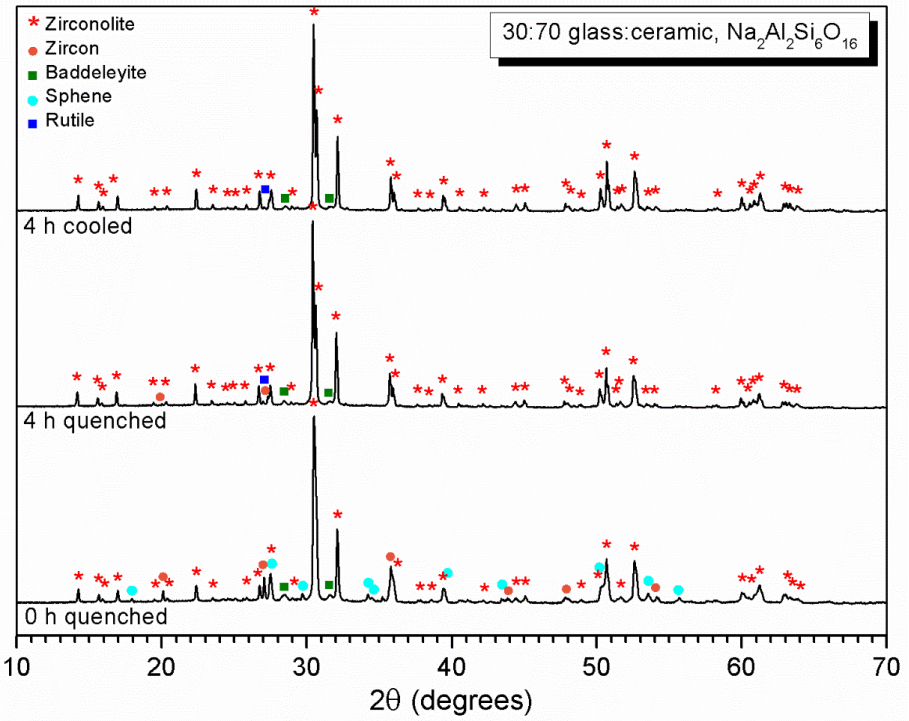

Figure 5.17: XRD data for 30 wt. % glass composition $Na_2Al_2Si_6O_{16}$ after each heat treatment. Incomplete incorporation of batch components was evident after 0 h dwell and precipitation of secondary phases during the cool down highlighted by the single phase zircon ($ZrSiO_4$) identified after 4 h dwell and quench.

5.4 Discussion

It has been demonstrated that the phase assemblage of this zirconolite ($CaZrTi_2O_7$) glass-ceramic system is sensitive to both Al_2O_3 : B_2O_3 and glass : ceramic ratios. This is illustrated by synthesis of the available XRD and SEM / SEM-EDX data for the 18 sample matrix, to yield the qualitative pseudo-phase diagram shown in Figure 5.18. With reference to this figure: the dark green region corresponds to $CaZrTi_2O_7$ as the exclusive crystalline phase; the yellow regions correspond to $CaZrTi_2O_7$ as the major crystalline phase; the red areas correspond to $ZrSiO_4$ as the major phase and $CaZrTi_2O_7$ as a trace or absent phase; other shades represent intermediate crystalline phase assemblages as shown in the legend of Figure 5.18.

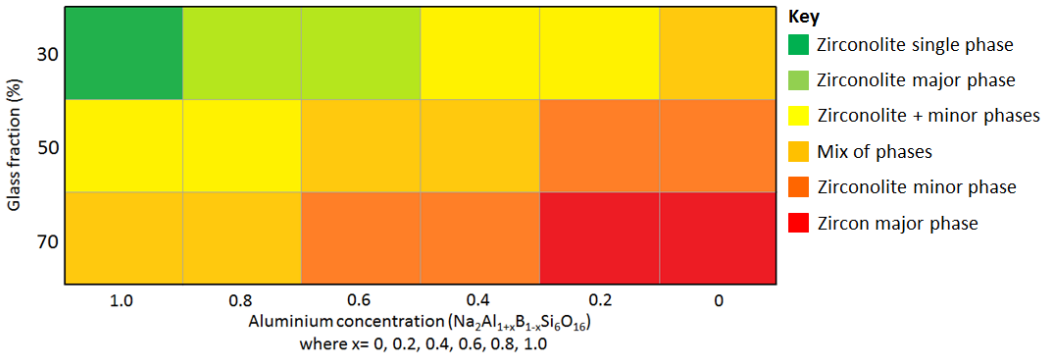

Figure 5.18: Qualitative phase map representing the glass-ceramic phase assemblage with respect to glass composition $Na_2Al_{1+x}B_{1-x}Si_6O_{16}$ and glass fraction.

5.4.1 Effect of glass fraction

The XRD and SEM / SEM-EDX results presented show that increasing the glass fraction at a constant glass composition reduces the yield of $CaZrTi_2O_7$, and increases the yield of accessory phases. The yield of Si-bearing crystalline phases $ZrSiO_4$ and $CaTiSiO_5$ was greater overall in the 70 wt. % glass samples. The role of SiO_2 in the system was as the primary glass network former and it was preferentially partitioned within the glass phase. One driving force for the formation of $ZrSiO_4$ and $CaTiSiO_5$ is considered to be the activity of SiO_2 within the glass, which increases with increasing abundance (i.e. a higher glass fraction) [227].

The observed increase of $CaZrTi_2O_7$ was directly related to a reduction in $ZrSiO_4$, $CaTiSiO_5$ and TiO_2, which was in argreement with our preliminary study that proposed the following equilibrium equation (Equation 10) [147].

$$CaZrTi_2O_7 + 2[SiO_2] \rightleftharpoons ZrSiO_4 + CaTiSiO_5 + TiO_2 \qquad \textbf{Eq. 10}$$

Maddrell *et al.* developed this hypothesis to explain the phase assemblage changes, on the grounds of thermodynamics [147]. The standard Gibbs free energies of formation were used to determine data for the equilibrium reaction, equation 10. This analysis concluded that the formation of $ZrSiO_4$, $CaTiSiO_5$ and TiO_2 was thermodynamically favourable over the formation of $CaZrTi_2O_7$ and incorporation of the SiO_2 in the amorphous phase (denoted by the square brackets in Equation 10); –128.5 $kJmol^{-1}$ over –92.0 $kJmol^{-1}$. Maddrell *et al.* concluded that the SiO_2 activity was the primary driving force controlling the shift in the equilibrium reaction with changes to glass composition, whereby a lower SiO_2 activity favours $CaZrTi_2O_7$ formation

[147]. This theory , however, is limited by the thermodynamic data available, which does not account for the processing conditions and does not consider potential kinetic effects in the melt. Based on these limitations in the use of thermodynamic data, here we aim to give an alternative hypothesis and explain the change in crystalline phase assemblage on the basis of a relationship between glass structure and composition.

5.4.2 Effect of glass compostion

In alkali aluminoborosilicate glasses Na_2O is present as a modifier and preferentially charge compensates tetrahedral Al units, such as $[AlO_{4/2}]^-$ [60]. If Na_2O is in excess relative to Al_2O_3, it would be expected that all Al is stabilised in tetrahedral co-ordination [59,61]. In all glass compositions studied here, the amount of Na_2O was equal to (Al_2O_3 + B_2O_3), thus, $Na_2O \geq Al_2O_3$ in all samples. ^{27}Al MAS-NMR confirmed that all the Al was present as tetrahedral $^{[4]}$Al units, believed to be charge compensated by Na^+ ions, resulting in a highly polymerised glass network. When ($Na_2O - Al_2O_3$) > 0, excess modifier ions are available to stabilise other units in the glass after full charge compensation of the tetrahedral Al units. In some cases, this will depolymerise the glass network by producing non-bridging oxygens (NBOs) and potentially increase the solubility of other elements, such as Ca, Zr and Ti [224]. The SEM-EDX and EPMA data confirmed an increase of Zr in the glass as the excess Na_2O increased with increased B_2O_3 in the formulation ($Na_2Al_{1+x}B_{1-x}Si_6O_{16}$). Interestingly, Ca solubility appeared to decrease with the increase of B_2O_3 in the formulation. This was thought to be the result of a lack of modifier cations available to charge balance other species in the glass when most Na_2O was expected to be associated with the Al. This theory was supported by the ^{27}Al MAS-NMR data that showed a chemical shift of the tetrahedral $^{[4]}$Al units in the 30 wt. % $Na_2Al_2Si_6O_{16}$ sample, which suggested a change in the local environment of the tetrahedral species, such as Ca charge compensation.

The ^{11}B NMR spectra confirmed a reduction of tetrahedral $^{[4]}$B units with increased Al_2O_3. Increasing the Al_2O_3 reduced the availability of Na_2O for stabilisation of the tetrahedral $^{[4]}$B units, which led to an increase of $^{[3]}$B units. This was confirmed by the deconvolution of the ^{11}B NMR data that confirmed an increase in non-ring $^{[3]}$B units. Due to the equimolar ratios of Na_2O to (Al_2O_3 + B_2O_3) in these glass compositions, the ratio of excess Na_2O to total B_2O_3 can be assumed equal. However, it is known that not all $^{[3]}$B units convert and stabilise as

tetrahedral $^{[4]}B$ units via alkali charge compensation and as a result, some Na_2O will not be associated with either Al or B species [46,56,57]. This Na_2O is therefore free to perform other roles within the glass structure, either stabilising other network formers or forming NBOs. This was again in good agreement with the EDX and EPMA data that showed an increase of Zr and Ti within the Al_2O_3 rich glass compositions.

The NMR spectra indicated a crystalline Na species present in the 30 wt. % glass samples. The SEM and XRD data did not identify a Na-bearing crystalline phase but a plausible trace phase may have been albite ($NaAlSi_3O_8$).

Connelly *et al.* developed a model to predict the preferential charge compensation of different cation species within alkali aluminoborosilicate glasses [58]. The model determined an order of preferential charge compensation, such that: $[AlO_{4/2}]^-$ > $[ZrO_{6/2}]^{2-}$ > $[TiO_{5/2}]^-$ > $[BO_{4/2}]^-$ > $[SiO_{3/2}O^-]$. The model results showed $[AlO_{4/2}]^-$ units are preferentially charge compensated first, which agreed with other literature as discussed previously [46,47,59,61]. The order of preferential charge compensation proposed by Connelly *et al.* suggested that $[SiO_{3/2}O^-]$ tetrahedra are stabilised after $[ZrO_{6/2}]^{2-}$, $[TiO_{5/2}]^-$ and $[BO_{4/2}]^-$ [58]. This may reduce the stability of SiO_2 in the glass, causing it to preferentially form the crystalline phases, $ZrSiO_4$ and $CaTiSiO_5$. ^{29}Si MAS-NMR would provide more information on the evolution of the tetrahedral $^{[4]}Si$ species with changes to the glass composition. If the N_4 species decrease with increased B_2O_3, it would show a depolymerisation of the glass network and therefore a higher propensity for SiO_2 to be consumed in crystalline phases. It is important to note, these charge compensation mechanisms within the glass are far more complex and will occur somewhat simultaneously, rather than individually and consecutively.

It is also known that the solubility of cation species in glass can strongly depend on their co-ordination, for example, 6-fold co-ordinated Zr $[ZrO_{6/2}]^{2-}$) has a higher solubility limit than 8-fold co-ordinated Zr species [228]. Increased stabilisation of $[ZrO_{6/2}]^{2-}$ and $[TiO_{5/2}]^-$ species in the glass may reduce the driving force for $CaZrTi_2O_7$ phase formation and potentially, help explain the changes in phase formation with changes to the glass composition; if more B_2O_3 results in more excess Na_2O available to stabilise more $[ZrO_{6/2}]^{2-}$ and $[TiO_{5/2}]^-$ in the glass, the availability of ZrO_2 and TiO_2 to form the crystalline $CaZrTi_2O_7$ phase will be reduced.

It has been hypothesised that increasing B_2O_3 (decreasing Al_2O_3) in the glass formulation increases the abundance of excess Na_2O, which has a two-fold effect on the glass structure; more $[ZrO_{6/2}]^{2-}$ and $[TiO_{5/2}]^{-}$ are stabilised in the glass thus the availability of ZrO_2 and TiO_2 for forming $CaZrTi_2O_7$ becomes reduced; depolymerisation of the glass network and reduced availability of Na_2O for stabilising $[SiO_{3/2}O^{-}]$ tetrahedra results in SiO_2 preferentially forming crystalline phases. Our results and hypothesis are in excellent agreement with Caurant *et al.*'s study on the effect of Al_2O_3 concentration on the crystallisation of $CaZrTi_2O_7$ [229]. At lower Al_2O_3 concentrations the $CaZrTi_2O_7$ yield was reduced. Caurant *et al.* discussed the relationship between reduced Al_2O_3 and the increase in excess modifier ions enabling stabilisation of $[ZrO_{6/2}]^{2-}$ and $[TiO_{5/2}]^{-}$ in the glass. The stabilisation of these cations in the glass decreased their activities thus reduced the $CaZrTi_2O_7$ nucleation rate and its crystallisation driving force [229]. Interestingly, this means that as the Al_2O_3 : B_2O_3 ratio changes, the ZrO_2 / TiO_2 : B_2O_3 ratio in the glass changes as well. Further investigations and quantification of the glass : ceramic ratio and glass composition may give further insight into this relationship. The EPMA data presented demonstrated more ZrO_2 in the glass with increased B_2O_3, but the TiO_2 behaviour remained inconclusive. The Reitveld refinement data suggested a reduction in the abundance of Zr-bearing crystalline phases ($CaZrTi_2O_7$ and $ZrSiO_4$) with increased B_2O_3, thus more Zr was consumed in the glass, which was in agreement with the EPMA data and proposed hypothesis. Unfortunately, as has been previously mentioned, the fine grain structure of these multiphase systems made quantification difficult and sufficient errors are associated with the results. Another way of estimating the crystalline phase abundance to support the quantified data presented would be to use quantitative ceramatography.

5.4.3 Ambient pressure experiments

The ambient pressure results were in good agreement with the HIPed samples and supported our hypothesis regarding glass structure on crystalline phase formation. By quenching the samples after different dwell periods, insight into the process of phase formation was gained. The formation of $CaZrTi_2O_7$ and $ZrSiO_4$ during the ramp to temperature indicated the glass-ceramics did not form by conventional routes [23] and that there was some degree of solid state reaction taking place as the glass melt formed and homogenised.

The presence of SiO_2 in the 70 wt. % glass sample ($Na_2Al_{0.5}B_{1.5}Si_6O_{16}$) after 0 h dwell showed that some of the batch remained undissolved during the ramp to temperature. It is well known that the dissolution of SiO_2 is rate determining during glass melting [230]. The presence of $ZrSiO_4$ showed it formed during the ramp to temperature and, after the melt equilibrated during the 4 hr dwell, was present as the only crystalline phase after the 4 h dwell. The Ti-bearing phases present in the slow cooled sample were therefore precipitation products as the glass melt equilibrated during the cool. This supports our hypothesis of increased Ti solubility in the glass melt with reduced Al_2O_3 concentrations, inhibiting the formation of $CaZrTi_2O_7$. The precipitation of the Ti-bearing phases during the cool was a result of excess TiO_2, initially targeted for the $CaZrTi_2O_7$ phase, being kicked out of the glass as the melt equilibrated during cooling. The abundance of Ti-bearing phases in the HIP samples increased as $CaZrTi_2O_7$ reduced. It can thus be assumed the Ti-bearing minor phases present in the high glass / low Al_2O_3 HIP samples also precipitated from the melt during cooling.

We can assume the ZrO_2 solubility limit in the glass was exceeded and that the crystals acted as nucleation sites for $ZrSiO_4$ growth. $ZrSiO_4$ has been reported to grow from ZrO_2 crystals by templating growth [231]. Through inward and outward diffusion mechanisms, a $ZrSiO_4$ layer initially surrounds the ZrO_2 crystals as the inward diffusion of SiO_2 gradually consumes all the ZrO_2 [231]. The presence of ZrO_2 at the centre of both $CaZrTi_2O_7$ and $ZrSiO_4$ crystals in the SEM implies similar diffusion mechanisms control the formation of both phases.

In contrast, the XRD data for the 30 wt. % and 50 wt. % glass fraction samples, showed that TiO_2 was not precipitated during cooling. For these compositions the abundance of TiO_2 reduced during the dwell as the reagent was gradually incorporated into the $CaZrTi_2O_7$ phase. Its minor presence after the 4 h dwell implied the system did not reach equilibrium.

The lower glass fraction samples (30 wt. % and 50 wt. %) yielded $CaZrTi_2O_7$ as the major phase during the ramp to temperature, with $ZrSiO_4$ and $CaTiSiO_5$ present as minor phases. These phases may be considered as intermediate phases that form before the melt is homogenised. As the samples equilibrated during the 4 h dwell, these phases were consumed in the formation of $CaZrTi_2O_7$ and glass, which was in agreement with equation 10. From the available data it was not possible to determine whether $CaZrTi_2O_7$ forms from the starting reagents or from the intermediate $ZrSiO_4$ and $CaTiSiO_5$ phases, but it is hoped

time-resolved *in-situ* neutron diffraction experiments will provide more insight into the formation of the target crystalline phase.

5.4.4 Wasteform properties

When selecting a glass-ceramic formulation the final wasteform performance must be considered. Whilst optimising the $CaZrTi_2O_7$ formation means higher actinide loadings can be achieved, enough glass needs to be present to immobilise the impurities within the waste. The glass : ceramic ratio must be determined as a compromise between loading capacity and the overall performance of the wasteform. From the phase map we can define a usable region of formulations that successfully yield a high fraction of $CaZrTi_2O_7$ for actinide incorporation and are flexible to accommodate varying levels of impurities. Small changes to the glass composition or glass fraction from the single phase $CaZrTi_2O_7$ sample (30 wt. % glass $Na_2Al_2Si_6O_{16}$), maintain $CaZrTi_2O_7$ as the major phase with only minor changes to the overall phase assemblage.

The addition of Na_2O and B_2O_3 to silicate glasses was originally done to reduce processing temperatures, but are detrimental to the durability performance of the glass [46,47]. Al_2O_3 was therefore added to counteract the detrimental effects of Na_2O and B_2O_3 on the glass durability [47]. However, our optimised glass formulation is an alkali aluminosilicate glass due to the complete removal of B_2O_3. The high refractory content of the glass and lack of B_2O_3 will result in a higher liquidus temperature and a viscous melt [232]. However, the manageability of the glass melt is less important when treated by HIP compared to other vitrification methods, as the hermetically sealed nature of the glass during processing means there is no need to decant the material from a melter. As such we are less constrained by the melt properties allowing for better optimisation of the wasteform performance; to be investigated through waste incorporation studies with Pu surrogates.

Although B is a neutron absorber, it is also an active neutron source for (α,n)-reactions [132]. By removing B_2O_3 from the glass-ceramic formulation the overall occurrence of damaging (α,n)-reactions is likely to be reduced. (α,n)-reactions occur between emitted α particles from Pu-decay and light elements, such as B, F and O, in the material [150]. The interaction of the α-particle with the B nucleus results in the emission of a high energy neutron that can create a chain reaction of damage through the wasteform. Such events may also result in the

emission of high energy gamma rays from metastable ions, which would warrant the need for extra shielding of the wasteform packages during transportation and storage [150]. As a result the elimination of neutron sources such as B is highly advantageous for the longevity of the wasteform and short term handling of the packages. The incorporation of neutron absorbers in Pu-bearing wasteforms is a method used to avoid criticality. Successful incorporation of alternatives such as Gd and Hf in $CaZrTi_2O_7$ has been reported extensively in the literature [99,101,132,229,233,234].

5.5 Conclusions

Zirconolite based glass-ceramics are being considered for the disposition of high level Pu wastes in the UK. The effect of glass composition and glass fraction on the yield of zirconolite in HIPed glass-ceramics has been investigated. It can be concluded that the combination of a low glass fraction and Al_2O_3 rich glass composition yields an optimum glass-ceramic phase assemblage of high-fraction zirconolite. A qualitative phase map of the glass-ceramic matrix demonstrated how the crystalline phase assemblage varied with the glass composition and glass fraction. From this, a suitable range of glass-ceramic formulations that yield high fraction zirconolite, whilst enabling wasteform flexibility to accommodate waste variations, can be selected.

Although the data presented is not sufficient to ascertain the mechanisms controlling the crystalline phase formation, a promising hypothesis has been put forward and mechanisms that may concurrently contribute to the phase assemblage variations have been proposed. The presence of B_2O_3 is thought to depolymerise the glass network and increase the solubility of ZrO_2 and TiO_2. It was hypothesised that this destabilises Si tetrahedra in the glass due to the preferential charge compensation of $[ZrO_{6/2}]^-$ and $[TiO_{5/2}]^-$ units. Subsequently, this increases the SiO_2 propensity to form crystalline phases. In contrast, the B_2O_3 free glass-ceramic systems resulted in a highly polymerised glass network that limited the ZrO_2 and TiO_2 solubilities, thus promoted the formation of zirconolite.

Whilst this study put forward a hypothesis based on glass structure for the mechanisms controlling the glass-ceramic phase assemblage, further investigations are required to robustly underpin our understanding of these wasteform systems. ^{29}Si MAS-NMR would reveal how the N_4 species change with Al_2O_3 concentration to further support the current

NMR data and the theory that Si tetrahedra destabilise with increased B_2O_3. Further consideration should be given to the B : Zr ratio in the glass phase, which may be a driving force for the formation of Si-bearing crystalline phases. To better understand the phase formation and evolution in these systems, *in-situ* neutron diffraction may provide a time resolved insight into the crystalline phase assemblage evolution during the ramp to temperature and dwell period. This may allow for better identification of intermediate phases, as well as determine whether zirconolite forms from the raw reagents or from the intermediate phases.

6 Cerium incorporation

A study of Ce incorporation in zirconolite glass-ceramics.

Stephanie M. Thornber[a], Martin C. Stennett[a], Ralph Wagner[b] & Neil C. Hyatt[a,*]

[a]*Immobilisation Science Laboratory, Department of Materials Science & Engineering, The University of Sheffield, Sir Robert Hadfield Building, Mappin Street, Sheffield S1 3JD, UK*

[b]*Bergische Universität Wuppertal, Gaußstr. 20, 42097 Wuppertal, Germany*

Author contributions: Stephanie M. Thornber designed and developed the experimental matrix, fabricated, characterised and analysed all samples and wrote the scientific report. Martin C. Stennett helped quantify the XANES data and provided useful communications. Ralph Wagner granted access to the DELTA B10 beamline and provided training and assistance. Neil C. Hyatt provided project oversight and supervision.

6.1 Introduction

Zirconolite glass-ceramics are considered to be potential wasteforms for the disposition of Pu in low purity waste-streams. Zirconolite is a naturally occurring mineral and has been proven to have excellent wasteform properties through studies of natural analogues and through its use as an actinide bearing phase in Synroc [80,132]. The Ca and Zr sites in the zirconolite structure can incorporate actinides such as Pu and U, whilst the Ti sites allow charge compensation to occur. Studies of natural analogues and synthetic zirconolite wasteforms show excellent radionuclide retention, radiation tolerance and durability [88,98,234,235]. The zirconolite structure is a derivative of the pyrochlore structure $A_2B_2O_7$, consisting of parallel planes of Ca and Zr ions alternated with planes of Ti octahedra [23,92]. Whilst the zirconolite-2M monoclinic structure is the nominal polytype, other polytypes have been reported including; zirconolite-4M, zirconolite-3T, zirconolite-3O and zirconolite-6T [236].

These wasteforms are of interest for Pu-residue waste-streams found in the UK, as well as for the potential future immobilisation of the bulk separated civil PuO_2 stockpile. Pu-residue wastes originate from multiple sources including; early research and development work, secondary reprocessing wastes and unused MOx materials. As a result, these wastes are

highly heterogeneous and contain various levels of Pu, glass formers and impurities [18,82,179]. Whilst full ceramic materials (or high ceramic fraction materials) are considered potential wasteform matrices for the purer streams of Pu-residue materials and for the potential future immobilisation of the PuO_2 stockpile, glass-ceramics are being developed to treat lower purity streams of these wastes. The glass-ceramic matrix results in the partitioning of actinides into the durable ceramic phase ($CaZrTi_2O_7$), whilst the glass phase provides flexibility to accommodate impurities and variations in the waste composition [17]. This dual barrier system of actinides partitioning into the durable ceramic phase, which is encapsulated in the amorphous glass phase, also ensures excellent proliferation resistance in a single processing step. Leaching experiments have shown preferential dissolution of the glass phase whilst the actinides are successfully retained in the ceramic [17]. Retrieval studies have also demonstrated the proliferation resistance of the glass-ceramics, whereby between 7,000 and 28,000 kg of the HIPed glass-ceramic wasteform would be required to extract 1 kg of Pu, compared to a borosilicate glass matrix, which was found to be 25 times less resistant [17,100,144].

Previously we have reported the selection of an optimised glass-ceramic formulation that maximised the yield of zirconolite over other ceramic phases (Chapter 5). In this chapter, we discuss the results of waste incorporation experiments with respect to Ce oxidation and the targeted substitution site. From the literature, other glass-ceramic formulations were originally designed around CaF_2 rich Pu-residue waste-streams [17,147]. These CaF_2 rich wastes were later reclassified, but the CaF_2 was believed to aid waste digestion into the Al_2O_3 rich glass-ceramic matrix [147]. As such, later formulations continued to include CaF_2 as a precursor to improve the incorporation of waste analogues and PuO_2 [82,143,147].

The presence of CaF_2 in actinide bearing wasteforms brings additional risks to the long-term integrity and wasteform performance due to ^{19}F being an active neutron source for (α,n)-reactions. When intimately mixed with actinides, the probability of α-particles interacting with the nucleus of the 100 % abundant ^{19}F ions is substantial and can have a detrimental effect on the long-term performance of the wasteform [148,149]. The interaction of an α particle with the ^{19}F nucleus results in the emission of a high energy neutron. This neutron can generate a neutron chain reaction with other ions in the wasteform and create structural damage through elastic collisions. The (α,n)-reactions also

generate high energy gamma ray (γ) emissions, in the region of 1.5 MeV and generate the need for extra shielding around the waste package for handling and storage [150]. By eliminating CaF_2 as a precursor, the presence of neutron sources for (α,n)-reactions is reduced. The standard glass-ceramic formulation discussed here does not include CaF_2, however we investigate the effect of CaF_2 on the waste incorporation into the glass-ceramic matrix.

CeO_2 was utilised as an inactive surrogate for PuO_2. Incorporation of Ce into the zirconolite structure was targeted for both the Ca and Zr sites and both Ce^{3+} and Ce^{4+} oxidation states. Three charge compensation mechanisms were targeted through starting stoichiometries; $Ca_{0.8}Ce_{0.2}ZrTi_{1.6}Al_{0.4}O_7$, $Ca_{0.9}Ce_{0.1}Zr_{0.9}Ce_{0.1}Ti_2O_7$ and $CaZr_{0.8}Ce_{0.2}Ti_2O_7$. These samples were subsequently repeated with CaF_2 additions and again with Ni powder, to study the effect of CaF_2 as a digesting agent and that of controlled oxygen fugacity. Two different milling conditions were used to further improve waste incorporation and to determine if milling affected the final wasteform product. Each matrix of samples was studied against each other to determine the effects of CaF_2, milling and redox control on the incorporation of CeO_2.

6.2 Experimental

All samples were formulated with the same baseline formulation, comprising 30 wt. % glass of target stoichiometry, $Na_2Al_2Si_6O_{16}$ and 70 wt. % ceramic forming oxides. CeO_2 was used as an inactive surrogate for PuO_2 and was targeted for incorporation into the zirconolite ceramic. The sample matrix investigated the success of Ce substitution by targeting either Ce^{3+} or Ce^{4+} incorporation onto the Ca^{2+} and / or Zr^{4+} sites. When targeting Ce^{4+} substitution on the Ca^{2+} site (sample A), Al_2O_3 was added for charge compensation. The formulation of sample C did not necessitate charge compensation. In the formulation of sample B, charge compensation was designed to be achieved by equimolar substitution of Ca^{2+} / Ce^{3+} and Zr^{4+} / Ce^{3+}.

The baseline formulation samples A – C were repeated, first with 4 wt. % Ni powder additions to study the effect of redox control on the incorporation of Ce in the glass-ceramic matrix and secondly, with 0.6 wt. % and 0.3 wt. % CaF_2 additions to determine whether or not CaF_2 had significant effects on waste digestion. Powder batches were milled at 500 rpm for 30 min and were calcined at 600 °C before being packed into stainless steel HIP canisters.

Samples A – C and H – M were milled in 50 ml volume pots. Sample A was repeated and milled in a 250 ml volume mill pot that achieved far better homogenisation of the powders. From the results of these comparative samples, it was concluded to use the 250 ml mill pot for all further batches (Samples E – G in Table 6.1).

The HIP canisters were evacuated at room temperature and at an elevated temperature (300 °C) before sealing to ensure complete densification during processing. All samples were processed at 1250 °C for 4 h under 103 MPa of argon gas pressure. Monolithic samples were ground and polished to study the microstructure and elemental distribution using a Hitatchi TM3030 analytical scanning electron microscope (SEM) and a Bruker Quantax energy dispersive X-ray spectrometer (EDX), with an accelerating voltage of 15 kV and a working distance of 8 mm. Phase analysis was done by powder X-ray Diffraction (XRD) using a Bruker D2 PHASER diffractometer with Cu Kα radiation (1.5418 Å) and a Lynxeye position sensitive detector.

Ce speciation was studied by Ce L_3 X-ray absorption near-edge spectroscopy (XANES) on both monolithic and bulk powder samples. The bulk powder pellet samples were prepared by mixing the finely ground sample with PEG (poly-ethanol-glycol) to achieve a thickness equal to a single absorption length. These samples were measured in transmission to gain data representative of the whole sample. Parallel-sided, monolith cross-sections of the canisters, polished to a 1µm finish, were analysed in fluorescence, using a pin-diode detector, to study the percentage of Ce^{3+} : Ce^{4+} through the sample (edge to centre). These data were collected on Beamline 10 at the DELTA beamline facility in Dortmund, Germany. Beamline 10 utilises a simple X-ray optical layout consisting of a fixed, water-cooled absorber mask, a tilt absorber and a Si(111) channel-cut monochromator, before two slit systems that define the final beam size [237]. A He atmosphere was used in the beam pathway and gas filled ionisation chambers measured the incident and transmitted beam intensities. Data analysis was performed using the Athena and Hephaestus software [206].

Table 6.1: Summary of all samples. Ce incorporation was targeted for both the Ca and / or the Zr sites (Samples A-C). Sample D was a repeat of sample A formulation milled in a 250 ml volume mill pot. Each stoichiometry was repeated with Ni and CaF_2 additions (samples E-G and H-M, respectively).

Sample	Target Composition	Weight % of oxides							Additions	Target Ce oxidation
		SiO_2	Al_2O_3	Na_2O	CaO	TiO_2	ZrO_2	CeO_2		
A	$Ca_{0.8}Ce_{0.2}ZrTi_{1.6}Al_{0.4}O_7$	20.62	9.9	3.55	8.95	25.51	24.6	6.87	50 ml mill pot	4+
B	$Ca_{0.9}Ce_{0.1}Zr_{0.9}Ce_{0.1}Ti_2O_7$	20.62	5.83	3.55	9.98	31.59	21.93	6.81	50 ml mill pot	3+
C	$CaZr_{0.8}Ce_{0.2}Ti_2O_7$	20.62	5.83	3.55	11.25	32.06	19.78	6.91	50 ml mill pot	4+
D	$Ca_{0.8}Ce_{0.2}ZrTi_{1.6}Al_{0.4}O_7$	20.62	9.90	3.55	8.95	25.51	24.60	6.87	250 ml mill pot	4+
E	$Ca_{0.8}Ce_{0.2}ZrTi_{1.6}Al_{0.4}O_7$	20.62	9.90	3.55	8.95	25.51	24.60	6.87	4wt. % Ni, 250 ml mill pot	4+
F	$Ca_{0.9}Ce_{0.1}Zr_{0.9}Ce_{0.1}Ti_2O_7$	20.62	5.83	3.55	9.98	31.59	21.93	6.81	4wt. % Ni, 250 ml mill pot	3+
G	$CaZr_{0.8}Ce_{0.2}Ti_2O_7$	20.62	5.83	3.55	11.25	32.06	19.78	6.91	4wt. % Ni, 250 ml mill pot	4+
H	$Ca_{0.8}Ce_{0.2}ZrTi_{1.6}Al_{0.4}O_7$	20.62	9.90	3.55	8.95	25.51	24.60	6.87	0.6wt. % CaF_2 50 ml mill pot	4+
I	$Ca_{0.8}Ce_{0.2}ZrTi_{1.6}Al_{0.4}O_7$	20.62	9.90	3.55	8.95	25.51	24.60	6.87	0.3wt. % CaF_2 50 ml mill pot	4+
J	$Ca_{0.9}Ce_{0.1}Zr_{0.9}Ce_{0.1}Ti_2O_7$	20.62	5.83	3.55	9.98	31.59	21.93	6.81	0.6wt. % CaF_2 50 ml mill pot	3+
K	$Ca_{0.9}Ce_{0.1}Zr_{0.9}Ce_{0.1}Ti_2O_7$	20.62	5.83	3.55	9.98	31.59	21.93	6.81	0.3wt. % CaF_2 50 ml mill pot	3+
L	$CaZr_{0.8}Ce_{0.2}Ti_2O_7$	20.62	5.83	3.55	11.25	32.06	19.78	6.91	0.6wt. % CaF_2 50 ml mill pot	4+
M	$CaZr_{0.8}Ce_{0.2}Ti_2O_7$	20.62	5.83	3.55	11.25	32.06	19.78	6.91	0.3wt. % CaF_2 50 ml mill pot	4+

6.3 Results

All samples obtained zirconolite ($CaZrTi_2O_7$) as the major crystalline phase with similar phase assemblages and microstructures. Although there were minor differences and varying degrees of Ce incorporation, the different additions to the baseline formulation did not majorly affect the final structure of the wasteforms. Here we discuss each set of samples and compare the effects of each addition against the baseline formulations.

Table 6.2 summarises the canister and material densifications achieved for each sample. The calculated material densification for samples E and F were slightly lower than expected, however, there was a larger uncertainty associated with these samples due to the Ni powder not being homogeneously distributed. Sample J also had a relatively low densification percentage due to complications during canister welding and evacuation.

Table 6.2: Canister and material densifications after HIPing. Canister volumes before and after were determined by water displacement measurements. The true density (pycnometric density) of the material was determined by helium gas pycnometry and the material density (displacement density) was measured by water displacement.

Sample	Canister Volume Before (cm^3) ($\pm$1.49)	Canister Volume After (cm^3) ($\pm$1.53)	Pycnometric Density (g/cm^3) ($\pm$0.02)	Displacement Density (g/cm^3) ($\pm$0.06)	Canister Densification % ($\pm$3)	Effective % of theoretical density ($\pm$0.1)
A	42	25	3.74	3.63	60	97.0
B	44	25	3.69	3.61	57	97.7
C	40	24	3.69	3.60	60	97.6
D	41	24	3.70	3.63	59	98.1
E	45	24	3.82	3.65	54	95.4
F	43	24	3.86	3.69	55	95.4
G	46	26	3.70	3.72	57	100.5
H	43	24	3.73	3.65	57	97.8
I	43	26	3.73	3.60	60	96.5
J	44	26	3.69	3.44	60	93.2
K	46	26	3.71	3.62	57	97.8
L	43	24	3.72	3.62	55	97.3
M	44	26	3.70	3.62	60	98.0

6.3.1 Baseline formulation (samples A – C)

Scanning electron microscopy – energy dispersive X-ray (SEM-EDX) analysis and powder X-ray diffraction (XRD) confirmed zirconolite ($CaZrTi_2O_7$) as the major crystalline phase with minor phases; zircon ($ZrSiO_4$), rutile (TiO_2), baddeleyite (ZrO_2) and ceria (CeO_2) common to all three samples (PDF cards: 04-007-6895, 00-006-0266, 04-008-7849, 00-013-0307, 04-014-5421, respectively). XRD analysis also identified sphene ($CaTiSiO_5$) and a perovskite phase (nominally ABO_3) in samples B and C and albite ($NaAlSi_3O_8$) in sample A (PDF cards: 01-076-6020, 01-077-8911, 01-083-1605, respectively). The formation of albite was a result of the extra Al_2O_3 added for charge compensation within the zirconolite phase. Unreacted Al_2O_3 crystals were also observed in sample A using SEM.

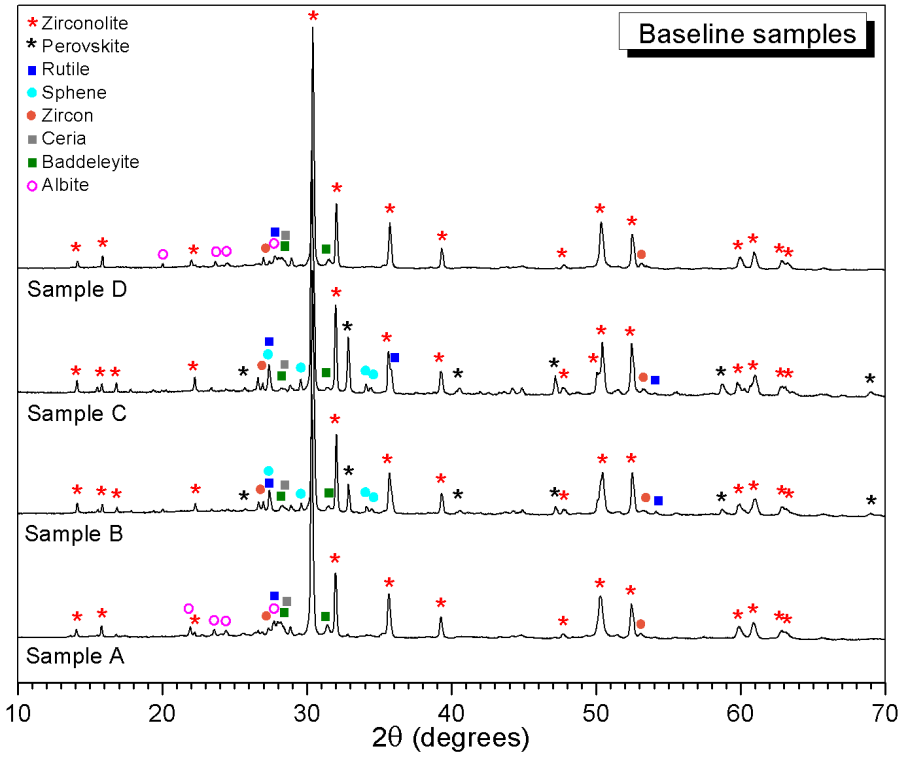

Figure 6.1: XRD data for samples A – C confirmed zirconolite as the major crystalline phase and the formation of perovskite when targeting Zr-substitution (samples B and C).

SEM-EDX revealed ZrO_2 was present at the centre of some zirconolite crystals (Figure 6.2). This observation, coupled with the presence of Al_2O_3 and small amounts of TiO_2, was indicative of an incomplete reaction. This was likely to be a result of slower kinetics caused by the added Al_2O_3, which would have increased the melt viscosity [230]. SEM-EDX analysis

revealed some Ce incorporation into the ceramic phase but CeO_2 hotspots indicated full digestion had not been achieved. The size of the CeO_2 hotspots was indicative of the starting material particle size, which implied its presence in the final products was a result of insufficient milling. To investigate this further, sample D, a repeat sample of formulation A, was prepared and milled in a larger (250 ml volume) mill pot. The larger diameter generates larger forces during milling resulting in better homogenisation of the powders. As a result, sample D obtained far better digestion of the waste analogue, with only minor spots of residual CeO_2 observed. A slightly smaller grain size was attained but the overall microstructure was in excellent agreement with sample A. Figure 6.1 and Figure 6.3 compare samples A and D and show no other changes to the crystalline phase assemblage or final microstructure as a result of the different milling parameters. It was therefore concluded to use the larger mill pot for the redox controlled samples to maximise waste digestion.

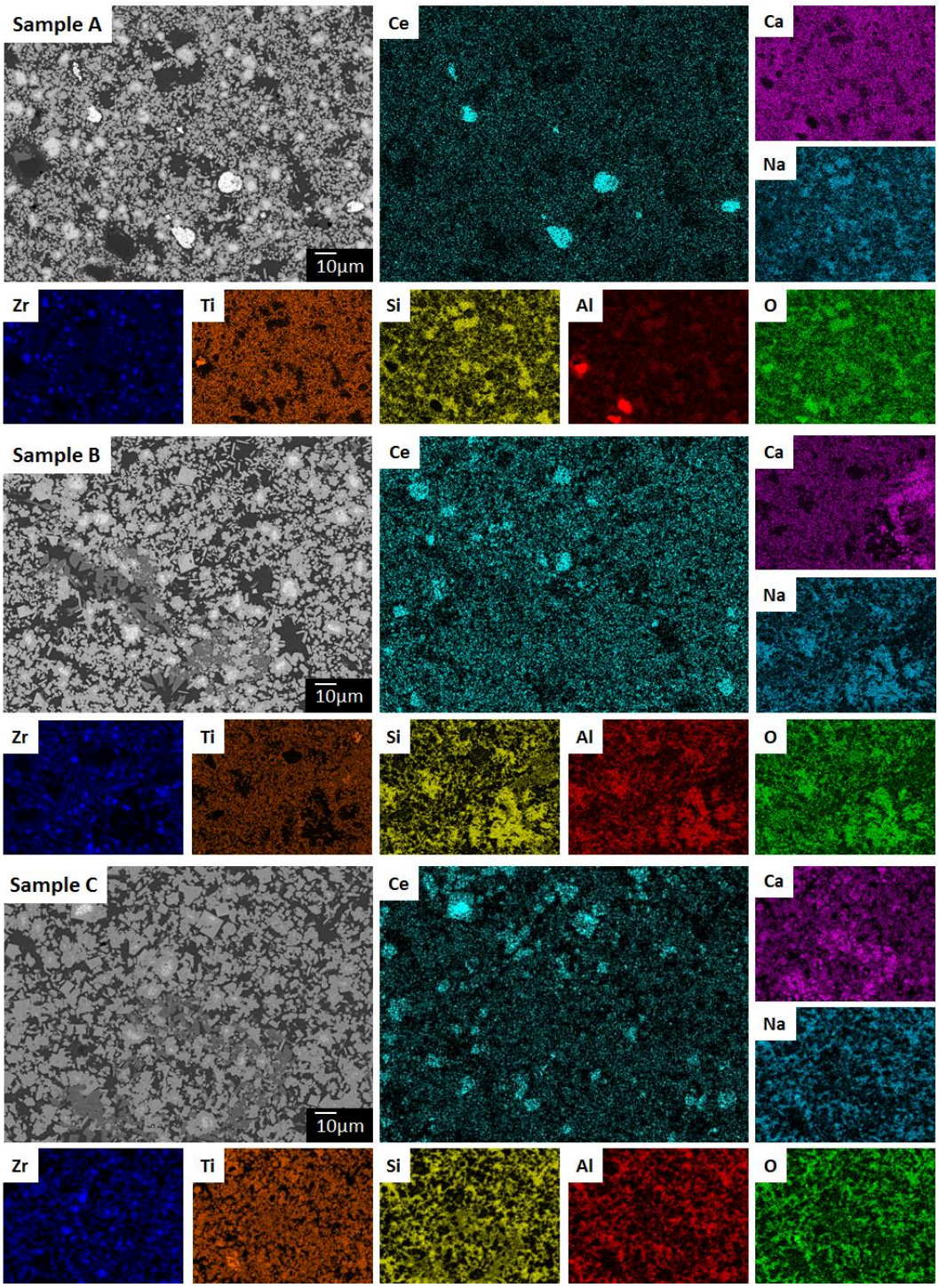

Figure 6.2: SEM-EDX showing the Ce distribution in samples A – C. The secondary Ce-bearing perovskite phase is evident in sample B and more so in sample C. The morphology of the perovskite crystals appear to be larger and more rectangular than the zirconolite crystals.

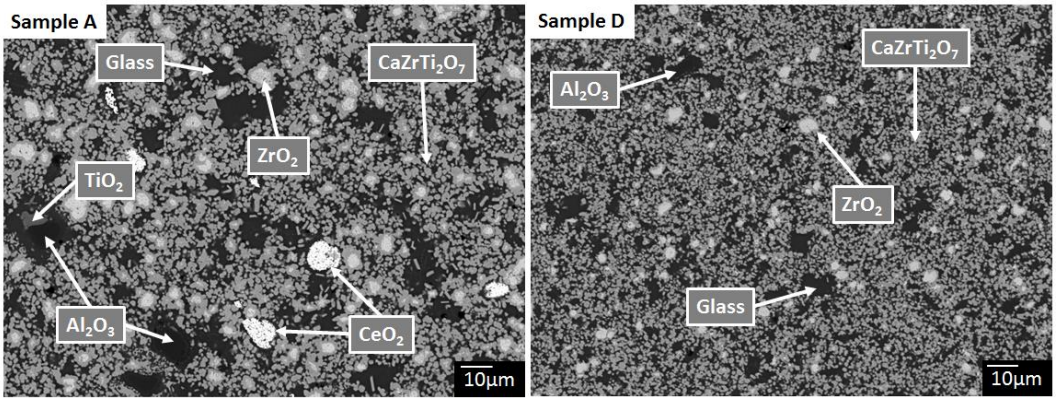

Figure 6.3: BSE micrographs of samples A and D comparing the effect of milling on the incorporation of CeO_2 into the glass-ceramic structure. No CeO_2 hotspots were observed in sample D.

A second Ce-bearing phase was observed by SEM-EDX in samples B and C. The abundance of this Ce-rich phase was more prominent in sample C and it was not seen in sample A. Coupled with the XRD data, this phase was identified as a perovskite ($(Ca,Ce)(Ti,Al)O_3$) and implied some Ce^{4+} was reduced to Ce^{3+} [238]. Perovskite readily accommodates Ce^{3+} into its structure, whereby, its ionic radii is equal to the size of the Ca^{2+} lattice site [93]. The absence of perovskite in sample A showed Al_2O_3 acted as a sufficient charge compensator and facilitated the incorporation of Ce^{4+} in the zirconolite phase. The perovskite phase in samples B and C was found be more abundant towards the edge of the sample, whilst residual CeO_2 was more abundant towards the centre (Figure 6.4). Coupled with a visible colour gradient through the HIP canisters, this highlighted the reducing effect the canister walls had on the CeO_2. The transition of Ce^{4+} to Ce^{3+} is coupled with a colour change from yellow to a brick red, thus the colour gradient through the HIP canister indicated more Ce^{3+} towards the edge of the canister [239]. This was investigated further using Ce L_3 XANES, which is discussed below.

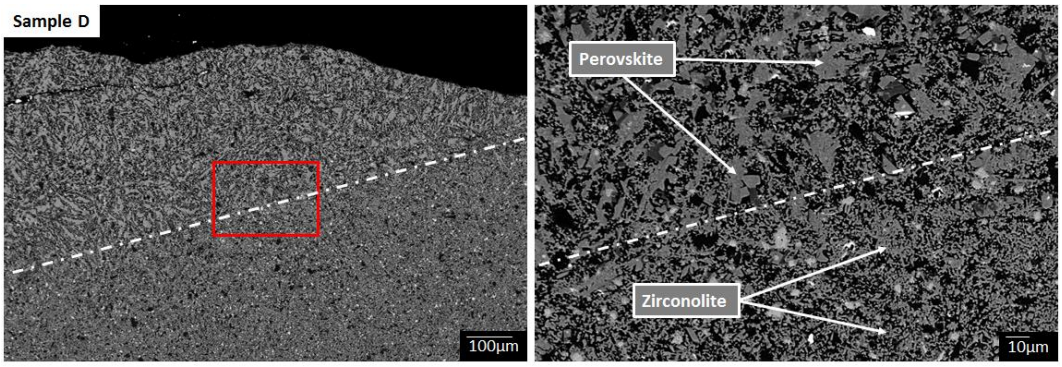

Figure 6.4: BSE micrographs showing the change in microstructure between the canister interface region and the bulk glass-ceramic.

Analysis of the SEM-EDX data for the glass, zirconolite and perovskite phases allowed for semi-quantitative analysis of the elemental distribution between phases. As shown in Figure 6.2, the Ce was preferentially incorporated into the ceramic phases. The SEM-EDX spectra in Figure 6.5 were averaged over 10 points at x3000 magnification for each phase in each sample. Sample A, $Ca_{0.8}Ce_{0.2}ZrTi_{1.6}Al_{0.4}O_7$, had a Ce partitioning ratio of 100 : 2 between the zirconolite and glass phase. This was in excellent agreement with the partitioning ratios reported in the literature [17]. In comparison, samples B and C had ratios of 100 : 13 and 100 : 10, zirconolite to glass, respectively. Whilst the Ce was still preferentially incorporated into the zirconolite phase, a factor of five increase of Ce in the glass was a direct result of Ce^{4+} reduction to Ce^{3+} [240]. When considering the perovskite phase as well, 80 % of the Ce was associated with the secondary phase and only 2 – 4 % was associated with the glass (sample B; 100 : 21.5 : 4 perovskite : zirconolite : glass, sample C; 100 : 23.4 : 2.4 perovskite : zirconolite : glass). That said, the relative abundance of the perovskite was very low compared to the presence of zirconolite, thus the overall majority of the Ce was present in the target zirconolite phase. It is promising that with sufficient charge compensation the reduction of Ce can be controlled and the amount of Ce in the glass can be minimised, as demonstrated by sample A.

In conjunction to the above SEM-EDX data that was collected at the University of Sheffield (UoS) on a Hitatchi TM3030, the zirconolite, perovskite and glass phases were also analysed on a more precise Zeiss Ultraplus SEM at ANSTO for more accurate quantitative analysis. These data, summarised in Table 6.3, showed the zirconolite : glass Ce partitioning was higher in all three compositions than the readings collected at UoS. In sample A, no Ce was

detected in the glass phase indicating a 100 % partitioning of the incorporated CeO_2 in the zirconolite phase. For samples B and C, the Ce signal in the glass was again lower with zirconolite : glass ratios; 100 : 8 and 100 : 4, respectively. Whilst both sets of data were in agreement and showed the same trends across the samples, the variation between the two sets of data highlights the error associated with this analysis on multiphase systems with such small grain sizes.

The approximate compositions of the zirconolite phase in samples A – C were found to be $Ca_{0.78(3)}Ce_{0.17(3)}Zr_{1.00(9)}Ti_{1.82(5)}Al_{0.18(2)}O_{7.00(2)}$, $Ca_{0.83(2)}Ce_{0.16(1)}Zr_{1.00(1)}Ti_{2.01(3)}Al_{0.07(1)}O_{7.00(1)}$ and $Ca_{0.85(3)}Ce_{0.15(2)}Zr_{1.00(4)}Ti_{2.01(4)}Al_{0.08(1)}O_{7.00(1)}$, respectively. Interestingly, all three compositions imply Ca site substitution despite samples B and C targeting Zr substitution. Valence state calculations, summarised in Table 6.4, assumed that Ce was the cation most likely to undergo reduction, due to the low oxygen potential required to reduce Ti and because Ca, Zr, Na, Al and Si only occupy single valance states, except under extremely reducing conditions [241,242]. The valence state calculations suggested Ce^{4+} was incorporated into the zirconolite phase in sample A, with a small amount of Ce^{3+}. Charge compensation in this sample was provided by Al^{3+} substitution on the Ti-sites, as targeted by the starting formulation. Samples B and C, however, seemed to incorporate Ce^{3+} only, with subsequent charge compensation provided by the reduction of Ti^{4+} to Ti^{3+}. Within the baseline samples, no reducing agents were included to generate a reducing atmosphere during HIPing, thus it cannot be known, at this point, whether the atmosphere inside the canister was substantial enough to reduce the Ce and Ti. Due to Ca, Zr, Na, Al and Si only having single valence states (expect under extreme conditions) and Ti only reducing at low oxygen pressures, it was assumed that Ce was the cation most likely to undergo reduction. This assumption was used in the valence state calculations.

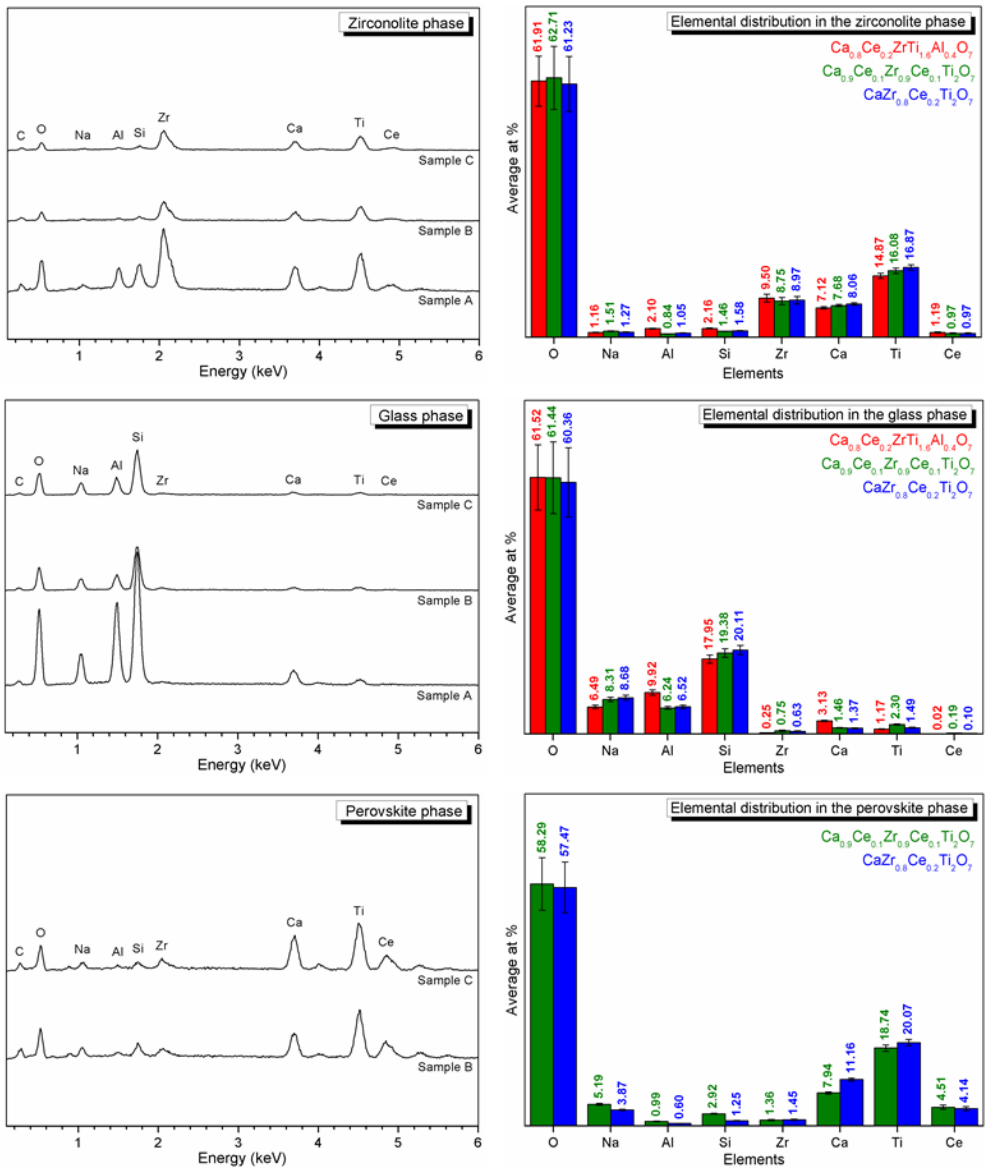

Figure 6.5: SEM-EDX spectra comparing the elemental distributions in the zirconolite, glass and perovskite phases in samples A in red, B in green and C in blue. Collected at UoS on a Hitatchi TM3030.

Table 6.3: Final stoichiometric compositions and partitioning ratios of Ce between the zirconolite (Z), glass (G) and perovskite (P) phases in samples A – C, calculated from SEM-EDX data collected at ANSTO on a Zeiss Ultraplus SEM.

	Final Stoichiometric compositions ANSTO data
Sample A	$Ca_{0.78(3)}Ce_{0.17(3)}Zr_{1.00(9)}Ti_{1.82(5)}Al_{0.18(2)}O_{7(2)}$
Sample B	$Ca_{0.83(2)}Ce_{0.16(1)}Zr_{1.00(1)}Ti_{2.01(3)}Al_{0.07(1)}O_{7(1)}$
Sample C	$Ca_{0.85(3)}Ce_{0.15(2)}Zr_{1.00-(4)}Ti_{2.01(4)}Al_{0.08(1)}O_{7(1)}$

Sample		Raw EDX data			Ratio Z : G	Ratio Z : G : P
		Zirconolite	Glass	Perovskite		
ANSTO Data	A	1.58	0.00		100 : 0	
	B	1.42	0.11	7.15	100 : 8	19 : 1 : 100
	C	1.30	0.05	4.47	100 : 4	29 : 1 : 100

Table 6.4: Valence checks for charge neutrality for the calculated stoichiometric zirconolite compositions in samples A – C.

Sample	Ca^{2+}	Ce^{4+}	Ce^{3+}	Zr^{4+}	Ti^{4+}	Ti^{3+}	Al^{3+}	O^{2-}	Valence check
A	**0.78**	**0.17**		**1.00**	**1.82**		**0.18**	**7.00**	
Charge balance	1.56	0.68		4.00	7.28		0.54	-14.00	0.06
	0.78	**0.11**	**0.06**	**1.00**	**1.82**		**0.18**	**7.00**	
Charge balance	1.56	0.44	0.18	4.00	7.28		0.54	-14.00	0
B	**0.83**	**0.16**		**1.00**	**2.01**		**0.07**	**7.00**	
Charge balance	1.66	0.64		4.00	8.04		0.21	-14.00	0.55
	0.83	**0.00**	**0.16**	**1.00**	**1.62**	**0.39**	**0.07**	**7.00**	
Charge balance	1.66	0.00	0.48	4.00	6.48	1.17	0.21	-14.00	0
C	**0.85**	**0.15**		**1.00**	**2.01**		**0.08**	**7.00**	
Charge balance	1.70	0.60		4.00	8.04		0.24	-14.00	0.58
	0.85	**0.00**	**0.15**	**1.00**	**1.58**	**0.43**	**0.08**	**7.00**	
	1.70	0.00	0.45	4.00	6.32	1.29	0.24	-14.00	0

Ce L_3 XANES data were collected for samples A – C to investigate the speciation of the Ce within the glass-ceramics. Figure 6.6 compares the bulk representative sample data against two Ce standards; $CePO_4$ as the Ce^{3+} standard and CeO_2 as the Ce^{4+} standard. All data demonstrated features characteristic of Ce^{3+} and Ce^{4+} signals and confirmed the presence of both oxidation states. The percentage of Ce^{3+} : Ce^{4+} in each sample was determined by linear combination fitting of the XANES data in Figure 6.6 against multiple Ce standards. These bulk

representative percentages are given as a bar chart in Figure 6.8 and confirmed sample A retained the highest amount of Ce^{4+}. Some of the Ce^{4+} signal corresponded to residual CeO_2 but also showed that Al_2O_3 acted as a sufficient charge compensator and inhibited Ce^{4+} reduction. The Ce^{3+} : Ce^{4+} percentages confirmed that sample C had the lowest amount of Ce^{4+} and was in agreement with the XRD and SEM data, such that, more Ce^{3+} promoted more perovskite to form. Due to the residual CeO_2 present in all samples, it was not possible to quantify the Ce^{4+} signal from the zirconolite phase. As a result, verfication of the Ce^{3+} and Ce^{4+} contributions in the SEM-EDX compositional data was not possible, but qualitatively the SEM-EDX and Ce L_3 XANES data were in agreement.

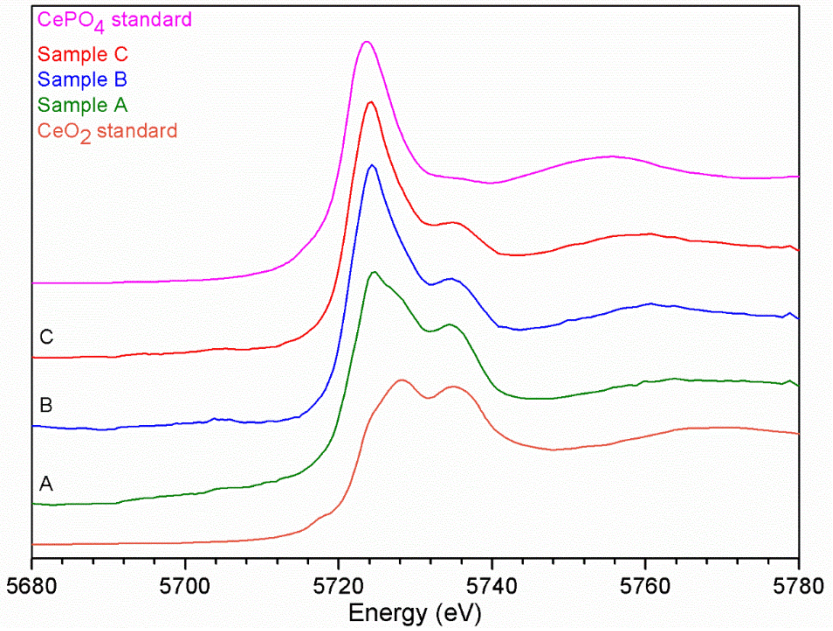

Figure 6.6: Ce L_3 XANES data for samples A – C compared against standards $CePO_4$ (Ce^{3+}) and CeO_2 (Ce^{4+}).

Monolithic cross-sections of the glass-ceramic HIP samples were also analysed by Ce L_3 XANES, to investigate the percentage of Ce^{3+} : Ce^{4+} with respect to distance from the centre of the canister. The cross-section samples were measured in increments from the centre to the edge, as demonstrated schematically in Figure 6.7. The plots in Figure 6.8 show the evolution of the Ce^{3+} : Ce^{4+} percentages through the samples. These plots confirm a gradual increase in Ce^{3+} towards the edge of the canister as a result of the reducing environment generated by the canister walls. Whilst this trend was seen in all three samples, sample C had a higher Ce^{3+} content throughout compared to samples A and B. At the edge, samples A and B had 75 % ($\pm$10 %) and 76 % ($\pm$10 %) Ce^{3+}, respectively, however sample C had 94 %

(±10 %). This implies that the reduction of Ce^{4+} is not solely due to the reducing effect of the canister walls, but that the glass-ceramic formulation ($CaZr_{0.8}Ce_{0.2}Ti_2O_7$) facilitated the further reduction.

The bulk representative data for the Ce^{3+} : Ce^{4+} percentages, shown in Figure 6.8, shows approximately 20 % less Ce^{4+} in sample B than sample A. However, the centre to edge progression data for samples A and B do not show this variation. This analysis was sensitive to experimental disparities and due to the size of the canisters, a slight deviation from the centre of the canister where the cross-sections were taken, would have had a significant effect on the XANES outcome. Due to the difficulty of removing the samples from the canisters and the irregular shape of the internal sample, it was not always possible to mount the samples and extract the cross-sections from precisely the same central locations. That said, the cross-sections were prepared from as close to the centre as practically possible to minimise this error.

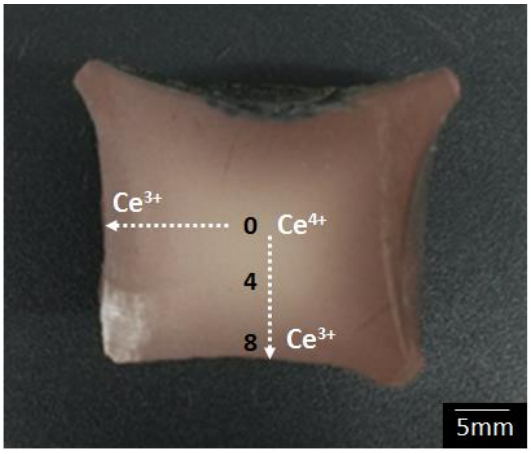

Figure 6.7: Cross-section of a HIPed sample showing the colour gradient towards the centre of the sample as a result of the reducing effect caused by the HIP canister walls. The schematic shows the progression of the XANES measurements taken from the edge to the centre of the sample to investigate the evolution of the Ce^{3+} : Ce^{4+} percentage.

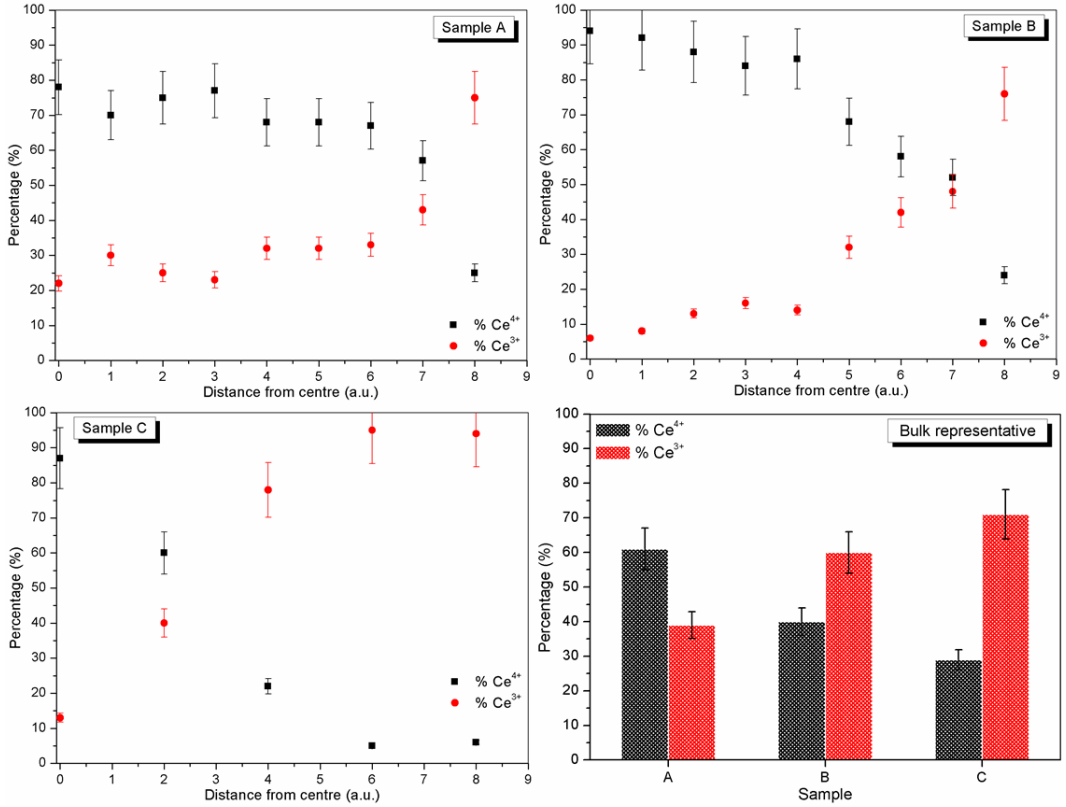

Figure 6.8: Plots show the percentage of Ce^{3+} : Ce^{4+} for samples A – C with respect to distance from the centre of the HIP canisters, measured across monolith cross-sections. The bulk representative data was calculated from transmission data collected on bulk powder samples.

6.3.2 Effect of redox control (samples E – G)

Ni powder was added to the calcined batches to control internal oxygen fugacity. The overall phase assemblage and microstructure remained largely the same as the baseline formulations, with a few minor differences. The redox controlled samples were milled in the 250 ml volume mill pot and therefore achieved better CeO_2 digestion throughout. Whilst the phase assemblages were in agreement, the redox samples demonstrated less sphene and ZrO_2, implying better kinetics during consolidation.

Large Ni particles were still present in the glass-ceramics confirming the Ni powder remained an active redox agent throughout consolidation. In sample E, $Ca_{0.8}Ce_{0.2}ZrTi_{1.6}Al_{0.4}O_7$, the smaller Ni particles appeared to react with the additional Al_2O_3 to produce what was thought to be a spinel phase around Al_2O_3 particles. This conclusion was based on the SEM-EDX ratios

of Ni and Al, which gave a ratio indicative of a $NiAl_2O_4$ spinel phase. This spinel phase was not detected by XRD and SEM-EDX analysis confirmed it was not associated with Ce. Its presence as a minor phase was not considered to be problematic and it did not inhibit the incorporation of CeO_2 into the glass-ceramic.

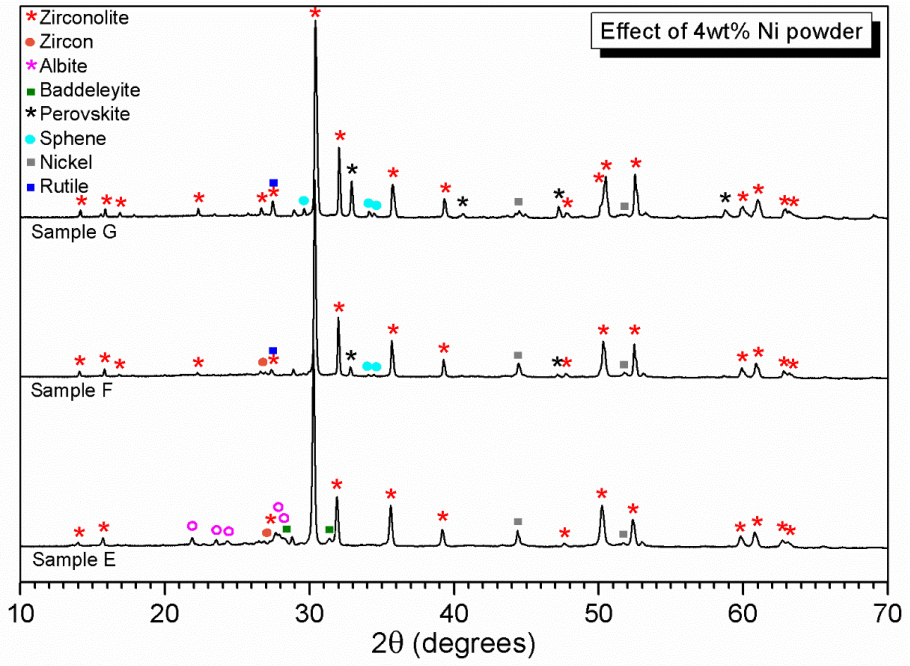

Figure 6.9: XRD data for the redox controlled samples E – G. Minor phases, sphene and baddeleyite were less abundant compared to the baseline formulation samples, but the same trend of increased perovskite abundance when targeting Zr substitution was observed.

In agreement with the baseline formulation samples, the formation of Ce-bearing perovskite occurred when targeting Zr substitution (samples F and G) although appeared to be less abundant in the BSE micrographs than samples B and C. Again, the perovskite phase was identifiable as large rectangular crystals distributed amongst the smaller zirconolite crystals. Figure 6.10 compares the microstructures of samples E – G against each equivalent baseline sample, A – C, whilst Figure 6.11 and Figure 6.12 display the EDX elemental distributions. Compositional analysis of the SEM-EDX data again confirmed preferential incorporation of Ce into the ceramic phases. The reducing conditions, caused by the Ni powder, resulted in the detection of more Ce in the glass phase for all formulations. The zirconolite : glass ratios were; 100 : 20, 100 : 15 and 100 : 27 for samples E, F and G, respectively.

Again, the SEM-EDX data was repeated on the Zeiss Ultraplus SEM with similar results to the baseline samples. The calculated partitioning ratios of the three samples were again higher than the initial data and showed sample E achieved the best separation of Ce into the zirconolite phase compared to samples F and G; 100 : 2, 100 : 9, 100 : 9, respectively. The measured compositions were consistent across all three samples and again showed Ca site substitutions; $Ca_{0.73(4)}Ce_{0.21(1)}Zr_{1.27(7)}Ti_{1.89(7)}Al_{0.11(1)}O_{7.00(4)}$, $Ca_{0.75(6)}Ce_{0.18(2)}Zr_{1.12(10)}Ti_{1.94(15)}Al_{0.06(1)}$-$O_{7.00(4)}$, $Ca_{0.74(1)}Ce_{0.19(4)}Zr_{1.01(6)}Ti_{1.93(4)}Al_{0.07(1)}O_{7.00(5)}$, samples E – G respectively (shown in Table 6.5 and Table 6.6). When considering valence states, the measured compositions suggest Ce^{3+} incorporation in all samples, with some Al^{3+} incorporation and Ti reduction for charge compensation. Some trace Ce was also detected in the sphene minor phase.

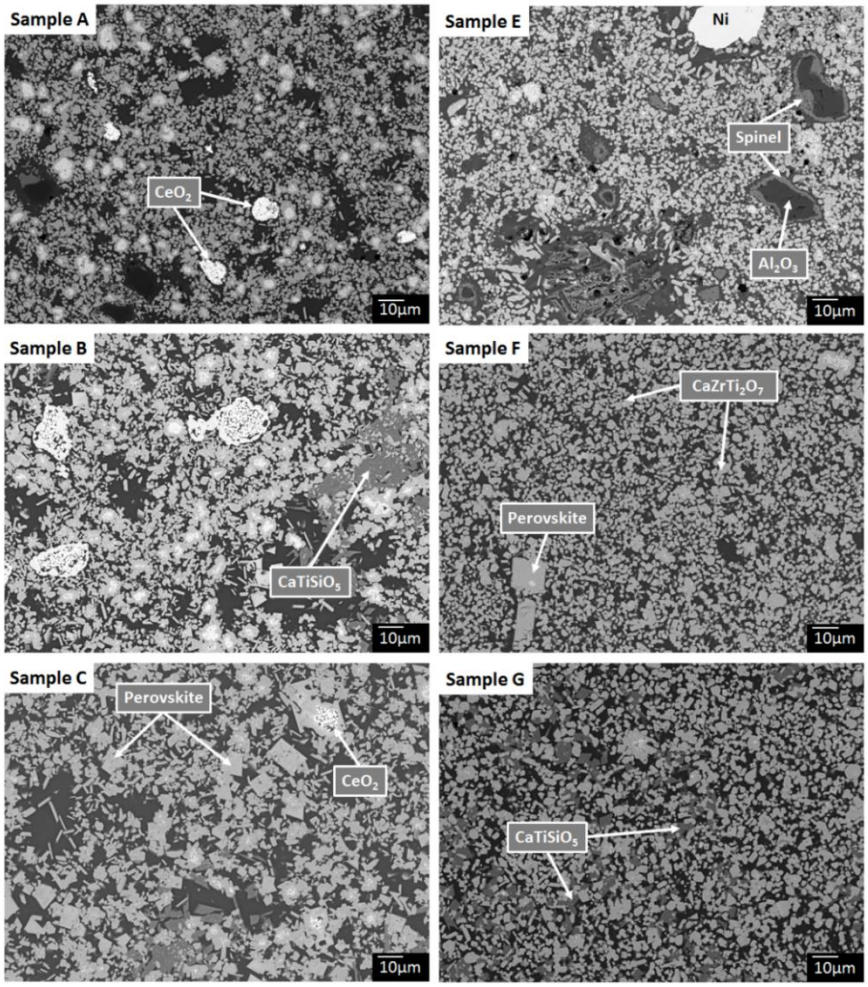

Figure 6.10: BSE micrographs of samples A – C and samples E – G comparing the microstructures with respect to target stoichiometry and effect of Ni powder additions.

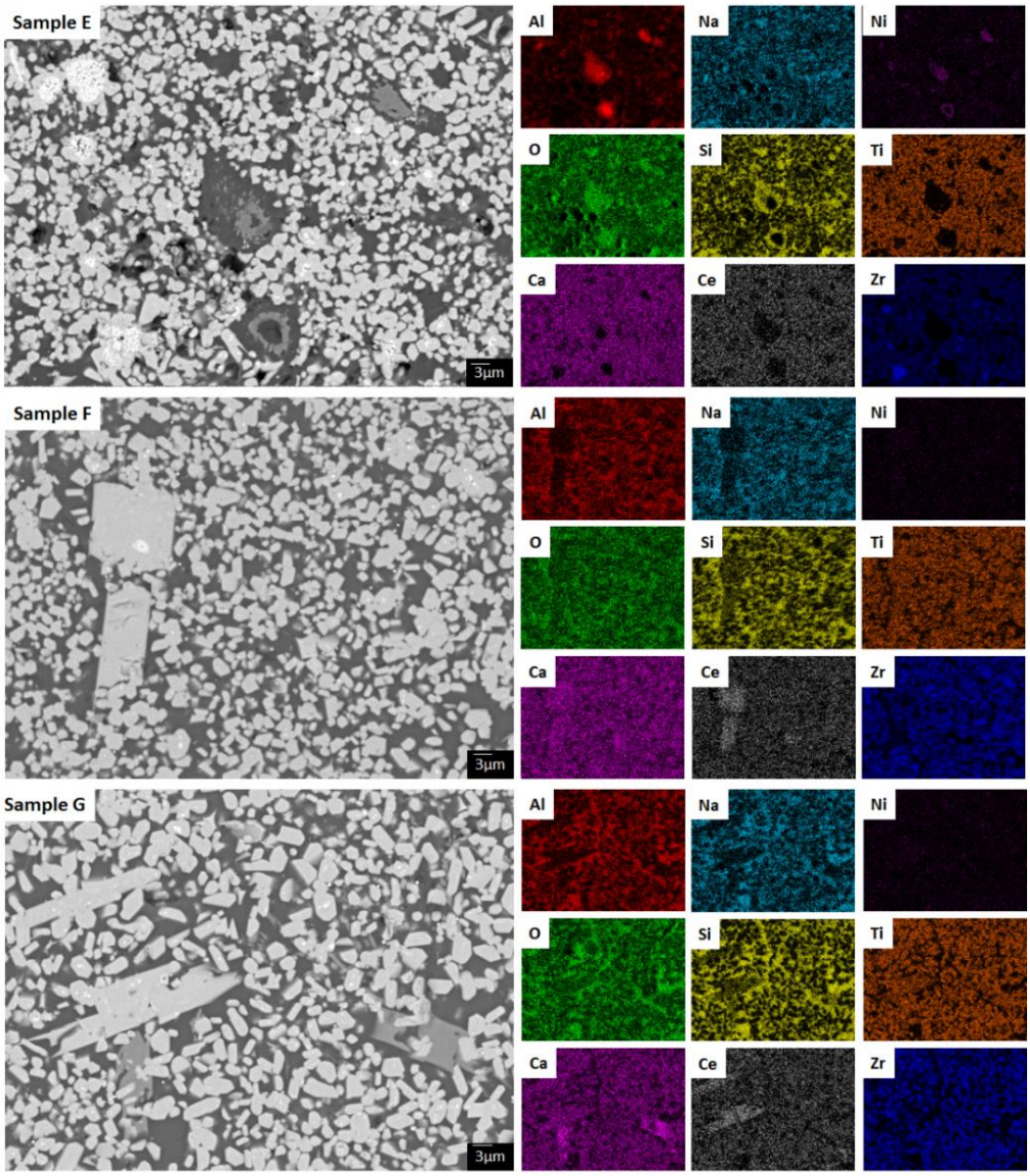

Figure 6.11: SEM-EDX maps for redox controlled samples E – G.

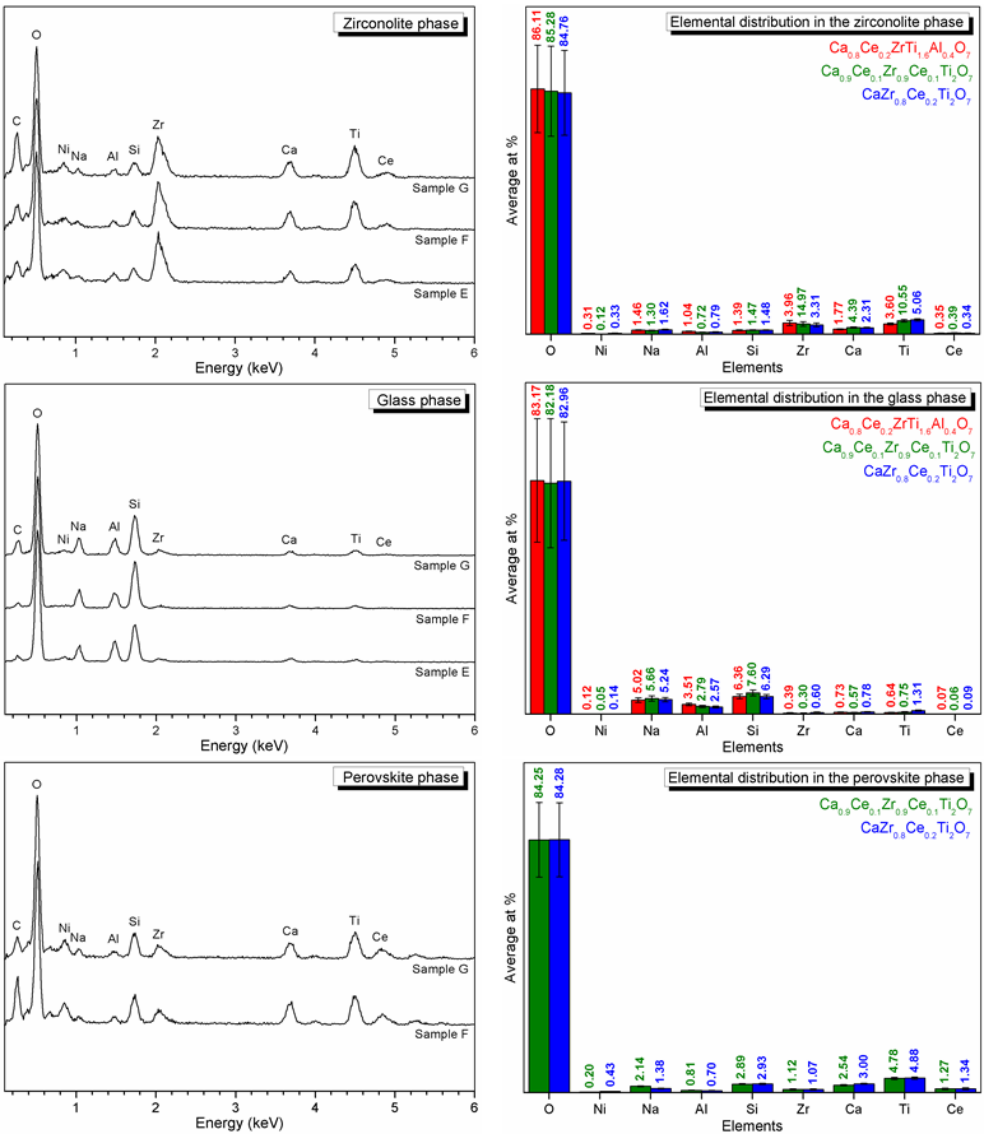

Figure 6.12: SEM-EDX spectra comparing the elemental distributions in the zirconolite, glass and perovskite phases in samples E in red, F in green and G in blue.

Table 6.5: Final stoichiometric compositions and partitioning ratios of Ce between the zirconolite (Z), glass (G) and perovskite (P) phases in samples E – G, calculated from SEM-EDX data collected at ANSTO on a Zeiss Ultraplus SEM.

	Final Stoichiometric compositions ANSTO data
Sample E	$Ca_{0.73(4)}Ce_{0.21(1)}Zr_{1.27(7)}Ti_{1.89(7)}Al_{0.11(1)}O_{7.00(4)}$
Sample F	$Ca_{0.75(6)}Ce_{0.18(2)}Zr_{1.12(10)}Ti_{1.94(15)}Al_{0.06(1)}O_{7.00(4)}$
Sample G	$Ca_{0.74(1)}Ce_{0.19(4)}Zr_{1.01(6)}Ti_{1.93(4)}Al_{0.07(1)}O_{7.00(5)}$

Sample		Raw EDX data			Ratio Z : G	Ratio Z : G : P
		Zirconolite	Glass	Perovskite		
ANSTO Data	E	1.74	0.03		100 : 2	
	F	1.64	0.14	6.82	100 : 9	24 : 3 : 100
	G	1.74	0.15	4.96	100 : 9	35: 3 : 100

Table 6.6: Valence checks for charge neutrality of the calculated stoichiometric zirconolite compositions in samples E – G.

Sample	Ca^{2+}	Ce^{4+}	Ce^{3+}	Zr^{4+}	Ti^{4+}	Ti^{3+}	Al^{3+}	O^{2-}	Valence check
E	**0.73**	**0.21**		**1.27**	**1.89**		**0.11**	**7.00**	
Charge balance	1.46	0.84		5.08	7.56		0.33	-14.00	1.27
	0.73		**0.21**	**1.27**	**0.83**	**1.06**	**0.11**	**7.00**	
Charge balance	1.46		0.63	5.08	3.32	3.18	0.33	-14.00	0
F	**0.75**	**0.18**		**1.12**	**1.94**		**0.06**	**7.00**	
Charge balance	1.50	0.72		4.48	7.76		0.18	-14.00	0.64
	0.75		**0.18**	**1.12**	**1.48**	**0.46**	**0.06**	**7.00**	
Charge balance	1.50		0.54	4.48	5.92	1.38	0.18	-14.00	0
G	**0.74**	**0.19**		**1.01**	**1.93**		**0.07**	**7.00**	
Charge balance	1.48	0.76		4.04	7.72		0.21	-14.00	0.21
	0.74		**0.19**	**1.01**	**1.91**	**0.02**	**0.07**	**7.00**	
	1.48		0.57	4.04	7.64	0.06	0.21	-14.00	0

6.3.3 Effect of CaF_2 addition (samples H – M)

To investigate the effectiveness of CaF_2 as a digesting agent, 0.6 wt. % was added to the baseline formulations. 0.6 wt. % CaF_2 was added to be consistent with previous work and to draw a comparison [154]. Additionally, samples were also produced with 0.3 wt. % addition,

with the aim of minimising the CaF_2 concentration and reduce the ^{19}F neutron source term for (α,n)-reactions to occur, as was discussed in section *6.1*.

The XRD data for each formulation were consistent with the baseline equivalents and confirmed that the CaF_2 additions did not affect the crystalline phase assemblage. Zirconolite was the major crystalline phase for all samples with each formulation yielding the same minor phases as the baseline samples; perovskite $(Ca,Ce)(Ti,Al)O_3$), rutile (TiO_2) and baddeleyite (ZrO_2) were present in all samples, whilst albite ($NaAlSi_3O_8$) was identified in samples J and K and sphene ($CaTiSiO_5$) was present in samples L and M. Figures 6.13, 6.14 and 6.15 show the XRD data for each formulation comparatively with the baseline samples.

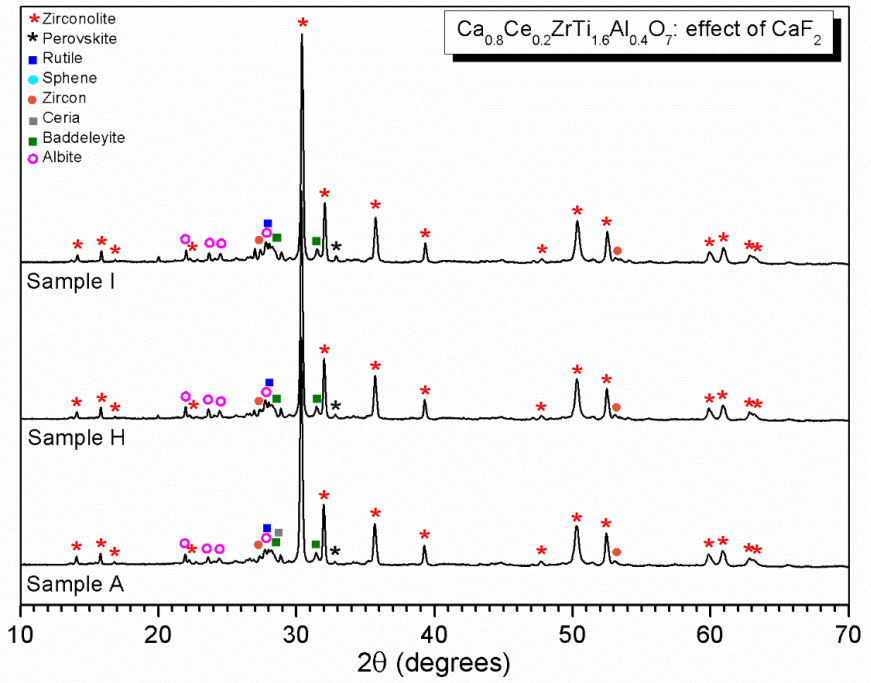

Figure 6.13: XRD plot showing the effect of CaF_2 additions to baseline formulation $Ca_{0.8}Ce_{0.2}ZrTi_{1.6}Al_{0.4}O_7$. Sample A: no CaF_2, Sample H: 0.6 wt. % CaF_2, Sample I: 0.3 wt. % CaF_2.

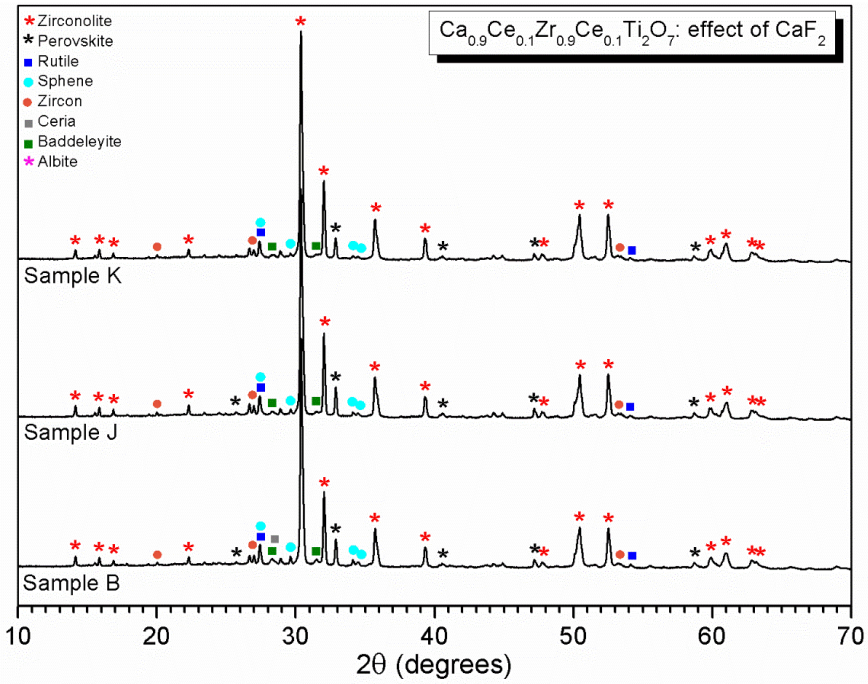

Figure 6.14: XRD plot showing the effect of CaF_2 additions to baseline formulation $Ca_{0.9}Ce_{0.1}Zr_{0.9}Ce_{0.1}Ti_2O_7$. Sample B: no CaF_2, Sample J: 0.6 wt. % CaF_2, Sample K: 0.3 wt. % CaF_2.

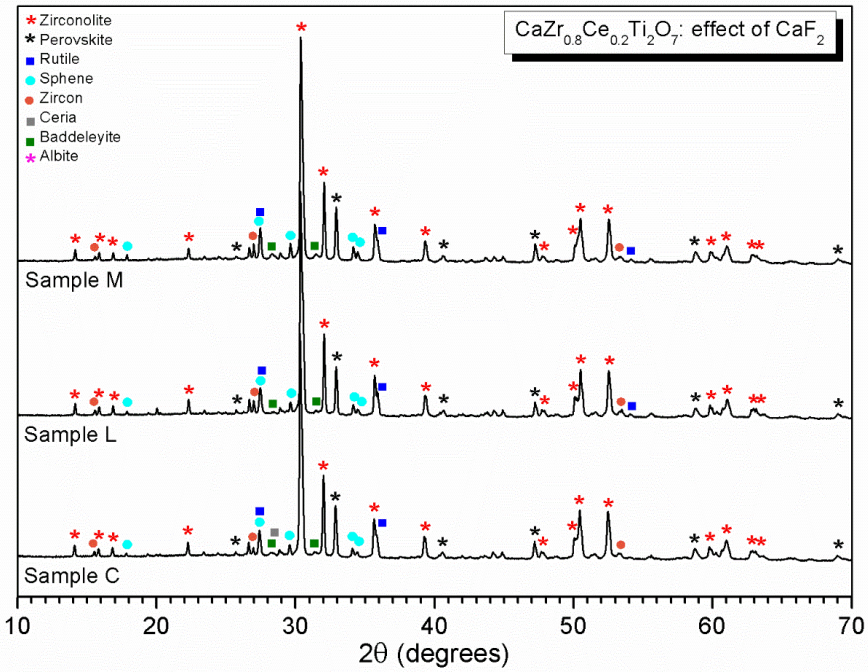

Figure 6.15: XRD plot showing the effect of CaF_2 additions on baseline formulation $CaZr_{0.8}Ce_{0.2}Ti_2O_7$. Sample C: no CaF_2, Sample L: 0.6 wt. % CaF_2, Sample M: 0.3 wt. % CaF_2.

Characterisation of the CaF_2 glass-ceramic samples by SEM-EDX confirmed the microstructures were congruent with the baseline equivalent samples, as shown in Figure 6.16, Figure 6.17 and Figure 6.18. No CeO_2 hotspots were observed, thus confirming better incorporation into the glass-ceramic. The 0.3 wt. % CaF_2 additions achieved the same level of CeO_2 incorporation as 0.6 wt. % CaF_2, which provided promising evidence that the (α,n) neutron source could be reduced, if not completely removed. No CaF_2 particles were observed.

Compositional SEM-EDX analysis was attempted but unfortunately due to the low concentrations, the ^{19}F signal could not be detected above the background, thus a full elemental suite could not be measured and accurate quantification could not take place.

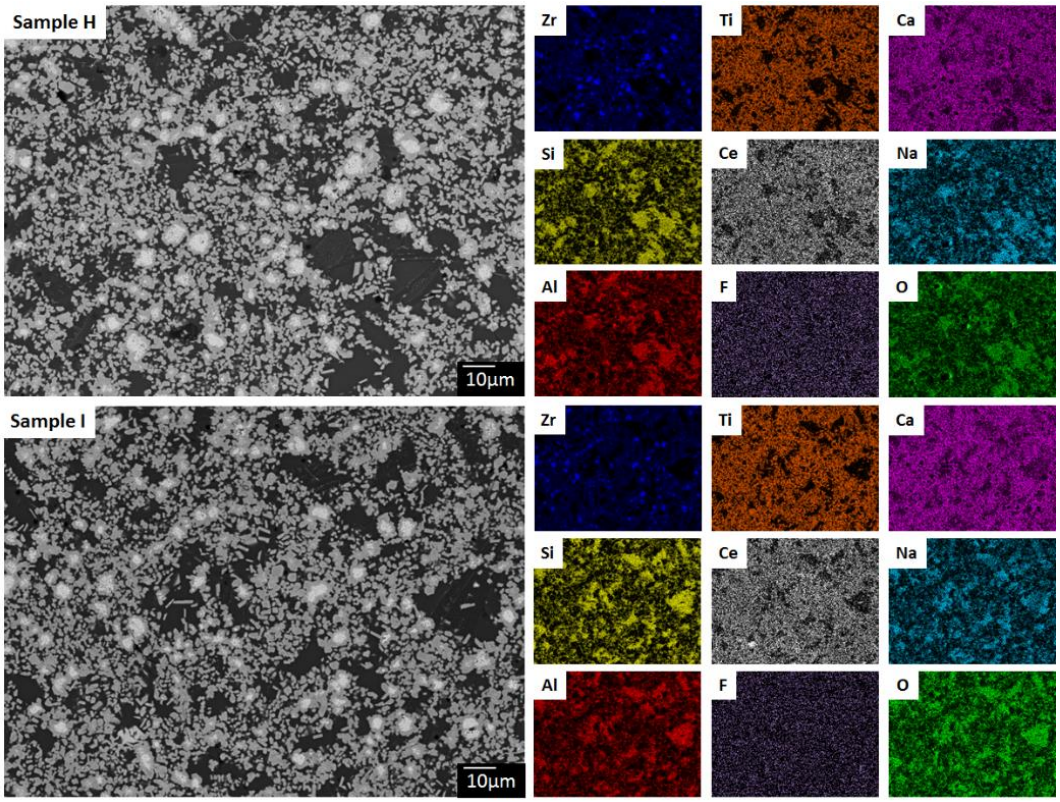

Figure 6.16: SEM-EDX maps for samples H and I: 0.6 wt. % and 0.3 wt. % CaF_2 additions to baseline formulation $Ca_{0.8}Ce_{0.2}ZrTi_{1.6}Al_{0.4}O_7$.

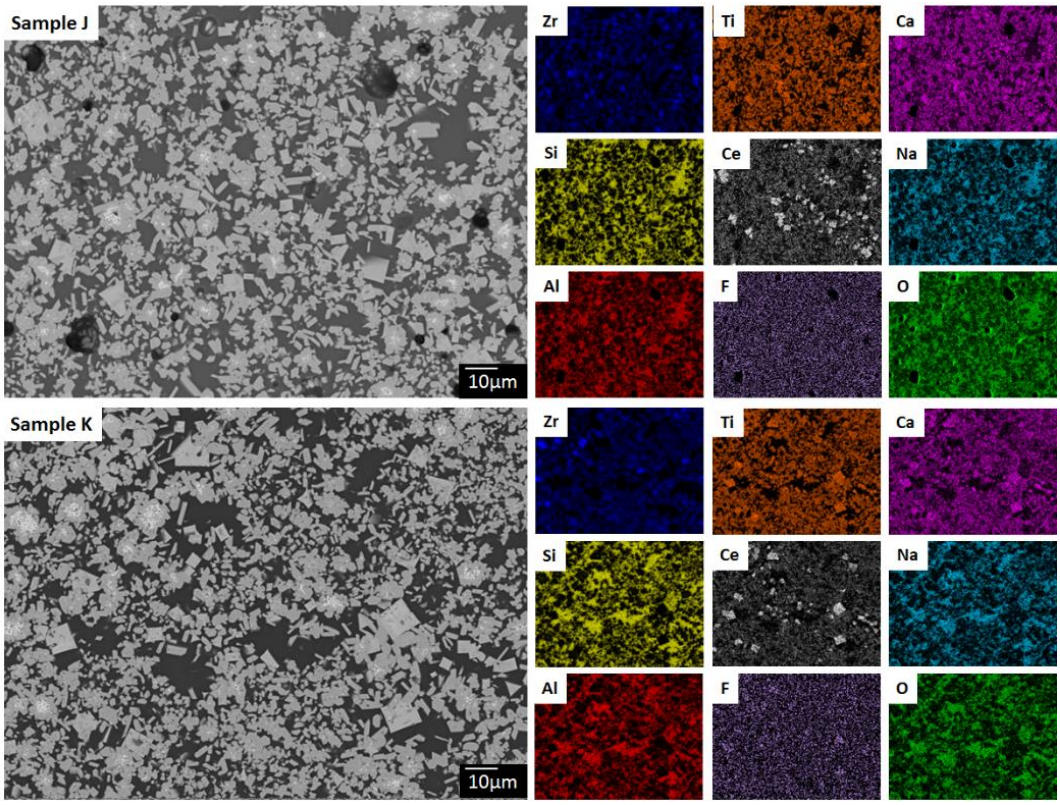

Figure 6.17: SEM-EDX maps for samples J and K: 0.6 wt. % and 0.3 wt. % CaF_2 additions to baseline formulation $Ca_{0.9}Ce_{0.1}Zr_{0.9}Ce_{0.1}Ti_2O_7$.

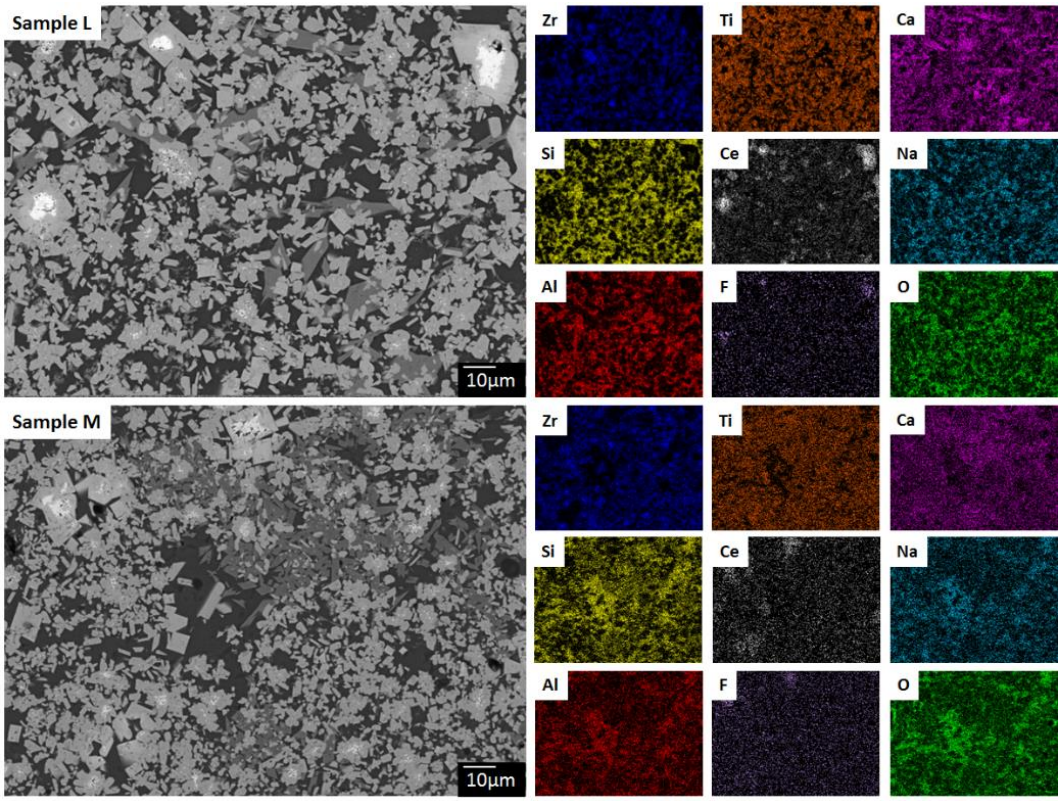

Figure 6.18: SEM-EDX maps for samples L and M: 0.6 wt. % and 0.3 wt. % CaF_2 additions to baseline formulation $CaZr_{0.8}Ce_{0.2}Ti_2O_7$.

6.4 Discussion

Effective Ce incorporation into the zirconolite phase of HIPed glass-ceramic wasteforms has been demonstrated. Whilst SEM-EDX evidenced that Ce was incorporated into the zirconolite phase, an accessory Ce-rich perovskite phase also formed. The formation of the Ce-bearing perovskite as a minor phase has been reported in the literature when incorporating both Ce and Pu into zirconolite full ceramics and glass-ceramics [106,97,108] and is known to readily accommodate Ce^{3+} into its structure [106,107]. Whilst perovskite is less durable than the target zirconolite phase, the formation of this phase is preferential over Ce^{3+} being incorporated into the glass phase. Perovskite has beneficial wasteform properties such as durability and radiation tolerance, thus is a superior host phase for actinides over the glass. Compared to the zirconolite the perovskite was Ce-rich, but its low abundance in all samples meant most of the Ce was incorporated in the target zirconolite phase.

To understand why perovskite forms we must first consider the zirconolite structure. Zirconolite-2M is the nominal monoclinic polytype and consists of parallel planes of Ca^{2+} and Zr^{4+} ions alternating with parallel planes of Ti^{4+} octahedra. The Ca^{2+} ions are in 8-fold co-ordination, the Zr^{4+} ions are in 7-fold co-ordination and the Ti^{4+} ions are in 5- and 6-fold co-ordination [89]. Actinides substitute for the Ca and / or Zr ions whilst charge compensation takes place on the partially filled Ti sites. The effective ionic radii of the Ca^{2+} and Zr^{4+} sites are summarised in Table 6.7, along with those for Ce^{3+}, Ce^{4+} and Pu^{4+} in each co-ordination [93].

Table 6.7: Ionic radii for different ions with respect to co-ordination number and oxidation states. Data highlighted with an asterisk are estimated based on linear interpolation.

Ion	Ionic Radii (Å)			
	12-fold	8-fold	7-fold	6-fold
Ce^{4+}	1.14	0.97	0.92*	0.87
Ce^{3+}	1.34	1.14	1.07	1.01
Pu^{4+}	-	0.96	0.91*	0.86
Ca^{2+}	1.34	1.12	1.06	1.00
Zr^{4+}	-	0.84	0.78	0.72

From the ionic radii data in Table 6.7, both Ce^{3+} and Ce^{4+} are smaller than (or almost equal to) the Ca ions in 8-fold co-ordination thus making their substitutions energetically favourable within the zirconolite structure. In comparison, the size mismatch between Ce^{3+} and Zr in 7-fold co-ordination is approximately 37 %, making this substitution very unfavourable. Although a better size match, Ce^{4+} is also slightly larger than the Zr site in zirconolite. For a larger ion to displace a smaller ion from its lattice site, an increase of the unit cell must be incurred. Such increases can lead to structural changes. Begg *et al.* investigated the incorporation of Ce^{3+} and Ce^{4+} in zirconolite full ceramics with respect to different sintering temperatures and atmospheric conditions [97]. Successful Ce incorporation on both the Ca and Zr sites was achieved, with a maximum loading in zirconolite-2M of 0.2 f.u. on the Ca site and 0.4 f.u. achieved on the Zr site. Increasing Ce substitution resulted in structural changes from zirconolite-2M to zirconolite-4M and to the pyrochlore structure. The level of Ce detected in the zirconolite phase in the samples discussed here, were no greater than 0.2 f.u. on the Ca-site, thus were in agreement with Begg *et al.*'s results that the zirconoite-2M structure was stabilised. The ionic size mis-match

between Ce^{4+} and the Zr lattice sites may have inhibited substitution of the Zr site, despite successful incorporation being reported in the literature [97,98,108].

A similar study by Meng *et al.* looked at Ce substitution on both Ca and Zr sites and also confirmed structural changes from zirconolite-2M to zirconolite-4M and to cubic pyrochlore with increasing Ce substitutions [108]. In both studies perovskite was also reported to form with increased substitutions or when heated under reducing conditions. The ionic radii of Ca^{2+} and Ce^{3+} ions in 12-fold co-ordination are equal making this substitution in the perovskite structure highly energetically favourable. Begg *et al.* stated that the instability of zirconolite was directly related to the stabilisation of perovskite when heated under reducing conditions [97]. This corresponds with the stabilisation of perovskite under the reducing conditions in the samples generated by the canister walls and Ni powder additions.

Baseline formulation A targeted Ce^{4+} substitution on the Ca site and whilst residual CeO_2 was seen, perovskite did not form in the bulk. The Ce L_3 XANES data revealed some Ce^{3+} was present but the lack of perovskite showed the Al_2O_3 acted as a sufficient charge compensator and successfully retained Ce^{4+}. Potentially, perovskite was present at the canister interface region due to the reducing effect of the canister walls, as was demonstrated in Figure 6.4 for baseline sample D that had the same starting formulation. The canister acts to reduce the partial oxygen pressure and promote Ce^{4+} reduction as was seen in the Ce L_3 XANES data. The reduced levels of Ca in baseline sample A may have discouraged perovskite formation, providing no excess to form the minor phase. This may also explain why the abundance of perovskite increased from sample B to C. Due to the Ca site substitution, samples B and C that targeted Zr substitution, had an excess of Ca in the system and subsequent Zr deficiency. Sample B targeted Ce^{3+} substitution on the Ca sites as well as the Zr sites within the zirconolite structure, which reduced the overall Ca excess and need for perovskite formation. It is possible that the formation of the perovskite occurred after the Ca solubility limit in the glass was reached, to accommodate the remaining excess and therefore promoted the reduction of Ce^{4+}.

The Ce L_3 XANES data confirmed the reduction of Ce^{4+} and revealed a strong correlation between the Ce oxidation state and the distance from the canister walls. At this small scale, HIP canisters are known to have a reducing effect on the sample and this was evident through

the change in microstructure at the interface [97,238,243], the colour gradient to the centre of the canister and the variation of Ce^{3+} : Ce^{4+} through the samples.

Due to the residual CeO_2 in the baseline samples and the mixed Ce^{3+} and Ce^{4+} signals in the XANES data, it was not possible to robustly determine the valence state of Ce in the zirconolite phase from the available data. The SEM-EDX data collected at ANSTO allowed for a more precise compositional analysis and from these data the valence state of Ce was approximated and appropriate charge compensation mechanisms were proposed. Baseline sample A was found to contain primarily Ce^{4+} with charge compensation provided by Al^{3+} substitution on the Ti site, as targeted by the starting formulation. Samples B and C contained Ce^{3+} with charge compensation provided primarily by the reduction of Ti^{4+}. These samples were targeted for self-charge compensation mechanisms by stoichiometric substitutions, however due to the preferential Ca site substitution of the Ce, an alternative mechanism was required. The reduction of Ti for charge compensation has been observed in the literature and is a potential mechanism in place within these samples [97,238]. Further analysis such as diffuse reflectance spectroscopy (DRS) could help determine whether or not Ti^{3+} is present within these samples.

Ce is commonly used as an analogue for Pu due to their similar ionic radii allowing them to be accommodated on the same lattice sites. However, Ce is known to have its limitations as an analogue due to its higher reduction potential than Pu [244]. Due to its lower redox potential, the reduction of Pu^{4+} will occur less readily. Begg *et al.* [106] studied the incorporation of Pu into zirconolite ceramics and reported that the Pu-doped zirconolite-2M structure transitioned to the zirconolite-4M structure and then to a pyrochlore structure with increasing dopant levels, as was observed with the Ce work discussed above [97]. Each structure was only stable for small ranges of dopant levels, with the Pu substitution limit in zirconolite-2M being 0.15 f.u. and Pu substitutions of 0.6 f.u. on the Zr site resulting in the pyrochlore structure. Begg *et al*. also observed the formation of perovskite with increasing Pu substitution. This implied the presence of trivalent Pu. Some Pu^{3+} should be expected when processing these glass-ceramic wasteforms but we have shown that it can be successfully incorporated into a durable ceramic phase preferentially over the amorphous glass phase. Similarly with controlled oxygen fugacity during consolidation the extent of Pu^{3+} present can be controlled and minimised.

6.4.1 Effect of Ni

Due to the small scale HIP canisters used, the reducing effect of the canister walls was highly prominent in the final samples. On a full scale canister (5 – 10 ltr) however, these effects would be minor compared to the bulk material in the canister. To try and mitigate against the effect of the canister for a more representative outcome, Ni powder was added during the packing of the canister. Alternatively, Ni canisters could have been utilised to eliminate the effects of the stainless steel canisters completely [100]. The presence of bright Ni hotspots in the SEM confirmed the Ni powder remained active throughout consolidation and there were no colour gradients through the final samples. In comparison to the baseline samples, the SEM-EDX revealed a slight increase of Ce in the glass phase. The Ni powder acted as a reducing agent during consolidation therefore promoted Ce^{4+} reduction to Ce^{3+}, which is more soluble within the glass phase [240]. In agreement with the baseline samples, the Al charge compensated sample did not form perovskite, despite the reducing conditions, however, there was again an increase in perovskite formation from sample B to C, when targeting the Zr site substitution. It was confirmed by SEM-EDX that the Ce was preferentially incorporated into the ceramic phases within all samples, despite the increased solubility in the glass phase. This is a promising result when considering the immobilisation of Pu-based waste-streams.

6.4.2 Effect of CaF_2

CaF_2 was originally present in some CaF_2 rich Pu-residue wastes. Although these wastes were later reclassified, CaF_2 was believed to aid waste digestion thus was incorporated as a precursor material in later formulations [82,143,147]. However, (α,n)-reactions are heavily associated with light elements such as ^{19}F, which acts as a neutron source [148]. When α-particles emitted from actinide decay come into contact with the nucleus of the ^{19}F ions, a high energy neutron is emitted. This neutron may go on to cause structural damage through the material and generate a neutron chain reaction. Metastable isotopes may require stabilisation through the emission of high energy gamma rays [148,150]. These gamma emissions increase the risk of worker dose exposures and result in the wasteform package needing extra shielding during handling and storage. This would significantly increase the costs incurred for each waste package prior to geological disposal. The long-term effects

would result in the breakdown of the wasteform structure and long-term integrity due to the chain reaction of damage through the material. The production of the high energy neutrons will also contribute towards criticality concerns meaning the overall actinide loading capacity of the wasteforms will be significantly reduced.

The CaF_2 additions in the glass-ceramics appeared to successfully improve waste digestion with no CeO_2 hotspots present in the final materials unlike the equivalent baseline samples. The same results were achieved when the amount of CaF_2 added was halved (0.3 wt. %), thus the neutron source for (α,n)-reactions was reduced without any detrimental effects to the waste incorporation. However, the results of milling in a larger volume mill pot achieved equally successful CeO_2 incorporation without the addition of CaF_2. Sample D attained an equivalent phase assemblage and microstructure to the other samples and achieved almost complete digestion of the CeO_2 without the addition of neutron source terms. These results are highly promising that excellent waste incorporation into the optimised formulation can be achieved, as well as reducing the potential occurrence of (α,n)-reactions, thus improving the longevity of the actinide wasteform.

Calculations were performed at Sellafield Ltd. to estimate the neutron source term from (α,n)-reactions in Pu loaded zirconolite glass-ceramic wasteforms and highlighted the impact of lighter elements on the neutron source term of the wasteform compared to a straight PuO_2 package [245]. These calculations were conducted using the Los Alamos Source-4C software [246] and estimated the neutron source term of a straight PuO_2 package and a glass-ceramic wasteform package of equal mass with varying levels of Pu incorporated. The PuO_2 isotropic composition and the glass-ceramic composition used are given in Table 6.8. It was found that a 5 kg package of the glass-ceramic wasteform with 10 wt. % PuO_2 incorporated, had a neutron source term 33 % higher than that of a 5 kg PuO_2 package. In addition, the neutron source term scales directly with the overall mass of the package, thus a 10 kg package with 6 wt. % PuO_2 was estimated to have a neutron source term 40 % higher than a 10 kg PuO_2 package.

Table 6.8: Isotropic composition of PuO_2 and baseline glass-ceramic composition used by Sellafield Ltd. for (α,n) neutron source calculations in the actinide wasteforms [245].

Pu Isotropic composition	
Nuclide	**Wt. %**
Pu^{238}	0.0808
Pu^{239}	76.5
Pu^{240}	20.1
Pu^{241}	0.743
Pu^{242}	0.49
Am^{241}	2.12

Baseline glass-ceramic composition with 6 wt. % Pu loading	
Oxide	**Wt. %**
SiO_2	25.3
Al_2O_3	22.8
B_2O_3	5.0
Na_2O	5.7
CaO	6.2
Gd_2O_3	4.6
TiO_2	9.4
ZrO_2	10.2
CaF_2	4.7
PuO_2	6.0
Total	100

The neutron source term of the glass-ceramic composition used in these calculations was estimated to be 14 times higher, per unit mass of Pu, than in PuO_2. The source term for PuO_2 is constructed from (α,n)-reactions and spontaneous fission [247] Comparatively, the glass-ceramic wasteform neutron source term is totally dominated by (α,n)-reactions between α-particles and light elements, such as O, B and F. It is the larger spread of (α,n) interactions in the glass-ceramic that results in a larger spectrum of neutron energies, thus resulting in the need for extra shielding of the wasteform [247].

The baseline compositions used by Sellafield Ltd. were not representative of formulations considered for the immobilisation of Pu-residues in the UK. Comparatively, the optimised glass-ceramic formulation developed in this study has a higher ceramic fraction, more applicable to these waste-streams. In addition to this, the formulation work previously discussed in Chapter 5 led to the selection of a glass composition that does not contain B_2O_3, resulting in a significant reduction of the overall wasteform neutron source term, even if CaF_2 remains as a digesting agent. Per atom, ^{11}B is approximately twice as effective as an (α,n) source term than ^{19}F, thus its removal from the starting formulation is twice as effective at reducing the wasteform source term than removing the CaF_2 [150].

It was concluded by Sellafield Ltd. that the presence of B and F must have justifiable benefits in the wasteform to warrant the increased neutron source term and additional safety

measures for storage and transportation [245]. The results in this project have demonstrated that both B and F can be significantly reduced / removed and successful waste incorporation and suitable wasteform structures can still be achieved. Further work into the effect of different milling parameters and scale up tests should be conducted to further optimise this stage of consolidation and to ultimately remove the need for CaF_2 additions as a waste digestion agent.

6.5 Conclusions

Ce doped zirconolite glass-ceramics were consolidated by hot isostatic pressing to study the effect of different conditions on the incorporation and partitioning of Ce as a Pu surrogate. This study has shown that multiple factors can govern the success of waste incorporation into the glass-ceramic wasteform including, milling parameters, partial oxygen pressure (pO_2), formulation and additives.

The importance of milling during the sample preparation process was shown to significantly affect the waste incorporation into the glass-ceramic. Stronger forces are generated in larger mill pots that increase the homogenisation of the batch and reduce the overall particle size to aid the digestion of the CeO_2 into the melt. Whilst the importance of milling has been demonstrated at a small research scale and should be considered when scaling up the HIP technology, it is not expected to be the limiting criteria for waste digestion at an industrial scale.

A reduction of the partial oxygen pressure (pO_2) inside the canister was shown to increase the incorporation of CeO_2. The HIP canister provided a redox gradient through the sample and facilitated the reduction of Ce^{4+} to Ce^{3+}, which was more prominent towards the edge of the sample. At an industrial scale (5 – 10 ltr), the influence of the canister on pO_2 and waste digestion in the glass-ceramic will be less significant, but the pO_2 may still govern the waste digestion into the wasteform. The addition of Ni powder demonstrated the increased incorporation of CeO_2 into the glass-ceramic, again by promoting the reduction of Ce^{4+}. The increase of Ce^{3+} resulted in more Ce in the glass phase and the formation of a Ce-rich perovskite phase. Whilst Ni can sufficiently reduce the pO_2 to improve CeO_2 incorporation, it is not expected to have the same effect on PuO_2. Pu has a higher redox potential than Ce,

making the Pu^{4+} state more stable than Ce^{4+} under such conditions. The effect of controlled pO_2 on the incorporation of PuO_2 is discussed in more detail in Chapter 8.

The glass-ceramic formulation had a substantial influence on the phase assemblage and waste incorporation behaviour of the final wasteform. Whilst it has been demonstrated that a B_2O_3 and CaF_2 free formulation can successfully digest CeO_2, the final wasteform was affected by both the glass composition (see Chapter 5) and ceramic formulation. The zirconolite formulation was shown to have a controlling influence on the partitioning behaviour of Ce in the wasteform. Ce preferentially substituted on the Ca site of zirconolite in all samples and Al_2O_3 acted as a sufficient charge compensator for Ce^{4+} incorporation. However, when targeting Zr substitution, Ce reduction was increased and an accessory perovskite phase formed. The deficiency of Zr and excess of Ca in these systems were thought to facilitate the perovskite formation, which accommodated the majority of Ce^{3+} in the system. Due to the preference to immobilise Pu as Pu^{4+}, it was promising to observe successful retention and incorporation of Ce^{4+}, as well as the accommodation of Ce^{3+} into ceramic phases. This study confirms the flexibility of these wasteforms to accommodate changes in waste composition and requirements.

CaF_2 was investigated as an additive and was proven to improve waste digestion. Due to the problematic (α,n)-reactions associated with ^{19}F ions in actinide rich wasteforms, it is hoped the use of CaF_2 as a precursor can be avoided. If complete removal of CaF_2 cannot be achieved, this study has shown that CaF_2 can be reduced by 50 % and still obtain full waste incorporation. By milling in a larger mill pot to achieve better homogenisation of the powders, complete waste incorporation was achieved without the addition of CaF_2. These results are very promising and require further work to investigate the effect of milling parameters on waste incorporation to achieve full optimisation of the wasteform and processing parameters, to ultimately eliminate the need for CaF_2.

7 Chlorine contaminated Pu-residues

Zirconolite glass-ceramics for the immobilisation of Cl contaminated Pu-residues.

Stephanie M. Thornber[a], Lucy M. Mottram[a], Amber R. Mason[a], Paul Thompson[b], Martin C. Stennett[a] & Neil C. Hyatt[a,*]

[a]*Immobilisation Science Laboratory, Department of Materials Science & Engineering, The University of Sheffield, Sir Robert Hadfield Building, Mappin Street, Sheffield S1 3JD, UK*

[b]*European Synchrotron Radiation Facility, 71 Avenue des Martyrs, CS 40220, 38043 Grenoble Cedex 9, France*

Author contributions: Stephanie M. Thornber designed and developed the experimental matrix, fabricated, characterised and analysed all samples and wrote the scientific report. Amber R. Mason and Lucy M. Mottram ran the XANES experiment and collected the data at the European Synchrotron Radiation Facility (ESRF) alongside Paul Thompson. Lucy M. Mottram analysed and wrote the scientific output for the XANES data, with help from Neil C. Hyatt. Martin C. Stennett provided useful communications. Neil C. Hyatt provided project oversight and supervision.

7.1 Introduction

The UK holds the largest stockpile of civil separated Pu, stored as PuO_2, which is projected to exceed more than 140 tons at the end of reprocessing [11]. Current Government policy is that UK Pu should be reused as mixed oxide (MOx) fuel in civil nuclear reactors, with any material unsuitable for reuse immobilised and treated as a waste for geological disposal [10,11]. At present, this policy is challenged by lack of commercial interest in MOx offtake by reactor operators. In the event that reuse of Pu as MOx fuel cannot be delivered, immobilisation of the stockpile will be required since regulators require conversion of PuO_2 powder into an alternative passive form more suitable for long term storage [11].

Separated Pu unsuitable and uneconomic for reuse includes Pu-residues arising from early plutonium based research and development, secondary reprocessing wastes and unused MOx materials [18,82,179]. Powder Pu-residues are contained within PVC (polyvinyl chloride) packaging, within stainless steel or aluminium containers. Some PVC packaging has degraded during storage, as a result of radiogenic heating and radiolysis, which has resulted

in chloride contamination of the PuO_2 [15,145]. Waste PuO_2 originating from reprocessing may also have Cl present as a contaminant from the treatment process (e.g. as PuOCl) [145]. The upper bound of Cl contamination for PuO_2 residues is estimated at ca. 0.2 wt. %, although with considerable uncertainty and variation between packages [146]. A zirconolite glass-ceramic wasteform, manufactured by hot isostatic pressing has been developed as a flexible wasteform for the immobilisation of Pu-residues and stockpile material [16,26,100,142,144]. In this wasteform, Pu is targeted for solid solution in the zirconolite ceramic phase, prototypically $CaZrTi_2O_7$, and the accessory albite glass phase, prototypically $NaAlSi_3O_8$, acts to incorporate feed impurities. Zirconolite was selected as the Pu host phase due to its known chemical durability, radiation tolerance and demonstrable retention of actinides over geological timescales in mineral counterparts, see e.g. [235] for a comprehensive review. We have previously demonstrated a formulation and processing route to yield zirconolite glass-ceramics, targeting 70 wt. % zirconolite and 30 wt. % $NaAlSi_3O_8$, with efficient Pu and Ce surrogate partitioning between zirconolite and glass phases (100 : 1 and 20 : 1, respectively), and only trace accessory crystalline phases (e.g. $ZrSiO_4$, $CaTiSiO_5$, TiO_2) [248,249].

Cl contamination of Pu-residues could pose a challenge to the formulated zirconolite glass-ceramic wasteform. The zirconolite structure is not known to incorporate the chloride anion, whereas Cl solubility in alkali / alkaline earth aluminosilicate glasses is typically less than a few weight percent; above this threshold phase separation of an alkali or alkaline earth chloride occurs [250–254]. In respect of the composition of the current wasteform, phase separation of NaCl, and potentially $PuCl_3$, could be expected since there is no evidence of solid solution formation [255]; this would clearly be undesirable given the aqueous solubility of $PuCl_3$. In addition, Cl incorporation has been shown to result in a small, but measureable, increase in aluminosilicate melt viscosity [256–258]. Addition of 1.1 mol. % Cl (0.6 wt. %) in Na_2O-CaO-Al_2O_3-SiO_2 melts was reported to increase viscosity by a factor of 10 in peralkaline melts, whereas addition of 0.6 mol. % Cl (0.3 wt. %) in peraluminous melts was reported to reduce viscosity by a factor of 3 [259]. In the context of this study, the viscosity of the glass component will influence the kinetics of diffusion and hence zirconolite formation.

The current conceptual process for HIP immobilisation of plutonium residues incorporates a heat treatment facility to remove Cl contaminants prior to immobilisation, due to the uncertainty of Cl behaviour within the wasteform [25]. The technology roadmap for immobilisation could be significantly derisked if the requirement for a heat treatment plant could be removed and satisfactory incorporation of the Cl inventory within the wasteform assured. Consequently, a robust safety case for the wasteform should include determination of the Cl solubility limit in the glass phase and knowledge of the impact on the desired phase assemblage. This requires a mechanistic understanding of Cl incorporation at the molecular scale.

More broadly, the incorporation mechanism of Cl in aluminosilicate melts is of considerable significance for the global Cl cycle, since magmas transfer Cl from the mantle to the crust and atmosphere, and dissolved hydrosaline liquids have an important role in subsequent ore formation [260–262]. Cl solubility in aluminosilicate melts is known to depend on composition, temperature and pressure [253,254,260,261]. ^{35}Cl magic angle spinning – nuclear magnetic resonance (MAS-NMR) studies have yielded considerable insight into Cl incorporation mechanisms in aluminosilicate glasses. These studies have demonstrated co-ordination of Cl^- by alkali / alkaline earth modifier cations, with no discernible evidence for significant Al – Cl or Si – Cl bonds [261,263,264]. However, ^{35}Cl MAS-NMR is challenging since ^{35}Cl is a spin 3/2 quadrupole nuclide, with a low resonance frequency and large quadrupole moment, resulting in relatively broad signals [261,264]. Cl K-edge X-ray absorption spectroscopy (XAS) has not been extensively applied to understand the speciation of Cl in aluminosilicate glasses, no doubt due to the low energy of the Cl K-edge (2822.4 eV) for which there are relatively few tender synchrotron X-ray beamlines. These studies are typically constrained by the need to utilise fluorescence detection due to prohibitive sample attenuation in transmission mode, leading to distortion of the signal by self-absorption effects for concentrated compounds, although this can be corrected for post-measurement. Nevertheless, Cl K-edge X-ray absorption near-edge spectroscopy (XANES) studies of CaO-MgO-Al_2O_3-SiO_2 glasses suggested a mechanism of incorporation involving Cl^- co-ordinated to Mg^{2+} and Ca^{2+} network modifiers [265]. Likewise, a combined XANES and EXAFS (extended X-ray absorption fine structure) study of borosilicate glasses intended for radioactive waste immobilisation suggested Cl^- co-ordinated to Ca^{2+} [266].

Here, we investigate the Cl solubility limit in glass-ceramics formulated to yield 30 wt. % $Na_2Al_2Si_6O_{16}$ glass and 70 wt. % $CaZrTi_2O_7$ and the effect on the phase assemblage and Pu surrogate partitioning behaviour. Cl K-edge X-ray absorption spectroscopy (XAS) was applied to determine the chloride speciation and incorporation mechanisms within the glass phase. Our results demonstrate a Cl solubility limit in the aluminosilicate glass phase of 0.9 ± 0.1 wt. %, which is a factor of 4.5 times greater than the estimated Cl concentration at the expected PuO_2 incorporation rate, based on the upper bound of the Cl inventory. Consequently, from the perspective of wasteform formulation, a heat treatment plant would not be required to reduce the Cl contamination prior to immobilisation, as in the current conceptual process [25].

7.2 Experimental

Prototype glass-ceramics for plutonium immobilisation were formulated to a previously optimised baseline composition, targeting 30 wt. % glass of composition $Na_2Al_2Si_6O_{16}$ and 70 wt. % ceramic phase $CaZrTi_2O_7$. Cl was added to the baseline formulation by replacement of Na_2O with 2NaCl, to yield nominal Cl concentrations of 0.3, 0.6, 0.9, 1.7 and 2.5 wt. %. Two compositions were fabricated with CeO_2 as a PuO_2 surrogate, targeting incorporation as Ce^{4+} on the Zr^{4+} site of the zirconolite ($CaZr_{0.8}Ce_{0.2}Ti_2O_7$), to understand the potential association between Ce and Cl in the phase assemblage. Powder batches to yield 50 g of the compositions summarised in Table 7.1, were constituted from stoichiometric amounts of SiO_2, Na_2SiO_3, Al_2O_3, NaCl, $CaTiO_3$, TiO_2, ZrO_2, CeO_2 and NaCl. Powders were milled at 500 rpm for 30 min in a planetary mill with heptane as the milling medium (in which NaCl is insoluble). Milled powders were calcined overnight at 600 °C before packing into the HIP canisters. The canisters were evacuated at room temperature and baked-out at 300 °C before sealing, and were HIPed at 1250 °C for 4 h under 103 MPa of argon gas pressure.

Table 7.1: Compositions A – E had the same starting formulation with increasing levels of NaCl additions. Compositions F – G targeted Ce^{4+} incorporation on the Zr site within zirconolite.

Composition	Glass-ceramic formulation	Nominal Cl wt. % (added as NaCl)
A	30 wt. % $Na_2Al_2Si_6O_{16}$ 70 wt. % $CaZrTi_2O_7$	0.3
B	30 wt. % $Na_2Al_2Si_6O_{16}$ 70 wt. % $CaZrTi_2O_7$	0.6
C	30 wt. % $Na_2Al_2Si_6O_{16}$ 70 wt. % $CaZrTi_2O_7$	0.9
D	30 wt. % $Na_2Al_2Si_6O_{16}$ 70 wt. % $CaZrTi_2O_7$	1.7
E	30 wt. % $Na_2Al_2Si_6O_{16}$ 70 wt. % $CaZrTi_2O_7$	2.5
F	30 wt. % $Na_2Al_2Si_6O_{16}$ 70 wt. % $CaZr_{0.8}Ce_{0.2}Ti_2O_7$	0.9
G	30 wt. % $Na_2Al_2Si_6O_{16}$ 70 wt. % $CaZr_{0.8}Ce_{0.2}Ti_2O_7$	1.7

Monolithic glass-ceramic specimens were ground and polished to study the microstructure and elemental distribution using a Hitatchi TM3030 analytical scanning electron microscope (SEM) and a Bruker Quantax energy dispersive X-ray spectrometer (EDX). Compositional analysis was performed by powder X-ray diffraction (XRD) using a Bruker D2 PHASER diffractometer with Cu Kα radiation (1.5418 Å) and a Lynxeye position sensitive detector.

X-ray absorption spectroscopy (XAS) data were acquired on the XMAS bending magnet beamline (BM28) at the European Research Synchrotron Radiation Facility, Grenoble, France. The XMAS beamline was configured with a fixed exit, double crystal, Si (111) monochromator; a rhodium coated toroidal mirror of silicon crystal focused the beam to a spot size of 1 mm. Harmonic rejection was provided by rhodium coated pyrex mirrors [210]. Cl K-edge XAS data were acquired at room temperature in fluorescence mode, using a Vortex Si drift detector, with the samples orientated at an incidence angle of 45° between the beam and detector, under a helium atmosphere.

The absolute energy scale was calibrated to the L_3 absorption edge of a Rh reference foil set at $E_0 = 3004.0$ eV [211]. Since the XMAS beamline utilised an optically encoded monochromator, the energy drift between scans was expected to be negligible and this was

verified by periodic acquisition of data from the Rh reference foil. A comprehensive full account of the specifications for soft X-ray absorption fine structure (XAFS) measurements has been previously published [210].

Samples for XAS analysis were prepared as 6 mm pellets of a homogenous dispersion of analyte powder in PEG (poly-ethylene-glycol) powder as a binder. Data reduction and analysis were performed using the Athena, Artemis and Hephaestus softwares [206]. Data acquisition and analysis were restricted to the near-edge region due to the presence of trace Ar within the He gas environment and consequent absorption edge at 3207.0 eV [211], which prevented reliable background subtraction for analysis of the extended X-ray absorption fine structure. A series of 12 chemically plausible reference compounds were also analysed as potential standards: afghanite ($(Na,Ca,K)_8(Si,Al)_{12}O_{24}(SO_4,Cl,CO_3)_3.(H_2O)$), brearleyite ($(Ca,Na)_{12}(Al,Fe,Ti)_{14}O_{32}Cl_2$), calcium chloride ($CaCl_2$), calcium chloride dehydrate ($CaCl_2H_4O_2$), calcium chlorosilicate ($CaSiO_3$), davyne ($Na_4K_2Ca_2Si_6Al_6O_{24}(SO_4)Cl_2$), ellestadite ($Ca_5(SiO_4,PO_4,SO_4)_3(F,OH,Cl)$), eudialyte ($Na_{15}Ca_6(Fe,Mn)_3Zr_3SiO(O,OH,H_2O)_3(Si_3O_9)_2(Si_9O_{27})_2$-$(OH,Cl)_2$), marialite ($Na_4Al_3Si_9O_{24}Cl$), scapolite ($(Na,Ca)_4(Al,Si)_3Si_6O_{24}(Cl,CO_3)$), sodalite ($Na_8Al_6Si_6O_{24}Cl_2$) and sodium chloride (NaCl).

7.3 Results

7.3.1 Cl incorporation in baseline compositions

Phase assemblage and microstructure

Hot isostatic pressing of the baseline compositions in Table 7.1, produced high quality glass-ceramics with densities above 98 % of theoretical density (Table 7.2). Powder XRD analysis confirmed zirconolite ($CaZrTi_2O_7$) was the major crystalline phase in all samples, Figure 7.1, with zircon ($ZrSiO_4$), sphene ($CaTiSiO_5$) and baddeleyite (ZrO_2) present in trace quantities (PDF cards: 01-074-0669, 00-006-0266, 01-076-6576 and 01-080-0966, respectively). The XRD data of compositions D and E, with nominal 1.7 wt. % and 2.5 wt. % Cl, exhibited the most intense reflection of NaCl at 2θ = 31.7° (indexed as (2 0 0), PDF card: 00-005-0628), as shown in the inset of Figure 7.1. This reflection was not present in the XRD data of compositions A – C, with lower Cl content, implying a Cl solubility of ca. 0.9 wt. % in the aluminosilicate glass phase.

Table 7.2: Powder mass and canister volumes before and after processing. Pycnometry (true density) and water displacement (bulk density) measurements were used to determine the material densification for the final HIPed materials.

Composition	Powder mass (g) (±0.05)	Canister volume		Canister densification % (±0.8)	Density		Density % theoretical (±0.5)
		Before (cm^3) (±0.4)	After (cm^3) (±0.4)		True (g/cm^3) (±0.01)	Bulk (g/cm^3) (±0.04)	
A	44.41	41.9	25.9	38.3	3.57	3.54	99.3
B	34.82	34.6	21.6	37.5	3.56	3.56	99.7
C	46.63	43.3	25.9	40.3	3.57	3.51	98.6
D	45.00	42.8	25.7	39.8	3.55	3.51	99.1
E	44.43	42.8	25.7	39.9	3.51	3.51	99.8
F	49.35	45.6	27.9	38.7	3.66	3.58	97.7
G	48.09	44.0	27.4	37.7	3.58	3.56	99.4

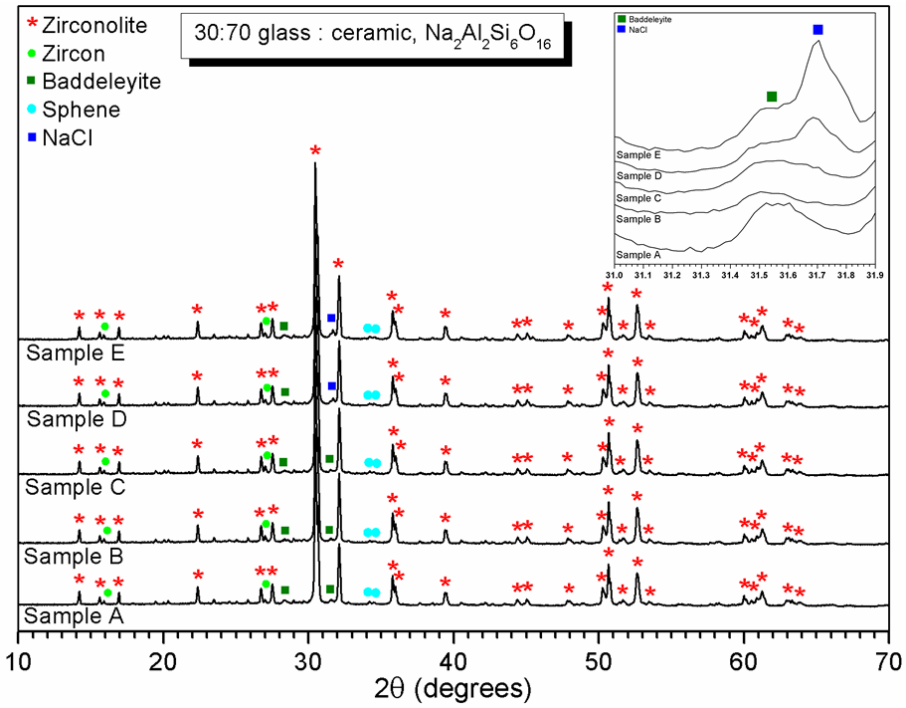

Figure 7.1: XRD data showed only minor changes to the relative intensities of minor phases with changes to the Cl additions. The major NaCl reflection was seen as a shoulder in sample C and was present as a peak in samples D and E, shown in the inset plot.

SEM-EDX analysis verified the phase assemblage determined by powder XRD. The backscattered electron (BSE) micrographs in Figure 7.2 show the microstructures were comprised of homogeneously distributed crystallites of $CaZrTi_2O_7$, with trace $CaTiSiO_5$, $ZrSiO_4$, ZrO_2 and TiO_2. As shown in Figure 7.3, bright ZrO_2 cores were observed in some ca. 1 μm sized $CaZrTi_2O_7$ crystallites, whereas some larger, ca. 10 μm, crystallites showed replacement of $ZrSiO_4$ by $CaZrTi_2O_7$. Thus, two distinctive dissolution – precipitation reactions are evidently involved in forming $CaZrTi_2O_7$ in this system, leading to two different crystallite sizes governed by that of the ZrO_2 and $ZrSiO_4$ templating phase, with inward diffusion of Ca and Ti, from the melt (in conjunction with an outward diffusion of Si).

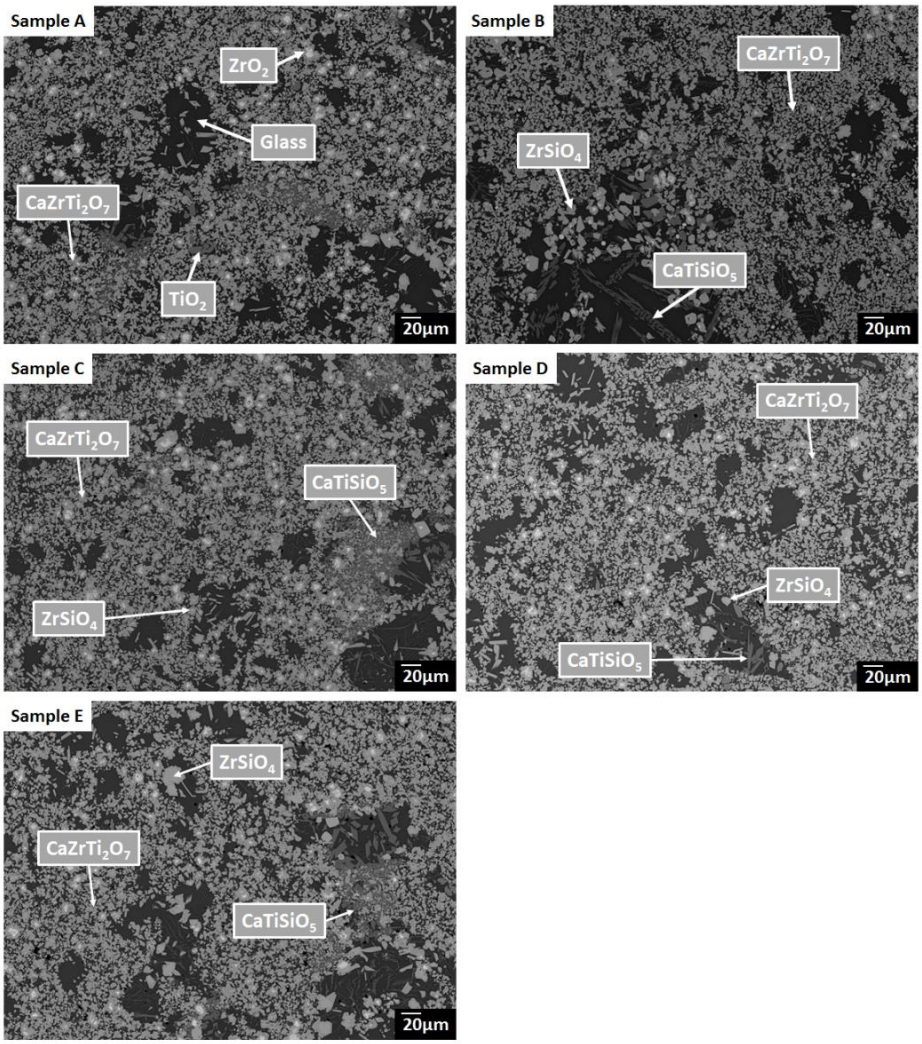

Figure 7.2: BSE micrographs showing similar microstructures for all samples with increasing Cl additions.

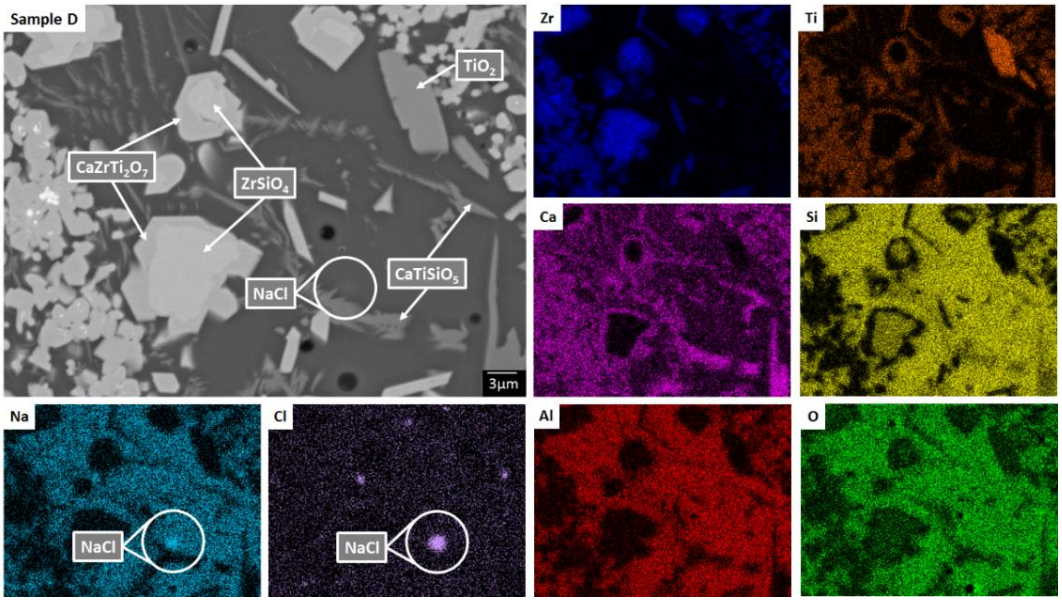

Figure 7.3: SEM-EDX showing the crystalline elemental distribution. NaCl hotspots are seen in the Cl signal showing the solubility limit has been exceeded. $ZrSiO_4$ crystals surrounded by $CaZrTi_2O_7$ imply an outward diffusion mechanism of Si and an inward diffusion mechanism of Ca and Ti from the glass phase.

To determine where Cl was located within the glass-ceramic, EDX point spectra were acquired from the zirconolite and glass phases. These analyses, shown in Figure 7.4, demonstrated that Cl was concentrated in the glass phase, with no evidence for Cl incorporation in the zirconolite phase. For compositions D and E, with nominal 1.7 wt. % and 2.5 wt. % Cl, EDX maps showed isolated, micron sized, association of Na and Cl, in high concentration, as demonstrated in Figure 7.3. Such an association of Na and Cl was not observed in compositions A – C, with lower Cl content. These data were consistent with XRD analysis, which revealed the presence of crystalline NaCl above an apparent Cl solubility limit of ca. 0.9 wt. % in the glass phase.

Quantitative EDX analysis of the glass phase, for each composition, was performed to determine the Cl solubility limit. The average compositions of the glass phases are reported in Table 7.3, determined from at least ten individual point analyses. Figure 7.5 shows the measured Cl content of the glass phase, as a function of the expected Cl content, in wt. %. A linear correlation between measured and expected content in the glass phase was apparent up to 0.9 wt. % Cl (see Figure 7.5), above which the measured Cl content remained independent of the amount of Cl in the batch composition. The Cl solubility limit in the glass

phase, estimated from the intercept of the plateau, was determined to be 0.9 ± 0.1 wt. % Cl, consistent with the phase separation of crystalline NaCl observed by XRD and SEM-EDX of compositions D and E, with nominal 1.7 wt. % and 2.5 wt. % Cl. Below the Cl solubility limit, the measured Cl content in the glass phase was always slightly greater than the expected Cl content; the origin of this discrepancy is not clear, but could imply a small systematic inaccuracy in EDX analysis.

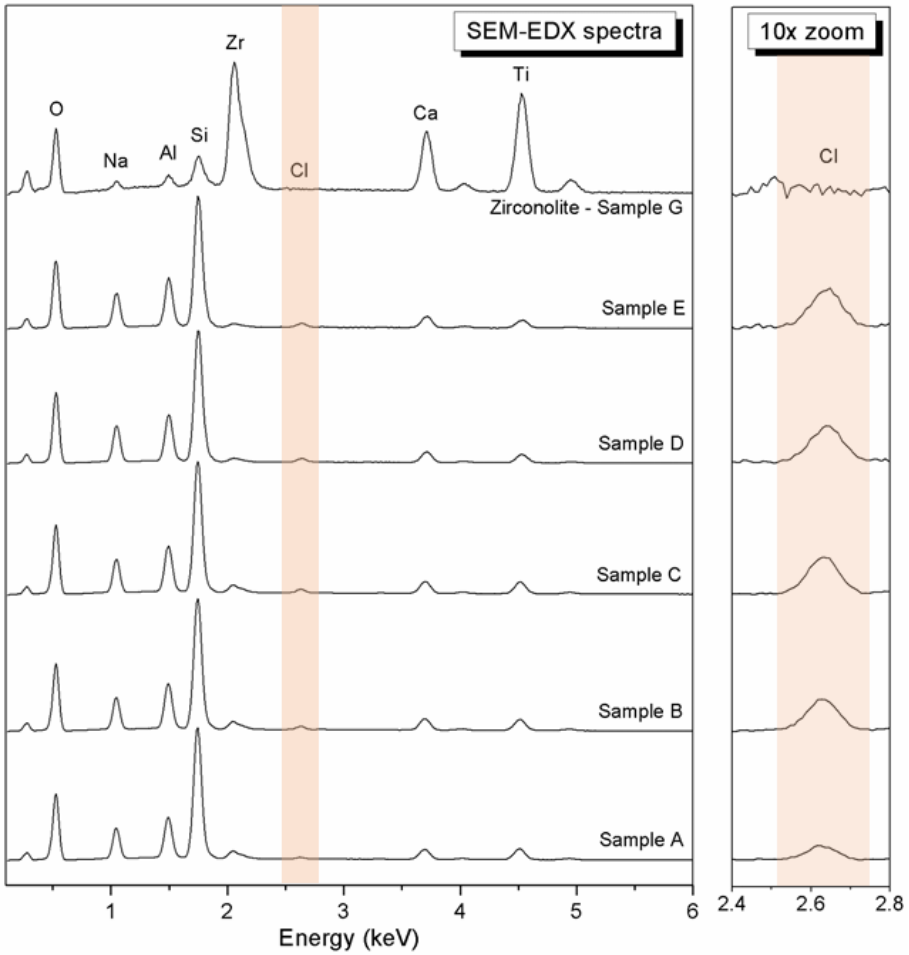

Figure 7.4: SEM-EDX spectra of the glass phase confirming retention and incorporation of Cl in the glass. The side plot isolates the Cl signal with a vertical scale 10x higher than the main figure.

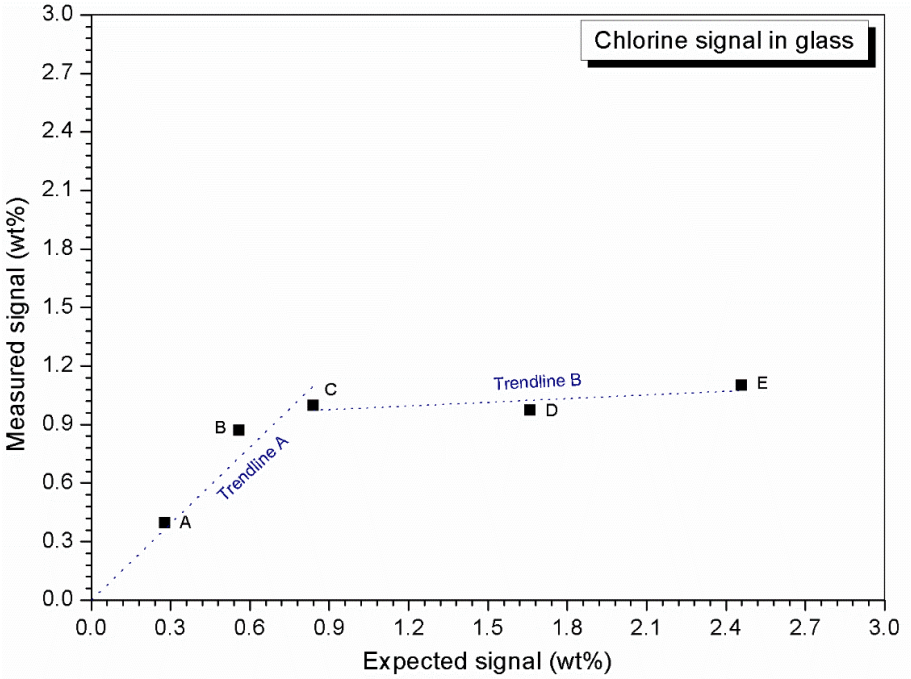

Figure 7.5: Measured versus expected Cl signal in the glass phase. A linear dependence is observed between the measured Cl signal and the expected Cl signal up to 0.9 wt. % addition. Above this level the measured signal does not increase proportionally to the Cl additions showing not all Cl is incorporated into the glass phase.

Table 7.3: SEM-EDX analysed compositions of the glass phase of glass-ceramic compositions A – G.

Oxide	Composition A		Composition B		Composition C		Composition D		Composition E		Composition F		Composition G	
	Wt. %	±	Wt. %	±	Wt. %	±	Wt. %	±	Wt. %	±	Wt. %	±	Wt. %	±
Na_2O	10.4	0.7	10.4	0.7	10.7	0.7	12.1	0.7	11.4	0.7	12.3	0.7	12.4	0.7
Al_2O_3	13.4	0.6	14.5	0.8	14.5	0.8	15.6	0.8	16.0	0.8	17.3	0.6	14.9	0.8
SiO_2	52.0	2.1	50.0	1.9	48.8	2.1	53.5	2.1	53.4	2.1	58.1	2.1	56.6	1.9
ZrO_2	6.1	0.3	6.0	0.3	5.7	0.3	3.1	0.1	3.1	0.1	0.6	0.3	1.2	0.3
Cl	0.4	0.1	0.9	0.1	1.0	0.1	1.0	0.1	1.1	0.1	1.0	0.1	1.1	0.1
CaO	6.1	0.3	6.9	0.3	6.9	0.3	6.5	0.3	7.2	0.3	4.7	0.3	5.1	0.3
TiO_2	13.0	0.3	12.9	0.3	13.3	0.3	9.0	0.3	9.2	0.3	4.7	0.3	6.6	0.3
CeO_2	-	-	-	-	-	-	-	-	-	-	0.3	0.1	0.1	0.1

Cl K-edge X-ray Absorption Near – Edge Spectroscopy

Figure 7.6, Figure 7.7 and Figure 7.8 show the merged, background subtracted, and normalised Cl K-edge XANES data for the glass-ceramic samples and selected reference compounds; a three point smoothing algorithm was applied to each data set. All data from reference compounds were corrected for self-absorption using the FLUO algorithm [267]. For reference compounds with relatively dilute Cl concentration (e.g. ellestadite, eudialyte, sodalite, and afghanite), the impact of this correction on the relative intensity of the white line features was marginal.

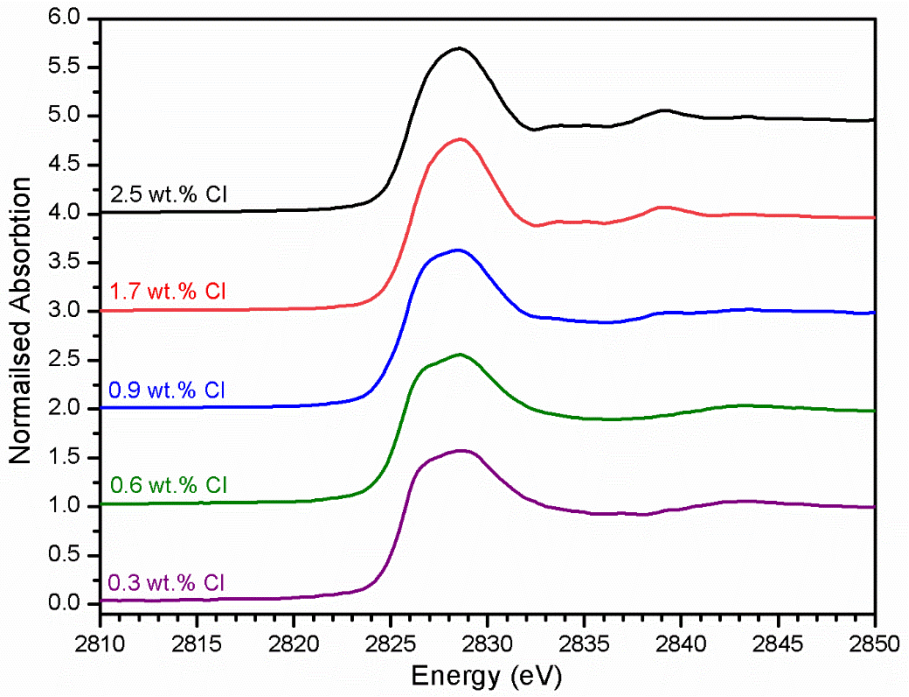

Figure 7.6: Plot showing the normalised Cl K-edge XANES data for glass-ceramic compositions A – E (bottom – top, respectively).

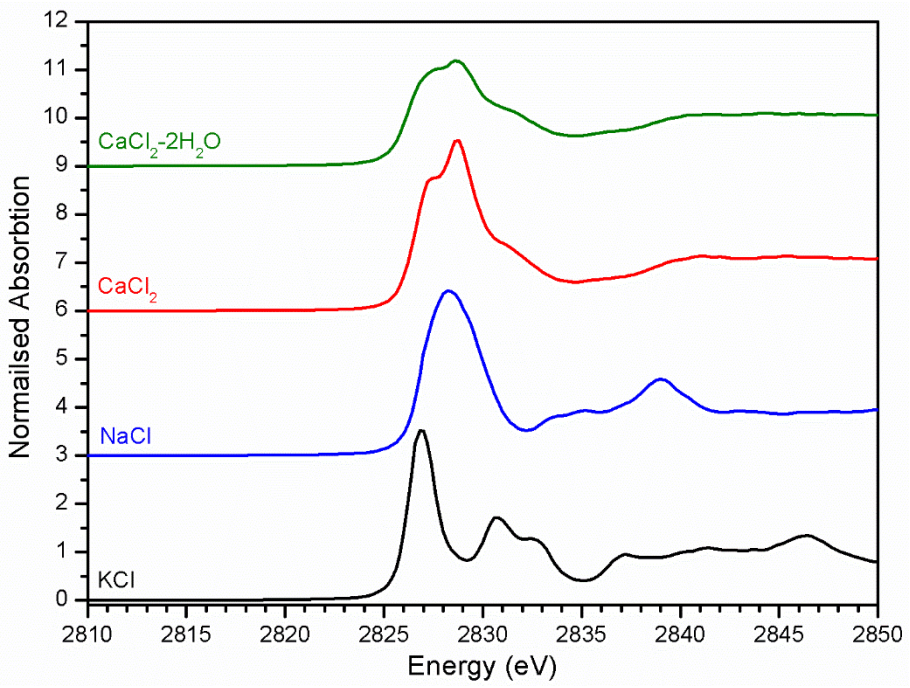

Figure 7.7: Plot showing the merged, background subtracted and normalised Cl K-edge XANES data for binary Cl standards.

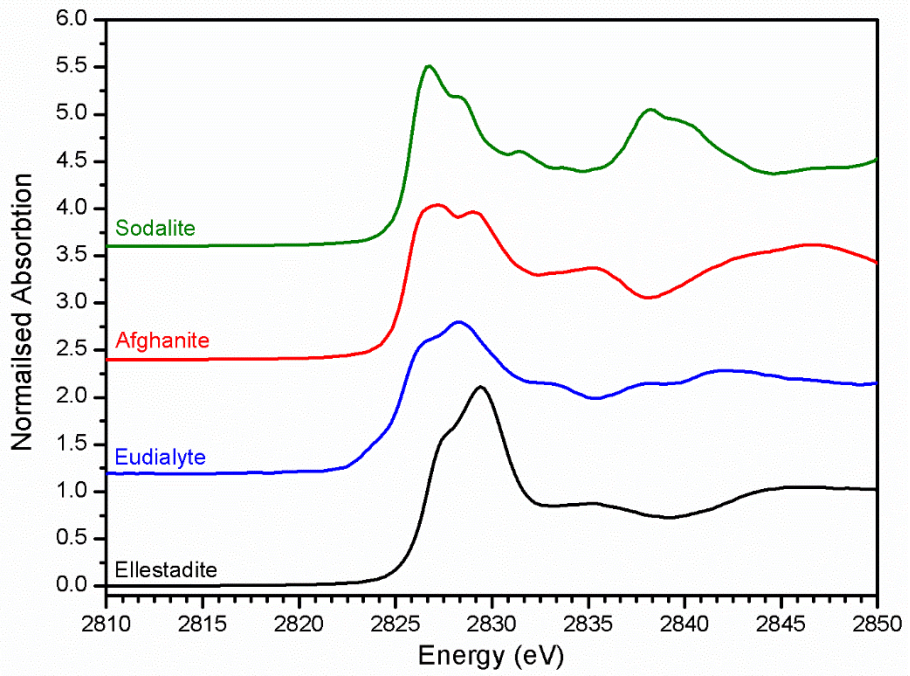

Figure 7.8: Plot showing the merged, background subtracted and normalised Cl K-edge XANES data for aluminosilicate Cl reference materials.

The XANES features of the glass-ceramics were typically damped compared to those of the crystalline reference compounds, as shown in Figures 7.6, 7.7 and 7.8, from which we infer that Cl is located in one or more disordered environments within the amorphous glass phase, consistent with interpretation of SEM-EDX data. Random phase coherence of scattering paths is known to attenuate XANES features in disordered materials, relative to crystalline counterparts [268].

The Cl K-edge XANES data of the reference compounds and glass-ceramics, shown in Figures 7.6, 7.7 and 7.8, all exhibited E_0 in the range 2825.6 – 2826.8 eV, with precision ± 0.2 eV (determined as the maximum of the first derivative). Since Cl is known to be speciated as the chloride anion in the reference compounds, the same characteristic E_0 implied speciation as Cl^- in the glass-ceramic materials. The XANES data of the glass-ceramics showed a small but systemic increase in E_0 with increased Cl content, from 2825.6 eV for nominal 0.3 wt. % Cl to 2826.0 eV for 2.5 wt. % Cl. Furthermore, with increased nominal Cl concentration in the glass-ceramics, a subtle change in the white line profile was apparent in the XANES data. At low Cl concentrations (≤ 0.9 wt.%), the white line was clearly composed of two distinct features, associated with maxima at ca. 2827.9 and 2828.6 eV. Whereas, at high Cl concentrations (≥ 1.7 wt.%), this distinction was no longer apparent and the features merged to give a single maximum at 2828.6 eV. These observations suggested a subtle change in Cl environment as a function of increasing Cl concentration. An additional, relatively sharp, feature was apparent at 2839.1 eV in the XANES data of the glass-ceramics with nominal 1.7 wt. % and 2.5 wt. % Cl, together with two additional subtle features in the range 2833.6 – 2835.2 eV. These features were also apparent at the same energy intervals in the XANES of the NaCl reference, from which it was inferred that a distinctive NaCl like environment was present in these compositions. This is consistent with the analysis of XRD and SEM-EDX data, which demonstrated phase separation of crystalline NaCl above the solubility limit of 0.9 ± 0.1 wt. % Cl in the glass phase.

Comparison of the Cl K-edge XANES data of the glass-ceramics with those of the binary chlorides, Figure 7.6 and Figure 7.7, did not reveal correspondence of similar characteristic features. In addition, the E_0 of the binary chlorides was typically 0.5 – 1.0 eV higher than that determined for the glass-ceramics. In contrast, the E_0 determined for the aluminosilicate reference compounds, Figure 7.8, was determined to be in the narrow range 2825.5 – 2825.8 eV, comparable with that determined for the glass-ceramic materials.

Comparison of the XANES features of aluminosilicate reference compounds and glass-ceramic materials, demonstrated that no individual aluminosilicate compound was a unique fingerprint for the Cl environments in the glass-ceramics. However, the XANES data of the glass-ceramic materials evidently tracked through the XANES features of eudialyte, sodalite, and afghanite, see Figure 7.9. This suggested that the Cl environments in these aluminosilicate reference compounds could be plausible models for those in the glass-ceramic materials. Furthermore, the white lines of the XANES of the aluminosilicate reference compounds were composed of two distinct features, similar to those observed in the glass-ceramic compounds with low nominal Cl concentration, as described above. Overall, from this comparative interpretation of the XANES data of glass-ceramics and reference compounds, it was concluded that Cl was incorporated as Cl^- anions in the aluminosilicate glass phase, below the Cl solubility limit, with a distribution of Cl environments which could be approximated by a combination of those characteristic of eudialyte, sodalite, and afghanite.

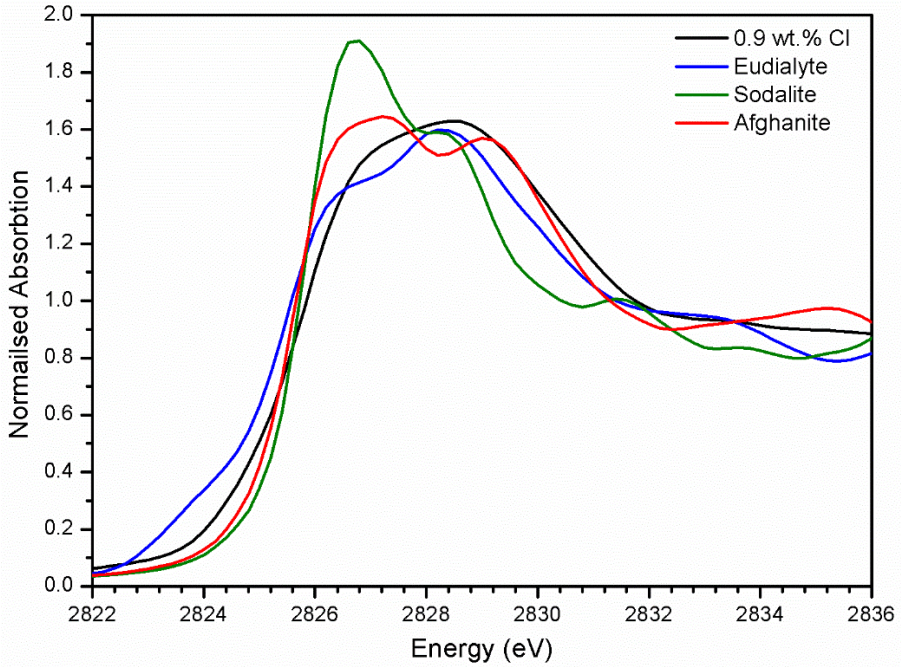

Figure 7.9: Cl K-edge XANES data for glass-ceramic composition C (0.9 wt. % Cl) compared against the XANES data for aluminosilicate reference materials eudialyte, sodalite and afghanite. The glass-ceramic data had features similar to those in the reference materials data, which implied similar Cl environments.

Combinatorial linear combination analysis was applied to the Cl K-edge XANES data of the glass-ceramic materials, with the aim of identifying and quantifying representative model Cl environments. An energy window of 2805 – 2850 eV was utilised for fitting a library of XANES data from 12 chemically plausible reference compounds: afghanite ($(Na,Ca,K)_8(Si,Al)_{12}O_{24}(SO_4,Cl,CO_3)_3.(H_2O)$), brearleyite ($(Ca,Na)_{12}(Al,Fe,Ti)_{14}O_{32}Cl_2$), calcium chloride ($CaCl_2$), calcium chloride dehydrate ($CaCl_2H_4O_2$), calcium chlorosilicate ($CaSiO_3$), davyne ($Na_4K_2Ca_2Si_6Al_6O_{24}(SO_4)Cl_2$), ellestadite ($Ca_5(SiO_4,PO_4,SO_4)_3(F,OH,Cl)$), eudialyte ($Na_{15}Ca_6(Fe,Mn)_3Zr_3SiO(O,OH,H_2O)_3(Si_3O_9)_2(Si_9O_{27})_2(OH,Cl)_2$), marialite ($Na_4Al_3Si_9O_{24}Cl$), scapolite ($(Na,Ca)_4(Al,Si)_3Si_6O_{24}(Cl,CO_3)$), sodalite ($Na_8Al_6Si_6O_{24}Cl_2$) and sodium chloride (NaCl).

Evaluation of all possible 2^{12} combinations of reference data was achieved using the combinatorial fitting tool in the Athena software [206]. The fitted weighting factors of the reference spectra (w_i) were constrained to the range $0 \leq w_i \leq 1$. Since it could not be assumed that the reference library would fully account for all Cl environments in the glass-ceramic materials, the sum of the weighting factors was not constrained to unity. The goodness of fit was evaluated using the R-factor defined in Athena as (Equation 11):

$$R = \frac{\sum_{i=1}^{N}\left(\mu_i(obs)-\mu_i(calc)\right)^2}{\sum_{i=1}^{N}\left(\mu_i(obs)\right)^2} \qquad \textbf{Eq. 11}$$

Where N is the number of data points in the XANES spectrum, μ_i is normalised absorption, and *obs* or *calc* refer to the observed and calculated μ_i values, respectively, at each point.

The Hamilton R-factor ratio test was applied to compare the fit with lowest R-factor to each fit with progressively higher factors, applying a significance level of 0.05 [269]. This analysis afforded a subset of between 4 and 20 fits which were not significantly different in terms of goodness of fit at the 95% confidence level. The subset of fits was combined to produce a mean weighted fit of component reference data with associated uncertainties. The resulting mean weighted fits were characterised by four common contributions: eudialyte, sodalite, ellestadite, and afghanite, plus NaCl for the glass-ceramics with nominal 1.7 wt. % and 2.5 wt. % Cl. All other contributions, with a weighting factor much smaller than the associated uncertainty, were not considered significant. Figure 7.10 shows the derived mean

weighted contributions of XANES data from reference compounds used to fit the glass-ceramics data, with associated uncertainties.

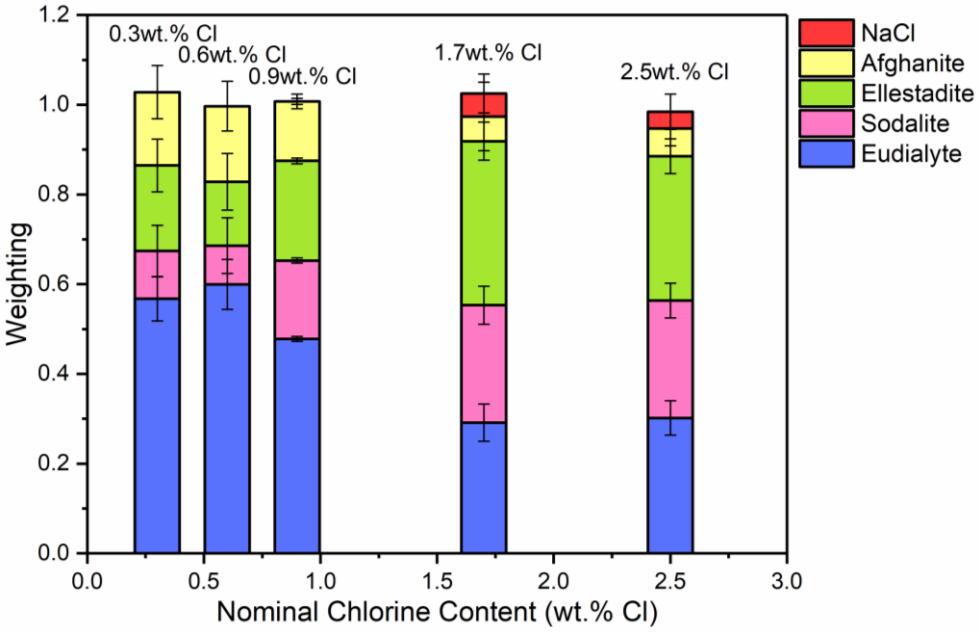

Figure 7.10: The mean weighted contributions of XANES data from reference compounds NaCl, afghanite, ellestadite, sodalite and eudialyte, which were used to fit the glass-ceramics data.

Figure 7.11a and Figure 7.11b show the linear combination fits with the lowest R factor for the glass-ceramics with nominal 0.9 wt. % and 1.7 wt. % Cl. Inspection of the fit and difference profile showed that, although the sum of the four weighted reference data sets (plus NaCl) provided a reasonable fit to the observed data, one or more additional components were evidently required for a complete description. Consequently, our interpretation of the model Cl environments present in the glass-ceramics is incomplete, however, the adequacy of the fit enables consideration of the relative proportion of model Cl environments, though absolute values should be treated with due caution.

Figure 7.10 shows a systematic evolution in Cl environments within the glass-ceramics with increasing Cl concentration. At low nominal Cl concentration (< 0.9 wt. % Cl), the major environment is described by eudialyte, with minor contributions from sodalite, afghanite and ellestadite. At higher concentrations, the Cl environments are described by approximately equal proportions of eudialyte, ellestadite, and sodalite, with a minor contribution from afghanite and NaCl. The contribution of NaCl was present only in glass-ceramic compositions

where the nominal Cl content exceeded the solubility limit of 0.9 ± 0.1 wt. % Cl in the glass phase, leading to phase separation of crystalline NaCl, as detected by XRD and SEM-EDX (see section *7.3.1*). The contribution of NaCl in fitting the XANES data of these compositions was also consistent with the appearance of relatively sharp and characteristic XANES features attributed to crystalline NaCl, and the small observed increase in E_0, due to the significantly higher edge shift of NaCl (2826.8 eV) relative to the glass-ceramics with lower Cl concentration (ca. 2825.6 eV). Thus, the NaCl environment identified from combinatorial linear combination analysis is considered to be associated with crystalline phase separated NaCl, to first order.

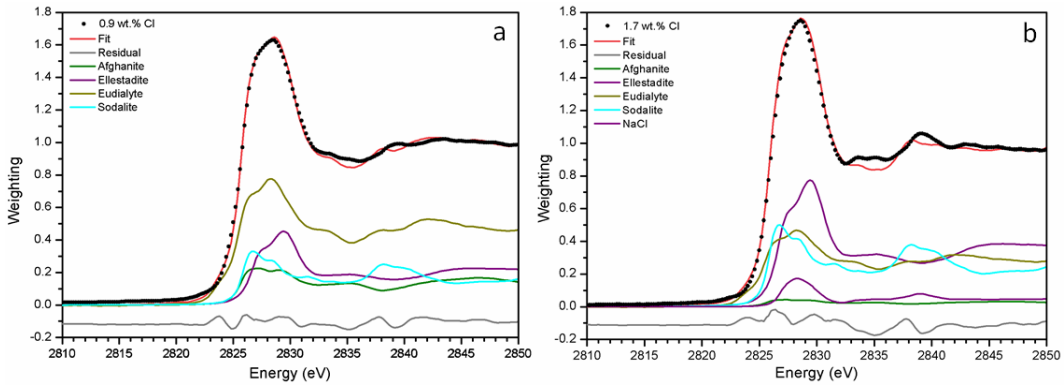

Figure 7.11: Linear combination fits with the lowest R factor for glass-ceramic compositions C and D (0.9 wt. % and 1.7 wt. % Cl, respectively). The fits show that one or more additional, unknown Cl contributions are present in the Cl K-edge XANES data, thus, a complete fit could not be obtained from the available data.

It should be stated that some caution should be taken when interpreting combination fits, which can easily be over analysed. Some limitations include the difficulty in selecting and sourcing correct standards and to know if all relevant standards have been considered. For these materials it is also difficult to know what features are indicative of crystalline sites or sites within amorphous regions.

7.3.2 CeO_2 incorporated glass-ceramic compositions

Phase assemblage and microstructure

Two glass-ceramic compositions were fabricated targeting Ce^{4+} incorporation on the Zr^{4+} sites within zirconolite ($CaZr_{0.8}Ce_{0.2}Ti_2O_7$). These compositions (F and G) were formulated

with Cl content of 0.9 wt. % and 1.7 wt. % Cl, straddling the Cl solubility limit of 0.9 ± 0.1 wt.% in the glass phase determined for the baseline compositions (A – E). Figure 7.12 and Figure 7.13 show the XRD and SEM-EDX data for the two Ce containing samples, respectively. These data show the glass-ceramic phase assemblage and microstructure to be unchanged by addition of CeO_2 to the formulation. Zirconolite ($CaZrTi_2O_7$) was obtained as the major crystalline phase with minor accessory phases zircon ($ZrSiO_4$), sphene ($CaTiSiO_5$), baddeleyite (ZrO_2) and perovskite ($CaTiO_3$, PDF card: 01-077-8911) present. The XRD data of composition G with nominal 1.7 wt. % Cl exhibited additional reflections characteristic of NaCl, which were not observed in the XRD data of composition F with nominal 0.9 wt. % Cl. SEM-EDX analysis again demonstrated the partitioning of Cl exclusively to the glass phase with no evidence of incorporation in the zirconolite phase, within precision. EDX maps revealed phase separation of NaCl in the microstructure of composition G with nominal 1.7 wt. % Cl, but not composition F, with nominal 0.9 wt. % Cl, in agreement with XRD data. The Cl content of the glass phase was determined to be 0.9 ± 0.1 wt. % for compositions F and G, respectively (Table 7.3), consistent with the Cl solubility limit of 0.9 ± 0.1 wt. % established for the glass phase in the baseline compositions, and observed phase separation of NaCl above this threshold.

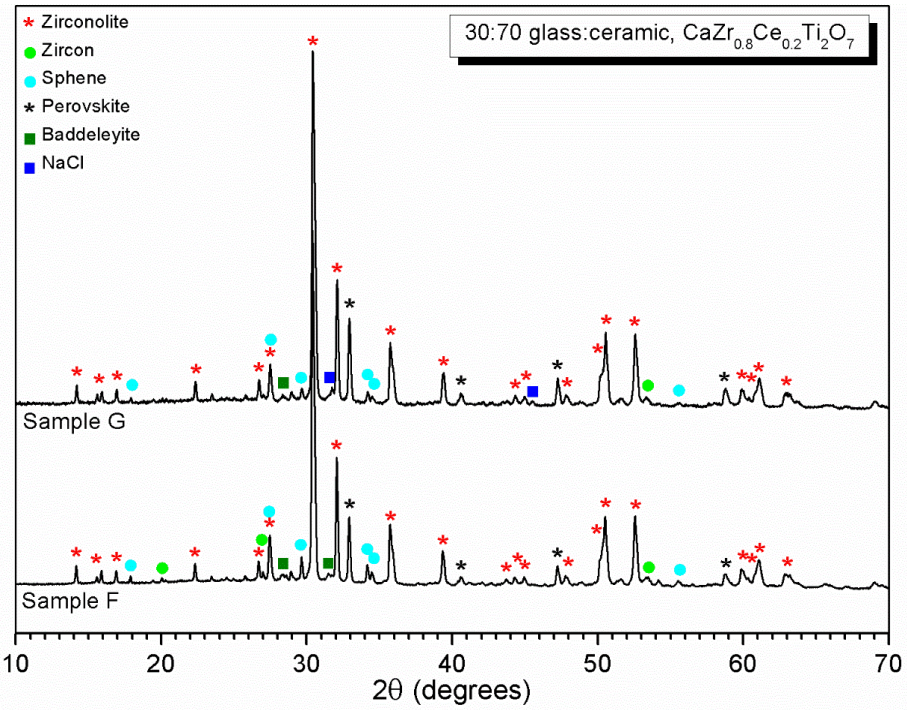

Figure 7.12: XRD data for Ce substituted $CaZrTi_2O_7$ glass-ceramics with 0.9 wt. % and 1.7 wt. % Cl additions. The formation of a perovskite phase showed some Ce reduction had taken place and is in good agreement with results for Cl-free samples [248].

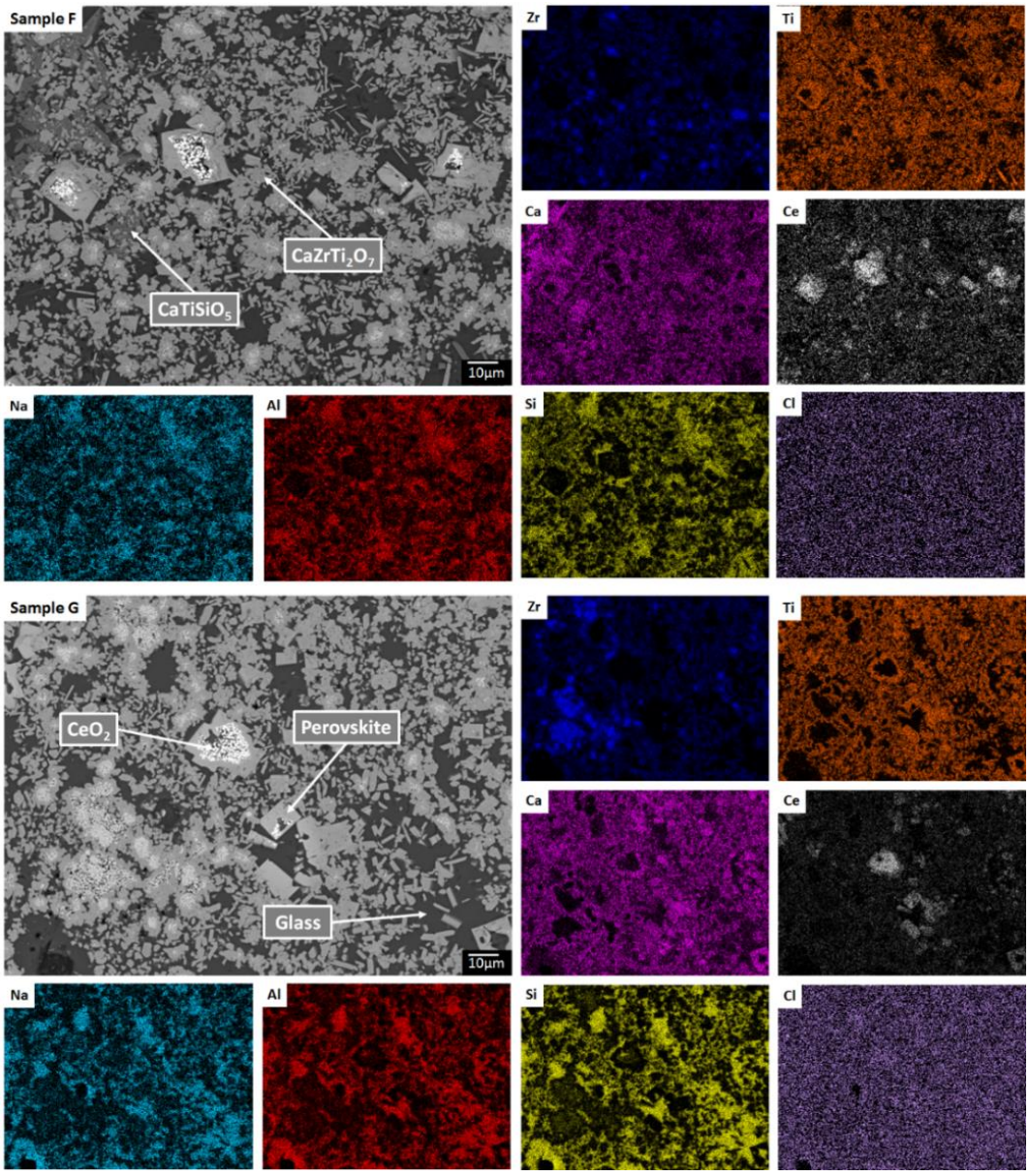

Figure 7.13: SEM-EDX of samples F and G showing the elemental distribution. Ce was preferentially incorporated in a perovskite phase and the zirconolite.

Cl K-edge X-ray Absorption Spectroscopy

Figure 7.14 and Figure 7.15 show the merged, background subtracted and normalised Cl K-edge XANES data for glass-ceramics incorporating Ce as a Pu surrogate, and, separately, data for CeOCl, $CeCl_3$ and $CeCl_3.7H_2O$ reference compounds; a three point smoothing algorithm was applied to each data set. All data from reference compounds were corrected for self-absorption using the FLUO algorithm [267].

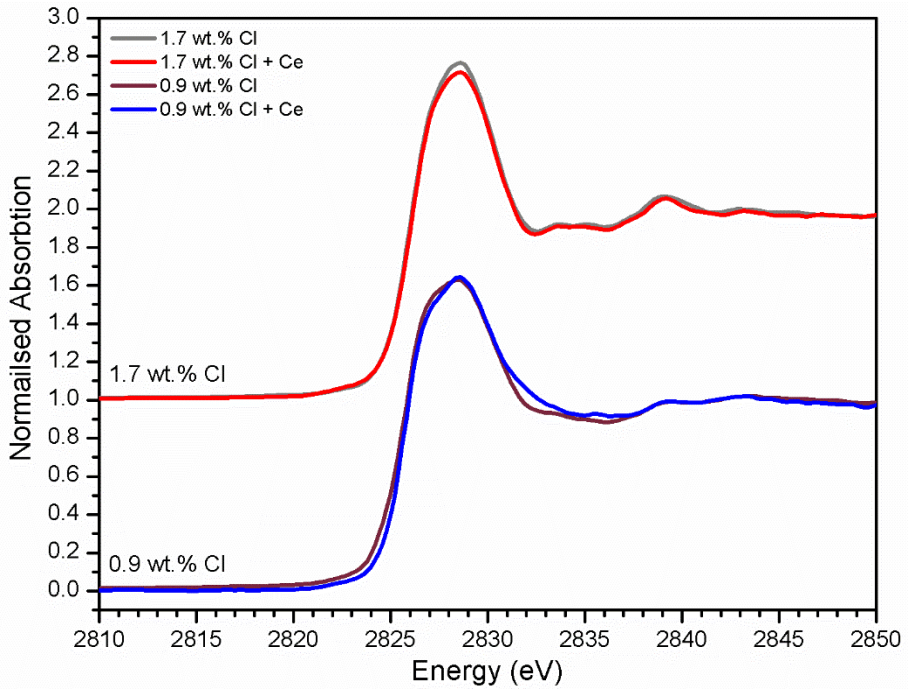

Figure 7.14: Cl K-edge XANES data for the Ce-incorporated glass-ceramic samples, either side of the identified Cl solubility limit, compared against the equivalent Ce-free glass-ceramics.

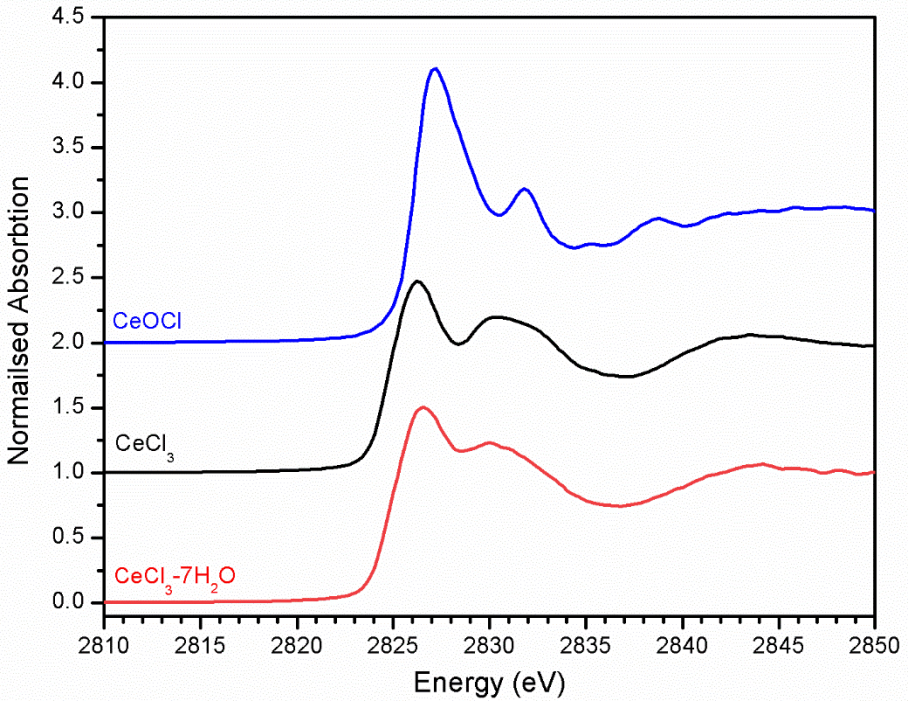

Figure 7.15: Plot showing the merged, background subtracted and normalised Cl K-edge XANES data for Ce-Cl reference materials.

The Cl XANES data of the Ce-free and Ce-incorporated glass-ceramics were very similar, as demonstrated by the comparison in Figure 7.14, for comparable nominal Cl content. The E_0 of Ce-incorporated glass-ceramics was within the range 2825.6 – 2826.8 eV, previously established for the Ce-free glass-ceramics. The similar XANES features and E_0 of the Ce-free and Ce-incorporated glass-ceramics implies a common primary Cl speciation as the Cl^- anion within the aluminosilicate glass phase, in agreement with SEM-EDX analysis (Table 7.3). Nevertheless, close comparison of the XANES features of Ce-free and Ce-incorporated glass-ceramics showed some subtle differences that suggested potentially different proportions of component Cl environments in the counterpart materials.

Combinatorial linear combination analysis was applied to the Cl K-edge XANES data of the Ce-incorporated glass-ceramic materials, with the aim of identifying and quantifying component model Cl environments. The same methodology was applied as summarised in section *7.3.1.* This analysis utilised a library of XANES data from 8 reference compounds, comprising: the four common reference compounds determined to fit the data of the Ce-free glass-ceramic materials, namely eudialyte, sodalite, ellestadite, and afghanite; plus, NaCl, CeOCl, $CeCl_3$, and $CeCl_3.7H_2O$. Figure 7.16 shows the derived mean weighted contributions of XANES data from reference compounds used to the fit the glass-ceramic data, with associated uncertainties, according to the methodology described in section *7.3.1.*

Figure 7.16 compares the weighted of reference compound contributions fitted to the Cl XANES data of Ce-free and Ce-incorporated glass-ceramics. The major environments are again of eudialyte, ellestadite, and sodalite, with a minor contribution from afghanite and NaCl. The contribution of NaCl was present only in composition G with nominal 1.7 wt. % Cl, for which phase separation of crystalline NaCl was detected by XRD and SEM-EDX (see section *7.3.2)*. For composition F, with nominal 0.9 wt. % Cl, a minor contribution of $CeCl_3$ and trace contribution of CeOCl were required to adequately fit the XANES data, implying a small fraction of Cl environments associated with Ce nearest neighbours.

Figure 7.17a and Figure 7.17b show the linear combination fits with the lowest R factor for the glass-ceramics with 0.9 wt. % Cl + Ce and 1.7 wt. % Cl + Ce. Inspection of the fit and difference profile showed that, although the sum of the 6 – 7 weighted reference data sets provided a reasonable fit to the observed data, one or more additional components were evidently required for a complete description. Consequently, our interpretation of the model

Cl environments present in the glass-ceramics is incomplete, however, the adequacy of the fit enabled consideration of the relative proportion of model Cl environments, though absolute values should be treated with due caution.

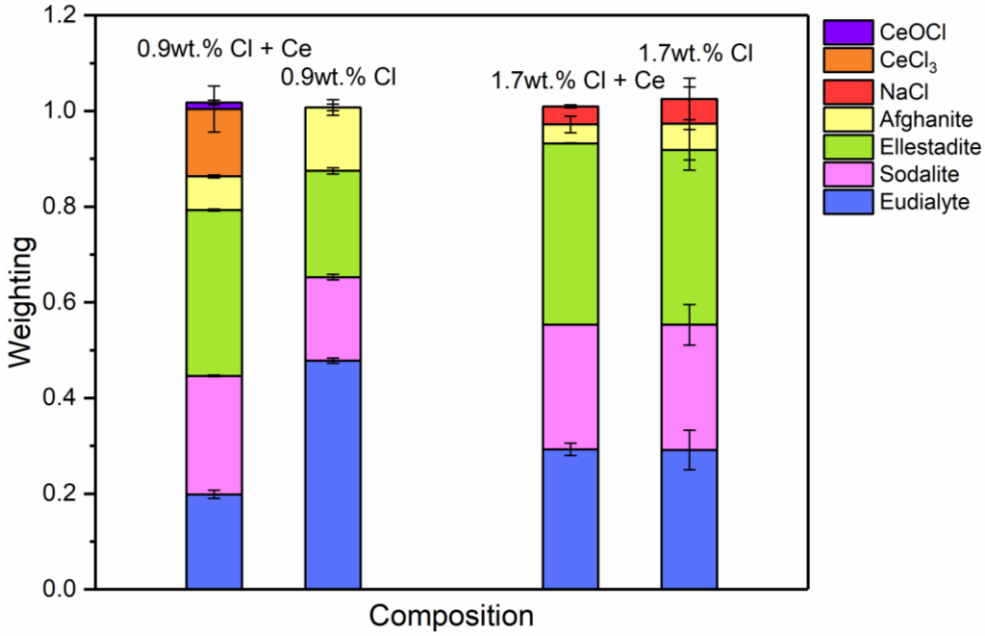

Figure 7.16: Comparison of the Ce-incorporated and Ce-free mean weighted contributions of XANES data from reference compounds CeOCl, $CeCl_3$, NaCl, afghanite, ellestadite, sodalite and eudialyte, which were used to fit the glass-ceramics data.

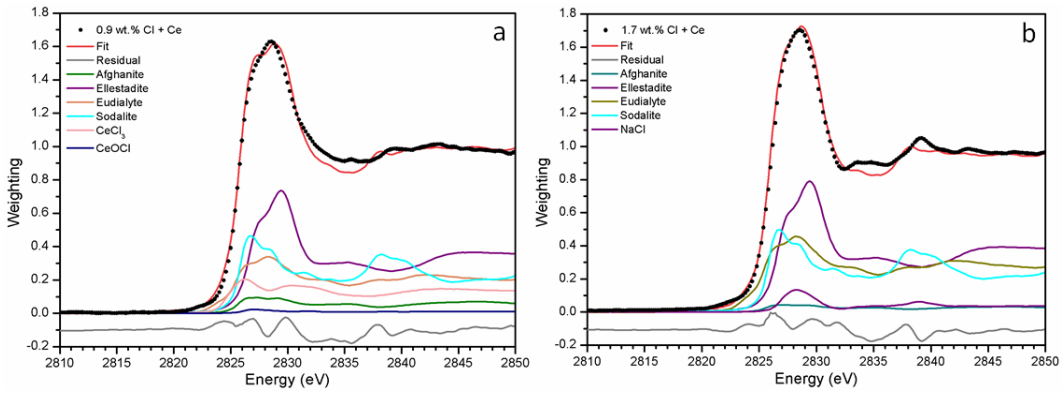

Figure 7.17: Linear combination fits with the lowest R factor for glass-ceramic compositions F and G (0.9 wt. % Cl + Ce and 1.7 wt. % Cl + Ce, respectively). The fits show that one or more additional, unknown Cl contributions are present in the Cl K-edge XANES data, thus, a complete fit could not be obtained from the available data.

7.4 Discussion

Our combined XRD, SEM-EDX and XANES data demonstrated that Cl partitions exclusively to the aluminosilicate glass phase of the zirconolite glass-ceramic formulations, below a solubility limit of 0.9 ± 0.1 wt. % Cl. Above this threshold, phase separation of NaCl occurs, as micron sized crystalline inclusions within the microstructure. In this study, NaCl was used as the Cl source, although NaCl is not considered representative of the contaminant Cl species in Pu-residues, although yet to be identified; however, its use as a Cl source is considered justified for the purpose of establishing the Cl solubility limit in the accessory glass phase. The phase assemblage and microstructure of the glass-ceramic formulation proved tolerant to Cl incorporation, with zirconolite formed as the dominant phase and trace zircon, sphene, rutile and baddeleyite present as accessory phases, independent of the Cl content. The addition of Cl to the formulation had no impact on Ce incorporation in the glass-ceramic materials, with Ce partitioning effectively to the zirconolite phase as intended; Ce also partitioned to the perovskite accessory phase present in these formulations. This behaviour is in agreement with Ce partitioning behaviour in glass-ceramic formulations reported previously, without Cl addition [248].

Our preliminary study of PuO_2 incorporation in the zirconolite glass-ceramic wasteform demonstrated that CeO_2 is an effective surrogate, achieving comparable partitioning between glass and ceramic phases [249]. The expected upper limit of Cl contamination in Pu-residue feedstock, would translate into a Cl concentration of ca. 0.4 wt. % in the aluminosilicate glass phase, well below the solubility limit established here. The current conceptual process for HIP immobilisation of plutonium residues incorporates a heat treatment facility to remove Cl contaminants prior to immobilisation, due to the uncertainty of Cl behaviour within the wasteform [25]. However, the results of this study imply that Cl contaminated Pu-residues should not require heat treatment prior to immobilisation, since the Cl inventory can be accommodated within the aluminosilicate glass phase, even at the upper limit of expectations. As such, this research could contribute to the wasteform safety case and improve the chances of these wasteforms obtaining a letter of compliance (LoC) for treatment of Pu-residues, in accordance with RWM guidelines, by providing conservative flexibility for accommodating changes in the waste feed and Cl solubility [270,271].

Processing by HIP minimises the release of volatiles to those observed during the front end pre-treatments, as the high temperature consolidation is performed in a hermetically sealed container. This must be considered when designing and optimising the front end system in order to minimise and accommodate the release of such volatiles [15]. Stewart *et al.* used HCl and PVC as sources of Cl and reported mass losses of 50 % during a 750 °C calcination and that these losses were both temperature and time dependant [146]. Stewart *et al.* determined a Cl solubility limit of 1.4 – 1.5 wt. %, but it was not clear whether or not this accounted for the volatile losses incurred. The glass-ceramic formulation studied by Stewart *et al.* utilised a higher glass fraction of 50 wt. %. Whilst the solubility limit appeared higher than that discussed in this study, the Cl solubility to glass fraction ratio between the two studies were very similar; a 0.8 wt. % Cl solubility in 30 wt. % glass fraction is ca. 3 % Cl incorporation and a 1.5 wt. % Cl solubility in 50 wt. % glass fraction is also ca. 3 % Cl incorporation. This confirms excellent agreement between the results in this study and the solubility limits reported in the literature.

These results were also in agreement with other work reported by Stewart *et al.* whom performed similar experiments on zirconolite glass-ceramics and full ceramics [42,146]. Stewart *et al.* added Cl impurities up to 1.86 wt. % with no detrimental effects on the wasteform structure or Ce incorporation and concluded that the expected Cl levels in the Pu-residues would not inhibit the incorporation of Pu into the wasteform [146].

Interpretation of Cl K-edge XANES data showed Cl to be speciated as the Cl^- anion, primarily co-ordinated to Na and Ca, within the aluminosilicate glass phase, with co-existence of several model environments characteristic of eudialyte, sodalite, ellestadite and afghanite (plus $CeCl_3$ and CeOCl). Figure 7.10 showed an increase in sodalite and ellestadite environments, with increased Cl concentration, at the expense of eudialyte and afghanite environments. Below the Cl solubility limit, the dominant Cl environment is described by eudialyte, in which Cl is co-ordinated (primarily) to 3 x Na cations, encapsulated by a framework comprised of corner sharing SiO_4, ZrO_6 and MO_n polyhedra (n = 4, 5, 6, depending on M = Fe, Mn, Nb) [272,273]. The eudialyte structure is known to be highly flexible toward isomorphic substitution, for example; Ca for Na, Al for Si, and Ti for Zr [272,273]. Thus, the local Cl environment in eudialyte is a plausible model for that in the aluminosilicate glass phase. Above the Cl solubility limit, the Cl environment is described by approximately equal

proportion of eudialyte, sodalite and ellestadite environments. In sodalite, Cl is co-ordinated to 4 x Na cations at the centre of tetrahedral clusters, encapsulated in an aluminosilicate cage [274]; whereas, in ellestadite, Cl is co-ordinated to 3 x Ca cations, within a one dimensional tunnel formed by corner sharing $(Si,S)O_4$ and CaO_9 polyhedra, with one short Cl – Cl contact along the tunnel axis [275]. A minor afghanite contribution was determined for all Cl concentrations; in the afghanite structure, there are three unique Cl environments located within the channels of the aluminosilicate framework, each comprises Cl co-ordinated to 2 x Ca cations [276]. These data imply the presence of four potential environments within the aluminosilicate glass phase of the glass-ceramics, with Cl co-ordinated to: a) 3 x Na (similar to eudialyte); b) 4 x Na (similar to sodalite); c) 2 x Ca (similar to afghanite); and, d) 3 x Ca plus 1 Cl (similar to ellestadite); however, we cannot rule out the presence of mixed Na / Ca environments, since these are not represented in our reference library. From Figure 7.10, we estimate Cl is co-ordinated, on average, to 3 ± 1 cations, independent of Cl concentration (within precision). This analysis suggests Cl has an apparent preference for co-ordination to Ca over Na, given the ratio Na_2O / CaO = 1.5 on a molar basis in the glass phase, from EDX analysis. Thus, we may conclude that Ca plays an important role in the solubility mechanism of Cl in the glass phase, through formation of Ca – Cl bonds. At low Cl concentrations, below the Cl solubility limit in the glass phase, the major eudialyte environment is correlated with the highest concentration of ZrO_2 and TiO_2 in the glass phase. The formation of sodalite and ellestadite environments at the expense of eudialyte environments, above the Cl solubility limit, is associated with the lowest concentration of ZrO_2 and TiO_2 in the glass phase. Thus, the presence of network forming ZrO_2 and TiO_2 in the glass phase also appears to be important in the solubility mechanism of Cl at low concentration, by effectively templating the local glass network to form a eudialyte like environment of corner sharing SiO_4, ZrO_6 and TiO_2 polyhedra, encapsulating (ideally) a Na_3Cl cluster. The increase in sodalite environments close to and above the Cl solubility limit, suggests that formation of Na_4Cl clusters may be the prelude to phase separation of NaCl.

The Cl environments determined in this study are in reasonable agreement with those identified in previous ^{35}Cl MAS-NMR and Cl K-edge XAS studies of aluminosilicate and aluminoborosilicate glasses [261,263,264]. Stebbins and Du investigated Cl speciation in sodium aluminosilicate glasses by ^{35}Cl MAS-NMR, including the composition $NaAlSi_3O_8$ + 1.5 wt. % NaCl (approximately between ideal glass composition C and D in this study) [264].

The ^{35}Cl chemical shift was determined to be intermediate between NaCl and sodalite, which was interpreted as evidence for between 4 – 6 Na nearest neighbours for Cl. Sandland *et al.* reported a ^{35}Cl MAS-NMR study of Na_2O-CaO-SiO_2 glasses, and concluded from analysis of chemical shift and quadrupolar coupling parameters, the presence of Cl environments with Na, Ca and both Ca and Na neighbours [261]. Baasner *et al.* investigated Cl speciation in peralkaline and peraluminous Na_2O-CaO-Al_2O_3-SiO_2 glasses using ^{35}Cl MAS-NMR [263]. For the peralkaline compositions, most relevant to this investigation, they determined the presence of Cl environments with Na, Ca and mixed Ca and Na neighbours, with a slight preference of Cl for Na over Ca [263]. McKeown *et al.*, applied Cl K-edge XAS to investigate Cl speciation in complex aluminoborosilicate glasses, for radioactive waste immobilisation [266]. Analysis of both XANES and EXAFS data suggested the dominant Cl environment to be similar to that in the mineral davyne, with Cl co-ordinated to two Ca cations; an additional $CaCl_2$ like environment, with Ca co-ordinated to 3 x Ca cations, was inferred, in compositions with high CaO content [266]. The glass compositions studied by McKeown had Na_2O / CaO > 2.0, which implies an apparent strong preference for Ca over Na.

Our data are consistent with presence of Cl co-ordination by both Na and Ca in the aluminosilicate glass phase of glass-ceramics, as determined by ^{35}Cl MAS-NMR studies of simple Na_2O-Al_2O_3-SiO_2 and Na_2O-CaO-Al_2O_3-SiO_2 glasses [261,263,264]. We cannot explicitly confirm or exclude the presence of Cl co-ordination by both Ca and Na, which is not an environment characteristic of our library of reference compounds; however, the consensus of ^{35}Cl MAS-NMR studies suggests this is likely. In contrast to the conclusion of these ^{35}Cl MAS-NMR studies, this investigation points to an apparent preference for Cl co-ordination to Ca over Na in the aluminosilicate glass phases. The aluminosilicate glass phase in this investigation also incorporates significant adventitious ZrO_2 and TiO_2, which require charge compensation by Na_2O. Consequently, the apparent preference of Cl for co-ordination to Ca over Na may arise from the limited availability of Na_2O as a result of the requirement to charge balance the incorporation of ZrO_2 and TiO_2. Such a mechanism could also explain the apparent strong preference of Cl for co-ordination to Ca rather than Na observed by McKeown *et al.* [266], since the complex waste glass compositions also contain B_2O_3 and minor oxides which would similarly require charge compensation by Na_2O.

The addition of Ce to the glass-ceramic formulation did not change the Cl environments determined to be present in the glass phase, although some minor variation in the proportion of environments was observed, consistent with changes in minor oxide concentration, see Table 7.3. The inference of a minor component of $CeCl_3$ environments below the Cl solubility limit is intriguing. Given that association of Ce and Cl was not observed by SEM-EDX, in contrast to phase separated NaCl, this implies Cl association with Ce within the aluminosilicate glass phase. In $CeCl_3$, Cl is co-ordinated to 3 x Ce cations at the apex of a flattened tetrahedron [277], whereas, in CeOCl, Cl is co-ordinated to 5 x Ce cations at the corners of a square pyramid [278]. The contribution of the eudialyte environment for the Ce-incorporated glass-ceramics was relatively low and consistent with the lower concentration of ZrO_2 and TiO_2 in the glass phase (see Table 7.3). The significant contribution of the ellestadite environment for Ce incorporated glass-ceramics again demonstrated that Ca plays an important role in the solubility mechanism of Cl in the glass phase, through formation of Ca – Cl bonds, consistent with the presence of minor CaO in the glass phase (see Table 7.3). No significant contribution of $CeCl_3$ or CeOCl environments was required to fit the XANES data of the Ce-incorporated glass-ceramic composition with 1.7 wt. % Cl, which is consistent with lower Ce content in the glass phase (see Table 7.3).

Ponader *et al.* applied Ln L_3 edge XAS to investigate the interaction of lanthanides (Ln = La, Gd, Yb) with halogens (Cl or F) in albite, sodium trisilicate, and peralkaline glasses (ideally, $NaAlSi_3O_8$, $Na_2Si_3O_7$, and $Na_{3.3}AlSi_7O_{17}$, respectively) [279]. In fluoride containing glasses, Ln-F complexes were formed, whereas no evidence was found for Ln-Cl complexes in chloride containing glasses. As demonstrated by Ponader *et al.*, the extended X-ray absorption fine structure (EXAFS) is sufficiently sensitive to differentiate LnO_8 and $LnCl_8$ species, due to the large difference in phase shift arising from O and Cl backscattering atoms. Although EXAFS data could be fitted using models involving mixed Ln-O/Cl co-ordination, the goodness of fit was significantly lower than models involving only Ln-O co-ordination. The proportion of Cl – Ce environments determined in our study, ca. 15 % of total, is consistent with dominant Ln – O co-ordination in chloride bearing aluminosilicate glasses, in agreement with Ponader *et al.*, and is expected to be at the margin of significance in analysis of Ln L_3 EXAFS data acquired from such disordered materials.

7.5 Conclusions

The fabrication and characterisation of glass-ceramics with Cl additions has been successfully demonstrated and a Cl solubility of 0.9 ± 0.1 wt. % was determined within the aluminosilicate glass phase. This solubility limit was substantially greater than the maximum Cl levels expected in the contaminated PuO_2 wastes, thus confirmed that the Cl contaminants could be sufficiently accommodated within the aluminosilicate glass matrix of the glass-ceramic wasteform, without the requirement of waste pre-treatment.

Whilst XRD confirmed the Cl did not affect the crystalline phase assemblage of the glass-ceramic, SEM-EDX confirmed the CeO_2 incorporation and partitioning behaviour was also unaffected. SEM-EDX analysis confirmed the overwhelming partitioning of the Cl into the glass phase, which, when coupled with the partitioning of actinides into the ceramic phase, confirmed the stabilisation of Cl and Pu in separate phases is possible within the wasteform. This is important to ensure the long term integrity and radionuclide retention properties of the actinide wasteform, and further work should include leach tests to determine if there is any effect on the samples durability as a result of the Cl present.

The Cl K-edge XANES data was consistent with the XRD and SEM-EDX data by highlighting the presence of Cl environments similar to NaCl above the 0.9 ± 0.1 wt. % solubility limit. Through combinatorial linear combination fittings against multiple reference compounds, it was found that Cl was predominantly associated with Na and Ca within the aluminosilicate glass matrix. This was in excellent agreement with the literature, which also reports Cl association with Na and Ca together. Whilst such environments could not be confirmed or denied, it was suggested that Ca – Cl environments were preferential to Na – Cl environments as a result of Na_2O stabilising ZrO_2 and TiO_2 within the glass. These results were in excellent agreement with previous studies and prove promising that Cl impurities will not affect the immobilisation of Pu in these glass-ceramic wasteforms.

8 Uranium and Plutonium incorporation

A preliminary validation study of PuO_2 incorporation into zirconolite glass-ceramics

Stephanie M. Thornber[a], Martin C. Stennett[a], Eric R. Vance[b], Dorji T. Chavara[b], Ian Watson[b], Miodrag Jovanovic[b], Joel Davis[b], Daniel Gregg[b] & Neil C. Hyatt[a,*]

[a]*Immobilisation Science Laboratory, Department of Materials Science & Engineering, The University of Sheffield, Sir Robert Hadfield Building, Mappin Street, Sheffield S1 3JD, UK*

[b]*The Australian Nuclear Science and Technology Organisation, Kirrawee DC, Locked Bag 2001, NSW 2231, Australia*

Author contributions: Stephanie M. Thornber designed and developed the experimental matrix, fabricated and characterised the U samples, analysed all U and Pu samples and wrote the scientific report. Eric R. Vance, Dorji T. Chavara, Ian Watson, Miodrag Jovanovic and Joel Davis provided guidance and support during the placement and conducted some of the experimental work where the student was not cleared to do so (i.e. preparation of PuO_2 powders, operation of the HIP, preparation of PuO_2 samples and operation of the SEM for PuO_2 analysis). Daniel Gregg provided supervision and project oversight whilst at ANSTO and Neil C. Hyatt provided project oversight and supervision from UoS.

The data in this Chapter was collected during a 4 month research placement at the Australian Nuclear Science and Technology Organisation (ANSTO) in New South Wales, Australia. This work was done in collaboration with ANSTO and was funded by ANSTO and the Nuclear Decommissioning Authority (NDA). The author would like to acknowledge all those involved in the project including; the funding bodies, Neil Hyatt and David Cartledge at UoS, Daniel Gregg, Lou Vance, Gerry Triani, Julie Nelson, Dorji Chavara, Ian Watson, Tim Palmer, Miodrag Jovanovic, Neil Webb and Yingjie Zhang at ANSTO, who all contributed to the outcome of the placement.

8.1 Introduction

Due to the hazards associated with working with Pu and the cost of fabricating and characterising these Pu-bearing materials, it was important to gain as much information as

possible on the waste incorporation behaviour of the glass-ceramics through surrogate studies, before fabricating the PuO_2 samples. Whilst it is essential practice to utilise inactive actinide surrogates in research, all surrogates have their limitations. Ce has a higher reduction potential than Pu and reduces more readily than Pu under waste processing conditions [244,280]. Similarly, U can obtain U^{5+} and U^{6+} oxidation states in conditions experienced in nuclear wasteforms, however, Pu would only obtain these oxidation states under highly oxidising conditions [280,281]. As a result, surrogates do not always provide an accurate representation of Pu behaviour within the target wasteform. When progressing from inactive surrogates, such as CeO_2, UO_2 is often used as a radioactive surrogate. This chapter discusses the fabrication and characterisation of U-bearing HIP samples that investigated waste incorporation and charge compensation mechanisms when targeting different stoichiometric substitutions, before the characterisation of PuO_2 doped samples.

Three U doped samples were fabricated with stoichiometries chosen based on the results of the Ce incorporation experiments discussed in Chapter 6. The samples targeted U^{4+} substitution on either the Ca or Zr sites with appropriate charge compensation mechanisms. One sample also included CeO_2 and targeted Ce^{3+} incorporation. The results from Chapter 6 revealed the preferential formation of a Ce-rich perovskite phase over the incorporation of Ce^{3+} into the zirconolite or glass phases. The CeO_2 was included in the U experiments to assess the potential of Ce^{3+} (as a Pu^{3+} surrogate) to trigger perovskite formation.

The results from the U samples allowed for an informed decision on the choice of composition for fabrication of the Pu samples. Before progressing to the Pu-doped HIP samples, a cold-press and sinter sample was fabricated and characterised to evaluate the reactivity of the PuO_2. These results provided a suitable test bed of data to confirm successful reactions and waste digestion.

The Pu HIP samples discussed are part of a five sample matrix that investigate the fundamental mechanism of Pu partitioning in the glass-ceramic under controlled oxygen fugacity. The same formulation will be utilised for all five Pu samples, which are to be fabricated with different redox agents and canister materials. Whilst it is known that glass-ceramics immobilise actinides by partitioning them into the ceramic phase, the effect of redox conditions on the behaviour of the Pu and this partitioning mechanism, has not been studied in detail. A recent paper by Zhang *et al.* discussed a similar set of Pu doped HIP

samples, however the starting formulations utilised CaF_2 as a waste digesting agent [143]. Such samples were prepared via a sol gel route as opposed to the dry oxide route utilised throughout this thesis. Zhang *et al.* studied the Pu valence and incorporation behaviour when under controlled oxygen fugacity by adding Ni / NiO and Fe / FeO buffer systems [143]. The samples discussed in this chapter are part of a bigger matrix that investigates the effect of Ni / NiO, Fe / FeO and Ti / TiO reducing agents and different waste loadings, on a glass-ceramic system more suitable for Pu disposition (high ceramic fraction prepared via a dry oxide route) and that does not contain CaF_2. The work of Zhang *et al.* will provide an almost direct comparison to see if there are any major discrepancies when utilising the different preparation method and when not using CaF_2 as a waste digestion agent. In this chapter, the first two Pu HIP samples of the whole five sample matrix are discussed[vi].

8.2 Experimental

8.2.1 Uranium samples

The inactive starting precursors; $CaTiO_3$, TiO_2, ZrO_2, SiO_2, Na_2SiO_3 and Al_2O_3, were dried at 200 °C overnight prior to batching. The starting compounds were the same as those used for all inactive samples fabricated at the UoS in order to maintain consistency. Three uranium samples were fabricated with target stoichiometries listed in Table 8.1. Each sample was batched at 100 g and milled in a 500 ml volume, ZrO_2 lined, stainless steel mill pot using a Retsch PM 100 planetary mill. Each batch was milled with 70 ml of isopropanol for 30 min at 500 rpm with 3 min intervals every 5 min. After drying overnight, the powders were sieved ready for transfer to the Material Fabrication Bay (MFB) where the U_3O_8 was added.

[vi] The samples discussed in this chapter were consolidated and analysed during the placement at ANSTO. The collaboration with ANSTO continues to fabricate and characterise the remaining samples of the whole matrix.

Table 8.1: Target stoichiometries for the U containing samples. All samples were formulated with 30 wt. % glass of target composition $Na_2Al_2Si_6O_{16}$.

Sample	Ceramic Target Stoichiometry	Precursors	Mass for 100 g batch (g) (±0.005)
SW-1803	$CaZr_{0.8}U_{0.2}Ti_2O_7$	$CaTiO_3$	25.683
		ZrO_2	18.623
		TiO_2	15.088
		U_3O_8	10.606
		SiO_2	17.185
		Na_2SiO_3	6.983
		Al_2O_3	5.833
SW-1804	$Ca_{0.8}U_{0.2}ZrTi_{1.6}Al_{0.4}O_7$	$CaTiO_3$	20.443
		ZrO_2	23.162
		TiO_2	12.010
		U_3O_8	10.553
		SiO_2	17.185
		Na_2SiO_3	6.983
		Al_2O_3	9.666
SW-1805	$(Ca_{0.95}Ce_{0.05})(Zr_{0.8}U_{0.15}Ce_{0.05})Ti_2O_7$	$CaTiO_3$	24.374
		ZrO_2	18.605
		TiO_2	15.827
		U_3O_8	7.947
		CeO_2	3.248
		SiO_2	17.185
		Na_2SiO_3	6.983
		Al_2O_3	5.833

U_3O_8 was selected as the uranium source due to the low reactivity of the available UO_2 source. The UO_2 inventory at ANSTO had undergone high temperature heat treatments making the UO_2 structure very stable and unreactive. The PuO_2 stockpile and Pu-residue materials that we are trying to represent, have not undergone any high temperature heat treatments and are thus highly reactive. It was therefore decided to use the U_3O_8 compound for its higher reactivity to assist incorporation within the glass-ceramic matrix. As such, dense UO_2 pellets were voloxidised in a furnace at 700 °C for 8 h. Voloxidation is a dry heat treatment process commonly used to separate spent fuel pellets from cladding and create a free flowing powder [282]. The voloxidation step resulted in oxidation of the UO_2 pellets, which broke down into a powder of U_3O_8. Figure 8.1 and Table 8.2 show the U_3O_8 before and after this process and the mass change observed.

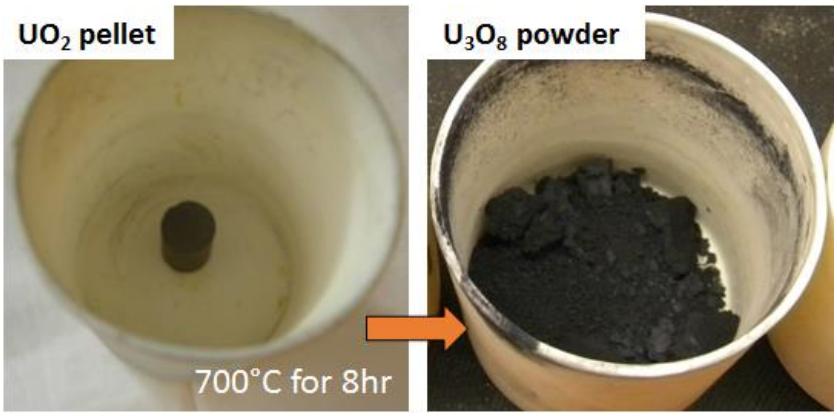

Figure 8.1: UO_2 pellet before and after voloxidation at 700 °C for 8 h resulting in the U_3O_8 powder.

The U_3O_8 was weighed out for a 50 g sample and added to half of the precursor batches (totalling 50 g of each batch). The U_3O_8 was gently mixed into the batch until a uniform colour was achieved and the powder was transferred into ball mill pots. Each batch was ball milled with 300 g of milling media and a sufficient amount of cyclohexane to produce a slurry during milling. The samples were ball milled overnight for approximately 18 h. The milled powders were washed out of the pots with more cyclohexane and were dried in a fume hood on hot-plates set at 80 °C. The dried powders were calcined at 700 °C for 3 h under a 3.5 % H_2/N_2 reducing atmosphere to convert the reactive U_3O_8 back to UO_2 to obtain the U^{4+} oxidation state, representative of Pu^{4+}. Table 8.3 summarises the mass loss observed during the calcination process.

Table 8.2: Increase in mass during voloxidation of the UO_2 pellets to U_3O_8. UO_2 pellets were heated at 700 °C for 8 h.

Sample	Mass of empty crucible (g) (±0.05)	Mass of pellet (g) (±0.05)	Total mass of crucible + pellet before (g) (±0.05)	Total mass of crucible + pellet after (g) (±0.05)	Mass of powder after (g) (±0.05)	% Mass increase (±0.2) (expected increase)
A	94.49	28.29	122.78	123.91	29.42	3.6 (3.95)
B	75.74	30.46	106.20	106.89	31.15	2.3 (3.95)
C	67.35	26.07	93.42	94.45	27.10	4.0 (3.95)
	Total	84.82			87.67	

Table 8.3: Mass loss observed during the calcination step of the uranium batches. Powders were calcined at 700 °C for 3 h under 3.5 % H_2/N_2 reducing atmosphere. Ti powder was added after the calcination, before packing the HIP canisters.

Sample	Mass of crucible (g) (±0.05)	Mass of crucible + powder before (g) (±0.05)	Mass of powder before (g) (±0.05)	Mass of crucible + powder after (g) (±0.05)	Mass of powder after (g) (±0.05)	% Mass Loss (±0.2) (expected increase)	Addition: 2 wt. % Ti powder (g) (±0.05)
SW-1803	75.72	118.87	43.15	117.38	41.66	-3.5 (-3.95)	0.83
SW-1804	67.35	115.31	47.96	113.54	46.19	-3.7 (-3.95)	0.92
SW-1805	94.49	140.58	46.09	138.98	44.49	-3.5 (-3.95)	0.89

The HIP canisters were fabricated from 304 stainless steel and had 316 stainless steel filters. Three 10 g pellets were pressed and inserted into each HIP canister. Loose powder was packed around each pellet to minimise the annular gap between the pellet and the canister wall. The welded canisters were evacuated simultaneously at 100 °C before increasing the bake-out temperature to 300 °C[vii]. After cooling overnight the canisters were crimped and sealed. The total evacuation and bake-out period was 48 h with a final vacuum pressure of 20 mTorr achieved.

The canisters were loaded into an alumina crucible placed inside ANSTO's Activity Containment Overpack (ACOP) designed to contain any free radioactive powders in the event of a ruptured canister [283,284]. The ACOP (discussed in Chapter 9) was loaded into the centre of the molybdenum furnace. The HIP used was an AIP10-30H model with a working zone of 15 x 30 cm. The structure of the HIP and loading / unloading process was the same as the smaller HIP at UoS except with an automated top-loader to lift the top screw head. The samples were HIPed at 1250 °C under 100 MPa of pressure for 4 h.

Analysis

Figure 8.2 shows a U HIP canister before and after consolidation and Table 8.4 summarises the dimensional changes and densifications achieved. The HIP canisters were sectioned on a slow saw using a low concentration diamond blade to retrieve monolith samples for SEM and XRD. XRD samples were prepared to a P500 grit finish for a flat and uniform finish. Each sample was characterised on a BRUKER D8 Advance diffractometer between $10° \leq 2\theta \leq 80°$ for 20 h, with Cu Kα radiation (1.5418 Å). SEM samples were cold mounted in epoxy resin and set at 35 °C overnight. The sample was ground and polished from a P500 grit SiC paper, 15 µm diamond paste on a hard Pellon polishing cloth, 3 µm diamond paste on a silk polishing cloth and a 1 µm diamond paste finish on a synthetic velvet cloth. Each polishing step was done with a non-polar Chemlube lubricant for 5 min at 150 rpm with 20 N of force. The samples were carbon coated before SEM analysis. SEM data were collected on a Zeiss

[vii] The 100 °C was standard bake-out procedure at ANSTO whilst the higher 300 °C bake-out condition was consistent with the optimised procedure utilised throughout this project. Starting at the lower temperature would not impact the final sample quality as all volatiles were removed as the temperature was increased, but it may have increased the total bake-out period to remove the volatiles.

Ultraplus microscope using 15 kV accelerating voltage, at a 14 mm working distance. A built-in Oxford Instruments X-Max 80 mm^2 silicon drift detector was used for semi-quantitative compositional analysis.

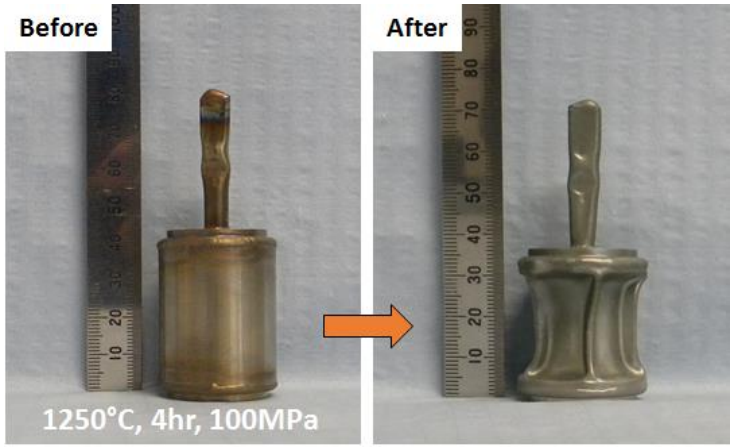

Figure 8.2: U HIP canister before and after consolidation at 1250 °C, 4 h under 100 MPa of pressure.

Table 8.4: Summary of canister dimensions before and after HIPing and the calculated densifications. Samples SW-1803, SW-1804 and SW-1805 are U loaded HIP samples. Samples SW-1811 and SW-1812 are Pu loaded HIP samples.

Sample	Mass before (g) (±0.05)	Height before (mm)	Middle diameter before (mm)	Volume displacement before (g/cm^3)	Mass after (g) (±0.05)	Height after (mm)	Middle diameter after (mm)	Volume displacement after (g/cm^3)	Canister densification %
SW-1803	103.43	42.9 (±0.4)	30.5 (±0.2)	27 (±0.5)	103.47	37 (±1.6)	24 (±1.5)	18 (±0.5)	33 (±1)
SW-1804	104.44	42.8 (±0.3)	30.6 (±0.1)	27 (±0.5)	104.47	36 (±0.6)	23 (±1.5)	18 (±0.5)	33 (±1)
SW-1805	101.42	42.9 (±0.2)	30.5 (±0.1)	27 (±0.5)	101.44	36 (±1.0)	24 (±3.2)	16 (±0.5)	41 (±1)
SW-1811	30.09	27.4 (±0.2)	17.0 (±0.1)	6.3 (±0.2)	30.10	24 (±1.4)	13.3 (±0.8)	3.9 (±0.3)	39 (±1)
SW-1812	30.66	27.4 (±0.2)	17.0 (±0.1)	6.4 (±0.2)	30.66	13 (±1.4)	24.1 (±0.8)	5.2 (±0.3)	18 (±1)

8.2.2 Plutonium samples

The precursor batches were prepared in the same way as for the U batches described above. 15 g batches were prepared and milled with 12 ml of isopropanol. The dried, homogeneous batches was weighed out for 10 g samples, to add the PuO_2 directly to the precursor mix. The powders were transferred to the actinide suite for addition of the PuO_2 and for canister packing, evacuation and sealing. Two waste loadings were investigated, first 5 wt. % PuO_2 targeting 0.1 f.u. substitution and second, 10 wt. % PuO_2 targeting 0.2 f.u. substitution, see Table 8.5.

Table 8.5: The target stoichiometry and mass of oxide precursors for a 10 g Pu doped batch, targeting two waste loadings.

Target formulation:	**$Ca(Zr_{0.9}Pu_{0.1})Ti_2O_7$**	**$Ca(Zr_{0.8}Pu_{0.2})Ti_2O_7$**
Precursors	**Mass for 10g (g)** ($\pm$0.005)	**Mass for 10g (g)** ($\pm$0.005)
SiO_2	1.719	1.719
Na_2SiO_3	0.698	0.698
Al_2O_3	0.583	0.583
$CaTiO_3$	2.690	2.582
TiO_2	1.558	1.517
ZrO_2	2.194	1.872
PuO_2	0.536	1.029

The PuO_2 was added to the precursors as a dry oxide powder and was mechanically stirred to achieve homogeneity. The powders were calcined at 750 °C for 3 h in an argon atmosphere before being pressed into pellets. A total of 5.0 g and 5.9 g of powder was used to fill the canisters, of approximately 4 ml internal volume. The canisters were evacuated at room temperature and at 300 °C before sealing. The canisters were sealed and decontaminated before removal from the glovebox. The Pu samples were contained within ANSTO's ACOP [283,284] and HIPed at 1250 °C for 4 h under 100 MPa of pressure.

Plutonium sinter

To verify the PuO_2 reactivity, 0.5 g of the remaining batch material was pressed into a pellet and sintered in a muffle furnace at 1250 °C for 4 h in an air atmosphere. The sintered sample

was analysed by SEM and XRD, to gain information on the PuO_2 reactivity before processing the larger scale HIP samples.

Analysis

Figure 8.3 shows a Pu HIP canister before and after consolidation and Table 8.4 summarises the dimensional changes and densifications achieved. Sectioned samples were analysed by SEM and XRD. A carbon coated, resin mounted sample, polished to a 1 µm finish, was analysed on a JEOL 6300 scanning electron microscope with a 15 kV accelerating voltage. A Tracor Northern TN5502 energy-dispersive X-ray detector was used for semi-quantitative compositional analysis. X-ray diffraction was conducted on a BRUKER D8 diffractometer with Cu Kα radiation (1.5418 Å). The patterns were collected over 20 h between $10° \leq 2\theta \leq 80°$ with a 0.02° step size.

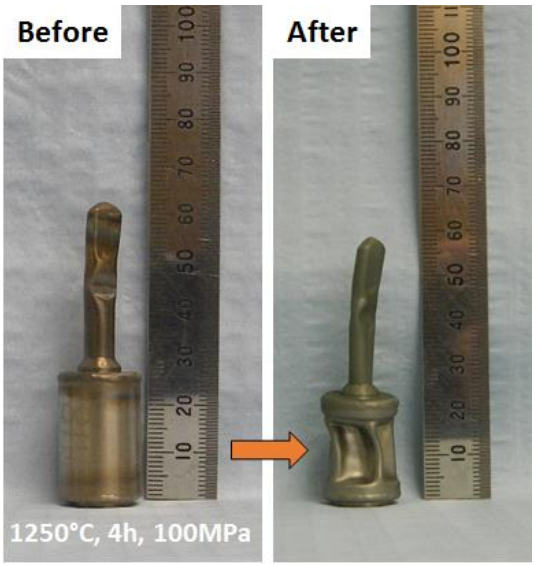

Figure 8.3: Pu HIP canister before and after processing at 1250 °C for 4 h under 100 MPa of pressure.

8.3 Results

8.3.1 Uranium samples

Powder X-ray diffraction confirmed complete voloxidation of the UO_2 pellets to U_3O_8 powder as shown in Figure 8.4. The diffuse scattering at lower angles was a result of the domed lid used to contain the powder and avoid contamination of the XRD machine.

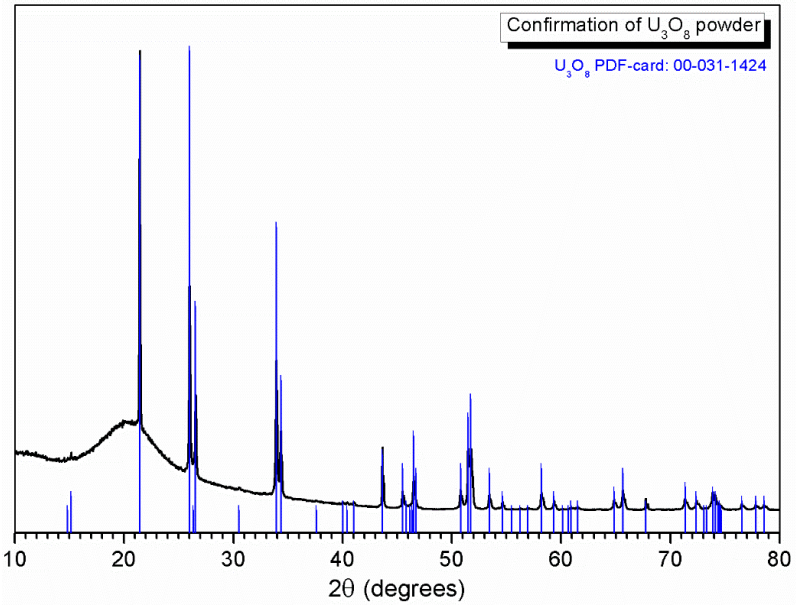

Figure 8.4: XRD data confirming single phase U_3O_8 was achieved after heating at 700 °C for 8 h.

SEM and XRD showed zirconolite was the major crystalline phase in all three U doped samples. XRD confirmed zirconolite ($CaZrTi_2O_7$), rutile (TiO_2) and a magneli phase (Ti_3O_5) were common to all three samples (PDF-cards: 00-054-1132, 04-008-7849, 01-082-1137, respectively). In addition, SW-1804 had minor phases; albite ($NaAlSi_3O_8$), sphene ($CaTiSiO_5$) and uraninite (UO_2) (PDF cards: 01-071-1150, 01-085-0395, 01-073-1715, respectively) and SW-1805 had minor phases; sphene, baddeleyite (ZrO_2) and perovskite ($CaTiO_3$) (PDF-cards: 01-085-0395, 01-089-9066 and 01-089-0056, respectively).

Further study of the zirconolite peaks led to the conclusion that the zironolite-3T structure had formed rather than the monoclinic zirconolite-2M structure. The absence of reflections at low angles implied a lack of the zirconolite-2M structure and the presence of the diagnostic reflection at $2\theta = 15.8°$ matched the zirconolite-3T PDF-card (00-054-1132). It must be noted that due to the lack of available refined data on the structure of zirconolite-3T, this PDF-card was only quality marked *blank*. That said, from the lack of peaks at low angles, and after review of the literature [106,110,112], it was concluded that the trigonal structure was obtained as a result of the U substitutions.

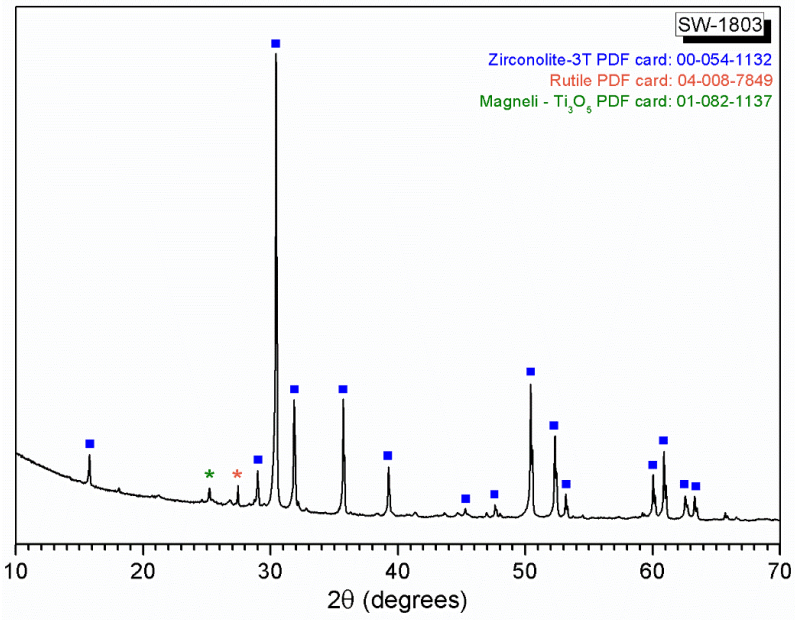

Figure 8.5: XRD plot of SW-1803. Major phase zirconolite-3T with minor phases; rutile (TiO_2) and magneli phase (Ti_3O_5) (PDF cards: 00-054-1132, 04-008-7849 and 01-082-1137, respectively).

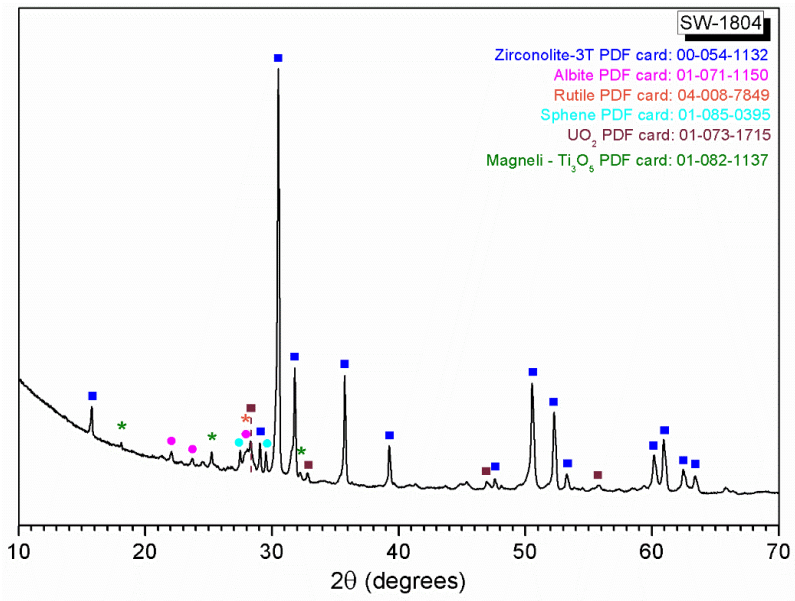

Figure 8.6: XRD plot of SW-1804. Major phase zirconolite-3T with minor phases; albite ($NaAlSi_3O_8$), rutile (TiO_2), sphene ($CaTiSiO_5$), uranium dioxide (UO_2) and magneli phase (Ti_3O_5) (PDF cards: 00-054-1132, 01-071-1150, 04-008-7849, 01-085-0395, 01-073-1715 and 01-082-1137, respectively).

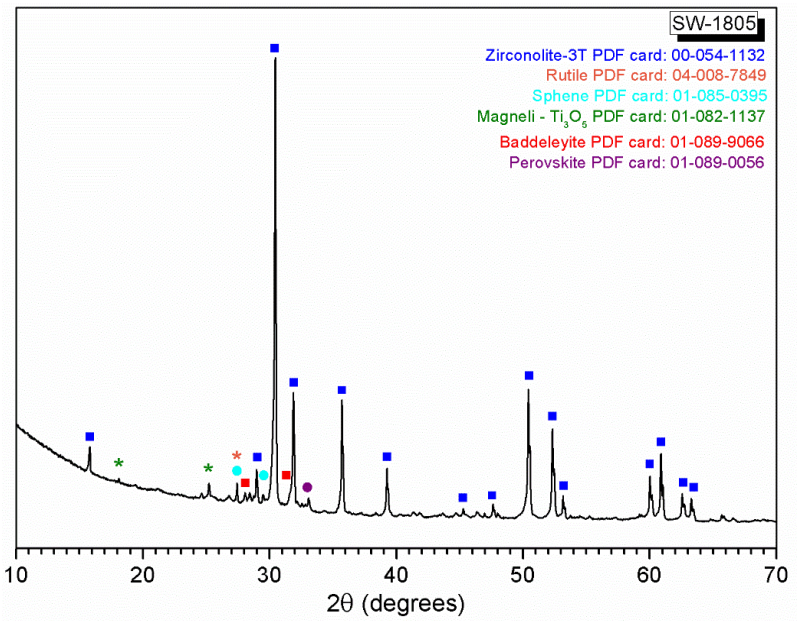

Figure 8.7: XRD plot of SW-1805. Major phase zirconolite-3T and minor phases; rutile (TiO_2), sphene ($CaTiSiO_5$), magneli phase (Ti_3O_5), baddeleyite (ZrO_2) and perovskite ($CaTiO_3$) (PDF cards: 00-054-1132, 04-008-7849, 01-085-0395, 01-082-1137, 01-089-9066 and 01-089-0056, respectively).

SEM / SEM-EDX revealed zirconolite grains uniformly distributed throughout sample SW-1803. Large TiO_2 particles were observed, indicative of oxidised Ti-metal particles that were added for redox control. Amongst the zirconolite, smaller grains of TiO_2 were also identified. It was presumed that small Ti-metal particles were incorporated into the glass-ceramic melt and precipitated as TiO_2 (rutile) during cooling. Such precipitation was observed and discussed in Chapter 5. From the BSE micrographs in Figure 8.8 and EDX maps in Figure 8.9, it was clear, excellent U incorporation was achieved ($CaZr_{0.8}U_{0.2}Ti_2O_7$), with only minor bright spots of UO_2 observed in some zirconolite crystals.

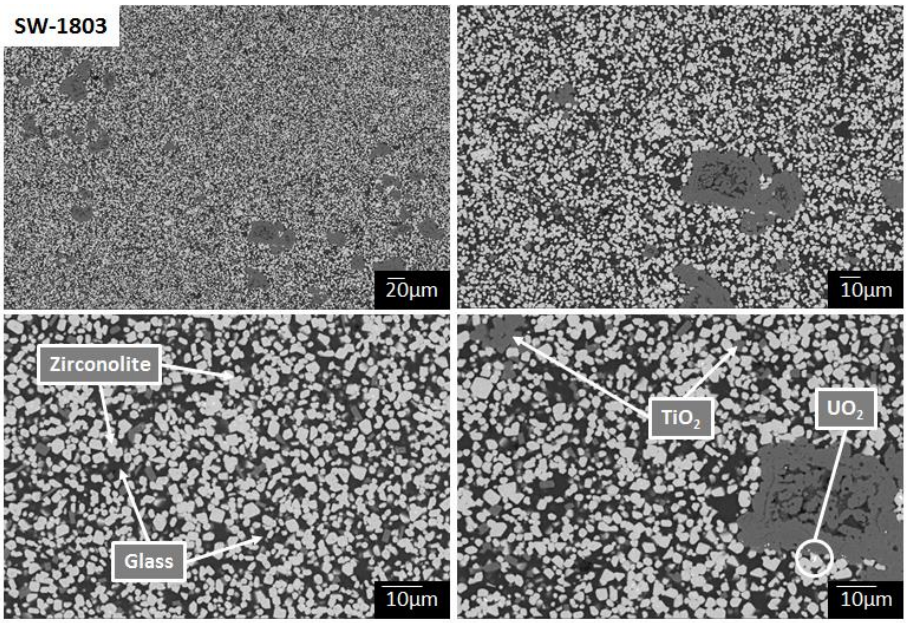

Figure 8.8: BSE micrographs for SW-1803 ($CaZr_{0.8}U_{0.2}Ti_2O_7$). Zirconolite crystals were uniformly distributed as the major crystalline phase, with minor TiO_2 crystals distributed amongst the zirconolite grains as well as large TiO_2 particles from the Ti-metal added for redox control.

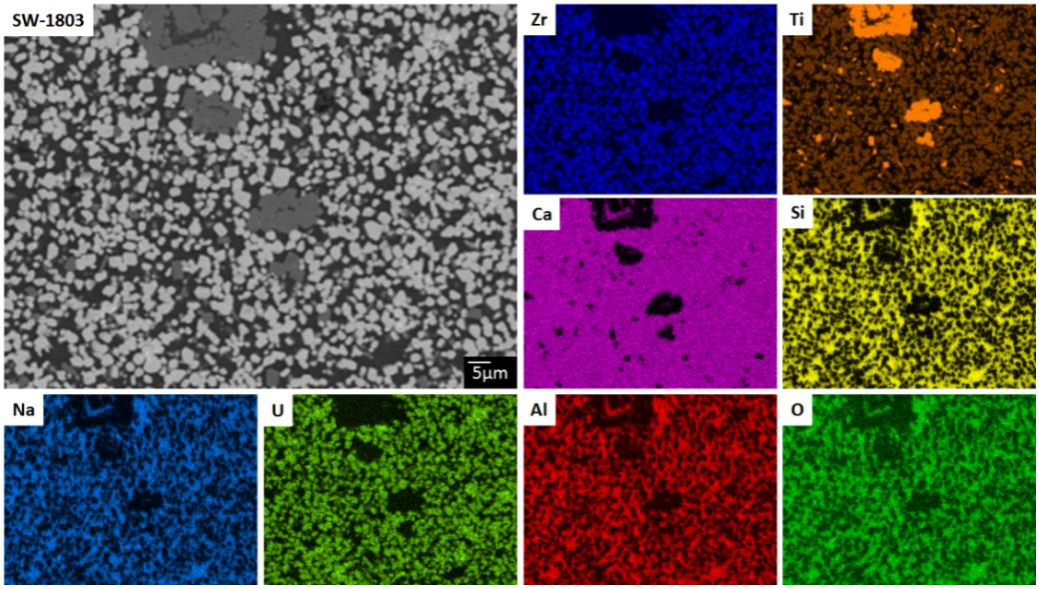

Figure 8.9: SEM-EDX elementals map for SW-1803 showing clear partitioning of the U into the zirconolite phase.

When targeting U^{4+} substitution on the Ca site (SW-1804), Al^{3+} acted as the charge compensator on the Ti sites. The BSE micrographs in Figure 8.10 clearly show excellent U

incorporation, although inferior compared to sample SW-1803. The bright hotspots at the centre of zirconolite grains, identified as UO_2 by SEM-EDX, were both larger and more abundant. A few large UO_2 particles were also seen. These large grains are thought to be artefacts of the voloxidation process when preparing the U_3O_8 powders. Although XRD confirmed the UO_2 pellets had been fully converted to U_3O_8, one pellet still contained coarse, hard particles that were crushed with a pestle and mortar. It is possible, some of these coarse grains were included in the HIP sample. The effect of waste particle size on the success of incorporation into zirconolite glass-ceramics was studied by Maddrell [154] who showed coarser waste particles inhibited their digestion into the matrix. It should be noted however, that the number of these large particles was few and far between thus do not give a fair representation of the waste incorporation into the glass-ceramic formulation.

The grain size of the zirconolite crystals in SW-1804 was smaller than samples SW-1803 and SW-1805, with some zirconolite grains sub-micron in size. Coupled with the slightly reduced U incorporation, this indicates slower reaction kinetics in the melt. Due to the already highly refractory glass composition ($Na_2Al_2Si_6O_{16}$), the additional Al_2O_3 made the melt more refractory and resulted in an increase in viscosity. This inhibited the diffusion of elements through the melt as well as crystal growth, thus, resulting in a finer grain size and reduced waste digestion. SEM-EDX analysis also revealed variations in the glass phase composition. This is further evidence that the additional Al_2O_3 led to reduced kinetics and diffusion rates through the melt, resulting in a heterogeneous glass phase.

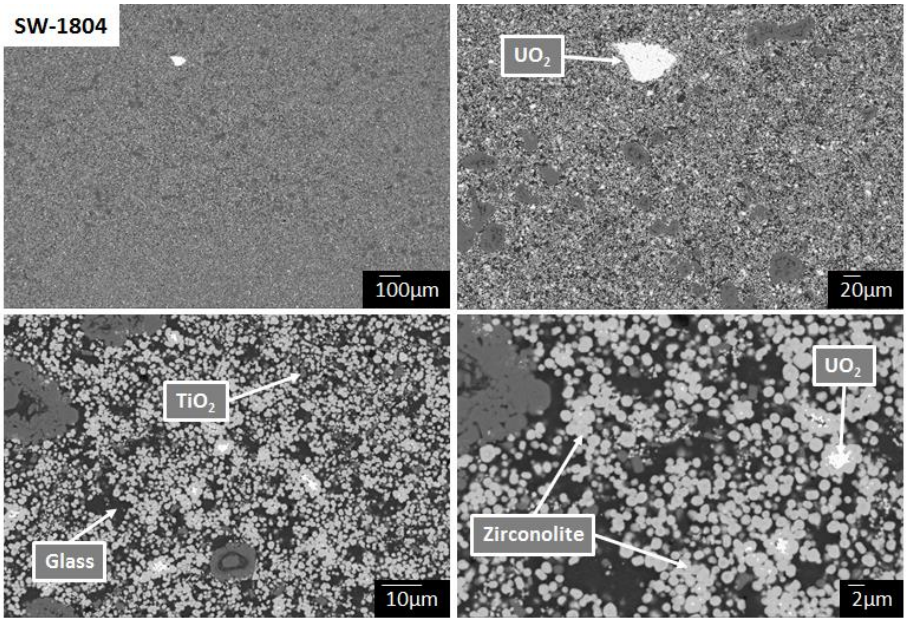

Figure 8.10: BSE micrographs for SW-1804 ($Ca_{0.8}U_{0.2}ZrTi_{1.6}Al_{0.4}O_7$). Zirconolite was the major crystalline phase and have a very fine grain size. UO_2 hotspots were identified showing incomplete waste digestion.

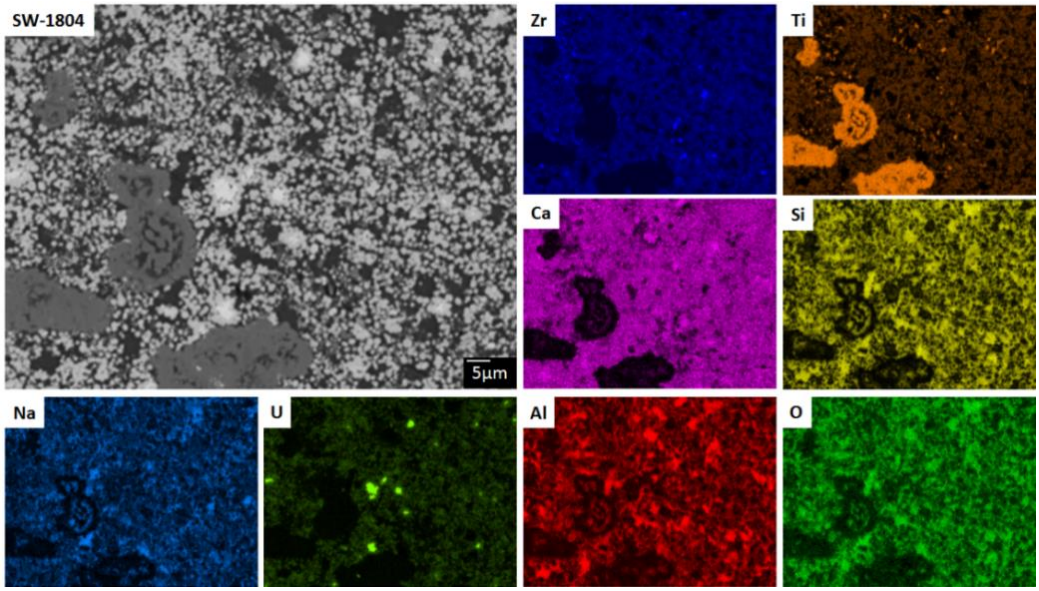

Figure 8.11: SEM-EDX elemental maps showing residual UO_2 hotspots.

The microstructure and crystallite size of SW-1805 ($Ca_{0.95}Ce_{0.05}Zr_{0.8}U_{0.15}Ce_{0.05}Ti_2O_7$) was very similar to SW-1803. Zirconolite was again the major phase distributed uniformly throughout, with TiO_2 present as a minor phase and large particles indicative of the Ti-metal additions. SEM-EDX identified sphene as an accessory phase, which had incorporated the bulk of the

Ce. A minor peak in the XRD data was identified as perovskite but this was not observed in the SEM.

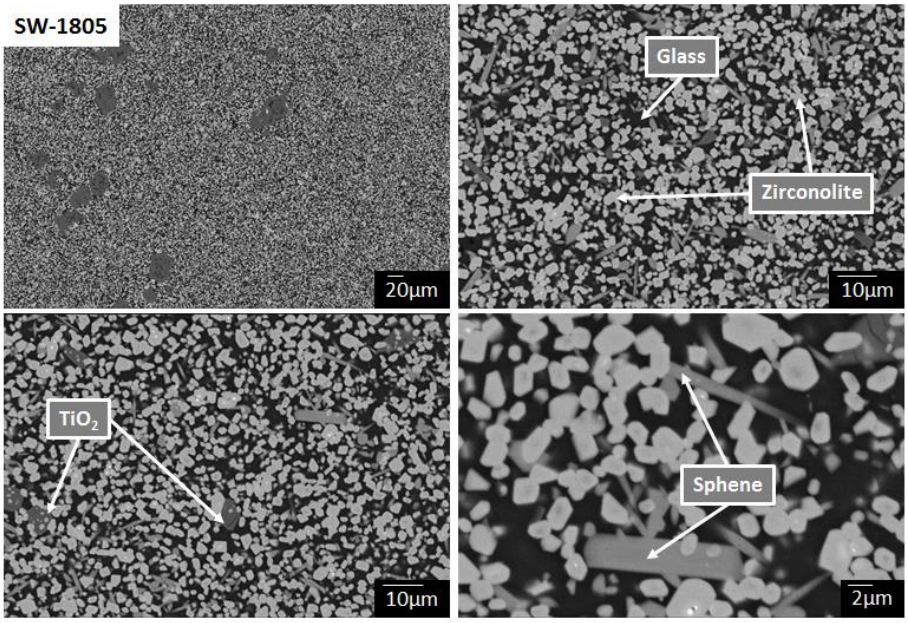

Figure 8.12: BSE micrographs of SW-1805 ($Ca_{0.95}Ce_{0.05}Zr_{0.8}U_{0.15}Ce_{0.05}Ti_2O_7$). Zirconolite was uniformly distributed throughout the glass-ceramic with minor phases, rutile and Ce-doped sphene.

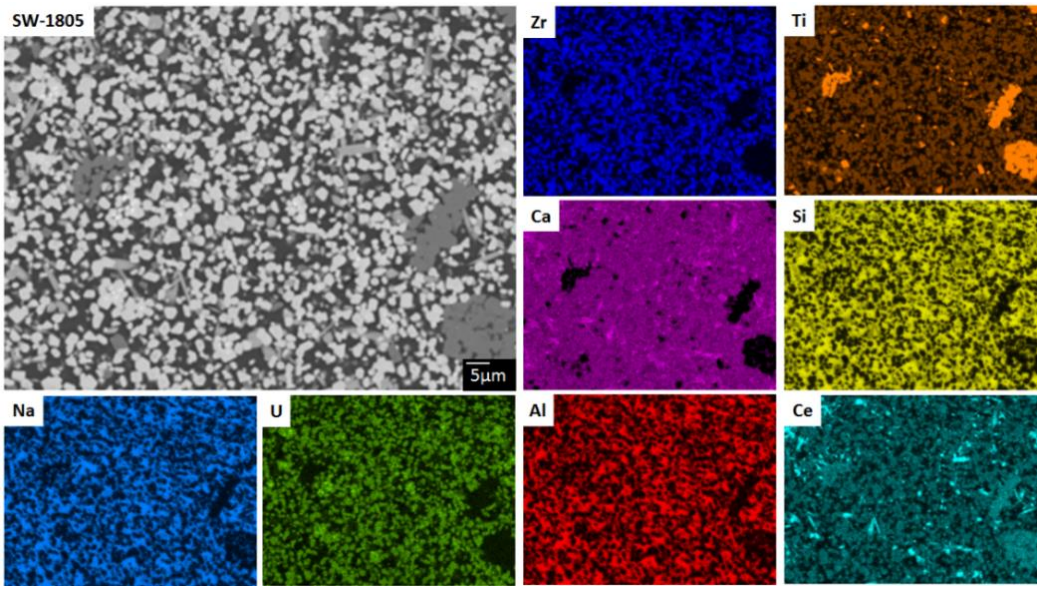

Figure 8.13: SEM-EDX elemental maps showing the partitioning of U into the zirconolite phase and incorporation of Ce ceramic phases sphene and zirconolite, preferentially over incorporation into the glass phase.

SEM-EDX data was collected for the zirconolite and glass phases in each sample, as well as the sphene phase in SW-1805. From the EDX data, semi-quantitative compositional analysis was done for the zirconolite phase and actinide partitioning ratios were determined between the ceramic and glass phases. It was found that in all three samples, the U had preferentially substituted on the Ca site. Table 8.6 summarises the calculations from the averaged measured data and gives the final zirconolite compositions determined. Table 8.7 shows the effective partitioning of the actinide surrogates between the glass and zirconolite phases. Due to the small grain size in SW-1804, some Na and Si were detected in the zirconolite EDX signal. These were assumed to be from the surrounding glass phase and were disregarded for the compositional analysis. Oxygen is often overestimated by SEM-EDX due to the limitations of the technique when detecting elements lighter than Na [187]. As a result of the strongly reducing atmosphere during calcination and consolidation of the samples, it was highly unlikely interstitial O^{2-} ions were present in the ceramic phase. Thus, O_x was assumed to be equal to the maximum stoichiometric formula unit and the additional signal was the associated error of the analysis technique. Due to the strongly reducing conditions during processing, we are confident that all the U was reduced to U^{4+} and the Ce was fully reduced to Ce^{3+}.

From the calculated compositions it was clear the U had substituted on the Ca site within the zirconolite structure in all three samples, despite SW-1803 and SW-1805 targeting Zr site substitution. The primary charge compensation mechanism for all three samples was determined to be the reduction of Ti^{4+} to Ti^{3+}. Compared to SW-1803, SW-1804 incorporated more Al^{3+} as targeted in the starting formulation, thus required less Ti^{3+} for complete charge compensation. SW-1805 had an equal amount of Ti to SW-1803 but the lower U substitution necessitated less Ti^{3+} charge compensation. The semi-quantitative compositions implied possible cation vacancies present in zirconolite due to the cation A-sites not equalling the stoichiometric $A_2B_2O_7$ (see Table8.6). Whilst, cation vacancies are possible, the measured vacancies were very low and within experimental errors.

Table 8.6: SEM-EDX compositional analysis for the U doped samples. Given in at. %. Errors were calculated at 3x standard deviation of the raw SEM-EDX data.

SW-1803								
	Ca^{2+} (±0.56)	**U^{4+}** (±0.66)	**Zr^{4+}** (±1.05)	**Ti^{4+}** (±0.70)	**Ti^{3+}** (±0.70)	**Al^{3+}** (±0.42)	**O^{2-}** (±0.25)	**Valence check**
averaged raw data	0.55	0.28	0.88	1.73		0.04	6.52	
scaled for $Ti_{2.00}$	0.62	0.32	0.99	1.95		0.05	7.37	
scaled oxygen error	0.62	0.32	0.99	1.95		0.05	7.00	
charge calc.	1.24	1.27	3.98	7.82		0.14	-14.00	0.45
Ti^{3+} charge balance	0.62	0.32	0.99	1.51	0.45	0.05	7.00	
charge calc.	1.24	1.27	3.98	6.03	1.34	0.14	-13.99	0
Final composition:	**0.62**	**0.32**	**0.99**	**1.51**	**0.45**	**0.05**	**7.00**	

SW-1804								
	Ca^{2+} (±0.64)	**U^{4+}** (±1.72)	**Zr^{4+}** (±1.66)	**Ti^{4+}** (±2.30)	**Ti^{3+}** (±2.30)	**Al^{3+}** (±0.94)	**O^{2-}** (±1.44)	**Valence check**
averaged raw data	0.52	0.28	0.89	1.59		0.15	6.58	
scaled for $Ti_{2.00}$	0.60	0.32	1.02	1.83		0.17	7.56	
scaled oxygen error	0.60	0.32	1.02	1.83		0.17	7.00	
charge calc.	1.20	1.29	4.09	7.31		0.52	-14.00	0.40
Ti^{3+} charge balance	0.60	0.32	1.02	1.43	0.40	0.17	7.00	
charge calc.	1.20	1.29	4.09	5.73	1.19	0.52	-14.00	0.00
Final composition:	**0.60**	**0.32**	**1.02**	**1.43**	**0.40**	**0.17**	**7.00**	

SW-1805									
	Ca^{2+} (±0.26)	**Ce^{3+}** (±0.82)	**U^{4+}** (±0.31)	**Zr^{4+}** (±0.21)	**Ti^{4+}** (±0.58)	**Ti^{3+}** (±0.58)	**Al^{3+}** (±0.19)	**O^{2-}** (±0.09)	**Valence check**
averaged raw data	0.58	0.05	0.19	0.9	1.78		0.04	6.47	
scaled for $Ti_{2.00}$	0.64	0.05	0.21	0.99	1.96		0.04	7.11	
scaled oxygen error	0.64	0.05	0.21	0.99	1.96		0.04	7.00	
charge calc.	1.27	0.16	0.84	3.96	7.82		0.13	-14.00	0.19
Ti^{3+} charge balance	0.64	0.05	0.21	0.99	1.77	0.19	0.04	7.00	
charge calc.	1.27	0.16	0.84	3.96	7.08	0.56	0.13	-14.00	0.00
Final composition:	**0.64**	**0.05**	**0.21**	**0.99**	**1.77**	**0.19**	**0.04**	**7.00**	

	Final stoichiometric compositions
SW-1803	$(Ca_{0.62}U_{0.32})Zr_{0.99}(Ti^{4+}_{1.51}Ti^{3+}_{0.45}Al_{0.05})O_7$
SW-1804	$(Ca_{0.60}U_{0.32})Zr_{1.02}(Ti^{4+}_{1.43}Ti^{3+}_{0.40}Al_{0.17})O_7$
SW-1805	$(Ca_{0.64}Ce_{0.05}U_{0.21})Zr_{0.99}(Ti^{4+}_{1.77}Ti^{3+}_{0.19}Al_{0.04})O_7$

Table 8.7: The measured partitioning ratios of the actinide surrogates.

Sample		Zirconolite	Glass	Sphene	Ratio Z : G	Ratio Z : G : S
SW-1803	U	2.82	0.06		100 : 2	
SW-1804	U	2.84	0.06		100 : 2	
SW-1805	U	1.85	0.07	0.20	100 : 4	100 : 4 : 11
SW-1805	Ce	0.47	0.00	4.27	100 : 0	10 : 0 : 100

The SEM-EDX analysis revealed an overwhelming partitioning of U into the target zirconolite phase. Both SW-1803 and SW-1804 achieved an average U partitioning ratio of 100 : 2 between the zirconolite and glass phases. SW-1805 only achieved a 100 : 4 average ratio, which was thought to be a result of the additional Ce present and the formation of sphene. When the sphene phase was included in the calculation, it was found that more U was present in the sphene phase than in the glass phase. Thus, whilst the incorporation of U in zirconolite was slightly lower than the other two samples, it was still preferentially incorporated into the secondary ceramic phase over the amorphous glass phase.

The Ce present in SW-1805 overwhelmingly partitioned into the ceramic phases and was predominantly incorporated into the secondary sphene phase. No Ce was detected in the glass phase despite the reducing atmosphere, which gave partitioning ratios of 100 : 0 ceramic : glass and 10 : 90 zirconolite : sphene. It was interesting that the sphene phase formed to incorporate the Ce^{3+} and not perovskite as was observed in the Ce doped samples in Chapter 6.

8.3.2 Plutonium sinters

XRD and SEM of Pu sinter sample Pu317-01, conducted on a polished monolith specimen, confirmed excellent reactivity of the PuO_2 and precursor materials, shown in Figure 8.14 and Figure 8.15. Zirconolite was obtained as the major crystalline phase and complete digestion of the PuO_2 was achieved. The diffuse scattering was a result of the glass phase and domed containment during characterisation to avoid contamination of the XRD equipment. The XRD of sample Pu317-01 in Figure 8.14 shows that zirconolite-2M (PDF card: 04-007-6895) was identified as the major phase, however reflections at low angle (2θ = 15.8° and 2θ = 28.8°) were identified to be indicative of the zirconolite-3T structure (PDF card: 00-054-1132). Minor phase $NiTiO_3$ (PDF card: 01-076-0336) was identified and was a direct result of the oxidising atmosphere that led to the oxidation of the Ni particles during heating. Rutile (TiO_2)

may have been present as a trace phase but the (h k l) reflections overlapped with other peaks in the XRD pattern, thus could not be accurately identified.

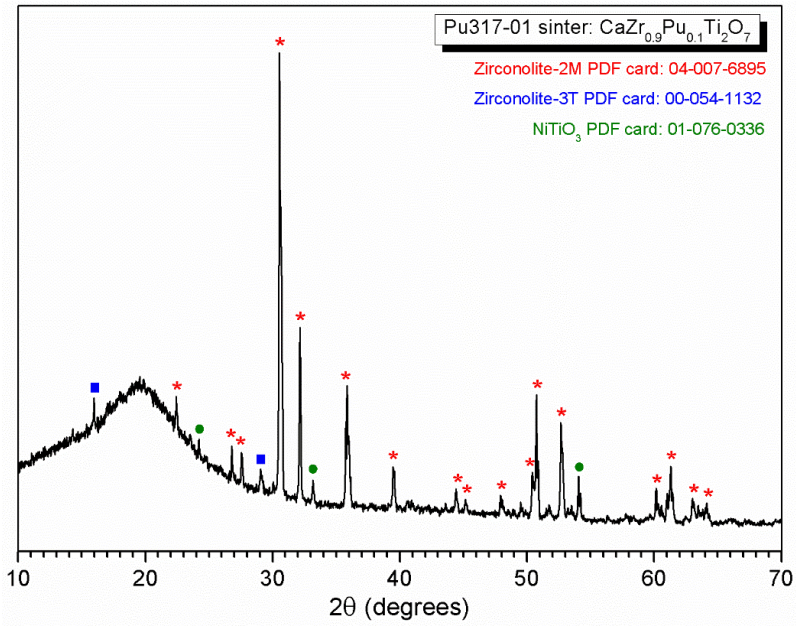

Figure 8.14: XRD of sintered sample Pu317-01 showing zirconolite-2M as the major crystalline phase and minor phases, zirconolite-3T and $NiTiO_3$. (PDF cards: 04-007-6895, 00-054-1132, 01-076-0336, respectively).

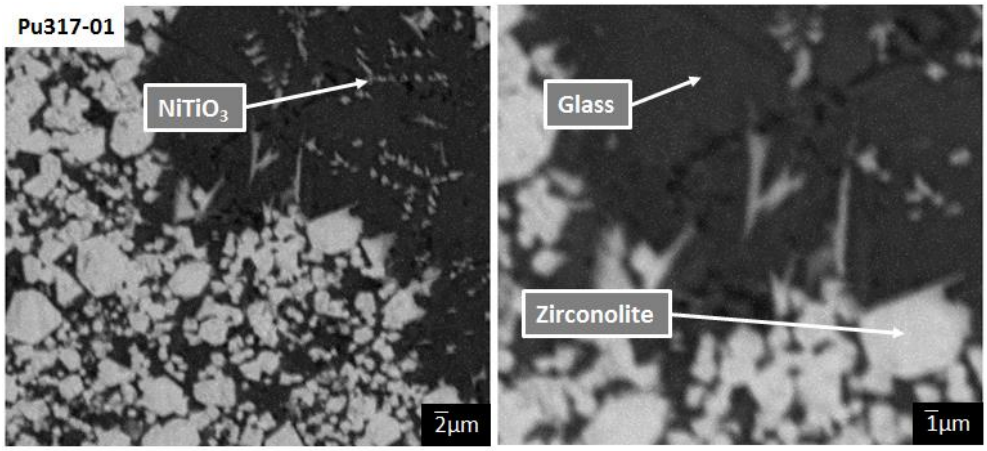

Figure 8.15: BSE micrographs of Pu sinter sample Pu317-01.

Compositional analysis of the zirconolite and glass phases confirmed preferential incorporation of Pu into the target ceramic phase. SEM-EDX data, summarised in Table 8.8, showed Pu substituted on the Ca site with approximate composition, $Ca_{0.76}Pu_{0.11}Na_{0.10}Zr_{1.04}Ti_{1.79}Al_{0.04}Ni_{0.15}O_7$. It was assumed the measured Si signal was associated

with the glass phase and was thus removed from the compositional analysis. There was a small overall negative charge on this composition that may have been a result of experimental error. The scanning electron microscope and EDX detector used were both very old, which, coupled with the radiation effects of the Pu and small grain size of the glass-ceramic, may have contributed to an accumulated experimental error. Due to the oxidising atmosphere oxygen vacancies were very unlikely.

As a result of the oxidising atmosphere, it was assumed the Pu obtained a Pu^{4+} oxidation state [285]. The Ni powder added for redox control would have oxidised at low temperatures as a result of heating in air, thus was unlikely to have any influential reducing properties within the sample. It was also unlikely that reduction of Ti^{4+} to Ti^{3+} would have occurred, so Ti was assumed to be Ti^{4+}.

Table 8.8: SEM-EDX data for zirconolite phase in Pu317-01 sintered sample. The at. % data was averaged and scaled to remove the Si that was assumed to be cross-contamination of the glass phase. Semi-quantitative compositional analysis was conducted assuming Pu^{4+} oxidation state. Errors were calculated as 3x standard deviation of the raw SEM-EDX data.

Pu317-01										
	Ca^{2+} (±0.62)	**Pu^{4+}** (±1.00)	**Na^{+}** (±0.91)	**Zr^{4+}** (±0.33)	**Ti^{4+}** (±1.43)	**Al^{3+}** (±0.56)	**Ni^{2+}** (±0.64)	**Si^{4+}** (±0.62)	**O^{2-}** (±0.36)	**Valence check**
Zirconolite 1	7.19	0.98	0.64	9.28	16.68	0.19	1.33	0.23	63.47	
Zirconolite 2	6.86	0.99	0.96	9.55	16.37	0.42	1.21	0.21	63.43	
Zirconolite 3	6.69	1.02	1.12	9.4	15.55	0.65	1.71	0.66	63.2	
Average	6.91	1.00	0.91	9.41	16.20	0.42	1.42	0.37	63.37	
Averaged raw data	**6.94**	**1.00**	**0.91**	**9.44**	**16.26**	**0.42**	**1.43**		**63.61**	
scaled for $Ti_{2.00}$	0.76	0.11	0.10	1.04	1.80	0.04	0.15		7.03	
scaled oxygen error	0.76	0.11	0.10	1.04	1.80	0.04	0.15		7.00	
charge calc.	1.52	0.44	0.10	4.16	7.20	0.12	0.30		-14	-0.16
Final composition:	**0.76**	**0.11**	**0.10**	**1.04**	**1.80**	**0.04**	**0.15**		**7.00**	
$Ca_{0.76}Pu_{0.11}Na_{0.10}Zr_{1.04}Ti_{1.80}Al_{0.04}Ni_{0.15}O_7$										

8.3.3 Plutonium HIP sample

Results of the Pu HIP sample SW-1811 were in excellent agreement with the sintered sample. The XRD pattern in Figure 8.16 showed zirconolite as the only crystalline phase. Due to the lower loading of Pu at 0.1 f.u., the zirconolite-2M structure was the primary polytype stabilised and the two low angle reflections indicative of the 3T structure were present as well. In comparison to the sintered sample (Pu317-01), the HIP sample does not contain $NiTiO_3$. This was a result of the reducing atmosphere during processing, which inhibited the oxidation of the Ni powder.

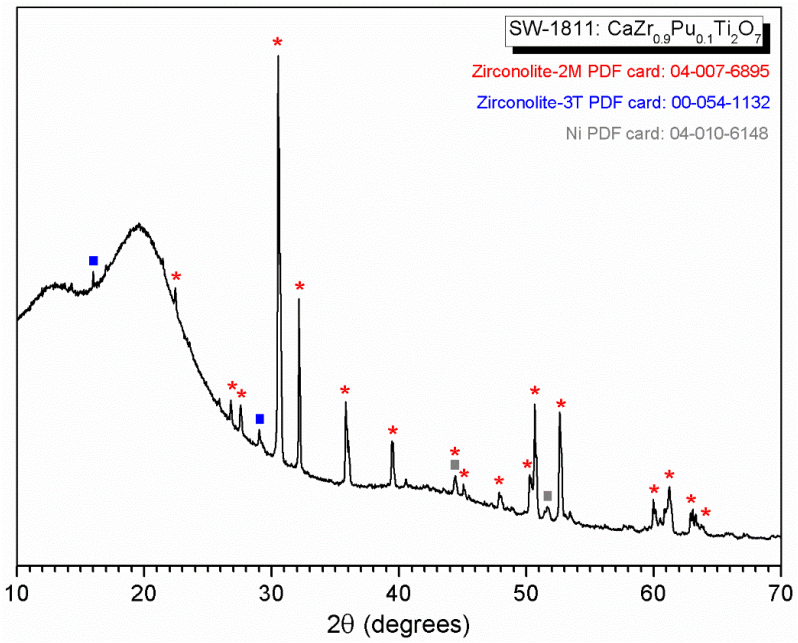

Figure 8.16: XRD of the Pu HIP sample SW-1811 showing zirconolite-2M to be the major phase with a low amount of zirconolite-3T present as well. Compared to the sinter sample of equal composition, the $NiTiO_3$ is absent as a result of processing under reducing conditions.

SEM confirmed a homogeneous microstructure with the single crystalline phase, zirconolite, uniformly distributed throughout the glass matrix and large Ni particles randomly distributed, see Figure 8.17. No PuO_2 hotspots were observed, thus confirming complete incorporation of the waste oxide. SEM-EDX compositional analysis was performed on the zirconolite phase, but due to the very fine grain size of the zirconolite, it was difficult to avoid phase overlap. Table 8.9 summarises the semi-quantitative compositional analysis process

from the SEM-EDX raw data and gives the resultant zirconolite composition, $Ca_{0.80}Pu_{0.10}Na_{0.09}Zr_{0.95}Ti_{1.82}Al_{0.17}Ni_{0.01}O_7$. From the SEM-EDX data, there was an overall negative charge to the given composition, but the results indicated that the level of Pu substitution was in agreement with the starting formulation at 0.1 f.u., substitution took place on the Ca site as with the previous U samples, and that charge compensation was provided by Al^{3+} substitution on the Ti sites.

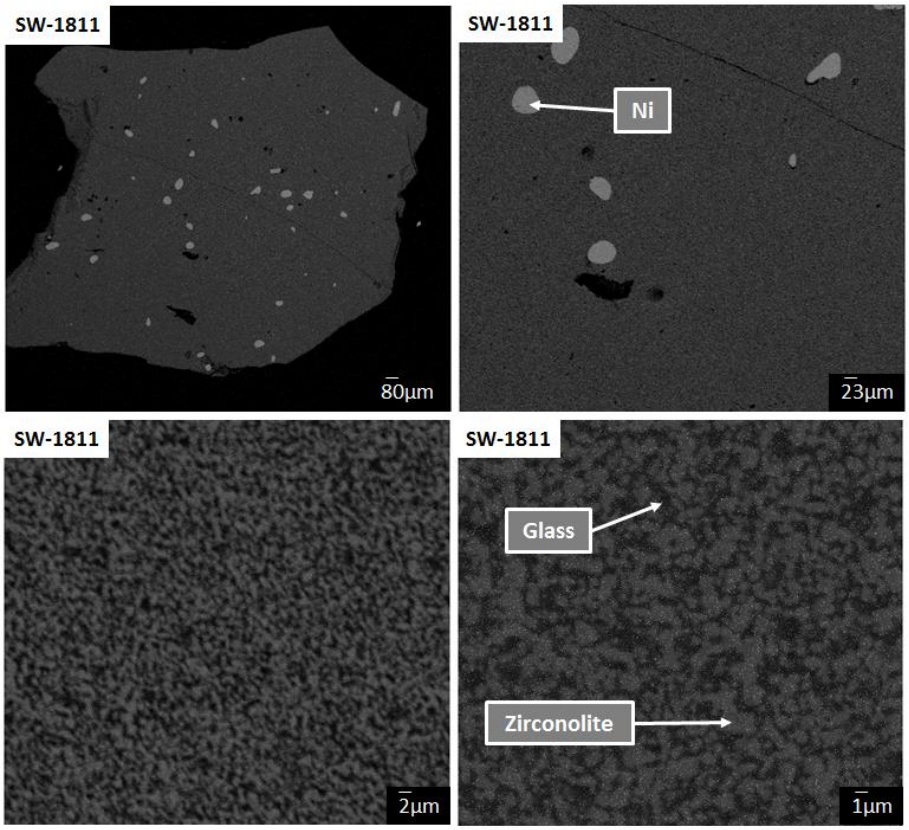

Figure 8.17: BSE micrographs for Pu HIP sample SW-1811. Zirconolite was the only crystalline phase identified and no PuO_2 hotspots confirmed complete waste incorporation.

Table 8.9: SEM-EDX data for the zirconolite phase in SW-1811e. The data was averaged and scaled to remove the Si that was assumed to be cross-contamination of the glass phase. Semi-quantitative compositional analysis was conducted assuming Pu^{4+} oxidation state. Errors were calculated as 3x standard deviation of the raw SEM-EDX data.

SW-1811										
	Ca^{2+} (±0.64)	**Pu^{4+}** (±0.43)	**Na^{+}** (±0.44)	**Zr^{4+}** (±0.74)	**Ti^{4+}** (±0.93)	**Al^{3+}** (±0.50)	**Ni^{2+}** (±0.22)	**Si^{4+}** (±1.50)	**O^{2-}** (±0.26)	**Valence check**
Zirconolite 1	6.99	1.05	0.59	8.42	15.75	1.21	0.13	2.06	63.79	
Zirconolite 2	6.83	0.78	0.94	7.89	15.00	1.60	0.17	3.18	63.60	
Zirconolite 3	6.48	0.72	0.70	7.90	15.49	1.52	0.00	3.05	63.78	
Average	6.77	0.85	0.74	8.07	15.41	1.44	0.10	2.76	63.72	
Averaged raw data	**6.96**	**0.87**	**0.76**	**8.30**	**15.85**	**1.48**	**0.10**		**65.53**	
scaled for $Ti_{2.00}$	0.80	0.10	0.09	0.95	1.82	0.17	0.01		7.52	
scaled oxygen error	0.80	0.10	0.09	0.95	1.82	0.17	0.01		7	
charge calc.	1.60	0.40	0.09	3.80	7.28	0.51	0.02		-14	-0.30
Final composition:	0.80	0.10	0.09	0.95	1.82	0.17	0.01		7	
$Ca_{0.80}Pu_{0.10}Na_{0.09}Zr_{0.95}Ti_{1.82}Al_{0.17}Ni_{0.01}O_7$										

The second Pu-bearing HIP sample targeted a higher waste loading. Sample SW-1812 targeted 0.2 f.u. Pu substitution on the Zr site; $CaZr_{0.8}Pu_{0.2}Ti_2O_7$ and was again fabricated with 4 wt. % Ni for controlled oxygen fugacity. The XRD data in Figure 8.18, confirmed zirconolite-2M as the major polytype, with the zirconolite-3T (h k l) reflections at 2θ = 15.8° and 28.8° present as well. Minor phases sphene and zircon were present, unlike in sample SW-1811 and a minor reflection at 2θ = 28.4° could be attributed to PuO_2. This implied incomplete waste digestion at the higher waste loading, however, no PuO_2 hotspots were observed by SEM. The SEM-EDX data again confirmed Pu incorporation into the zirconolite phase and correlated with the higher waste loading, such that 0.22 f.u. were substituted on the Ca site, see Table 8.10.

.

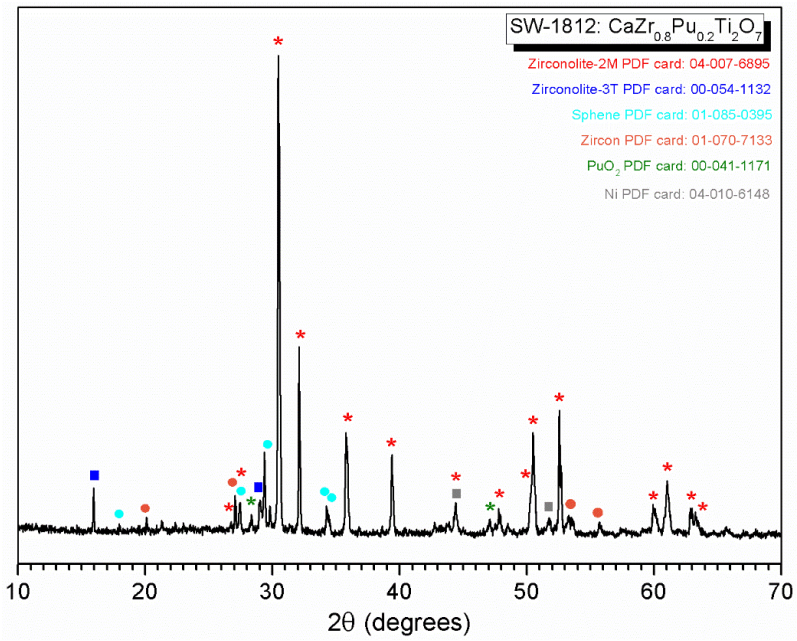

Figure 8.18: XRD of the Pu HIP sample SW-1812 showing zirconolite-2M to be the major phase with a low amount of zirconolite-3T present as well. Compared to sample SW-1811, additional minor phases were also present; sphene, zircon, Ni metal and PuO_2.

Table 8.10: SEM-EDX data for zirconolite phase in SW-1812 HIPed sample. The data was averaged and scaled to remove the Si that was assumed to be cross-contamination of the glass phase. Semi-quantitative compositional analysis was conducted assuming Pu^{4+} oxidation state. Errors were calculated as 3x standard deviation of the raw SEM-EDX data.

SW-1812										
	Ca^{2+} (±1.49)	**Pu^{4+}** (±0.73)	**Na^{+}** (±0.87)	**Zr^{4+}** (±1.73)	**Ti^{4+}** (±3.91)	**Al^{3+}** (±1.00)	**Ni^{2+}** (±0.42)	**Si^{4+}** (±4.69)	**O^{2-}** (±0.42)	**Valence check**
Zirconolite 1	4.79	2.03	0.65	8.15	15.19	1.32	0.30	3.15	64.42	
Zirconolite 2	6.00	1.51	0.07	7.07	15.26	1.06	0	4.58	64.45	
Zirconolite 3	5.53	2.02	0	8.40	17.99	0.52	0	0.79	64.73	
Average	5.44	1.85	0.24	7.87	16.15	0.97	0.10	2.84	64.53	
Averaged raw data	**5.27**	**1.80**	**0.23**	**7.63**	**15.65**	**0.94**	**0.10**		**62.55**	
scaled for $Ti_{2.00}$	0.63	0.22	0.02	0.92	1.88	0.11	0.01		7.51	
scaled oxygen error	0.63	0.22	0.02	0.92	1.88	0.11	0.01		7	
charge calc.	1.26	0.88	0.02	3.68	7.52	0.33	0.02		-14	-0.29
Final composition:	0.63	0.22	0.02	0.92	1.88	0.11	0.01		7	
$Ca_{0.63}Pu_{0.22}Na_{0.02}Zr_{0.92}Ti_{1.88}Al_{0.11}Ni_{0.01}O_7$										

Due to the very fine grain size of the zirconolite in both SW-1811 and SW-1812, the actinide partitioning ratio was found to be inconclusive. Calculations from the SEM-EDX data suggested a 2 : 1 partitioning ratio between the zirconolite and glass phases in each sample, however, significant phase overlap within these data meant a robust determination could not be achieved.

8.4 Discussion

The U samples were fabricated and characterised to confirm the behaviour of the glass-ceramic system with an active Pu surrogate before progressing to the PuO_2 samples. Due to the radiological and safety hazards associated with working with PuO_2, as well as the expense of material and facilities, it was essential the U work was first conducted to better ensure successful consolidation and waste incorporation with the PuO_2.

The three U doped samples were very successful, with almost full waste incorporation into the glass-ceramic. As a baseline, SW-1803 achieved excellent waste incorporation into the

zirconolite phase and a uniform microstructure throughout the glass-ceramic. Sample SW-1804 targeted U^{4+} substitution on the Ca site with additional Al_2O_3 for charge compensation. The heterogeneous glass phase, sub-micron grain size and residual UO_2 in the final wasteform suggested slower kinetics during consolidation. This result was believed to be caused by the additional Al_2O_3, a refractory material that increases glass connectivity and viscosity [47,230]. This increased viscosity was pertinent to the reduced kinetics of the melt, which inhibited grain growth and waste digestion. Whilst the viscosity impeded waste digestion, the SEM-EDX data proved it did not affect the partitioning of the U into the zirconolite phase. The zirconolite SEM-EDX data was in agreement with that of SW-1803, with a partitioning ratio of 100 : 2 between the zirconolite and glass phases.

The CeO_2 in sample SW-1805 was primarily incorporated into an accessory phase, sphene ($CaTiSiO_5$). SW-1805 had a similar microstructure and waste digestion results to sample SW-1803, with the addition of the Ce-rich crystalline phase. The SEM-EDX data confirmed the Ce was preferentially incorporated into the sphene phase, with low levels detected in the glass and zirconolite phases. Whilst the U partitioning ratio between zirconolite and glass was slightly lower than samples SW-1803 and SW-1804, the U was still preferentially incorporated in the durable crystalline phases rather than the glass phase.

All three U samples stabilised the zirconolite-3T polytype. Zirconolite undergoes a phase transition with increased U substitution within the lattice. Under oxidising conditions, the monoclinic 2M structure is reported to transition to the 4M polytype at substitutions around 0.4 f.u. [106]. Under reducing conditions, the 3T structure is reported to form around 0.3 f.u. substitutions [106,112]. Whilst there are very limited refined data available on the 3T structure, it is believed to have a higher degree of symmetry compared to the 2M polytype and consists of two Ca sites rather than one [110,112]. The SEM-EDX data confirmed sufficient U incorporation had occurred to maintain the stabilisation of the 3T polytype and implied that the substitution took place on the Ca sites. Coupled with the XRD data that had diagnostic 3T reflections at $2\theta = 15.8°$ and 28.8°, and a lack of low angle reflections indicative of the 2M polytype, the phase transition was confirmed and was in excellent agreement with the literature [91,97,106,108,110,112].

Multiple charge compensation mechanisms have been discussed in the literature pertaining to zirconolite including cation vacancies, B-site substitutions and Ti reduction [238,286]. The

stoichiometries of each sample targeted charge compensation by either stoichiometric substitution or Al^{3+} substitution on the Ti-sites. Due to the strongly reducing conditions during calcination and consolidation, it was assumed sufficient conditions were exhibited to ensure U^{4+} and Ce^{3+} valence states. The SEM-EDX data confirmed some Al^{3+} substitution and suggested low levels of cation vacancies ($\leq$ 0.1 f.u.). The combined effect of the Al^{3+} and cation vacancies was not enough to charge balance the full actinide inventory, thus another mechanism must have been in effect. From the SEM-EDX compositional data it was concluded that charge compensation was provided primarily by the reduction of Ti^{4+} to Ti^{3+}. This was supported by diffuse reflectance spectroscopy (DRS) where the intended U valence(s) was unidentified due to a strong Ti^{3+} signal that dominated any U signals present. The low levels of cation vacancies suggested by the SEM-EDX data were within experimental error and further analysis would be required to determine if the cation vacancies were present or not.

8.4.1 Plutonium samples

The results from the Pu sinter sample were in excellent agreement with the HIPed samples and proved that small scale, ambient pressure trials can be utilised to gain representative information of HIP products before progressing to the larger scale experiments. It should be noted that the sintered sample was highly porous due to the lack of applied pressure, but achieved a representative phase assemblage and microstructure of the HIP samples despite the oxidising atmosphere.

The sintered sample Pu317-1 and HIP sample SW-1811 had lower PuO_2 loadings than the U samples and stabilised the zirconolite-2M structure. This was again in agreement with the literature that the level of Pu incorporation was below that expected for the 3T structure to be stabilised [106]. The two (h k l) reflections at $2\theta = 15.8°$ and 28.8° indicative of the 3T polytype were present in the XRD data, which indicated that the 3T polytype was present in smaller quantities. The 4M polytype was not observed in the sintered sample despite the oxidising conditions.

The successful consolidation of the PuO_2 sample SW-1811 allowed for progression to a higher PuO_2 waste loading (0.2 f.u.) and the fabrication of HIP sample SW-1812. Whilst a minor peak at $2\theta = 28.4°$ in the XRD data suggested some residual PuO_2 was present, no Pu hotspots

were observed by SEM. The successful incorporation of the higher waste loading led to the decision that all further samples would be fabricated with the higher loading to better determine how different redox conditions affect the digestion of the PuO_2.

Due to the fine microstructure of the HIPed samples, it was difficult to obtain accurate compositional data for the zirconolite phase. The data obtained correlated well with the expected Pu levels in the ceramic, but overlap with the glass phase made quantitative analysis problematic. The proposed compositions had an overall negative charge, which may have been a normalisation error. If the Ni and / or Na were not present in the ceramic, their detection would have incorrectly adjusted the normalisation of the SEM-EDX data and decreased the atomic percentages of higher valence elements. Further analysis on these samples is expected to take place at ANSTO pending the arrival of a new scanning electron microscope in the actinide facility to obtain more accurate readings.

Interestingly, from the compositional data obtained so far, there was no suggestion of charge compensation by Ti reduction. This was in agreement with Zhang *et al.* who did not observe Ti reduction in similar samples [143]. Zhang *et al.* processed Pu doped zirconolite glass-ceramics by HIP under Ni / NiO and Fe / FeO reducing conditions and reported charge compensation by Al^{3+} substitution on the Ti sites and low levels of cation vacancies [143]. The SEM-EDX data for the PuO_2 HIP samples discussed here also suggest cation vacancies and Al^{3+} substitution. Thus, irrespective of the glass overlap and residual negative charge, the HIP samples appeared to be in agreement with the literature. It is possible the Ti^{3+} charge compensation observed in the U samples was a result of the Ti / TiO buffer system applied, or was a discrepancy related to the actinide surrogate. The PuO_2 HIP samples are part of a five sample matrix investigating the effect of partial oxygen pressure (pO_2) on the incorporation and partitioning behaviour of Pu in the glass-ceramic wasteforms. Consolidation of the remaining samples in this matrix, which will utilise Fe / FeO and Ti / TiO reducing atmospheres, is underway at ANSTO and will give more information with regards to the effect of pO_2 on PuO_2 incorporation and the charge compensation mechanisms in place within these wasteforms.

From the Ellingham diagram, Figure 8.19, it was not expected that the Ni powder would create a pO_2 low enough to reduce Pu^{4+} to Pu^{3+} within the HIP samples [241,285,287]. The Ellingham diagram is used to determine the conditions at which compounds will reduce at

certain temperatures. According to Atlas *et al.* [288] (taken from [285]), at 1300 °C a pO_2 of 10^{-13} atm would result in the formation of 0.1 f.u. of oxygen vacancies in PuO_2 ($PuO_{1.9}$), representing a reduction of 0.02 f.u. of Pu^{4+} to Pu^{3+} ($Pu^{4+}_{0.98}Pu^{3+}_{0.02}O_{1.9}$) [285]. The Ellingham diagram shows that Ni will oxidise to NiO at pO_2 of ca. 10^{-7}atm at 1300 °C, thus will undergo oxidation before the reduction of PuO_2. Whilst Fe is more reducing than Ni, it is also expected to oxidise at pO_2 levels above 10^{-13} atm, thus may not reduce Pu [241,287]. That said, variations of Pu valence between Ni / NiO and Fe / FeO buffered systems have been reported in the literature [17,144]. Day *et al.* saw an increase in Pu^{3+} from Ni / NiO controlled systems to Fe / FeO controlled systems [17,144]. The results confirmed more Pu^{3+} in the glass phase of the Fe / FeO controlled samples, which had a direct impact on the extractability of the actinide from the glass-ceramic [144]. These results suggest that pO_2 is not the only factor controlling Pu valence and that some variation between the Ni / NiO and Fe / FeO samples will be observed in the sample matrix underway. It is hoped this sample matrix will give a better understanding of how pO_2 affects the behaviour of Pu in these wasteforms.

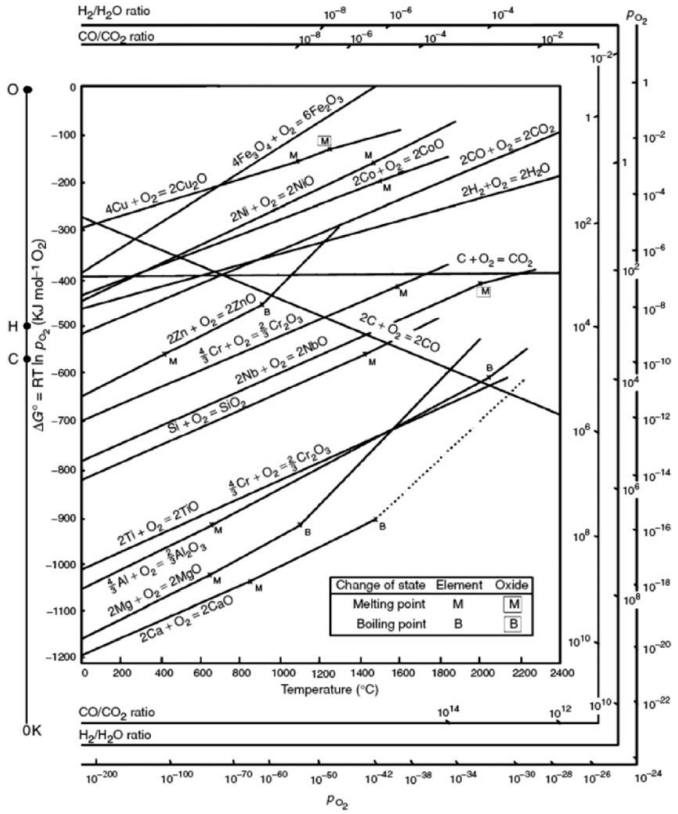

Figure 8.19: The Ellingham diagram showing the stability of different compounds in relation to temperature and atmospheric conditions (Taken from [289]).

8.5 Conclusions

Through the consolidation and characterisation of U and Pu doped HIP samples, this work has demonstrated successful PuO_2 incorporation into the selected glass-ceramic formulation. The use of surrogate studies was proven to give representative information on the incorporation behaviour of actinides into glass-ceramic wasteforms, and the sintered sample was found to produce a phase assemblage and microstructure indicative of the HIPed wasteforms.

This work is a key advancement of the current UK experience on HIP research for Pu disposition. Currently, the UK does not have the infrastructure to perform radioactive HIP research, which is a major hold-up for the development of this technology for treating radioactive wastes. This research has not only demonstrated the ability of these materials to incorporate PuO_2, it has shown that the HIP technology can be designed and operated to successfully handle radioactive materials.

9 Nuclearisation of a research HIP facility

During this PhD project Stephanie M. Thornber invested a significant amount of time to upgrade and commission the University of Sheffield's (UoS) hot isostatic press facility as the first such research facility in the UK suitable for processing radioactive samples. This chapter details the challenges and considerations involved and details the safety measures and procedures implemented for safe and efficient operation. A brief timeline is given of events that led to the approval to operate the radiological HIP facility.

Author Contribution: Stephanie M. Thornber facilitated and managed the AFIC project. Stephanie initiated the collaborations with AIP Inc., GeoRoc Ltd. and AMEPT and contributed to the grant proposal that secured the project funding. Stephanie co-ordinated all parties throughout the project, drew up the costings, wrote the initial safety procedures and documentations, sourced all items purchased and ensured all equipment was suitable for application. Stephanie was fundamental to the delivery of this project; the installation and commissioning of the UK's first research HIP facility capable of processing radioactive materials.

The nuclearisation of the research HIP facility was in collaboration with American Isostatic Press Inc. (AIP) whom designed and manufactured the Active Furnace Isolation Chamber; a first of a kind activity containment device that ensures complete containment of loose radioactive material, in the event of ruptured canisters during HIPing.

Full acknowledgement must be given to; AIP/AMEPT team for the design and manufacture of the AFIC and HIP canisters (Sam Moricca[1, 3], Reggie Persaud[1], Jeff Moller[1], Simon Cheung[3] and Michael Hatheier[3]); Sam Moricca[1, 3] and Paul Heath[2, 4] installed and commissioned the AFIC; John Lowndes[4] installed the second evacuation line; Laura Gardner[4] and Amber Mason[4] for their contributions and inputs on all health and safety documentation; Martin Stennett[4], Millie Gillatt[4] and Neil Hyatt[4] as acting Radiation Protection Officers who approved all documentation and procedures in place. The HIP upgrade was funded in-part by EPSRC under grant EP/L014041/1 - Decommissioning, immobilisation and storage solutions for nuclear waste inventories (DISTINCTIVE).

[1]AIP Inc. 1205 South Columbus Airport Road, Columbus Ohio, 43207, USA
[2]GeoRoc Limited, Unit 1- Building 3, Advanced Manufacturing Park (AMP), Rotherham, S60 5WG
[3]AMEPT, 4/50 Campbell Street, Woonona, NSW, 2517, Australia
[4]Immobilisation Science Laboratory, Department of Materials Science & Engineering, The University of Sheffield, Sir Robert Hadfield Building, Mappin Street, Sheffield S1 3JD, UK

Timeline of AFIC installation and radioactive commissioning of UoS HIP

- **February 2014:** Management approval granted to pursue radioactive HIP.
- **August 2015:** Facility maintenance requirements set out by UoS Radiation Protection Officer.
- **January 2016:** Work certificate granted for uranium HIP work.
- **April 2016:** Funding awarded by DISTINCTIVE EPSRC. Maintenance work to the HIP area took place including floor resurfacing and sealing of gaps.
- **October – December 2016:** Purchase of all PPE, welding extraction system, HIP canisters and AFIC furnace. Installation and commissioning of second vacuum line, welding extraction system, and ancillary equipment.
- **June 2017:** Final approval of all health and safety documentation – risk assessments, standard operating procedures, COSHH forms, spill training and transport of radioactive material.
- **July 2017:** Installation of AFIC furnace and official sign-off for radioactive HIP operation.

9.1 The risks and the implemented safeguards

There are many challenges associated with the commercialisation of HIP for nuclear waste immobilisation. One of the major challenges is ensuring reliable containment of radioactive materials in the event of a canister rupture during processing. Demonstrating this ability and producing an effective operating procedure at a research scale, is a positive step towards improving the TRL of HIP technology for nuclear waste disposal. When developing the radiological HIP facility at the UoS it was important to ensure all risks and hazards were mitigated to ensure the risks to operators, other laboratory users, future service engineers and equipment were as low as reasonably achievable (ALARA).

9.1.1 Contamination

The key risks when processing radioactive materials are the inhalation of α-particles and the spread of contamination. At the UoS, radioactive samples are prepared in the controlled radioactive laboratory facility on M-floor of the Sir Robert Hadfield Materials Science & Engineering building. The samples are then transported to C-floor where the HIP facility is located in the Quarrel Laboratory. It was important to limit the movement of radioactive material to minimise the risk of inhalation and spread of contamination from M-floor to C-floor, as well as during canister packing, welding, evacuation, sealing and processing.

The first level of security against contamination is provided by handling all loose radioactive powders in a designated glovebox in the M-floor active laboratory. The batched powders are pressed into pellets with a diameter approximately equal to the inside diameter of the HIP canisters. By pressing pellets, no loose powder is present inside the canister or at any subsequent stage of the HIP cycle. This helps to minimise unwanted transportation of loose radioactive particles during the rest of the canister preparation process.

The second barrier is the HIP canister itself. Thanks to AMEPT and AIP, a new straight walled HIP canister design has been provided to the UoS. The canisters are designed so the lids lock into place without welding. As a result, the canister provides the first sealed containment for transportation and allows the active samples to be treated as sealed sources after removal from the glovebox.

The location of the UoS HIP facility means radioactive samples are transported through the building before welding the canister lid. It was essential that all possible measures were taken to ensure safe transportation so there was no risk to other building users and members of the public. As already mentioned, the canister design ensures the canister lid locks into place. For safe transportation the locked canisters are carried in an up-right position, within a closed container. Obvious care must be taken when transporting the samples, but the double containment strategy reduces the risk of powder release in the event the sample is dropped to be as low as reasonably achievable.

The standard operating procedure (SOP) requires that the locked canister must not be removed from the transport container until the operator is ready to weld. In the event of a

failure during welding that means the sample cannot be HIPed, the canister is to be returned to the transport container and returned to the M-floor active laboratory for suitable storage and waste disposal.

9.1.2 Inhalation

When working with powders there is always a risk of dust inhalation. By filling the HIP canisters with pressed powders in a glovebox, the risk of inhalation is significantly reduced. During welding, there is potential for volatilisation or spread of powders due to the high energy and temperature. A triple filtered welding evacuation system was put in place to draw the welding fumes away from the operator (Figure 9.1). The triple layer filter system allows for easy maintenance and disposal by replacement of individual layers.

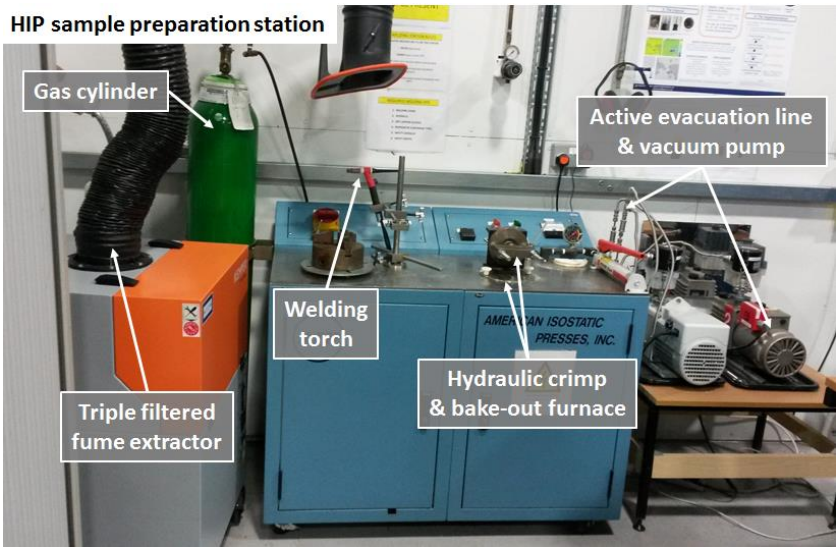

Figure 9.1: Key components of the HIP sample preparation station including the triple filter extraction unit and active evacuation line.

During welding the operator must be accompanied by a suitably qualified person (SQP) and both must wear full personal protective equipment (PPE). PPE for radioactive HIP work is stored away when not in use and consists of overalls, safety shoes, welding gloves, respirator for the SQP, welding visor for the SQP and a welding visor with a built-in Adflow air-flow respiratory system for the operator (Figure 9.2). The Adflow air-flow system supplies clean air to the operator to eliminate the risk of inhaling the welding fumes.

Figure 9.2: Operator PPE for welding radioactive HIP samples includes; welding visor with built-in Adlfow air-flow respiratory system, protective overalls, welding gloves and safety shoes.

9.1.3 Workstation / equipment contamination

A second evacuation line was installed on the sample preparation station for active samples only (Figure 9.1). The original evacuation line remains inactive and is to be used for all other samples. By having separate lines, cross-contamination of radioactive material between samples is mitigated against and allows for easy maintenance of the inactive line. The active line and vacuum pump, may, if required, be disposed of as contaminated materials at the end of its service life. Integrated into the active evacuation line are sintered metal filters to capture any particles in the line to mitigate against contamination of the vacuum pump oil. The HIP canisters themselves also contain built-in sintered metal filters to again minimise the risk of radioactive powder entering the evacuation line or damaging the vacuum pump.

Throughout all stages of canister preparation, wet-wipes are available for cleaning and contamination monitoring at regular intervals during welding, evacuation, bake-out, crimping and sealing. Before and after any active work takes place at the sample preparation station, the surface should be wiped and monitored to ensure it is clear from contamination.

The operator must be accompanied by a SQP during canister welding. The SQP should monitor the operators' hands after welding to ensure no spread of contamination across the work bench. The SQP is also present to assist the operator in the event of an emergency or radioactive spill incident. A fully stocked radioactive spill clean-up kit is to be present at the HIP facility and should be accessible during all radioactive work.

After processing, HIPed samples are removed from the pressure vessel but maintained inside the AFIC. The AFIC is then transported in a sealed container to the M-floor active laboratory for opening in a fume hood. The HIP canisters are sectioned on a Buehler Isomet™ 1000 high speed saw. The saw is for active samples only and is located in the M-floor active laboratory for safe operation. Canisters are sectioned using either high concentration or low concentration diamond blades, depending on the hardness and density of the wasteform material inside. The monolith samples are then cold mounted in epoxy resin and ground and polished, either manually or on active-only polishing apparatus.

9.1.4 Signage

When working with radioactive materials it is important to maintain radiation safety standards. All measures implemented and discussed in this chapter act to minimise and eliminate the risks associated with working with radioactive research scale HIP samples in a University environment.

Clear, signage must be displayed warning other laboratory users of the radiological hazard present at all times. Transport and storage containers must be labelled and clear signs must be displayed around the HIP facility when radioactive sample preparation and HIP operations are taking place. Once the radioactive material is returned to M-floor the signage should be removed to indicate the area has been monitored, is clear of contamination and that the radiological hazard is no longer present.

To minimise user dose uptake, three principles can be implemented; time, distance and shielding. The HIP canister itself provides suitable shielding from α-irradiation. Minimising the time around the radiation source minimises dose uptake. As such, during canister evacuation and bake-out, it is safe practise to minimise time spent around the sample by leaving the near vicinity. The SOP states to ensure the preparation station is in a safe and

tidy manner, to display clear signage warning other laboratory users of the radiological hazard present, cordon off the area and vacate. All radioactive canisters are engraved with a serial number and the radiation trefoil symbol so that clear identification can be made and an inventory of the material and radiation source inside can be determined.

9.1.5 Training

Only fully trained HIP users are authorised to conduct any radioactive HIP work and all work must be authorised by a SQP. Additional training for active HIP work must include: all UoS online radiation safety courses, full laboratory induction and relevant equipment training for the UoS M-floor active laboratory and UoS radiation spill handling safety course. It is imperative that no radioactive welding takes place without two people present, full PPE is employed and a complete radioactive spill kit is present.

9.2 Active Furnace Isolation Chamber (AFIC)

All radioactive HIP samples are contained in the Active Furnace Isolation Chamber (AFIC) during consolidation. The AFIC is designed to ensure full containment of radioactive powders in the event of ruptured canisters during HIP processing. The O-ring sealing system is located in the cold zone of the furnace, so does not experience high temperatures during the HIP cycle. As a result, the O-ring seal does not degrade with each operation and provides a reliable seal each and every time. The sealing mechanism of the AFIC ensures a tight and secure seal that will not fail during processing and will withstand accidental dropping of the chamber itself.

The AFIC has a two layered filter house system that captures loose powder particles, whilst allowing gas flow in and out of the chamber. The gas flow is essential to consolidate the HIP canister inside and not the AFIC itself. If gas cannot flow inside the chamber, the chamber acts as a sealed vessel thus would undergo compaction / deformation, rendering it nonoperational for further radioactive work. If gas cannot flow out of the chamber, the AFIC would become a highly pressurised vessel that could be very dangerous and unsafe to handle due to the risk of sudden high pressure release. The two layered filter house system is highly effective at ensuring safe containment of loose radioactive powders but also efficiently allows suitable gas flow in and out of the chamber, thus ensuring these events do not occur.

The filter house is also located in the cold zone of the furnace thus does not observe temperatures high enough to undergo oxidation. Gradual oxidation of the filters would increase the risk of a blockage that could inhibit the gas flow through the chamber. As a result of the innovative AFIC design, such an event is highly unlikely to occur and additional safety measures are built-in to ensure safe and reliable operation.

The HIP canister sits inside a boron nitride crucible, which is easily removed and replaced if required. A top cap sits over the canister and allows the chamber to be laid horizontally, or vertically inclined, whilst keeping the HIP canister secure and avoiding damage to the crimp seal. This enables us to insert the AFIC into a glovebox if required and also protects the canister during transportation.

The AFIC components are protected and contained inside the chamber cover that slides over the O-ring seal and is locked into place ready for HIPing. Figure 9.3 is a picture of the whole AFIC system with the major components labelled. The UoS was supplied with two chamber covers; one fabricated from 310 stainless steel suitable for temperatures up to 1150 °C and a second made of APMT alloy (advanced powder metallurgical Fe-Cr-Al-Mo alloy) suitable for temperatures up to 1300 °C. Both chambers are certified for operations up to 200 MPa of argon gas pressure.

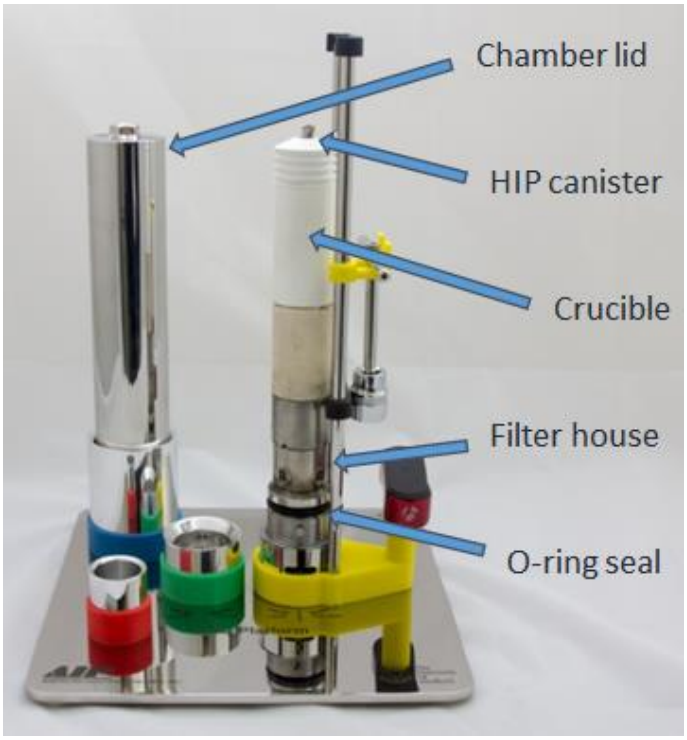

Figure 9.3: Image showing the major components of the AFIC system.

The assembled AFIC sits in the centre of a specially designed Mo furnace. The schematic in Figure 9.4 demonstrates the loading of the AFIC and the subsequent location of the HIP canister during the HIP cycle. AIP Inc. have designed the AFIC to be user friendly, making loading and unloading simple for operation in radioactive environments (fume hood or glovebox) and easy disassembly for decontamination and maintenance.

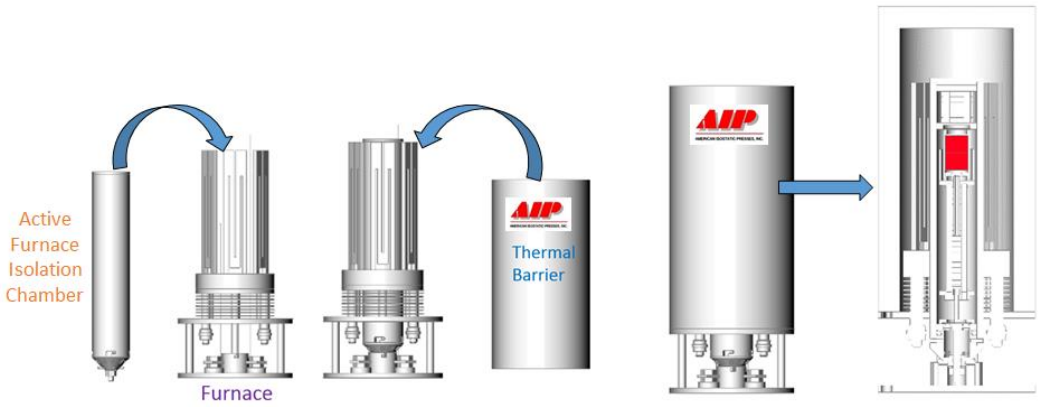

Figure 9.4: Schematic of the AFIC loading process into the HIP furnace. (Courtesy of AIP Inc.)

To ensure safe operation of the AFIC, the cycle recipes for active HIP cycles at the UoS are more conservative than the standard cycles used for inactive samples to date. Short intermittent dwell(s) during the ramp to temperature are included to allow for pressure and temperature equilibrium between the pressure vessel, furnace and AFIC. The delay for the AFIC to achieve the set-point conditions is not of huge concern and these dwells are not essential for successful operation, however, their incorporation into the UoS standard active HIP cycle recipe was to avoid unnecessary damage to the AFIC and to ensure the samples experience the target processing conditions. Such dwells are only included for high temperature (< 900 °C) or high pressure (< 50 MPa) HIP cycles.

9.3 Radioactive test sample

A UO_2 bearing glass-ceramic sample was fabricated following the standard operating procedure. The formulation of the glass-ceramic targeted U^{4+} incorporation on the Zr site, $CaZr_{0.8}U_{0.2}Ti_2O_7$, with 30 wt. % of $Na_2Al_2Si_6O_{16}$ glass. A total batch of 30 g was prepared in six individual 5 g batches, summarised in Table 9.1. The batch was milled in three lots of 10 g since the maximum mill pot size available for radioactive samples was 45 ml.

Table 9.1: Batch summary for the UO_2 bearing sample. A 30 g batch was prepared in six 5 g batches.

Oxide	Mass for 30 g batch (g) (±0.005)	Mass for 5 g batch (g) (±0.005)
$CaTiO_3$	7.749	1.292
TiO_2	4.553	0.759
ZrO_2	5.619	0.937
UO_2	3.079	0.513
SiO_2	5.155	0.859
Na_2SiO_3	2.095	0.349
Al_2O_3	1.750	0.292
Total	30.000	5.000

The UO_2 was weighed out and added to the inactive precursors, in the mill pot, inside a glovebox. The 10 g batches were milled in 8 g of IPA for 30 mins at ca. 500 rpm. After drying the powders at 80 °C, the mill pot was returned to the glovebox where the batch was carefully removed from the milling media and mill pot. The whole batch was calcined at 700 °C for 3 h under 3.5 % H_2/N_2 atmosphere.

The powder was pressed into pellets and inserted into the HIP canister (Figure 9.5). A total of 18.31 g of powder was used to fill the HIP canister. For this test sample, the annulus around the pellets was left unfilled to observe the maximum canister deformation with just the pressed powder. To avoid inserting loose powder inside the canister, stainless steel collars provide an alternative method for filling the void to reduce the level of canister deformation during HIPing.

Once packed, the canister rim was decontaminated before fixing the lid in place. The sealed source was then decontaminated and removed from the glovebox for welding. The welded canister was evacuated at room temperature and at 300 °C, using the radioactive vacuum line, before crimping and sealing.

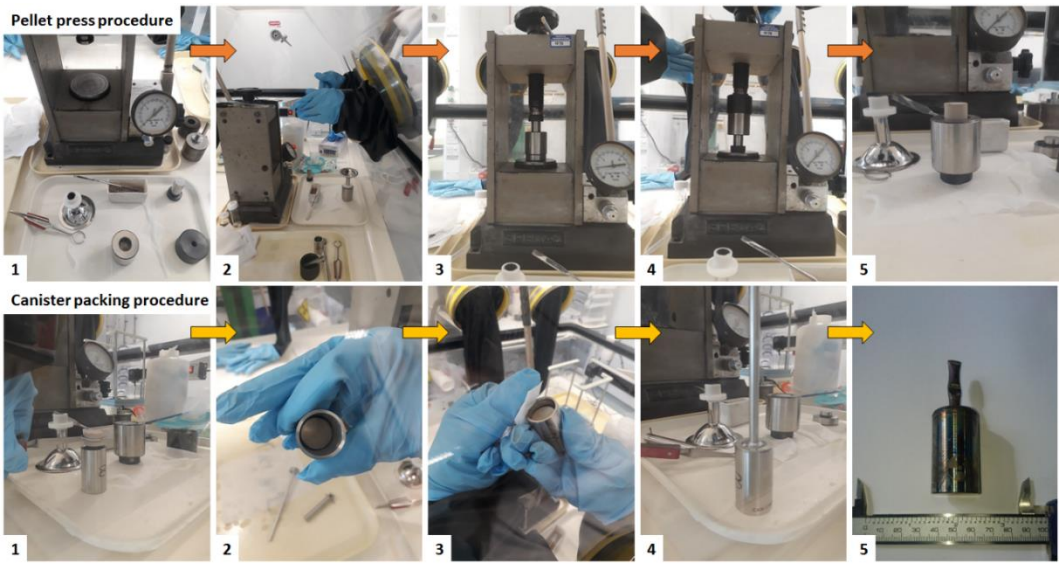

Figure 9.5: Powders were pressed into pellets inside the glovebox. The HIP canister was packed, decontaminated and removed from the glovebox for welding, evacuation, bake-out and sealing. Pellet press procedure: 1) Set-up of all equipment inside the glovebox, 2) Powder added to the die through a funnel, 3) Pellet pressed under a 2 tonne force, 4) Die inverted for pellet removal, 5) Pellet removed from the die. Canister packing procedure: 1) Pellet transferred from the die to the HIP canister, 2) The pellet inside the HIP canister, 3) Decontamination of the canister, 4) Canister lid fitted, 5) Final HIP canister after evacuation and welding, ready for HIPing.

The final sealed canister was loaded into the AFIC as shown in Figure 9.6. The active furnace was loaded into the HIP before inserting the AFIC chamber. Figure 9.7 summarises the

applied HIP cycle recipe that had an additional 30 min dwell at 700 °C and 13.8 MPa (2000 psi), before ramping to the final dwell conditions of 1250 °C, 103 MPa (15,000 psi) for 4 h. The 700 °C dwell was included as a conservative step, to ensure the centre of the AFIC chamber observed the set-point temperature before ramping to the higher temperatures. This was a conservative step made to ensure the sample received the target processing conditions and that no damage was inflicted to the AFIC.

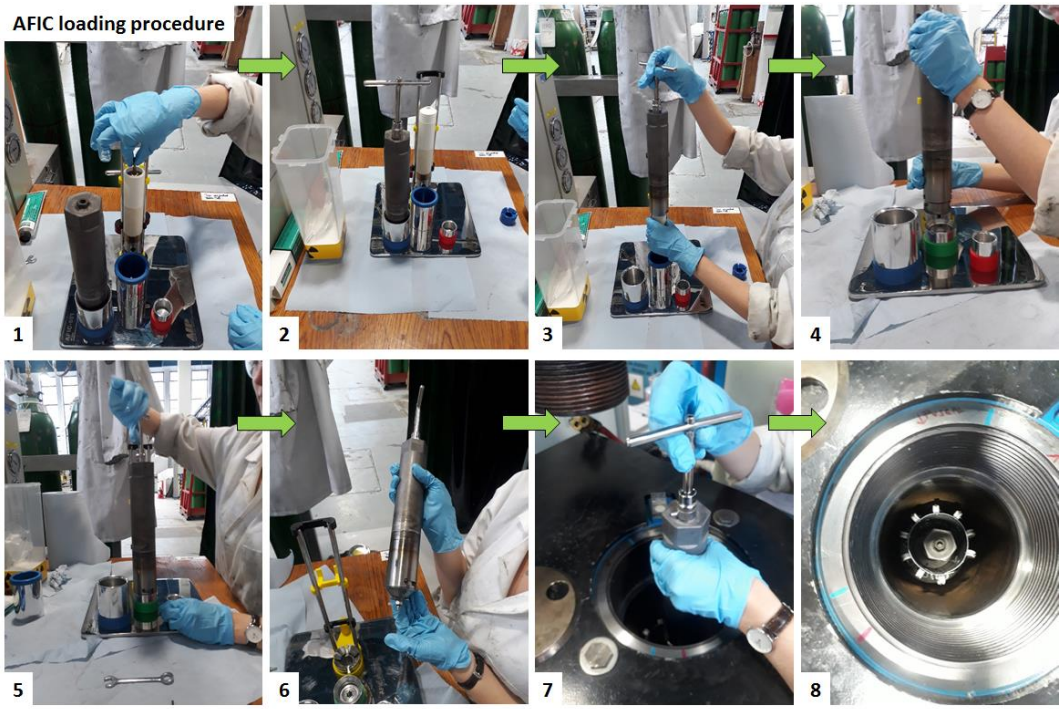

Figure 9.6: The HIP canister was loaded into the AFIC, which was then loaded into the furnace inside the HIP. 1) HIP canister inserted into the crucible, 2) Lid placed over HIP canister to keep secure, 3) Chamber lowered over the assembly, 4-5) Locking of the chamber to engage the O-ring seal, 6) The locked and sealed AFIC ready for HIPing, 7) Lowering of the AFIC into the furnace inside the HIP pressure vessel, 8) AFIC secured in the furnace inside the HIP pressure vessel.

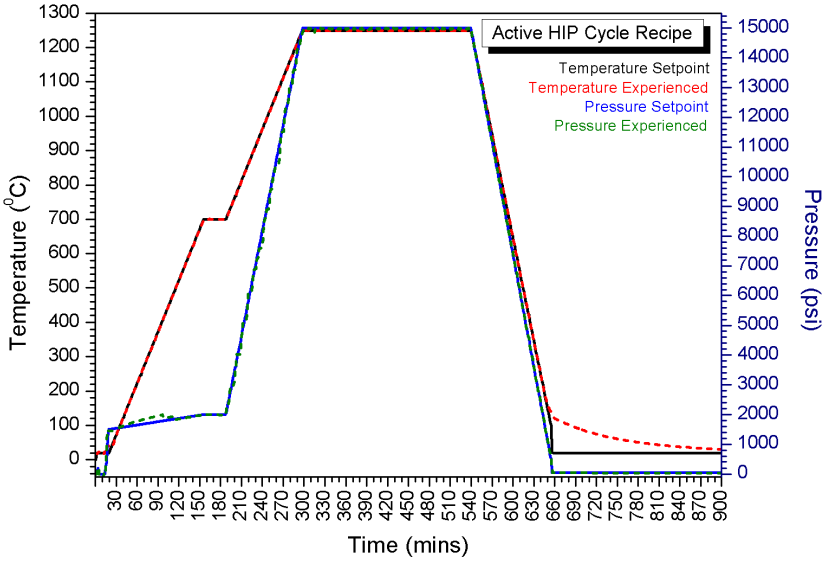

Figure 9.7: Schematic representation of the HIP cycle showing the additional 30 min dwell at 700 °C, 13.8 MPa (2000 psi). The final dwell conditions were 1250 °C for 4 h under 103 MPa (15,000 psi).

Figure 9.8 shows the unloading process inside a fumehood and Table 9.2 summarises the canister dimensions before and after processing. The sample was sectioned on a Buehler Isomet™ 1000 high speed saw using a HC diamond blade at 975 rpm with a 500 g load. The SEM sample was cold mounted in epoxy resin and ground and polished, by hand, to a 1 µm finish before carbon coating. SEM data was collected on a Hitachi TM3030 microscope with an accelerating voltage of 15 keV at a working distance of 8 mm. A 1.5 mm thick cross-section was taken from the centre of the canister and was crushed in a pestle and mortar for powder XRD. The XRD data was collected on a Bruker D2 PHASER with Cu Kα radiation (1.5418 Å) between $10° < 2\theta < 70°$, with a 0.02° step size, over 3 h.

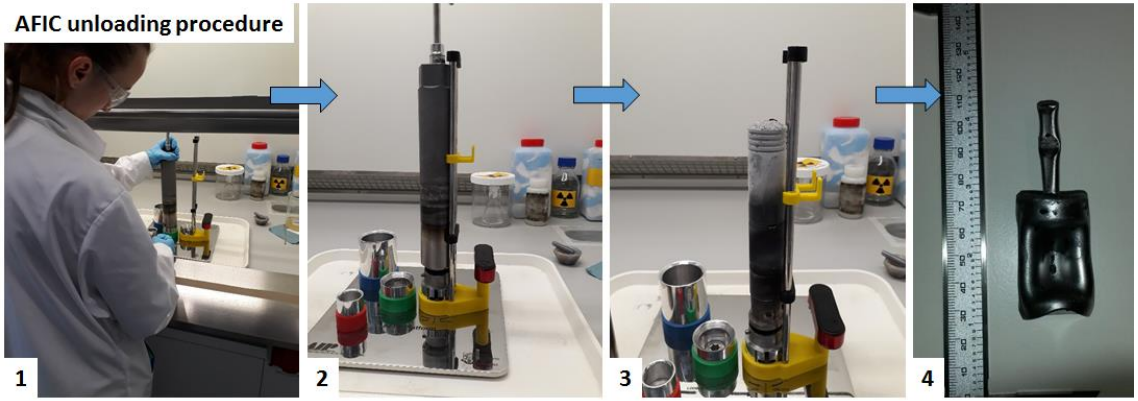

Figure 9.8: The AFIC was transported from the HIP in a sealed container and was opened inside a fumehood in a controlled area. Regular monitoring was performed during the unloading process. 1) Unlocking of the AFIC to disengage the O-ring seal, 2-3) Chamber carefully lifted and removed from the AFIC assembly, 4) The HIP canister after processing.

Table 9.2: Canister dimensions before and after HIPing.

Sample	**Mass before (g)** (±0.05)	**Height before (mm)** (±0.02)	**Middle diameter before (mm)** (±0.02)	**Volume displacement before (g/cm³)** (±0.05)	**Mass after (g)** (±0.05)	**Height after (mm)** (±0.05)	**Middle diameter after (mm)** (±0.05)	**Volume displacement after (g/cm³)** (±0.05)	**Canister densification %** (±0.1)
A	104.38	45.32	25.99	22.20	104.45	41.30	20.15	15.16	68.3

9.3.1 Results

The canister dimensions before and after consolidation confirmed successful densification of the sample. The large, 68 %, volume reduction was partly a result of the annular gap around the pellets and confirmed the canister design was suitable for operation. Regular monitoring was conducted throughout the sample preparation process and no contamination was detected at any stage. On opening of the AFIC, a fibrous residue was present inside that covered the crucible and lid. The residue was not radioactive and was a result of organic compounds decomposing from structural components that experienced the high temperatures for the first time. The residue was not found inside the filter house or outside the AFIC chamber, which, although not radioactive, confirmed successful containment during the HIP cycle.

The HIPed canister was sectioned successfully and was analysed by SEM and XRD. The BSE micrographs in Figure 9.9 show the fine microstructure of the glass-ceramic, representative of previous samples. Coupled with the XRD data, zirconolite ($CaZrTi_2O_7$) was identified as the major crystalline phase, with minor phases; sphene ($CaTiSiO_5$), baddeleyite (ZrO_2), rutile (TiO_2) and unincorporated uranium dioxide (UO_2). Zirconolite-2M was the main polytype stabilised and two low angle reflections, at $2\theta = 15.8°$ and 28.8°, in the XRD data indicated the presence of the zirconolite-3T polytype as well. UO_2 reflections in the XRD pattern confirmed incomplete waste digestion and SEM revealed small particles of UO_2 throughout the glass-ceramic.

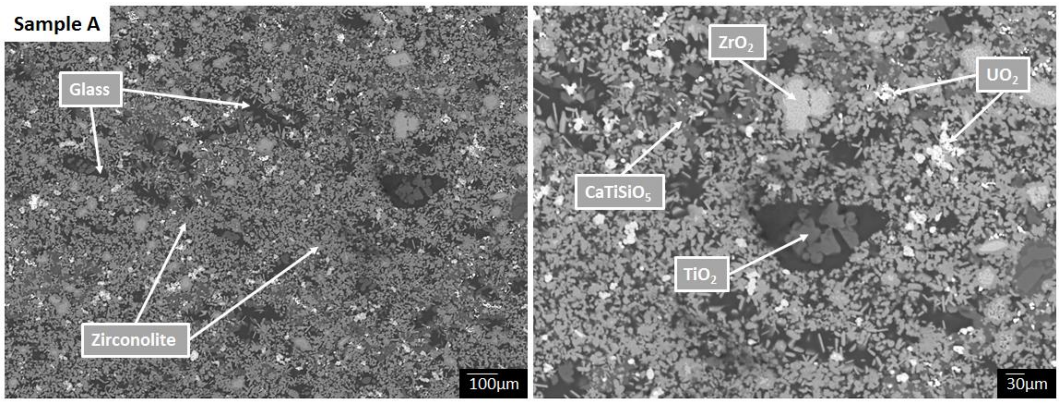

Figure 9.9: BSE micrographs showing the microstructure of the HIPed sample. Zirconolite-2M ($CaZrTi_2O_7$) was the major crystalline phase, with minor phases; zirconolite-3T ($CaZrTi_2O_7$), baddeleyite (ZrO_2), rutile (TiO_2), sphene ($CaTiSiO_5$) and unincorporated uranium dioxide (UO_2).

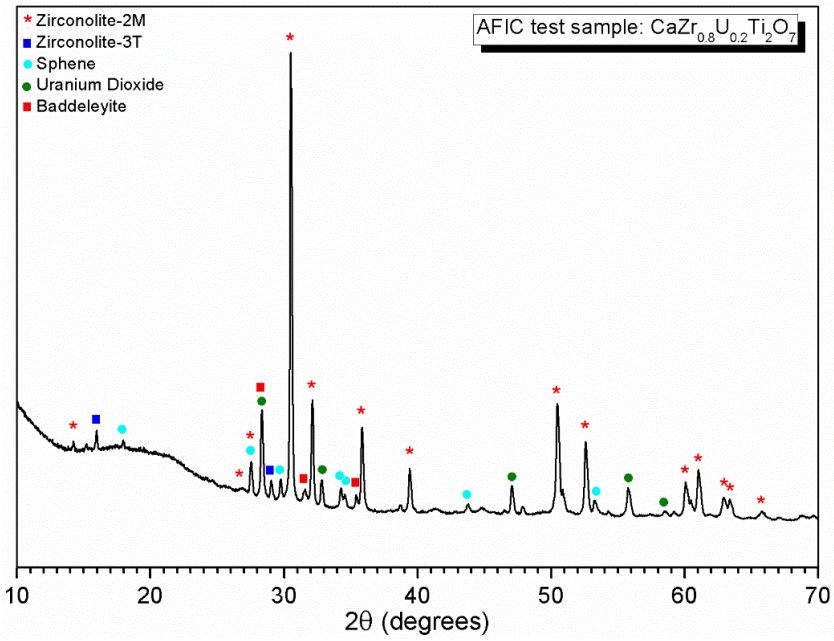

Figure 9.10: XRD data confirmed zirconolite-2M was the main polytype stabilised with minor phases; zirconolite-3T ($CaZrTi_2O_7$), sphene ($CaTiSiO_5$), baddeleyite (ZrO_2) and uranium dioxide (UO_2) (PDF cards: 04-007-6895, 00-054-1132, 01-085-0395, 01-089-9066, 01-078-0664, respectively). The UO_2 present confirmed complete waste incorporation was not achieved. The SEM data revealed rutile (TiO_2) was also present, but was not identified in the XRD pattern due to peak overlap.

SEM-EDX analysis of the zirconolite and glass phases allowed for an estimated U partitioning ratio to be established. Despite the incomplete waste digestion, the SEM-EDX confirmed preferential incorporation of the U into the zirconolite phase at a ratio of 100 : 3, zirconolite : glass. This was in agreement with the U samples fabricated and characterised at ANSTO in Chapter 8.

For compositional analysis, the glass forming components were disregarded and the Ca, U, Zr and Ti data were used to determine an approximate cation stoichiometry for the ceramic phase. By scaling all elements for an ideal B-site stoichiometry (Ti_x where x=2), the cation ratio was in line with that of zirconolite $CaZrTi_2O_7$, see Table 9.4, with a total of 3.73 cations. The small cation deficiency was thought to be a result of the analysis method and the assumption that no Al was present. From previous results discussed in Chapters 6 and 8, it was assumed the cation deficiency corresponded to Al. Thus, a resultant composition of $Ca_{0.87}Zr_{0.70}U_{0.16}Ti_{2.00}Al_{0.27}O_7$ was determined. The composition implied the U substitution took place on the Zr site, with a near 1 : 1 ratio between Ca and (Zr + U), and charge balance calculations gave an average U valence state of 4.1 (see Table 9.4).

Table 9.3: The U partitioning ratio between the zirconolite, glass and sphene phases, calculated from the averaged at. % SEM-EDX data.

Sample		Zirconolite	Glass	Ratio Z : G
A	U	0.37	0.01	100 : 3

Table 9.4: SEM-EDX compositional analysis of the zirconolite phase. The cation ratio determined suggested U substitution on the Zr site to achieve a 1 : 1 ratio between Ca and (Zr + U) and an average U valence state of 4.1.

Sample A									
	Ca^{2+} (±0.18)	U^{4+} (±0.20)	Zr^{4+} (±0.43)	Ti^{4+} (±0.45)	Na^{+} (±0.15)	Al^{3+} (±0.06)	Si^{4+} (±0.12)	O^{2-} (±11.73)	Valence check
Average data	2.03	0.37	1.64	4.69	1.26	0.50	1.05	88.45	
	2.03	0.37	1.64	4.69					
scaled for $Ti_{2.00}$	**0.87**	**0.16**	**0.70**	**2.00**					
	0.87	**0.16**	**0.70**	**2.00**		**0.27**			
charge calc.	1.74		2.80	8.00		0.81		-14.00	-0.65
charge balance	1.74	0.65	2.80	8.00		0.81		-14.00	0
$Ca_{0.87}Zr_{0.70}U_{0.16}Ti_{2.00}Al_{0.27}O_7$									

9.3.2 Discussion

A UO_2 containing HIP sample was fabricated and analysed following the new SOP and safety procedures for conducting radioactive HIP work at the University of Sheffield (UoS). Successful fabrication and consolidation of the HIP sample was achieved and no contamination was detected throughout the entire procedure. Not only did this confirm the SOP was sufficient for maintaining a safe and practical operating procedure, this demonstration provided a significant advancement of the HIP technology for processing radioactive waste. The AFIC is a first of its kind containment device for consolidating radioactive material in a HIP that ensures a reliable seal with repeated operation. An earlier method of containment, known as the Activity Containment Overpack (ACOP), was designed at ANSTO (by Salvatore Moricca) for single use operation [283,284]. The ACOP utilises a flat flange-to-lid surface seal where a gasket is bolted secure in-between. This provides the seal for the internal chamber of the ACOP during processing. The lid has one or more built in filters that allow gas flow in and out of the ACOP for consolidation of the sample inside. Whilst the ACOP design is more suitable for single use operation, it cannot be assured for a reliable, repeatable seal each and every time. The design utilises a gasket and metal thread seals that are located in the hot zone of the HIP and experience the full conditions of the HIP cycle. This results in a gradual degradation of the gasket and threads with each operation.

Overtime, a build-up of oxidation on the metal threads and sintered metal filters may render the seal and air flow insufficient for safe operation. The ACOP design relies on human operation to achieve the seal when affixing the lid with bolts and there is no measurable way of determining whether or not a secure seal is achieved before processing.

In comparison, the AFIC is designed such that the filter house and O-ring seal are located in the cold zone of the furnace, thus do not experience the high temperatures of the HIP during processing. Thus all the seals and filters remain within (and never exceed) the design limits as certified by the manufacturer. This minimises the degradation of the seal and filters during operation to maintain their efficiency. The location of the filters in the cold zone of the furnace means oxidation degradation does not occur and blockages are highly unlikely. There are multiple layers to the filter system, such that if a blockage was to occur, the AFIC performance would not be inhibited and there is no risk of a blockage sealing in high pressures. The locking procedure of the AFIC ensures a complete and reliable seal, which minimises the influence of human error when engaging the O-ring seal. The overall design of the AFIC makes it simple and easy to operate within radioactive facilities and fits inside a glovebox. The assembly allows for easy decontamination of all components, as well as easy maintenance and replacement of individual parts.

The UO_2 test sample achieved a similar phase assemblage and microstructure to samples discussed throughout this thesis, but did not achieve the same level of waste incorporation, as was observed in the U samples fabricated at ANSTO (Chapter 8). The equivalent sample, $CaZr_{0.8}U_{0.2}Ti_2O_7$, fabricated at ANSTO, achieved near complete waste incorporation and single phase zirconolite, except for accessory phases TiO_2 and Ti_3O_5 that resulted from the Ti metal powder (Figure 8.5). The incomplete waste digestion observed in the UoS sample discussed here, may have been a result of insufficient milling or a less reactive starting reagent. The milling equipment available for active samples could only accommodate small mill pots (45 ml). The importance of milling for successful waste incorporation has been previously discussed (Chapter 6) and it is possible that the forces required for complete waste digestion were not achieved in the smaller mill pots and therefore inhibited the UO_2 incorporation.

In Chapter 8, the UO_2 was voloxidised to U_3O_8 to increase the reagent reactivity and maximise its incorporation into the glass-ceramic. The UO_2 here was not voloxidised, which may have limited its reactivity and consequently, its incorporation into the glass-ceramic. The use of

U_3O_8 in Chapter 8 may have facilitated the incorporation of the U by increasing its solubility into the glass melt. Whilst the U_3O_8 was calcined under reducing atmosphere to regain the U^{4+} oxidation state, the degree of success of this heat treatment was not confirmed by XRD. If the waste incorporation mechanism takes place by first incorporating the U into the glass melt, the UO_2 will have a lower solubility compared to U_3O_8 [290,291]. It is possible, despite the reducing atmosphere during calcination, that U_3O_8 was still present in the ANSTO samples and was first incorporated into the glass melt, before the Ti metal acted to reduce the U^{5+} to U^{4+}. At this point the solubility of the U would decrease, resulting in the U^{4+} being kicked out of the glass and incorporated into the zirconolite ceramic. In order to determine if this is the case, or if the milling conditions inhibited the waste digestion, further investigations must be conducted.

9.4 Conclusions

In collaboration with AIP and AMEPT, the first of a kind Active Furnace Isolation Chamber (AFIC) has been installed at the University of Sheffield. The AFIC is a significant advancement of the HIP technology for processing radioactive waste materials in the UK, by providing safe and reliable containment during processing. It is envisaged that the research conducted in the Immobilisation Science Laboratory at The University of Sheffield will provide useful information on the operation and performance of the AFIC, to enable AIP and AMEPT to further develop this innovative piece of equipment and further the technology readiness level of hot isostatic pressing for the treatment of radioactive waste.

10 Conclusions

This thesis was focused on the development of zirconolite glass-ceramics for the immobilisation of the UK's Pu-residues inventory and for the potential future treatment of the civil separated PuO_2 stockpile material. The success of this study has been clearly demonstrated in the progression of this research, through process and formulation optimisation, inactive and low activity surrogate studies, the fabrication of PuO_2 loaded HIP samples and the nuclearisation of a research HIP facility. The relevance and impact of this work to the UK's current plutonium management strategic plan is significant and will contribute fundamentally to the development of HIP technology for the treatment of Pu wastes in the UK.

The main aim of this thesis project was *"to develop a high fraction zirconolite glass-ceramic wasteform, consolidated by hot isostatic pressing, for the disposition of Pu-based higher activity wastes within the UK".* The glass-ceramic system needed to achieve suitable waste incorporation levels and actinide partitioning ratios, whilst reducing the overall neutron source term of the wasteform matrix. Throughout this thesis the results have been discussed within each chapter and this chapter will provide an overall summary of the main findings and propose areas for further investigation.

This study has demonstrated multiple factors that govern the quality, phase assemblage and waste incorporation behaviour of zirconolite glass-ceramic wasteforms, including; formulation, milling parameters, pO_2, and additives. To underpin the relationship between the glass composition and glass-ceramic phase assemblage, a sample matrix was fabricated varying both the glass composition and glass fraction. The dependence of the crystalline phase assemblage on the glass composition was clearly demonstrated and highlighted the sensitivity of these glass-ceramic systems to variations in the formulation. Whilst this sensitivity can provide flexibility to the wasteform, it must be robustly understood in order to define a suitable operational formulation window. Without this understanding it may not be possible to build a safety case for these materials or gain the required international, regulatory approval for these wasteforms to be accepted. That said, the flexibility of these systems allows for minor variations in formulation to accommodate changes in waste feed composition. It is proposed that, with sufficient waste characterisation, this would allow

glass-ceramic formulations to be customised in order to accommodate waste variations and impurities on a case by case basis. This might be facilitated by increasing or reducing the glass fraction to accommodate more or less impurities, or alternatively to accommodate lower or higher actinide loadings.

The work in this thesis led to the conclusion that the phase assemblage is largely controlled by the glass and that certain phases act as intermediates whilst others precipitate during cooling. The hypothesis proposed was that the phase assemblage is largely controlled by changes to the glass structure, whereby additions of B_2O_3 reduced the connectivity of the glass network thus increased the solubility of Zr. The hypothesis was supported by EPMA compositional data that showed a reduction of Zr solubility with reduced levels of B_2O_3 in the formulation. To further underpin crystalline phase formation and the relevant mechanisms involved, *in-situ* high temperature neutron diffraction experiments are scheduled to observe the melt behaviour and stages of crystalline phase formation with increased time resolution. These experiments will take place at the Oak Ridge National Laboratory (ORNL).

With an optimised formulation that maximised the yield of zirconolite and minimised the presence of accessory phases, CeO_2 incorporation experiments were conducted to investigate the waste incorporation behaviour of the glass-ceramic. Previous formulations have utilised CaF_2 to aid waste digestion, however, ^{19}F acts as a neutron source for (α,n)-reactions within the wasteform. This thesis aimed to minimise or eliminate the need for the CaF_2 in order to reduce the neutron source term of the wasteform precursor. Initial CeO_2 samples did not achieve full waste incorporation and small CaF_2 additions were shown to improve the digestion of CeO_2. Despite the high Al_2O_3 glass composition in the new glass-ceramic formulation, full waste incorporation was achieved with just 0.3 wt. % CaF_2 additions. This was a 50 % reduction of the CaF_2 compared to previous trials performed at NNL. However, equivalent results were obtained without CaF_2 by milling in a larger mill pot. The implementation of a 250 ml mill pot provided sufficient milling for complete waste digestion. These results showed that alternative methods can improve waste digestion without increasing the neutron source term for (α,n)-reactions. These results could remove the need for CaF_2 as a digestion agents and help keep the neutron source term as low as reasonably practical, without inhibiting the waste incorporation.

It has also been discussed that B can act as a neutron source for (α,n)-reactions and can lead to higher worker dose exposures, without the implementation of extra shielding. The new baseline glass-ceramic formulation did not include B_2O_3, as its removal from the glass formulation yielded better formation of zirconolite in the HIPed products. This result also led to the subsequent elimination of the B source term for (α,n)-reactions. Results so far have provided promising evidence that the need for CaF_2 could be eliminated, however, if further research deems the advantages of CaF_2 out-weigh the contributing (α,n) effects, then the removal of B_2O_3 will still have significantly reduced the overall neutron source term of the wasteform. In addition, the results in this thesis have demonstrated that full waste incorporation can be achieved in the B_2O_3 free formulation with 50 % less CaF_2 than has been previously reported, thus further reducing the effective source term of the wasteform precursor.

Effective glass-ceramic wasteforms will ideally partition actinides into the ceramic phase. The partitioning ratios achieved throughout this thesis were found to be comparable to those reported in the literature. The elimination of CaF_2 and application of a more intensive milling regime did not inhibit the actinide partitioning into the ceramic phase, which proved that alternative measures and process parameters can be implemented for complete waste digestion and effective actinide partitioning.

A significant portion of Pu waste materials are identified as being Cl contaminated, due to the degradation of PVC packaging during storage. NaCl was added to the glass-ceramic baseline formulation to determine the Cl solubility limit within the aluminosilicate glass phase. NaCl was chosen to minimise the effects of volatilisation during these studies and allowed for maximum Cl incorporation in the glass to be achieved. Results identified a solubility limit of 0.9 ± 0.1 wt. % Cl, which was substantially greater than the conservative, maximum levels of Cl expected in the wastes. Through Cl K-edge XANES analysis, the Cl was found to be preferentially speciated with Ca and Na in the aluminosilicate glass. Combinatorial linear combination fits against multiple binary and aluminosilicate based reference materials, revealed multiple Cl environments present within the glass and that eudialyte environments were most abundant below the Cl solubility limit. The literature was in excellent agreement with the XANES data presented and confirmed preferential association of Cl with Ca and Na within aluminosilicate glass matrices.

SEM-EDX confirmed the overwhelming incorporation of the Cl into the glass phase and that the contaminant did not affect the incorporation of Ce into the ceramic phases, thus showing that it is possible to stabilise Cl and Pu in separate phases within the wasteform. This is preferential within these wasteforms for radionuclide retention properties during long-term storage and disposal.

The importance and impact of inactive surrogate work is well known and accepted, however, each surrogate has its limitations. The utilisation of Ce and U surrogates throughout this project provided a detailed suite of data on the waste incorporation behaviour of the glass-ceramic, in order to progress to PuO_2 incorporation. The Ce work provided confirmation that the new glass-ceramic formulation was in-line with previous formulations reported in the literature, with regards to waste incorporation behaviour, actinide partitioning and phase assemblage. It was shown that Ce^{3+} promoted the formation of a Ce-rich perovskite phase, which was favourable over the incorporation of Ce in the glass. Whilst not all the Ce was incorporated into the zirconolite the formation of perovskite is considered highly advantageous for an actinide bearing wasteform over the Ce being present in the glass. The reduction of Ce^{4+} to Ce^{3+} is a known limitation of Ce as a Pu surrogate. Pu is less likely to reduce under equivalent conditions thus the results with the Ce may not be representative of Pu behaviour in the wasteform. In order to confirm or deny this, the consolidation and characterisation of PuO_2 loaded samples was required.

Before progressing to the Pu work, U samples were first investigated. The U samples were highly successful at incorporating the waste into the zirconolite phase and provided clear distinction between the small variations in stoichiometry and the degree of waste digestion and U partitioning. The added Al_2O_3 for charge compensation reduced the reaction kinetics of the melt resulting in a smaller grain size and less effective waste digestion. Al_2O_3 has been commonly used as a charge compensator in glass-ceramic systems, however, these results show that with the new glass formulation $Na_2Al_2Si_6O_{16}$, Al_2O_3 impedes the waste incorporation and growth of the ceramic phase. The SEM-EDX results for the other U samples confirmed Ti^{3+} charge compensation. Further work may look into targeting Ti^{3+} charge compensation in the starting formulation as a way to optimise and maximise the waste incorporation into the zirconolite.

Fabrication of PuO_2 loaded HIP samples was an important advance within this project. The UK does not currently have the facilities to perform radioactive HIP research of this kind, thus, outside of the BNFL – ANSTO collaboration on the Pu-residues HIP project, no PuO_2 HIP research had been achieved within the UK at this scale. The PuO_2 samples here were hugely successful and achieved full waste incorporation at 10 wt. % actinide loading. At 5 wt. % loading only single phase zirconolite was identified by SEM and XRD and only minor changes to phase assemblage were observed at the higher loading. Unfortunately, due to the fine grain size, limited microscopy facilities and time available, accurate actinide partitioning ratios could not be attained. Further work to characterise these samples should aim to obtain SEM-EDX data for compositional and partitioning analysis, DRS will give insight into the oxidation state of Pu within the glass-ceramic matrix and PCT / MCC-1 dissolution studies will give insight into the actinide retention properties of these wasteforms. The samples here are part of a five sample matrix investigating the effect of partial oxygen pressure (pO_2) on the oxidation state and incorporation behaviour of Pu in the glass-ceramics. The remaining samples to this matrix are currently being fabricated and characterised at ANSTO and will give an insight to how the incorporation of Pu changes with changes to the atmospheric conditions inside the HIP canister.

It is hoped the results presented will contribute to current information / knowledge available for determining a suitable operation and formulation window for treatment of Pu-residues and civil separated PuO_2 stockpile material. Throughout this thesis the same HIP conditions and standard HIP cycle recipe were used that were consistent with previous work at NNL. The HIP cycle can have significant impact on the deformation of HIP canisters and provides the operator with significant control over what forces the canister is subjected too and how it deforms. Similarly, the HIP cycle may be optimised for sample quality, energy efficiency, safety cases and longevity. Unfortunately time did not allow for different HIP conditions and HIP cycle recipes to be investigated but for commercialisation of this technology, further work should be done investigating the effects of individual processing steps and HIP parameters, to determine an optimised process and suitable operating window.

In collaboration with AIP, the Active Furnace Isolation Chamber was installed at the University of Sheffield to enable the processing of radioactive research samples. This furnace is a first of its kind containment device for repeated use in a HIP facility and makes UoS the first research HIP facility suitable for processing radioactive materials in the UK. This provides

a unique facility for radioactive research to support industrial projects and advancements of the HIP technology readiness level for treating radioactive waste.

It is hoped the results presented in this thesis will add to the current framework of knowledge and understanding of glass-ceramic materials for the immobilisation of actinide wastes. The UK is developing hot isostatic pressing for the potential treatment of the Pu stockpile material and there is a significant amount of industrial interest in developing the HIP technology to a maturity level suitable for building pilot demonstration plants. The radioactive wasteform work in this thesis demonstrates that at a laboratory scale, HIP can be used to safely process low levels of active material, whilst the installation of the active furnace isolation chamber and nuclearisation of Sheffield's HIP facility is a huge step forward in demonstrating this technology to industrial, governmental and regulatory bodies within the nuclear industry.

11 References

[1] M. Jervis, Reprocessing in the UK - the history, the present and the future, (2009).

[2] Department of Business, Energy and Industrial Strategy (BEIS), Nuclear Decommissioning Authority (NDA), 2016 UK Radioactive Waste and Materials Inventory: UK radioactive waste inventory report, 2016.

[3] M.I. Ojovan, An introduction to nuclear waste immobilisation, 1st ed, Elsevier, Amsterdam ; Boston, 2005.

[4] Radioactive Waste Management, World Nuclear Association. (2017). http://www.world-nuclear.org/information-library/nuclear-fuel-cycle/nuclear-wastes/radioactive-waste-management.aspx (accessed September 5, 2017).

[5] Sellafield Ltd., ILW treatment and storage, (2017). http://www.sellafieldsites.com/solution/waste-management/ilw-treatment-and-storage/ (accessed December 7, 2017).

[6] Department of Energy and Climate Change (DECC), Implementing Geological Disposal: A framework for the long-term management of higher activity radioactive waste, 2014.

[7] Nuclear Decommissioning Authority (NDA), Geological Disposal: An introduction to the disposal system specification, 2010.

[8] Nuclear Decommissioning Authority (NDA), Progress on approaches to the management of separated plutonium - Position paper - v1.0, Nuclear Decommissioning Authority, 2014.

[9] Nuclear Decommissioning Authority (NDA), NDA Plutonium Topic Strategy: Credible Options Summary, 2009.

[10] Department of Energy and Climate Change (DECC), Management of the UK's plutonium stocks. A consultation response in the long-term management of UK-owned separated civil plutonium, 2011.

[11] N. C. Hyatt, Plutonium management policy in the United Kingdom: The need for a dual track strategy., Energy Policy. 101 (2017) 303–309.

[12] Department of Energy and Climate Change (DECC), Management of the UK's plutonium stocks. A consultation response on the proposed justification process for the reuse of plutonium, 2013.

[13] Office of Nuclear Regulations (ONR), Annual civil plutonium and uranium figures as of 31 December 2014, (2017). http://www.onr.org.uk/safeguards/civilplut14.htm.

[14] M.W.A. Stewart, S.A. Moricca, B.D. Begg, R.A. Day, C.R. Scales, E.R. Maddrell, A.B. Eilbeck, Flexible process options for the immobilisation of residues and wastes containing plutonium, in: The 11th International Conference on Environmental

Remediation and Radioactive Waste Management, American Society of Mechanical Engineers, 2007: pp. 1453–1460. http://proceedings.asmedigitalcollection.asme.org/proceeding.aspx?articleid=1601615 (accessed February 3, 2016).

[15] C.R. Scales, E.R. Maddrell, N. Gawthorpe, B.D. Begg, S. Moricca, R.A. Day, M.A. Stewart, Demonstrating a Glass Ceramic route for the Immobilisation of Plutonium containing Wastes and Residues on the Sellafield Site, Proceedings WM. 6 (2006).

[16] J.W. Hobbs, C.R. Scales, E.R. Maddrell, M.W.A. Stewart, S.A. Moricca, A programme to immobilise plutonium residues at Sellafield, in: Paper for the Institute of Nuclear Materials Management 53rd Annual Meeting, Orlando, Florida, 2012.

[17] R.A. Day, S. Moricca, M.W.A. Stewart, B.D. Begg, E.R. Maddrell, C.R. Scales, N. Gawthorpe, Technical Demonstration of Zirconolite Glass-Ceramics Processed in a Hot Isostatic Press: An Option for Immobilisation of Actinide Containing Residues at Sellafield, in: ICEM, Scotland, UK, 2005.

[18] Nuclear Decommissioning Authority (NDA), Conditioning of Plutonium Residues by Hot Isostatic Pressing and Options for packaging and Disposal (pre-conceptual stage) Summary of Assessment Report, 2009.

[19] International Atomic Energy Agency (IAEA), IAEA Safety Standards for protecting people and the environment. Classification of Radioactive Waste. General Safety Guide, 2009.

[20] International Atomic Energy Agency (IAEA), Development of Specifications for Radioactive Waste Packages, 2006.

[21] International Atomic Energy Agency, Disposal of Radioactive Waste: Specific Safety Requirements, 2011.

[22] Nuclear Decommissioning Authority, Geological Disposal: Generic Waste Package Specification, 2012.

[23] D. Caurant, ed., Glasses, glass-ceramics and ceramics for immobilization of highly radioactive nuclear wastes, Nova Science Publishers, New York, 2009.

[24] A. Macfarlane, Immobilization of excess Weapon Plutonium: A Better alternative to glass, Science & Global Security. 7 (1998) 271–309.

[25] Nuclear Decommissioning Authority (NDA), Plutonium credible options analysis (Gate A), 2010.

[26] C.R. Scales, E.R. Maddrell, N. Gawthorpe, B.D. Begg, S. Moricca, R.A. Day, Development of a Process for the Immobilisation of Actinide Containing Residues on the Sellafield site, in: ICEM, Scotland, UK, 2005.

[27] ANL, Plutonium - Human health fact sheet, (2001).

[28] J. P. Patterson, P. Parkes, Chapter 8: Recycling uranium and plutonium, in: The Nuclear Fuel Cycle: From Ore to Wastes, Oxford University Press, Oxford ; New York, 1996: pp. 138–160.

[29] Physical, nuclear and chemical properties of Plutonium, Institute for Energy and Environmental Research. (2012). http://ieer.org/resource/factsheets/plutonium-factsheet/ (accessed July 2, 2017).

[30] Mixed Oxide (MOX) fuel, World Nuclear Association. (2017). http://www.world-nuclear.org/information-library/nuclear-fuel-cycle/fuel-recycling/mixed-oxide-fuel-mox.aspx (accessed June 9, 2018).

[31] E. D. Clayton, Anomalies of Nuclear Criticality, revision 6, Pacific Northwest National Laboratory (PNNL), Richland, WA (US), Environmental Molecular Sciences Laboratory (EMSL), 2010.

[32] J. S. Choi, Long-term criticality concerns associated with disposition of weapons plutonium., in: Proceedings of the Nuclear Criticality Technology Safety Project, Los Alamos National Laboratory, Virginia USA, 1994: pp. 89–90.

[33] MIT NSE Nuclear Information Hub: What is Criticality?, Nuclear Science and Engineering at MIT. (2011). https://mitnse.wordpress.com/2011/03/18/what-is-criticality/.

[34] M.W.A. Stewart, B.D. Begg, R.A. Day, S. Moricca, E.R. Vance, P.A. Walls, Low-risk alternative waste forms for actinide immobilization, in: Proceedings of the Annual Waste Management Symposium (WM'05), 2005. http://www.wmsym.org/archives/pdfs/5212.pdf (accessed February 3, 2016).

[35] Nuclear Forensic Search Project, Decay Chains, (2011). http://metadata.berkeley.edu/nuclear-forensics/Decay%20Chains.html (accessed February 25, 2018).

[36] C. Burrows, C. Phillips, A. Milliken, The Thermal Oxide Reprocessing Plant at Sellafield - Lessons Learned from 10 Years of Hot Operations and their Applicability to the DOE Environmental Management Program., in: WM'06 Conference Proceedings, Tucson, Arizona, USA, 2006: pp. 1–17.

[37] Parliamentary Office of Science and Technology, Managing the UK Plutonium Stockpile, The Houses of Parliament, 2016.

[38] I. S. Denniss, A. P. Jeapes, Chapter 7: Reprocessing irradiated fuel, in: The Nuclear Fuel Cycle: From Ore to Wastes, Oxford University Press, Oxford ; New York, 1996: pp. 117–137.

[39] Nuclear Energy Agency, Spent Nuclear Fuel Reprocessing Flowsheet, NEA Nuclear Science Committee, 2012.

[40] Radioactive Waste Management (RWM), Geological Disposal: The 2013 Derived Inventory, 2015.

[41] National Nuclear Laboratory (NNL), Australian Nuclear Science and Technology Organisation (ANSTO), Sellafield Ltd., Immobilisation of Pu residues using HIP, (2009).

[42] M.W.A. Stewart, S.A. Moricca, E.R. Vance, R.A. Day, E.R. Maddrell, C.R. Scales, J. Hobbs, Hot-Isostatic Pressing of Chlorine-Containing Plutonium Residues and Wastes, in: Tms (Ed.), TMS2013 Supplemental Proceedings, John Wiley & Sons, Inc., Hoboken, NJ, USA, 2013: pp. 675–682. http://doi.wiley.com/10.1002/9781118663547.ch83 (accessed November 2, 2014).

[43] Department of Energy (DOE), Record of decision: Storage and disposition of weapons-usable fissile materials, Federal Register. 68 (2003) 64611–64614.

[44] Department of Energy (DOE), Record of decision for the storage and disposition of weapons-usable fissile materials. Final Programmatic environmental impact statement, Federal Register. 62 (1997) 3014–3030.

[45] National Academy of Sciences (U.S.), Panel to Review the Spent-Fuel Standard for Disposition of Excess Weapon Plutonium, Spent fuel standard for disposition of excess weapon plutonium: application to current DOE options, National Academies Press, Washington, D.C., 2003. http://search.ebscohost.com/login.aspx?direct=true&scope=site&db=nlebk&db=nlabk&AN=87198 (accessed February 22, 2017).

[46] Arun Varshneya, Fundamentals of Inorganic Glasses, 2. ed, Society of Glass Technology, Sheffield, 2006.

[47] J. E. Shelby, Introduction to glass science and technology, 2nd ed, Royal Society of Chemistry, Cambridge, 2005.

[48] R.H. Doremus, Glass science, 2nd ed, Wiley, New York, 1994.

[49] W. H. Zachariasen, The atomic arrangement in glass, Journal of American Chemistry Society. 54 (1932) 3841–3851.

[50] B. E. Warren, Summary of work on atomic arrangement in glass, Journal of American Ceramics Society. 24 (1941) 256–261.

[51] G. N. Greaves, EXAFS and the structure of glass, Journal of Non-Crystalline Solids. 71 (1985) 203–217.

[52] Arun Varshneya, Chapter 3: Glass formation principles, in: Fundamentals of Inorganic Glasses, 2nd ed, Society of Glass Technology, 2006.

[53] Arun Varshneya, Chapter 5: Glass compositions and structures, in: Fundamentals of Inorganic Glasses, 2nd ed, Royal Society of Chemistry, Sheffield, 2006: pp. 101–160.

[54] J. E. Shelby, Chapter 5: Structure of Glasses, in: Introduction to Glass Science and Technology, 2nd ed, The Royal Society of Chemistry, Cambridge, 2005: pp. 72–109.

[55] M. Hubert, A. J. Faber, On the structural role of boron in borosilicate glasses, Physics and Chemistry of Glasses. 55 (2014) 136–158.

[56] J. Biscoe, B. E. Warren, X-ray diffraction study of soda-boric oxide glass, Journal of Amercan Ceramics Society. 21 (1938) 287–293.

[57] P. J. Bray, J. G. O'Keefe, Physics and Chemistry of Glasses. 4 (1963) 37–46.

[58] A. J. Connelly, N. C. Hyatt, K. P. Travis, R. J. Hand, E. Maddrell, Predicting the preference for charge compensation in silicate glasses., Physics and Chemistry of Glasses. 52 (2011).

[59] Q. J. Zheng, R. E. Youngman, C. L. Hogue, J. C. Mauro, M. Potuzak, M. M. Smedskjaer, Y. Z. Yue, Structure of boroaluminosilicate glasses: Impact of [Al2O3/SiO2] ratio on the structural role of sodium, Physical Review B. 86 (2012) 1–12.

[60] L. Cormier, D. Ghaleb, J. M. Delaye, G. Calas, Competition for charge compensation in borosilicate glasses: wide-angle X-ray scattering and molecular dynamics calculations, The American Physical Society. 61 (2000) 495–499.

[61] H. Li, P. Hrma, J. D. Vienna, M. Qian, Y. Su, D. E. Smith, Effects of Al2O3, B2O3, Na2O and SiO2 on nepheline formation in borosilicate glasses: chemical and physical correlations, Journal of Non-Crystalline Solids. 331 (2003) 202–216.

[62] I.W. Donald, Waste immobilization in glass and ceramic based hosts: radioactive, toxic and hazardous wastes, Wiley, Chichester, U.K, 2010.

[63] I. W. Donald, B. L. Metcalfe, R. N. J. Taylor, Review: The immobilisation of high level radioactive wastes using ceramics and glasses, Journal of Materials Science. 32 (1997) 5851–5887.

[64] G. G. Wicks, Immobilisation of hazardous and radioactive wastes into glass structures, Westinghouse Savannah River Technology Centre, 1997.

[65] W. J. Weber, A Navrotsky, S. Stefanovsky, E. R Vance, E. Vernaz, Materials Science of High-Level Nuclear Waste Immobilisation, MRS Bulletin. 34 (2009) 46–53.

[66] A.J. Connelly, R.J. Hand, P.A. Bingham, N.C. Hyatt, Mechanical properties of nuclear waste glasses, Journal of Nuclear Materials. 408 (2011) 188–193.

[67] M.W.A. Stewart, B.D. Begg, S. Moricca, R.A. Day, others, Low-Risk Tailored Waste Forms for Problematic High-level and Long-lived Nuclear Wastes, in: Pacific Basin Nuclear Conference 2006, Australian Nuclear Association, 2006: p. 745. http://search.informit.com.au/documentSummary;dn=225938704900819;res=IELENG (accessed February 3, 2016).

[68] J. Bates et al., Glass corrosion and irradiation damage behaviour, in: Plutonium Stabilisation and Immobilisation Workshop, Department of Energy, Washington, D.C., 1995: pp. 375–388.

[69] J.K. Bates et al, Performance of high plutonium-containing glasses for the immobilisation of surplus fissile materials, in: V. Jain, R. Palmer (Eds.), Environmental Issues and Waste Management Technologies in the Ceramic and Nuclear Industries, American Ceramic Society, Westerville, Ohio, 1995.

[70] A. E. Ringwood, S. E. Kesson, N. G. Ware, W. Hibberson, A. Major, Immobilisation of high level nuclear reactor wastes in SYNROC, Nature. 278 (1979) 219–223.

[71] D. Riley, W. Bourcier, J. Vienna, T. Meaker, D. Peeler, J. Maffa, Dissolution studies of plutonium oxide in LaBS glass, Lawrence Livermore National Lab., CA (United States), 1997. http://www.osti.gov/scitech/biblio/303868 (accessed February 3, 2016).

[72] W. Lutze, Silicate Glasses, in: Radioactive Waste Forms for the Future, Elsevier, Amsterdam, 1988.

[73] B. R. Myers, W. Brummond, G. Armantrout, H. Shaw, C. M. Jantzen, A. Jostsons, M. McKibben, D. Strachan, J. D. Vienna, Fissile materials disposition program technical evaluation panel summary report: ceramic and glass immobilisation options., Lawrence Livermore National Lab., CA (United States), 1997.

[74] J. E. Shelby, Chapter 3: Glass Melting, in: Introduction to Glass Science and Technology, 2nd ed., Royal Society of Chemistry, Cambridge, 2005: pp. 26–48.

[75] D. F. Bickford, A. Applewhite-Ramsey, C. M. Jantzen, K. G. Brown, Control of radioactive waste glass melters: I, preliminary general limits at Savannah River, Journal of American Ceramics Society. 73 (1990) 2896–2902.

[76] Rodney C Ewing, Werner Lutze, High-Level Nuclear Waste Immobilisation with Ceramics, Ceramics International. 17 (1991) 287–293.

[77] F.W. Clinard, E.M. Foltyn, R.C Ewing, Self-irradiation effects in 238Pu-substituted zirconolite I. Temperature dependence of damage, Journal of Nuclear Materials. 126 (1984) 245–254.

[78] R.C. Ewing, Nuclear waste forms for actinides, Proceedings of the National Academy of Sciences. 96 (1999) 3432–3439.

[79] E. R. Vance, C. J. Ball, R. A. Day, K. L. Smith, M. G. Blackford, B. D. Begg, P. J. Angel, Actinide and rare earth incorporation into zirconolite, Journal of Alloys and Compounds. 213/214 (1994) 406–409.

[80] E. R. Vance, Synroc: A suitable waste form for actinides, MRS Bulletin. (1994).

[81] B. D. Begg, R. A. Day, S. Moricca, M. W. A. Stewart, E.R. Vance, Low-risk waste forms to lock up high-level nuclear waste, in: WM'05, Arizona, 2005.

[82] Martin W.A. Stewart, Glass-Ceramic Waste Forms for Uranium and Plutonium Residues Wastes, in: Phoenix Arizona USA, 2013: pp. 1–12.

[83] Lumpkin et al., Alpha-recoil damage in zirconolite (CaZrTi2O7), Journal of Materials Research. 1 (1986) 564–576.

[84] K. L. Smith, Z. Zhang, P. McGlinn, D. Attard, H. Li, G. R. Lumpkin, M. Colella, T. McLeod, Z. Aly, E. Loi, S. Launng, K. P. Hart, M. Ridgway, W. J. Weber, S. Thevuthasan, The effect of radiation damage on zirconolite dissolution, Material Research Society. 757 (2003) 1–8.

[85] R.C. Ewing, T.J. Headley, Alpha-recoil damage in natural zirconolite (CaZrTi2O7), Journal of Nuclear Materials. 119 (1983) 102–109. doi:10.1016/0022-3115(83)90058-2.

[86] F.W. Clinard, E.M. Foltyn, R.C. Ewing, Stored energy in natural zirconolite and its synthetic counterpart after alpha recoil self-irradiation damage, Journal of Nuclear Materials. 185 (1991) 202–207.

[87] G. R. Lumpkin, M. Colella, K. L. Smith, R. H. Mitchell, A. O. Larsen, Chemical composition, geochemical alteration, and radiation damage effects in natural perovskite, Material Research Society. 506 (1998) 207–214.

[88] F. Bellatreccia, G. Della Ventura, E. Caprilli, C.T. Williams, G.C. Parodi, Crystal-chemistry of zirconolite and calzirtite from Jacupiranga, Sao Paulo (Brazil), Mineralogical Magazine. 63 (1999) 649–660.

[89] Ashkan Salamat et al., Structural transformations and disordering in zirconolite (CaZrTi2O7) at high pressure, Journal of Inorganic Chemistry. 52 (2013) 1550–1558.

[90] Tim J White, The microstructure and microchemistry of synthetic zirconolite, zirkelite and related phases, American Mineralogist. 69 (1984) 1156–1172.

[91] E.R. Vance, G.R. Lumpkin, M.L. Carter, D.J. Cassidy, C.J. Ball, R.A. Day, B.D. Begg, Incorporation of uranium in zirconolite (CaZrTi2O7), Journal of the American Ceramic Society. 85 (2002) 1853–1859.

[92] R.W. Cheary, A.A. Coelho, A site occupancy analysis of zirconolite CaZr x Ti 3-x O 7, Physics and Chemistry of Minerals. 24 (1997) 447–454. doi:10.1007/s002690050059.

[93] R. D. Shannon, Revised effective ionic radii and systematic studies of interatomic distances in halides and chalcogenides, Acta Crystallographica. A32 (1976) 751–767.

[94] E. R. Vance, P. J. Angel, B. D. Begg, R. A. Day, Zirconolite-rich titanate ceramics for high-level actinide wastes, Material Research Society. 333 (1994) 1–6.

[95] A. E. Ringwood, S. E. Kesson, N. G. Ware, W. O. Hibberson, A. Major, The SYNROC process: A geochemical approach to nuclear waste immobilisation, Geochemical Journal. 13 (1979) 141–165.

[96] A. Jostsons, Synroc - Progress and Future Prospects, Australian Nuclear Science and Technology Organisation, Australia, (date unknown).

[97] B. D. Begg, E. R. Vance, The incorporation of cerium in zirconolite, Material Research Society. 465 (1997) 333–340.

[98] S. Wang, K. Zhang, Incorporation of cerium in zirconolite-sphene synroc, Journal of Nuclear Materials. 443 (2013) 424–427.

[99] Daniel Caurant, Pascal Loiseau, Isabelle Bardez, Structural characterisation of Nd-doped Hf-zirconolite Ca(1-x)NdxHfTi(2-x)AlxO7 ceramics, Journal of Nuclear Materials. 407 (2010) 88–99.

[100] R. A. Day, S. Moricca, B. D. Begg, Y. Zhang, T. Eddowes, N. Webb, A. Brownscombe, H. Li, T. McLeod, E. Keegan, P. Yee, N. Scales, G. Smith, T. Tapsell, T. Hughes, S. Brodala, E. R. Vance, Effect of redox, temperature, and actinide concentration on actinide partitioning, chemical durability, and resistance to Pu retrieval of zirconolite glass-ceramics for Pu residues immobilisation. Phase III Part B: Demonstration of cans-free formulation using uranium and thorium. Phase III Part C: Validation of cans-free formulation using actual plutonium, Australian Nuclear Science and Technology Organisation, 2003.

[101] Y. Zhang, K.P. Hart, B.D. Begg, E.A. Keegan, A.R. Day, A. Brownscombe, M.W.A. Stewart, Durability of Pu-doped Titanate and Zirconate Ceramics Designed for Pu Immobilisation, in: MRS Proceedings, Cambridge Univ Press, 2002: pp. 1–7. http://journals.cambridge.org/abstract_S1946427400632396 (accessed February 3, 2016).

[102] D.M. Strachan, R.D. Scheele, E.C. Buck, A.E. Kozelisky, R.L. Sell, R.J. Elovich, W.C. Buchmiller, Radiation damage effects in candidate titanates for Pu disposition: Zirconolite, Journal of Nuclear Materials. 372 (2008) 16–31.

[103] R.B. Greegor et al., X-Ray Spectroscopic Investigation of Pu-substituted zirconolite, Journal of Nuclear Materials. 152 (1988) 270–277.

[104] M. Gilbert, J. H. Harding, Energetics of Ce and Pu incorporation into zirconolite waste-forms, Physical Chemistry Chemical Physics. 13 (2011) 13021–13025.

[105] R. Chang, Chapter 9: Chemical Bonding I: Basic Concepts, in: Chemistry, 8th edition, Mcgraw-Hill College, 2003.

[106] B.D. Begg, R.A. Day, A. Brownscombe, Structural Effect of Pu Substitutions on the Zr-Site in Zirconolite, MRS Proceedings. 663 (2000) 1–8. doi:10.1557/PROC-663-259.

[107] N. S. Mikhailenko, S. V. Stefanovsky, A. V. Ochkin, M. I. Lapina, Phase relations and elemental distribution among co-existing phases in the ceramics of the pseudobinary system CaZrTi2O7-CeAlO3, in: WM'06 Conference Proceedings, Tucson, Arizona, USA, 2006: pp. 1–10.

[108] C. Meng, X. Ding, W. Li, J. Zhao, H. Yang, Phase structure evolution and chemical durability studies of Ce-doped zirconolite–pyrochlore synroc for radioactive waste storage, Journal of Materials Science. 51 (2016) 5207–5215. doi:10.1007/s10853-016-9822-x.

[109] M. Jafar, P. Sengupta, S.N. Achary, A.K. Tyagi, Phase Evolution and Microstructural Studies in $CaZrTi_2O_7$-$Nd_2Ti_2O_7$ System, Journal of the American Ceramic Society. 97 (2014) 609–616. doi:10.1111/jace.12664.

[110] A. A. Coelho, R. W. Cheary, K. L. Smith, Analysis and Structural Determination of Nd-Substituted Zirconolite-4M, Journal of Solid State Chemistry. 129 (1997) 346–359.

[111] F. Mazzi, R. Munno, Calciobetafite (new mineral of the pyrochlore group) and related minerals from Campi Flegrei, Italy; crystal structures of polymignyte and zirkelite: comparison with pyrochlore and zirconolite, American Mineralogist. 68 (1983) 262–276.

[112] I.E. Grey, W.G. Mumme, T.J. Ness, R.S. Roth, K.L. Smith, Structural relations between weberite and zirconolite polytypes—refinements of doped 3T and 4M Ca2Ta2O7 and 3T CaZrTi2O7, Journal of Solid State Chemistry. 174 (2003) 285–295. doi:10.1016/S0022-4596(03)00222-6.

[113] J. W. Wald, P. Offermann, W. Lutze, in: North-Holland, Amsterdam, 1982.

[114] R.C. Ewing, A. Meldrum, L. Wang, S. Wang, Radiation-Induced Amorphization, Reviews in Mineralogy and Geochemistry. 39 (2000) 319–361. doi:10.2138/rmg.2000.39.12.

[115] W.J. Weber, The radiation-induced crystalline-to-amorphous transition in zircon, Journal of Materials Research. 9 (1994) 688.

[116] M. L. Swanson, J. R. Parsons, C. W. Hoelke, edited by J. W. Corbett and G. D. Watkins, Radiation Effects in Semiconductors, Gordon and Breach, New York, 1971.

[117] F. Lu, Y. Shen, X. Sun, Z. Dong, R. Ewing, J. Lian, Size dependence of radiation-induced amorphisation and recrystallisation of synthetic nanostructured CePO4 monazite, Acta Meterialia. 61 (2013) 2984–2992.

[118] S.X. Wang, G. R. Lumpkin, L. M. Wang, R. C. Ewing, Ion-irradiation-induced amorphisation of six zirconolite compositions, Nuclear Instruments and Methods in Physics Research B. (2000) 293–298.

[119] T. Beirau, C. Paulmann, U. Bismayer, Recrystallization of metamict allanite, Mineralogical Magazine. 75 (2011) 2393–2399. doi:10.1180/minmag.2011.075.4.2393.

[120] R.C. Ewing, W.J. Weber, F.W. Clinard, Radiation effects in nuclear waste forms for high-level radioactive waste, Progress in Nuclear Energy. 29 (1995) 63–127.

[121] H. Hamdy, El-Naby ABD, Role of geochemical alteration on the formation of secondary Zr- and U-bearing minerals in El Atshan trachyte, central Eastern Desert, Egypt, Journal of Mineralogical and Petrological Sciences. 104 (2009) 37–51. doi:10.2465/jmps.080506.

[122] J.C.M. de Hoog, M.J. van Bergen, Notes on the chemical composition of zirconolite with thorutite inclusions from Walaweduwa, Sri Lanka, Mineralogical Magazine. 61 (1997) 721–725.

[123] H.F. Chappell, M.T. Dove, K. Trachenko, R.E.A. McKnight, M.A. Carpenter, S.A.T. Redfern, Structural changes in zirconolite under α-decay, Journal of Physics: Condensed Matter. 25 (2013) 1–7. doi:10.1088/0953-8984/25/5/055401.

[124] E.M. Foltyn et al., Self-irradiation effects in 238Pu-substituted zirconolite: II. Effect of damage microstructure on recovery, Journal of Nuclear Materials. 136 (1985) 97–103.

[125] R.C. Ewing, L.M. Wang, Amorphization of zirconolite: alpha-decay event damage versus krypton ion irradiation, Nuclear Instruments and Methods in Physics Research Section B: Beam Interactions with Materials and Atoms. 65 (1992) 319–323. doi:10.1016/0168-583X(92)95059-Z.

[126] F.W. Clinard et al., Alpha decay self-irradiation damage in 238Pu-substituted zirconolite, Journal of Nuclear Materials. 105 (1982) 248–256.

[127] A.E. Ringwood, V.M. Oversby, W. Sinclair, The Effects of Radiation Damage on Synroc, in: C.J.M. Northrup (Ed.), Scientific Basis for Nuclear Waste Management, Springer US, Boston, MA, 1980: pp. 273–280. http://dx.doi.org/10.1007/978-1-4684-3839-0_33.

[128] V. M. Oversby, A. E. Ringwood, Leach testing of synroc and glass samples at 85 and 200c, Nuclear and Chemical Waste Management. 2 (1981) 201–206.

[129] E.R. Vance, M.W.A. Stewart, S.A. Moricca, Progress at ANSTO on SYNROC, Journal of the Australian Ceramics Society. 50 (2014) 38–48.

[130] D. J. Gregg, E. R. Vance, Synroc tailored waste forms for actinide immobilisation, Radiochimica Acta. 105 (2016) 907–925.

[131] B. B. Ebbinghaus, G. A. Armantrout, L. Gray, C. C. Herman, H. F. Shaw, R. A. Van Konynenburg, Plutonium Immobilisation Project Baseline Formulation, Lawrence Livermore National Lab., CA (United States), USA, 2000.

[132] A. Jostsons, E. R. Vance, Synroc for plutonium disposal, Proceeding Conference of Nuclear Science and Engineering. (1999) 61–66.

[133] A. D. Cozzi, J. C. Marra, Plutonium Immobilization Project (PIP) Precursor Material Calcine Temperature, Savannah River Site (US), 1999. http://www.osti.gov/scitech/biblio/9313 (accessed February 3, 2016).

[134] M. Stewart, SYNROC - demonstrated capabilities, project status and related Mo-99 production applicability, (2010).

[135] B. B. Ebbinghaus, R. A. Van Konynenburg, E. R. Vance, M. W. Stewart, A. Jostsons, J. S. Allender, D. T. Rankim, Ceramic composition for immobilisation of actinides, 6,137,025, 2000.

[136] K. A. Boult, J. T. Dalton, J. P. Evans, A. R. Hall, A. J. Inns, J. A. C. Marples, E. L. Paige, The preparation of fully-active Synroc and its radiation stability., UKAEA Harwell Lab, London (UK), 1988.

[137] Australian Nuclear Science and Technology Organisation, ANSTO program of research 1989-1900, IAEA-INIS, Australia, 1989.

[138] B. B. Ebbinghaus, O. H. Krikorian, E. R. Vance, M. W. A. Stewart, Ternary phase diagrams that relate to the plutonium immobilisation ceramic, Lawrence Livermore National Lab., CA (United States), 2001.

[139] B. B. Ebbinghaus, R. A. VanKonynenburg, F. J. Ryerson, E. R. Vance, M. W. A. Stewart, A. Jostsons, J. S. Allender, T. Rankin, J. Congdon, Ceramic formulation for the immobilisation of plutonium, http://www.wmsym.org/archives/1998/html/sess65/65-04/65-04.htm. (1998). http://www.wmsym.org/archives/1998/html/sess65/65-04/65-04.htm (accessed February 21, 2017).

[140] P.W. McMillan, Glass-ceramics, 2d ed, Academic Press, London ; New York, 1979.

[141] S. V. Raman, Microstructures and leach rates of glass-ceramic nuclear waste forms developed by partial vitrification in a hot isostatic press., Journal of Materials Science. 33 (1998) 1887–1895.

[142] R. A. Day, S. Moricca, B. D. Begg, Y. Zhang, T. Eddowes, N. Webb, A. Brownscombe, T. McLeod, E. Keegan, P. Yee, G. Smith, S. Brodala, E. R. Vance, Effect of redox, temperature, and actinide concentration on actinide partitioning and resistance to Pu retrieval of zirconolite glass-ceramics for Pu residues immobilisation. Phase III Extension March Progress report. Part A: Pu partitioning and Pu retrieval resistance of zirconolite glass-ceramics, under Ni-buffered redox conditions, inside nickel HIP cans, Part B: Chemical durability and Pu retrieval resistance of Pu-doped No. 3 Vit. Line V26 borosilicate glass at different redox, melting temperatures, and Pu concentrations, Australian Nuclear Science and Technology Organisation, 2004.

[143] Y. Zhang, D.J. Gregg, L. Kong, M. Jovanovich, G. Triani, Zirconolite glass-ceramics for plutonium immobilization: The effects of processing redox conditions on charge compensation and durability, Journal of Nuclear Materials. 490 (2017) 238–241. doi:10.1016/j.jnucmat.2017.04.015.

[144] R. A. Day, S. Moricca, B. D. Begg, T. Eddowes, N. Webb, A. Brownscombe, H. Li, Y. Zhang, T. McLeod, N. Scales, E. R. Vance, Effect of redox, temperature, and actinide concentration on actinide partitioning, chemical durability, and resistance to Pu retrieval of zirconolite glass-ceramics for Pu residues immobilisation. Phase III Part A: Validation of cans-included formulation using actual plutonium, Australian Nuclear Science and Technology Organisation, 2003.

[145] M.W.A. Stewart, E.R. Vance, Interim report - NNL work package W4.2 Examination of high-chlorine effects on the wasteform., ANSTO synroc, 2011.

[146] M.W.A. Stewart, E.R. Vance, Final report - NL work package W4.2: Examination of high-chlorine effects on the wasteform. With comments on HIP can interface reactions, ANSTO synroc, 2012.

[147] E. Maddrell, S. Thornber, N.C. Hyatt, The Influence of Glass Composition on Crystalline Phase Stability in Glass-Ceramic Wasteforms, Journal of Nuclear Materials. 456 (2015) 461–466. doi:10.1016/j.jnucmat.2014.10.010.

[148] W. N. Hess, Neutrons from (alpha, n) sources, Annals of Physics. 2 (1959) 115–133.

[149] W.B. Wilson, SOURCES: a code for calculating (,n), spontaneous fission, and delayed neutron sources and spectra, Radiation Protection Dosimetry. 115 (2005) 117–121. doi:10.1093/rpd/nci260.

[150] N. Ensslin, Nuclear Regulatory Commission, The origin of neutron radiation, in: Passive Nondestructive Assay of Nuclear Materials, US Department of Commerce, National Technical Information Service, Springfield, VA, 1991.

[151] T. Murata, K. Shibata, Evaluation of the (alpha,n) reaction nuclear data for light nuclei, Journal of Nuclear Science and Technology. 2 (2002) 76–79.

[152] P. Loiseau, D. Caurant, O. Majerus, N. Baffier, Crystallisation study of (TiO2, ZrO2)-rich SiO2-Al2O3-CaO glasses. Part 1 Preparation and characterisation of zirconolite-based glass-ceramics, Journal of Materials Science. 38 (2003) 843–852.

[153] M. L. Carter, H. Li, Y. Zhang, A. Gillen, E. Vance, HIPed Tailored Pyrochlore-rich Glass-ceramic wasteforms for the immobilisation of Nuclear waste, Scientific Basis for Nuclear Waste Management. 1124 (2008). doi:10.1557/PROC-1124-Q04-01.

[154] Ewan Maddrell, Development of High Volume Fraction Zirconolite Glass Ceramic Wasteforms, National Nuclear Laboratory, 2013.

[155] C. B. Boyer, Historical review of HIP equipment, in: Japan Research Association of Isostatic Pressing and Processing (Ed.), Hot Isostatic Pressing: Theory and Applications: Proceedings of the Third International Conference, Osaka, Japan, 10-14 June 1991, Elsevier Applied Science, London ; New York, 1992: pp. 465–510.

[156] The American Society of Mechanical Engineers, The evolution of HIP: Commemorating the first hot and cold isostatic pressing vessels, (1985) 1–12.

[157] M.H. Bocanegra-Bernal, Review Hot Isostatic Pressing (HIP) technology and its applications to metals and ceramics, Journal of Materials Science. 39 (2004) 6399–6420.

[158] H.V. Atkinson, S. Davies, Invited review: Fundamental Aspects of Hot Isostatic Pressing: An Overview, Metallurgical and Materials Transactions. 31A (2000) 2981–3000.

[159] N.L. Loh, K.Y. Sia, An overview of hot isostatic pressing, Journal of Materials Processing Technology. 30 (1992) 45–65.

[160] S. Forberg, T. Westermark, H. Larker, B. Widell, Synthetic rutile microencapsulation: A radioactive waste solidification system resulting in an extremely stable product, Scientific Basis for Nuclear Waste Management. 1 (1979) 201–205. doi:10.1007/978-1-4615-9107- 8_23.

[161] H.T. Larker, Hot Isostatic Pressing for the Consolidation and Containment of Radioactive Waste, in: G.J. McCarthy, R.L. Schwoebel, R.W. Potter, A.M. Friedman, J.G. Moore, H.C. Burkholder, W. Lutze (Eds.), Scientific Basis for Nuclear Waste Management: Volume 1 Proceedings of the Symposium on "Science Underlying Radioactive Waste Management," Materials Research Society Annual Meeting, Boston, Massachusetts, November 28–December 1, 1978, Springer US, Boston, MA, 1979: pp. 207–210. https://doi.org/10.1007/978-1-4615-9107-8_24.

[162] H. Larker, R. Tegman, Method of preparing spent nuclear fuel rods for long-term storage, US4491540 A, 1985.

[163] R. Tegman, M. Burstrom, Treatment of zircaloy cladding hulls by isostatic pressing, Robertsfors, Sweden, 1984.

[164] M. Maserumule, S. Moricca, Technical support for waste management of fission-based Mo-99 production, Australian Nuclear Science and Technology Organisation, 2014.

[165] K. J. Bateman, R. H. Rigg, J. D. Wiest, Hot isostatic pressing of ceramic waste form from spent nuclear fuel, in: Proceeding of ICONE10, Arlington, VA, USA, 2002: pp. 1–7.

[166] K. J. Bateman, E. P. Hart, W. M. McCartin, D. L. Wahlquist, Summary of calcine disposal development using hot isostatic pressing, Idaho National Laboratory, 2013.

[167] S. Moricca, A.J. Brownscombe, N. Webb, M.W.A. Stewart, R.A. Day, M. Hambley, E.R. Vance, V. Jostsons, Demonstration of Pu immobilization in synroc at the 50g of PuO2 scale, Lawrence Livermore National Lab., Livermore, CA (US), 1997. http://www.osti.gov/scitech/biblio/15007247 (accessed February 3, 2016).

[168] D. Wahlquist, K. Bateman, T. Malewitz, Remote Sealing of Canisters for Hot Isostatic Pressing, in: Proceeding of the ASME 2014 International Mechanical Congress & Exposition, 2014: pp. 1–7.

[169] E. Maddrell, A. Gandy, M. Stennett, The durability of iodide sodalite, Journal of Nuclear Materials. 449 (2014) 168–172.

[170] B.D. Preussner, J.A. Nenni, V.J. Balls, An Overview of Risk Management Planning for Hot-Isostatic Pressure Treatment of High-Level Waste Calcine for the Idaho Cleanup Project, in: ASME, 2012: p. 11. doi:10.1115/PVP2012-78150.

[171] K. M. Goff, M. F. Simpson, K. J. Bateman, D. W. Esh, Unirradiated testing of the demonstration-scale ceramic wasteform at ANL-West, Transactions of the American Nuclear Society. 77 (1997) 79–80.

[172] J. Ackerman, Wasteform development and characterisation in pyrometallurgical treatment of spent nuclear fuel, The American Nuclear Society. (1998) 1–11.

[173] Department of Energy (DOE), Amended record of decision: Idaho High-level waste facilities disposition final environmental impact statement revised by state, Federal Register. 75 (2010) 137.

[174] ARPANSA, Regulation and Licensing: ANSTO Mo99 and SyMo application information, Australian Radiation Protection and Nuclear Safet Agency. (2014).

[175] C.K. Cheung, E.L.R. Vance, M.W. Stewart, D.R. Brew, W. Bermudez, T. Eddowes, S. Moricca, The intermediate level liquid molybdenum-99 waste treatment process at the Australian nuclear science and technology organisation, Procedia Chemistry. 7 (2012) 548–553.

[176] M.W.A. Stewart, E.R. Vance, S.A. Moricca, D.R. Brew, C. Cheung, T. Eddowes, W. Bermudez, Immobilisation of Higher Activity Wastes from Nuclear Reactor Production of 99Mo, Science and Technology of Nuclear Installations. 2013 (2013) 1–16. doi:10.1155/2013/926026.

[177] Nuclear Decommissioning Authority (NDA), NDA: Plutonium Strategy - Current Position Paper, 2011.

[178] J. K. Mackenzie, R. Shuttleworth, A phenomenological theory of sintering, Proceeding of Physical Chemistry. 62 (1949) 833–852.

[179] C. R. Scales, E. R. Maddrell, J. Hobbs, R. Stephen, S. Moricca, M. W. A. Stewart, Building flexibility into the design of a pilot plant for the immobilisation of Pu containing residues and wastes., Brussels, Belgium, 2013.

[180] P. G. Heath, Hot isostatic pressing can substantially reduce the volume of nuclear waste, Research Features. (2017) 26–29.

[181] P. G. Heath, Scale-up of HIP technology for the treatment of Sellafield ILW sludges and slurries., in: Glasgow, 2015.

[182] M. D. Staiger, M. C. Swenson, Calcined waste storage at the Idaho Nuclear Technology and Engineering Center, Idaho National Laboratory, 2011.

[183] Australian Nuclear Science and Technology Organisation (ANSTO), Overview Presentation: SyMo Facility, (2012).

[184] Australian Nuclear Science and Technology Organisation (ANSTO), ANSTO's production of medical isotopes, (2014) 2.

[185] Nuclear Decommissioning Authority (NDA), Geological Disposal: Review of Alternative Radioactive Waste Management Options, 2017.

[186] C. L. Hoenig, H. T. Larker, Large scale densification of a nuclear waste ceramic by hot isostatic pressing, Journal of American Ceramics Society. 62 (1983) 1–62.

[187] Peter J. Goodhew, John Humphrey, Richard Beanland, Electron Microscopy and Analysis, Third Edition, 3, Illustrated, revised, CRC Press, 2000.

[188] R.F. Egerton, Physical principles of electron microscopy: an introduction to TEM, SEM, and AEM, Springer, New York, NY, 2005.

[189] J. Goodge, Electron probe micro-analyzer (EPMA), Geochemical Instrumentation and Analysis. (2017). https://serc.carleton.edu/research_education/geochemsheets/techniques/EPMA.html (accessed October 2, 2018).

[190] D. Henry, J. Goodge, Wavelength Dispersive X-ray Spectroscopy (WDS), Geochemical Instrumentation and Analysis. (2016). https://serc.carleton.edu/research_education/geochemsheets/wds.html (accessed October 2, 2018).

[191] J. Marra, C. Crawford, D. Peeler, Milestone letter report on composition measurements of "common simple" glass, Savannah River National Laboratory, Aiken, SC, USA, 2012.

[192] B. D. Cullity, S. R. Stock, Elements of X-ray diffraction, third edition, Prentice Hall, 2001.

[193] A. R. West, 3.3 X-ray diffraction, in: Basic Solid State Chemistry, second addition, Wiley & Sons, 1999: pp. 127–160.

[194] B. D. Cullity, S. R. Stock, Chapter 3 Diffraction I: Geometry, in: Elements of X-Ray Diffraction, third edition, Prentice Hall, 2001: pp. 89–118.

[195] L. B. McCusker, R. B. Von Dreele, D. E. Cox, D. Louer, P. Scardi, Rietveld refinement guidelines, Journal of Applied Crystallography. 32 (1999) 36–50.

[196] B. H. Toby, EXPGUI, a graphical user interface for GSAS, Journal of Applied Crystallography. 34 (2001) 210–213.

[197] A. R. West, Chapter 4: Other techniques: Microscopy, spectroscopy, thermal analysis, in: Basic Solid State Chemistry, second edition, Wiley & Sons, 1999: pp. 167–206.

[198] J. Clark, http://www.chemguide.co.uk/analysis/masspec/howitworks.html, ChemGuide. (2015). http://www.chemguide.co.uk/analysis/masspec/howitworks.html (accessed January 30, 2017).

[199] K.J.D. MacKenzie, M.E. Smith, Multinuclear solid-state NMR of inorganic materials, 1st ed, Pergamon, Oxford ; New York, 2002.

[200] L. J. Gardner, Assessment of Magnesium Potassium Phosphate Cement Systems for Radioactive Waste Encapsulation, The University of Sheffield, 2016.

[201] C. E. Housecroft, E. C. Constable, NMR spectroscopy, in: Chemistry: An Introduction to Organic, Inorganic and Physical Chemistry, 3rd ed., Pearson Prentice Hall, England, 2006: pp. 401–428.

[202] T.N. Mitchell, B. Costisella, NMR - from spectra to structures: an experimental approach, 2nd rev. and expanded ed, Springer, Berlin ; New York, 2007.

[203] P. Atkins, J. De Paula, Molecular spectroscopy 3: magnetic resonance, in: Atkins' Physical Chemistry, 8th ed., Oxford University Press, 2006: pp. 513–560.

[204] http://www.micromeritics.com/Product-Showcase/AccuPyc-II-1340.aspx, Micrometrics. (2014). http://www.micromeritics.com/Product-Showcase/AccuPyc-II-1340.aspx (accessed January 30, 2017).

[205] S. Calvin, XAFS for everyone, CRC Press, 2013.

[206] B. Ravel, M. Newville, *ATHENA* , *ARTEMIS* , *HEPHAESTUS* : data analysis for X-ray absorption spectroscopy using *IFEFFIT*, Journal of Synchrotron Radiation. 12 (2005) 537–541. doi:10.1107/S0909049505012719.

[207] A. V. Soldatov, T. S. Ivanchenko, S. Della Longa, A. Kotani, Y. Iwamoto, Crystal-structure effects in the Ce L3-edge X-ray absorption spectrum of CeO2: Multiple-scattering resonances and many-body final states, Physical Review B. 50 (1994) 5074–5080.

[208] K.O. Kvashnina, S.M. Butorin, P. Glatzel, Direct study of the f-electron configuration in lanthanide systems, Journal of Analytical Atomic Spectrometry. 26 (2011) 1265. doi:10.1039/c0ja00142b.

[209] M. C. Stennett, C. L. Freeman, A. S. Gandy, N. C. Hyatt, Crystal structure and non-stoichiometry of cerium brannerite: Ce0.975Ti2O5.95, Journal of Solid State Chemistry. 192 (2012) 172–178.

[210] P. B. J. Thompson, B. N. Nguyen, R. Nciholls, R. A. Bourne, J. B. Brazier, K. R. J. Lovelock, S. D. Brown, D. Wermeille, O. Bikondoa, C. A. Lucas, T. P. A. Hase, M. A. Newton, X-ray spectroscopy for chemistry in the 2-4keV energy regime at the XMaS beamline: ionic liquids, Rh and Pd catalysts in gas and liquid environments, and Cl contamination in y-Al2O3, Journal of Synchrotron Radiation. 22 (2015) 1426–1439.

[211] A. C. Thompson, J. Kirz, D. T. Attwood, E. M. Gullikson, M. R. Howells, J. B. Kortright, Y. Liu, A. L. Robinson, J. H. Underwood, K. Kim, I. Lindau, P. Pianetta, H. Winick, G. P. Williams, J. H. Scofield, Center for X-ray optics advanced light source. X-ray data booklet, 3rd ed., Lawrence Berkeley National Laboratory, 2009.

[212] W.E. Lee, M.I. Ojovan, M.C. Stennett, N.C. Hyatt, Immobilisation of Radioactive Waste in Glasses, Glass Composite Materials and Ceramics, Advances in Applied Ceramics. 105 (2006) 3–12. doi:10.1179/174367606X81669.

[213] E. R. Merz, C. E. Walter, Disposal of Weapon Plutonium, Kluwer Academic Publishers, Netherlands, 1996.

[214] E. Maddrell, S. Thornber, N. Hyatt, The Influence of Glass Composition on Crystalline Phase Stability in Glass-Ceramic Wasteforms, Journal of Nuclear Materials. (2014). doi:10.1016/j.jnucmat.2014.10.010.

[215] A. Ekmekyapar, A. Baysar, A. Kunkul, Dehydration Kinetics of Tincal and Borax by Thermal Analysis, Industry and Engineering Chemistry Research. 36 (1997) 3487–3490.

[216] A. Di Paola, M. Bellardita, L. Palmisano, Brookite, the Least Known TiO2 Photocatalyst, Catalysts. 3 (2013) 36–73. doi:10.3390/catal3010036.

[217] D. S. Schwartz, D. S. Shih, R. J. Lederich, R. L. Martin, D. A. Deuser, Development and Scale-up of the Low Density Core Process for Ti-64, in: Materials Research Society Symposium Proceedings, Materials Research Society, San Francisco USA, 1998: pp. 224–230.

[218] Y. Gu, X. Lui, G. Meng, D. Peng, Porous YSZ ceramics by water-based gelcasting, Ceramics International. 25 (1999) 705–709.

[219] H.V. Atkinson, S. Davies, Fundamental Aspects of Hot Isostatic Pressing: An Overview, Metallurgical and Materials Transactions. 31A (2000) 2981–3000.

[220] M. Nanko, K. Ishizaki, T. Fujikawa, Porous Ceramic Filters Produced by Hot Isostatic Pressing, Journal of American Ceramics Society. 77 (1994) 2437–2442.

[221] E. R. Vance, B. D. Begg, R. A. Day, C. J. Ball, Zirconolite-rich ceramics for actinides wastes, Material Research Society. 353 (1995) 767–774.

[222] S. Thornber, E. R. Maddrell, M. C. Stennett, N. C. Hyatt, The Consolidation of Glass-Ceramic Wasteforms by Hot Isostatic Pressing: Sample Optimisation, in: WM'16 Conference Proceedings, Phoenix Arizona USA, 2016.

[223] S. M. Thornber, P. G. Heath, G. P. Da Costa, M. C. Stennett, N. C. Hyatt, The effect of pre-treatment parameters on the quality of glass-ceramic wasteforms for plutonium immobilisation, consolidated by hot isostatic pressing., Journal of Nuclear Materials. 485 (2017) 253–261.

[224] H. Darwish, M. Gomaa, Effect of compositional changes on the structure and properties of alkali-alumino borosilicate glasses, Journal of Materials Science in Electronics. 17 (2006) 35–42.

[225] D. Massiot, F. Fayon, M. Capron, I. King, S. Le Calvé, B. Alonso, J.-O. Durand, B. Bujoli, Z. Gan, G. Hoatson, Modelling one- and two-dimensional solid-state NMR spectra: Modelling 1D and 2D solid-state NMR spectra, Magnetic Resonance in Chemistry. 40 (2002) 70–76. doi:10.1002/mrc.984.

[226] M. Magnin, S. Schuller, C. Mercier, J. Trébosc, D. Caurant, O. Majérus, F. Angéli, T. Charpentier, Modification of Molybdenum Structural Environment in Borosilicate Glasses with Increasing Content of Boron and Calcium Oxide by 95Mo MAS NMR, Journal of the American Ceramic Society. 94 (2011) 4274–4282. doi:10.1111/j.1551-2916.2011.04919.x.

[227] C.E. Housecroft, E.C. Constable, Chemistry: an introduction to organic, inorganic, and physical chemistry, 3rd ed, Pearson Prentice Hall, Harlow, England ; New York, 2006.

[228] A. J. Connelly, N. C. Hyatt, K. P. Travis, R. J. Hand, R. J. Short, The structural role of Zr within alkali borosilicate glasses for nuclear waste immobilisation, Journal of Non-Crystalline Solids. 357 (2011) 1647–1656.

[229] D. Caurant, P. Loiseau, I. Bardez, C. Gervais, Effect of Al2O3 concentration on zirconolite (Ca(Zr,Hf)Ti2O7) crystallization in (TiO2,ZrO2,HfO2)-rich SiO2–Al2O3–CaO–Na2O glasses, Journal of Materials Science. 42 (2007) 8558–8570. doi:10.1007/s10853-007-1810-8.

[230] M. D. Dolan, S.T. Misture, Analysis of glass batch reactions using in-situ X-ray diffraction. Part III. Borosilicate glass batches, Glass Technology. 45 (2004) 212–219.

[231] S. Wang, C. Peng, H. Xiao, J. Wu, Microstructural evolution and crystallisation mechanism of zircon from frit glaze, Journal of European Ceramic Society. 35 (2015) 2671–2678.

[232] National Institute of Industrial Research, ed., The complete book on glass and ceramics technology, Asia Pacific Business Press, Delhi, 2006.

[233] Y. Zhang, Z. Zhang, G. Thorogood, E.R. Vance, Pyrochlore based glass-ceramics for the immobilisation of actinide-rich nuclear wastes: from concept to reality, Journal of Nuclear Materials. 432 (2013) 545–547.

[234] E. R. Vance, K. P. Hart, R. A. Day, B. D. Begg, P. J. Angel, E. Loi, J. Weir, V. M. Oversby, Excess Pu disposition in zirconolite-rich synroc containing nepheline, Material Research Society. 412 (1996) 1–7.

[235] Gregory R. Lumpkin, Alpha-decay damage and aqueous durability of actinide host phases in natural systems, Journal of Nuclear Materials. 289 (2001) 136–166.

[236] K. L. Smith, G. R. Lumpkin, Defect and Process in the solid state: Geosciences Applications., in: Elsevier Science Publishers, Amsterdam, The Netherlands, 1993: pp. 401–422.

[237] D. Lützenkirchen-Hecht, R. Wagner, R. Frahm, XAFS at the new materials science beamline 10 at the DELTA storage ring, Journal of Physics: Conference Series. 712 (2016) 1–4. doi:10.1088/1742-6596/712/1/012026.

[238] B.D. Begg, E.R. Vance, G.R. Lumpkin, Charge Compensation and the Incorporation of Cerium in Zirconolite and Perovskite, MRS Proceedings. 506 (1997) 79–86. doi:10.1557/PROC-506-79.

[239] R.E. Sykora, L. Deakin, A. Mar, S. Skanthakumar, L. Soderholm, T.E. Albrecht-Schmitt, Isolation of Intermediate-Valent Ce(III)/Ce(IV) Hydrolysis Products in the Preparation of Cerium Iodates: Electronic and Structural Aspects of $Ce_2(IO_3)_6(OH_x)$ ($x \approx 0$ and 0.44), Chemistry of Materials. 16 (2004) 1343–1349. doi:10.1021/cm035147e.

[240] C. Lopez, X. Deschanels, J. M. Bart, J. M. Boubals, C. Den Auwer, E. Simoni, Solubility of actinide surrogates in nuclear glasses., Journal of Nuclear Materials. 312 (2003) 76–80.

[241] H. J. T. Ellingham, J. Soc Chem Ind. 63 (1944) 125.

[242] N. N. Greenwood, A. Earnshaw, Chemistry of the Elements, second, Butterworth-Heinemann, 1997.

[243] M.W. Stewart, S.A. Moricca, T. Eddowes, Y. Zhang, E.R. Vance, G.R. Lumpkin, M.L. Carter, M. Dowson, M. James, The use of hot-isostatic pressing to process nuclear waste forms, in: ASME 2009 12th International Conference on Environmental Remediation and Radioactive Waste Management, American Society of Mechanical Engineers, 2009: pp. 611–616. http://proceedings.asmedigitalcollection.asme.org/proceeding.aspx?articleid=1645834 (accessed February 3, 2016).

[244] J. Diwu, S. Wang, Z. Liao, P.C. Burns, T.E. Albrecht-Schmitt, Cerium(IV), Neptunium(IV), and Plutonium(IV) 1,2-Phenylenediphosphonates: Correlations and Differences between Early Transuranium Elements and Their Proposed Surrogates, Inorganic Chemistry. 49 (2010) 10074–10080. doi:10.1021/ic1015912.

[245] E. R. Maddrell, Personal communications, National Nuclear Laboratory. (2015).

[246] W. B. Wilson, R. T. Perry, E. F. Shores, W. S. Charlton, T. A. Parish, G. P. Estes, T. H. Brown, E. D. Arthur, M. Bozoian, T. R. England, D. G. Madland, J. E. Stewart, Sources

4C: A code for calculating (alpha,n), spontaneous fission, and delayed neutron sources and spectra, Los Alamos National Lab., NM (United States), 2002.

[247] I. C. Gauld, E. F. Shores, R. T. Perry, New neutron source algorithms in the ORIGEN-S Code, Proceedings of the 12th Biennial Topical Meeting off the Radiation Protection and Shielding Divisision of the American Nuclear Society. (2002) 1–10.

[248] S.M. Thornber, M.C. Stennett, N.C. Hyatt, Investigation of Ce incorporation in zirconolite glass-ceramics for UK plutonium disposition, MRS Advances. (2017) 1–6. doi:10.1557/adv.2017.32.

[249] S.M. Thornber, M.C. Stennett, E.R. Vance, D.T. Chavara, I. Watson, M. Jovanovic, J. Davis, D. Gregg, N.C. Hyatt, A preliminary validation study of PuO2 incorporation into zirconolite glass-ceramics, MRS Advances. (2018) 1–7. doi:10.1557/adv.2018.109.

[250] N. Metrich, M. J. Rutherford, Experimental study of chlorine behaviour in hydrous silicic melts, Geochimica et Cosmochica Acta. 56 (1991) 607–616.

[251] J. D. Webster, R. J. Kinzler, E. A. Mathez, Chloride and water solubility in basalt and andesite melts and implications for magmatic degassing, Geochimica et Cosmochica Acta. 63 (1999) 729–738.

[252] P.J. Wallace, Volatiles in subduction zone magmas: concentrations and fluxes based on melt inclusion and volcanic gas data, Journal of Volcanology and Geothermal Research. 140 (2005) 217–240. doi:10.1016/j.jvolgeores.2004.07.023.

[253] M. R. Carroll, J. D. Webster, Solubilities of sulfur, noble-gases, nitrogen, chlorine, and fluorine in magmas, Reviews in Mineralogy and Geochemistry. 30 (1994) 231–279.

[254] M. R. Carroll, Chlorine solubility in evolved alkaline magmas, Annals of Geophysics. 48 (2005) 619–631.

[255] C.W. Bjorklund, J.G. Reavis, J.A. Leary, K.A. Walsh, Phase Equilibria in the Binary Systems $PuCl_2$ –NaCl and $PuCl_2$ –LiCl, The Journal of Physical Chemistry. 63 (1959) 1774–1777. doi:10.1021/j150580a049.

[256] D. B. Dingwell, K. U. Hess, Melt viscosities in the system Na-Fe-Si-O-F-Cl: Contrasting effects of F and Cl in alkaline melts, American Mineralogist. 83 (1998) 1016–1021.

[257] D. R. Baker, J. Vaillancourt, Cl in albite melt: a volatile which increases melt viscosity, Eos. 76 (1995) F646 (abstr.).

[258] C. Hirayama, F. E. Camp, The effect of fluorine and chlorine substitution on the viscosity and fining of soda-lime and potassium-barium silicate glass, Glass Technology. 10 (1969) 123–127.

[259] A. Baasner, B. C. Schmidt, S. L. Webb, Compositional dependance of the rheology of halogen (F, Cl) bearing aluminosilicate melts, Chemical Geology. 346 (2013) 172–183.

[260] J. D. Webster, B. De Vito, Experimental and modelled solubilities of chlorine in aluminosilicate melts, consequences of magma evolution, and implications for

exsolution of hydrous chloride melt at Mt. Somma-Vesuvius., American Mineralogist. 87 (2002) 1046–1061.

[261] T.O. Sandland, L.-S. Du, J.F. Stebbins, J.D. Webster, Structure of Cl-containing silicate and aluminosilicate glasses: A 35Cl MAS-NMR study, Geochimica et Cosmochimica Acta. 68 (2004) 5059–5069. doi:10.1016/j.gca.2004.07.017.

[262] T. E. Graedel, W. C. Keene, The budget and cycle of Earth's natural chlorine, Pure and Applied Chemistry. 68 (1996) 1689–1697.

[263] A. Baasner, I. Hung, T. F. Kemp, R. Dupree, B. C. Schmidt, S. L. Webb, Constraints on the incorporation mechanism of chlorine in peralkaline and peraluminous Na2O-CaO-Al2O3-SiO2 glasses, American Mineralogist. (2014) 1713–1723.

[264] J. F. Stebbins, L. Du, Chloride ion sites in silicate and aluminosilicate glasses: A preliminary study by 35Cl solid-state NMR, American Mineralogist. 87 (2002) 359–363.

[265] K.A. Evans, J.A. Mavrogenes, H.S. O'Neill, N.S. Keller, L.-Y. Jang, A preliminary investigation of chlorine XANES in silicate glasses: INVESTIGATION OF CHLORINE XANES, Geochemistry, Geophysics, Geosystems. 9 (2008) 1–15. doi:10.1029/2008GC002157.

[266] D.A. McKeown, H. Gan, I.L. Pegg, W.C. Stolte, I.N. Demchenko, X-ray absorption studies of chlorine valence and local environments in borosilicate waste glasses, Journal of Nuclear Materials. 408 (2011) 236–245. doi:10.1016/j.jnucmat.2010.11.035.

[267] D. Haskel, FLUO: Correcting XANES for self-absorption in fluorescence measurements, University of Washington, 1999.

[268] F. Farges, G.E. Brown, J.J. Rehr, Ti K -edge XANES studies of Ti coordination and disorder in oxide compounds: Comparison between theory and experiment, Physical Review B. 56 (1997) 1809–1819. doi:10.1103/PhysRevB.56.1809.

[269] W. C. Hamilton, Significance tests on the crystallographic R factor, Acta Crystallographica. 18 (1965) 502–510.

[270] Nuclear Decommissioning Authority (NDA), Geological Disposal, Guidance on the application of the waste package specifications for the shielded waste packages, 2014.

[271] Nuclear DeNDA Waste & Nuclear Materials Unit, Letter of Compliance (LoC) Assessment process - position paper, Nuclear Decommissioning Authority, 2008.

[272] O. Johnsen, G. Ferraris, The nomenclature of eudialyte-group minerals, The Canadian Mineralist. 41 (2003) 785–794.

[273] O. Johnsen, J. D. Grice, The crystal chemistry of the eudialyte group, The Canadian Mineralist. 37 (1999) 865–891.

[274] I. Hassan, H. D. Grundy, The crystal structures of sodalite-group minerals, Acta Crystallographica. B40 (1984) 6–13.

[275] Y.N. Fang, C. Ritter, T.J. White, Crystal chemical characteristics of ellestadite-type apatite: implications for toxic metal immobilization, Dalton Trans. 43 (2014) 16031–16043. doi:10.1039/C4DT02088J.

[276] P. Ballirano, F. Bosi, Thermal behaviour of afghanite, an ABABACAC member of the cancrinite group, American Mineralogist. 97 (2012) 630–640.

[277] W. H. Zachariasen, Crystal chemical studies of the 5f-series of elements. I. New structure types, Acta Crystallographica. 1 (1948) 265–268.

[278] M. Wolcyrz, L. Kepinski, LETTERS TO THE EDITOR Reitveld refinement of the structure of CeOCl formed in Pd/CeO2 catalyst: notes on the existence of a stabilised tetragonal phase of La2O3 in La-Pd-O system, Journal of Solid State Chemistry. 99 (1992) 409–413.

[279] C. W. Ponader, G. E. Brown Jr., Rare earth elements in silicate glass/melt systems: II. Interactions of La, Gd, and Yb with halogens, Geochimica et Cosmochica Acta. 53 (1989) 2905–2914.

[280] P.A. Bingham, R.J. Hand, M.C. Stennett, N.C. Hyatt, M.T. Harrison, The Use of Surrogates in Waste Immobilization Studies: A Case Study of Plutonium, MRS Proceedings. 1107 (2008). doi:10.1557/PROC-1107-421.

[281] P.A. Korzhavyi, L. Vitos, D.A. Andersson, B. Johansson, Oxidation of plutonium dioxide, Nature Materials. 3 (2004) 225–228. doi:10.1038/nmat1095.

[282] R. T. Jubin, G. D. DelCul, B. D. Patton, R. S. Owens, D. W. Ramey, B. B. Spencer, Advanced fuel cycle initiative coupled end-to-end research, development, and demonstration project: Integrated off-gas treatment system design and initial performance-9226, in: WM2009 Conference, Phoenix Arizona USA, 2009: p. 13.

[283] S. Moricca, Method and apparatus for isolating material from its processing environment, EP 1 908 081 B1, 2008.

[284] S. Moricca, Container for receiving a substance including nuclear material, US 8,662,338 B2, 2010.

[285] L.R. Morss, ed., Chapter 7: Plutonium, in: The Chemistry of the Actinide and Transactinide Elements, 3rd ed., Springer, Dordrecht, 2010: pp. 1025–1033.

[286] B. D. Begg, E. R. Vance, B. A. Hunter, J. V. Hanna, Zirconolite transformation under reducing conditions, Journal of Materials Research. 13 (1998) 3181–3190.

[287] F. D. Richardson, J. H. E. Jeffes, The thermodynamics of substances of interest in iron and steel making from 0c to 2400c: I-oxides, Journal of Iron Steel Inst. 160 (1948) 261.

[288] L. M. Atlas, G. J. Schlehman, Defect equilibria of nonstoichiometric plutonium dioxide, Plutonium 1965 Proc. Third Int. Conf. on Plutonium. (1967) 838–844.

[289] N. Birks, G. H. Meier, F. S. Pettit, Introduction to the high temperature oxidation of metals, second, Cambridge University Press, Cambridge, 2006.

[290] H. D. Schreiber, G. B. Balazs, The chemistry of uranium in borosilicate glasses. 1. Simple base compositions relevant to the immobilisation of nuclear waste, Physics and Chemistry of Glasses. 23 (1982) 139–146.

[291] A.J. Connelly et al., The effect of uranium oxide additions on the structure of alkali borosilicate glasses, Journal of Non-Crystalline Solids. 378 (2013) 282–289.

Appendix A: List of Figures

Appendix B: List of Tables

Appendix C: List of Equations

Eq. 1 - $^{19}F + \alpha \rightarrow {}^{22}Na^{*} + {}^{1}_{0}n$; $^{22}Na + \gamma$ (1528 keV)

Eq. 2 - $^{19}F + \alpha \rightarrow {}^{22}Ne^{*} + {}^{0}_{1}p$; $^{22}Ne + \gamma$ (1275 keV)

Eq. 3 - $^{10}B + \alpha \rightarrow {}^{13}N + {}^{1}_{0}n$

Eq. 4 - $^{11}B + \alpha \rightarrow {}^{14}N + {}^{1}_{0}n$

Eq. 5 - $$P = \frac{2\gamma}{r}$$

Eq. 6 - $$Ca_{1-x}Zr_{1-y}Ce_{x+y}Ti_{2-2x}Al_{2x}O_7 + Na_2Al_{1+z}B_{1-z}Si_6O_{16}$$

Eq. 7 - $$70 \text{ wt. \% } Ca_{1-x}Zr_{1-y}Ce_{x+y}Ti_2O_7 + 30 \text{ wt. \% } Na_2Al_2Si_6O_{16}$$

Eq. 8 - $$n\lambda = 2d \sin\theta$$

Eq. 9 - $$\rho_s = \frac{m_a \times \rho_f}{m_a - m_f}$$

Eq. 10 - $$CaZrTi_2O_7 + 2[SiO_2] \rightleftharpoons ZrSiO_4 + CaTiSiO_5 + TiO_2$$

Eq. 11 - $$R = \frac{\sum_{i=1}^{N}\left(\mu_i(obs) - \mu_i(calc)\right)^2}{\sum_{i=1}^{N}\left(\mu_i(obs)\right)^2}$$

Appendix D: List of Abbreviations

<	-	Less than
>	-	More than
α	-	Alpha
γ	-	Gamma
AFIC	-	Active Furnace Isolation Chamber
AIP	-	American Isostatic Presses
AMEPT	-	Advanced Materials Engineering and Processing Technologies
AMPT	-	Advanced Powder Metallurgical (Fe-Cr-Al-Mo) Alloy
ANL	-	Argonne National Laboratory
atm	-	atmospheres
BEIS	-	Department of Business, Energy and Industrial Strategy
ANSTO	-	Australian Nuclear Science and Technology Organisation
BNFL	-	British Nuclear Fuels Limited
BO	-	Bridging Oxygen
BSE	-	Backscattered Secondary Electron
ca.	-	approximately
CIP	-	Cold Isostatic Pressing
CRN	-	Continuous Random Network
CSI	-	Co-ordination Stabilisation Index
DRS	-	Diffuse Reflection Spectroscopy
DTA	-	Differential Thermal Analysis
EDX	-	Energy Dispersive X-ray spectroscopy
EPMA	-	Electron Probe Micro-Analysis
EXAFS	-	Extended X-ray Absorption Fine Structure
f.u.	-	formula units
GDF	-	Geological Disposal Facility
HC	-	High Concentration
HIP	-	Hot Isostatic Pressing
HLW	-	High Level Waste

HPTE - High Performance Thermoplastic Elastomer

ILW - Intermediate Level Waste

INL - Idaho National Laboratory

IPA - Isopropanol

LaBS - Lanthanide BoroSilicate

LC - Low Concentration

LLNL - Lawrence Livermore National Laboratory

LLW - Low Level Waste

LoC - Letter of Compliance

MAS-NMR - Magic Angle Spinning - Nuclear Magnetic Resonance

MRN - Modified Random Network

MS - Mass Spectroscopy

NBO - Non-Bridging Oxygen

NNL - National Nuclear Laboratory

ONR - Office of Nuclear Regulation

PIP - Plutonium Immobilisation Project

PLC - Programmable Logic Controller

PNNL - Pacific Northwest National Laboratory

***p*O$_2$** - Partial Oxygen Pressure

PPE - Personal Protective Equipment

PSD - Particle Size Distribution

PUREX - Plutonium and Uranium Extraction

RWM - Radioactive Waste Management

SE - Secondary Electron

SEM - Scanning Electron Microscopy

SNF - Spent Nuclear Fuel

SOP - Standard Operating Procedure

SQP - Suitably Qualified Person

SR - Synchrotron Radiation

SRTC - Savannah River Technology Centre

SynRoc - Synthetic Rock

TGA - ThermoGravimetric Analysis

TRL - Technology Readiness Level

UHQ - Ultra-High Quality

UoS - University of Sheffield

VLLW - Very Low Level Waste

WINCO - Westinghouse Idaho Nuclear Company

XANES - X-ray Absorption Near Edge Spectroscopy

XRD - X-Ray Diffraction

Notes